



# A Drive System for Six-Phase Switched Reluctance Motors

Xu Deng

B.Eng., M.Eng.

A thesis submitted for the degree of

Doctor of Philosophy

October, 2017

School of Engineering

Newcastle University



To my husband, Xiang  
and daughter, Wei Yi



## **Abstract**

---

Switched Reluctance Motor (SRM) drives have been developed for decades. They are advantageous because of their simple structure, low manufacturing cost, high system reliability and wide speed range. They are one of the types of traction drive system employed for electric vehicles and are also used in the aviation industry. In this thesis, a novel six-phase SRM is selected to be the research object.

Two converters with fewer switches are proposed which are a circle converter and a circle converter with extra diodes. Conventional control methods are modified to suit the selected SRM and applied with the proposed converters. Simulation results are compared with the conventional Asymmetric Half Bridge (AHB) converter and show that the proposed converters can work effectively as the conventional converter.

In order to further reduce the torque ripple of the six-phase SRM, a Direct Torque Control (DTC) method is developed and applied to the AHB converter and the proposed converters. Simulation results show that the DTC method can reduce torque ripple throughout the whole speed range compared with traditional control methods.

The effects of winding connections on performance of the six-phase SRM are discussed to find the optimum winding connection type. The effects are first studied from a single-phase excitation. Subsequently five different winding connection types are proposed and analysed. Both torque performance and mutual inductance distribution are discussed through multi-phase excitation simulations and an optimum winding connection type is proposed.

A 4.0kW SRM test rig is built and commissioned in Newcastle University. Experimental results validate the optimum decoupled winding connection type, demonstrate the feasibility of the proposed circle converters, and verify the highly effective torque ripple reduction performance of the DTC method throughout the whole speed range.



## **Acknowledgement**

---

I would like to express my sincere appreciation to my supervisors, Prof. Barrie Mecrow and Dr. Shady Gadoue for their patient supervisions and supports during this project. Their continuous support, expertise, patience, and generous guidance made it possible.

I thank my colleagues Dr. Richard Martin, Dr. Steve McDonald and Dr. James Widmer for their generous guidance and advice in different stages of my PhD program. My great gratitude also goes to Dr. Dave Atkinson for his generous support, insightful comments and of course his general control board, which has helped almost all PhD students in our lab to implement their experimental works.

I would express my gratitude to James Richardson and Gordon Marshall for their assistance with my experimental work, Darren Mackie for his technical supports on PCB design and manufacture and all the staff in mechanical workshop for their technical supports on test rig assembling.

I am grateful to Prof. Mingyao Ma, Dr. Bing Ji, Dr. Haimeng Wu, Dr. Zheng Tan, Zheng Liu, Huaxia Zhan, and Xiang Lu for wonderful memories of lab life with them.

I would like to especially thank my parents, for their continuous love and encouragements throughout my PhD career. I thank my husband, Xiang, for firmly supporting my study and making me laugh while he is pursuing his PhD.

This work is funded by China Scholarship Council (CSC)/ Newcastle University Joint PhD scholarship.



ABSTRACT .....	I
ACKNOWLEDGEMENT .....	III
CONTENTS .....	V
LIST OF FIGURES .....	X
LIST OF TABLES .....	XIX
ACRONYMS AND SYMBOLS .....	XXI
CHAPTER 1. INTRODUCTION .....	- 1 -
1.1 Motivation and Objectives.....	- 1 -
1.2 Statement of Novelty .....	- 1 -
1.3 Publication arising from this work .....	- 2 -
1.4 Thesis Overview .....	- 2 -
CHAPTER 2. LITERATURE REVIEW .....	- 5 -
2.1 History and applications of SRMs.....	- 5 -
2.2 Fundamental principles of SRMs .....	- 6 -
2.2.1 Typical topologies .....	- 6 -
2.2.2 Mathematic model .....	- 7 -
2.2.3 Traditional control methods .....	- 9 -
2.3 Torque ripple and reduction methodologies for SRMs .....	- 10 -
2.3.1 Machine optimization methodologies .....	- 10 -
2.3.2 Control methods .....	- 14 -

2.4	Power converters for SRMs .....	19 -
2.5	Summary .....	20 -
CHAPTER 3. CONVERTER TOPOLOGIES FOR SIX-PHASE SRMS .....		22 -
3.1	Considered converter topologies for six-phase SRMs .....	22 -
3.1.1	Six-phase asymmetric half bridge converter .....	22 -
3.1.2	Six-phase split DC link converter .....	23 -
3.1.3	Three-phase full bridge converter .....	24 -
3.1.4	Six-phase dissipative converter .....	25 -
3.1.5	Six-phase bifilar converter .....	25 -
3.2	Circle converter for six-phase SRM .....	26 -
3.3	Simulation analysis .....	28 -
3.3.1	Current control .....	29 -
3.3.2	Voltage control .....	36 -
3.3.3	Converter loss analysis .....	39 -
3.4	Summary .....	42 -
CHAPTER 4. DIRECT TORQUE CONTROL OF SIX-PHASE SRMS .....		43 -
4.1	Basic principle of DTC method .....	43 -
4.1.1	DTC method for six-phase AHB converter .....	45 -
4.1.2	DTC method for circle converter .....	50 -
4.2	Simulation analysis with the AHB converter .....	52 -
4.2.1	Simulation results at 200r/min ( $T_{ref}=20Nm$ ) .....	52 -
4.2.2	Simulation results at 800r/min ( $T_{ref}=13.5Nm$ ) .....	55 -
4.2.3	Simulation results at 1500r/min ( $T_{ref}=10Nm$ ) .....	57 -
4.3	Simulation analysis with the circle converters .....	60 -
4.3.1	Simulation results at 200r/min ( $T_{ref}=20Nm$ ) .....	60 -
4.3.2	Simulation results at 800r/min ( $T_{ref}=13.5Nm$ ) .....	63 -

4.3.3	Simulation results at 1500r/min ( $T_{ref}=10Nm$ ).....	- 65 -
4.4	Summary.....	- 68 -
CHAPTER 5. EFFECTS OF WINDING CONNECTION ON PERFORMANCE OF SIX-PHASE SRMS.....		- 69 -
5.1	Topology of a six-phase SRM.....	- 69 -
5.2	Single-phase connection types.....	- 70 -
5.3	Five winding connection types .....	- 74 -
5.4	Multi-phase FEM analysis.....	- 77 -
5.5	Mutual-inductance effects .....	- 83 -
5.6	Summary.....	- 90 -
CHAPTER 6. DESIGN AND IMPLEMENTATION OF A SIX-PHASE SRM DRIVE SYSTEM		- 91 -
6.1	Overview of test rig .....	- 91 -
6.2	Hardware implementation .....	- 93 -
6.2.1	General control board .....	- 93 -
6.2.2	Power converters and gate drivers.....	- 94 -
6.2.3	Sensors and interfaces .....	- 97 -
6.2.4	The encoder and its interface.....	- 98 -
6.2.5	Safety circuit.....	- 101 -
6.2.6	Brake chopper.....	- 102 -
6.3	Software implementation.....	- 103 -
6.3.1	DSP.....	- 103 -
6.3.2	LABVIEW.....	- 104 -
6.4	Summary.....	- 105 -

CHAPTER 7. EXPERIMENTAL VALIDATION .....	106 -
7.1 Torque performance comparison of five winding connection types.....	106 -
7.1.1 Single-phase excitation tests .....	106 -
7.1.2 Multi-phase excitation tests .....	107 -
7.2 Experimental validation of traditional control methods and the proposed DTC method with the AHB converter .....	113 -
7.2.1 Traditional control methods .....	113 -
7.2.2 DTC method.....	118 -
7.3 Experimental validation of traditional control methods and the proposed DTC method with the proposed converters .....	124 -
7.3.1 Circle converter with traditional control methods .....	125 -
7.3.2 Circle converter with extra diodes by traditional control methods.....	133 -
7.3.3 Efficiency comparison .....	138 -
7.3.4 The circle converter with the DTC method .....	139 -
7.3.5 Torque-Speed Performance comparison.....	145 -
7.4 Summary .....	146 -
CHAPTER 8. CONCLUSIONS AND FUTURE WORK .....	148 -
8.1 Conclusions.....	148 -
8.1.1 Power converters.....	148 -
8.1.2 Advanced control techniques .....	148 -
8.1.3 Winding connection types.....	149 -
8.2 Future work.....	150 -
REFERENCES.....	152 -
APPENDIX A PROGRAM FOR DSP CONTROLLER.....	159 -
APPENDIX B SENSOR INTERFACES DESIGN .....	169 -

APPENDIX C TORSIONAL VIBRATION ..... - 173 -

---

List of figures

---

CHAPTER 2

Figure 2.1 Typical SRM stator and rotor topologies: (a) two-phase 4/2 pole SRM (b)three-phase 6/4 pole SRM (c) three-phase 12/8 pole SRM (d) four-phase 8/6 pole SRM.....- 6 -

Figure 2.2 Illustration for a m-phase SRM system. ....- 7 -

Figure 2.3 Control diagram and current waveform with the traditional CCC method .....- 9 -

Figure 2.4 Control diagram and current waveform with the traditional APC method .....- 9 -

Figure 2.5 Dimensions of punched hole on rotor[19] .....- 11 -

Figure 2.6 Comparison of the initial and optimized shapes[20] .....- 11 -

Figure 2.7 Comparison of the initial and optimized flux barrier inserted rotor shapes[21] - 12 -

Figure 2.8 Phase current for a six-phase SRM driven by full bridge converter [31].....- 12 -

Figure 2.9 Winding connection types for a 12/8 dual channel three-phase SRM: .....- 13 -

Figure 2.10 Transient torque waveforms: (a) with balanced current excitation (b) with increased chopping current excitation [42] .....- 14 -

Figure 2.11 Typical TSF profile for a three-phase SRM .....- 15 -

Figure 2.12 Control diagram of the DITC method .....- 17 -

Figure 2.13 Diagram of torque hysteresis controller: (a) single phase active (b) during commutation.....- 17 -

Figure 2.14 Definition of voltage vectors for three-phase SRM drive [60].....- 18 -

Figure 2.15 Classification of SRM power converters .....- 20 -

CHAPTER 3

Figure 3.1 Six-phase asymmetric half bridge converter .....- 22 -

Figure 3.2 Multi-level converter for six-phase SRMs .....- 23 -

Figure 3.3 Split DC link converter for six-phase SRMs .....- 24 -

Figure 3.4 Three-phase full bridge converter for six-phase SRMs.....- 24 -

List of figures

---

Figure 3.5 Dissipative converter for six-phase SRMs ..... - 25 -

Figure 3.6 Bifilar converter for six-phase SRMs ..... - 25 -

Figure 3.7 Circle converter for six-phase SRMs ..... - 26 -

Figure 3.8 Control diagram of six-phase circle converter ..... - 27 -

Figure 3.9 Nonlinear electromagnetic characteristics of a six-phase SRM prototype: (a) relationship between rotor position, current and flux-linkage (b) relationship between rotor position, current and torque ..... - 28 -

Figure 3.10 Dynamic simulation model of a six-phase SRM prototype ..... - 29 -

Figure 3.11 Simulation result of six phase current under current control (a) AHB converter (b) circle converter ..... - 30 -

Figure 3.12 Torque comparison between AHB converter and circle converter under current control: (a) same current reference (b) same average torque ..... - 31 -

Figure 3. 13 Part of the circle converter topology with three phases ..... - 33 -

Figure 3.14 Phase current with different conduction widths of circle converter ..... - 34 -

Figure 3.15 Current loops in circle converter ..... - 34 -

Figure 3.16 Circle converter with extra diodes for six-phase SRMs..... - 35 -

Figure 3.17 Optimized current waveforms of circle converter with extra diodes..... - 36 -

Figure 3.18 Phase voltage and current waveforms of the circle converter under ..... - 37 -

Figure 3.19 Phase voltage and current waveforms of circle converter with extra diodes under voltage control: (a) six phase voltage (b)six phase current ..... - 38 -

Figure 3.20 Torque comparison between circle converter and circle converter with extra diodes under voltage control ..... - 38 -

CHAPTER 4

Figure 4.1 Energy conversion diagram considering saturation ..... - 43 -

Figure 4.2 Phase voltage states: (a) state '+1' (b) state '0' (c) state '-1' ..... - 45 -

Figure 4.3 Arrangement of flux directions and voltage vectors ..... - 46 -

## List of figures

---

Figure 4.4 Definition of stator flux .....	47 -
Figure 4.5 Zones arrangement for AHB converter .....	48 -
Figure 4.6 Relationship between stator flux vector and voltage vector .....	48 -
Figure 4.7 Control diagram of the proposed DTC method for a six-phase SRM.....	50 -
Figure 4.8 Zones arrangement for the circle converter .....	51 -
Figure 4.9 Simulation results of the AHB converter at 200r/min: (a) six phase flux, current and torque of the CCC method (b) six phase flux, current and torque of the DTC method (c) instantaneous torque and flux speed of the DTC method.....	54 -
Figure 4.10 Total torque output and flux trajectory comparison of the AHB converter at 200r/min: (a) total torque output of CCC method and DTC method (b) flux trajectory of CCC method and DTC method.....	55 -
Figure 4.11 Simulation results of the AHB converter at 800r/min: (a) six phase flux, current and torque of CCC method (b) six phase flux, current and torque of DTC method....	56 -
Figure 4.12 Total torque output and flux trajectory comparison of the AHB converter at 800r/min: (a) total torque output of CCC method and DTC method (b) flux trajectory of CCC method and DTC method.....	57 -
Figure 4.13 Simulation results of the AHB converter at 1500r/min: (a) six phase flux, current and torque of APC method (b) six phase flux, current and torque of DTC method....	58 -
Figure 4.14 Total torque output and flux trajectory comparison of the AHB converter at 1500r/min: (a) total torque output of CCC method and DTC method (b) flux trajectory of CCC method and DTC method.....	59 -
Figure 4.15 Simulation results of the circle converter at 200r/min: (a) six phase flux, current and torque of the CCC method (b) six phase flux, current and torque of the DTC method (c) instantaneous torque and flux speed of the DTC method.....	62 -
Figure 4.16 Total torque output and flux trajectory comparison of the circle converter at 200r/min: (a) total torque output of the CCC method and the DTC method (b) flux trajectory of the CCC method and the DTC method. ....	63 -
Figure 4.17 Simulation results of the circle converter at 800r/min: (a) six phase flux, current and torque of CCC method (b) six phase flux, current and torque of DTC method....	64 -

Figure 4.18 Total torque output and flux trajectory comparison of the circle converter at 800r/min: (a) total torque output of CCC method and DTC method (b) flux trajectory of CCC method and DTC method ..... - 65 -

Figure 4.19 Total torque output and flux trajectory comparison of the circle converter at 1500r/min: (a) six phase flux, current and torque of APC method (b) six phase flux, current and torque of the DTC method..... - 66 -

Figure 4.20 Total torque output and flux trajectory comparison of the circle converter at 1500r/min: (a) total torque output of the CCC method and the DTC method (b) flux trajectory of the CCC method and the DTC method. .... - 67 -

**CHAPTER 5**

Figure 5.1 Six-phase 12/10 SRM prototype: (a) wound stator (b) rotor ..... - 69 -

Figure 5.2 2D FEA model for the six-phase SRM ..... - 70 -

Figure 5.3 Flux distribution of single phase excitation for a six-phase SRM: (a) N-S connection (b) N-N connection. .... - 71 -

Figure 5.4 Six phase flux linkages of N-N and N-S connection with single-phase excitation ... - 72 -

Figure 5.5 Single-phase output torque and six single-phase torque summation of N-S and N-N connection..... - 73 -

Figure 5.6 Phase flux linkage of single phase excitation: (a) N-S connection (b) N-N connection..... - 74 -

Figure 5.7 The winding connections: (a) Type 1: NSNSNSNSNSNS (b) Type 2: NSNSNSSNSNS (c) Type 3: NNSSNNSSNNSS (d) Type 4: NNNSSNNNNSSS (e) Type 5: NNNNNSSSSSS ..... - 76 -

Figure 5.8 Six phase unipolar excitation currents in FEM analysis ..... - 77 -

Figure 5.9 FEM output torque of five winding connection types ..... - 78 -

Figure 5.10 Output torques of five winding configurations with thicker core back. .... - 79 -

Figure 5.11 Comparisons of flux distributions when phase A,E,F are active ..... - 80 -

## List of figures

---

Figure 5.12 Comparisons of flux distributions when phase A,B,F are active .....	81 -
Figure 5.13 Comparisons of flux distributions when phase A,B,C are active .....	82 -
Figure 5.14 Definition of three conducting phases .....	83 -
Figure 5.15 Six phase flux linkages of five different winding connection types excited by 180° square wave current: (a) Type 1 (b) Type 2 (c) Type 3 (d) Type 4 (e) Type 5.....	86 -
Figure 5.16 Six phase mutual-inductances of three different winding connection types excited by 180° square wave current: (a) Type 1 (b) Type 2 (c) Type 3.....	87 -
Figure 5.17 Six phase current of five different winding connection types under volatge control at high speed: (a) Type 1 (b) Type 2 (c) Type 3 (d) Type 4 (e) Type 5.....	90 -

## CHAPTER 6

Figure 6.1 Schematic diagram of the test rig .....	91 -
Figure 6.2 Photographs of the test rig: (a) machanical part (b) electrical part .....	92 -
Figure 6.3 Internal photographs of the drive box.....	93 -
Figure 6.4 General control board .....	93 -
Figure 6.5 TMS320F28335 eZdsp board.....	94 -
Figure 6.6 Construction of power converters and gate drive solution: (a) IGBT module SKM150GAR12T4 and SKM150GAL12T4 (b) IGBT driver core (c) adaptor board (d) heat sink assembly photograph .....	95 -
Figure 6.7 Construction of three different converters: (a) AHB converter (b) circle converter (c) circle converter with extra diodes.....	96 -
Figure 6.8 Output waveform of ePWM module and gate drive waveform .....	96 -
Figure 6.9 Sensor borads: (a) current sensor board (b) voltage sensor board.....	97 -
Figure 6.10 Tested conversion results of current and voltage sensor board.....	98 -
Figure 6.11 Absolute encoder HENGSTLER AC 58 .....	98 -
Figure 6.12 Interface between encoder and general control board: (a) schematic (b) PCB .....	99 -

Figure 6.13 Communication waveforms between DSP SPI module and encoder: (a) differential data and clock signals on encoder side (b) enable signal, clock signal and data on DSP side..... - 100 -

Figure 6.14 Conversion algorithm from gray code to natural binary ..... - 101 -

Figure 6.15 Schematic and photographs of safety circuit ..... - 102 -

Figure 6.16 Schematic for brake chopper..... - 102 -

Figure 6.17 Flow charts of DSP control programs..... - 103 -

Figure 6.18 LABVIEW front user control panel..... - 104 -

CHAPTER 7

Figure 7.1 Single-phase excitation test waveforms: (a) N-S connection output torque (b) N-N connection output torque ..... - 106 -

Figure 7.2 Current waveforms of five winding connection types under current control: (a) winding connection Type 1 (b) winding connection Type 2 (c) winding connection Type 3 (d) winding connection Type 4 (e) winding connection Type 5 ..... - 108 -

Figure 7.3 Output torque of five winding connection types under current control at 200r/min : (a) winding connection Type 1 (b) winding connection Type 2 (c) winding connection Type 3 (d) winding connection Type 4 (e) winding connection Type 5 ..... - 109 -

Figure 7.4 Output torque comparison of five winding connection types under current control at 200/min: (a) average output torque (b) torque ripple ratio ..... - 110 -

Figure 7.5 Voltage and current waveforms of five winding connection types under voltage control: (a) Type 1 (b) Type 2 (c) Type 3 (d) Type 4 (e) Type 5 ..... - 112 -

Figure 7.6 Output torque comparison of five winding connection types under voltage control.- 112 -

Figure 7.7 Current waveforms with different loads at 200r/min under current control with the AHB converter: (a) 5.0Nm (b) 10.0Nm (c) 15.0Nm (d) 20.1Nm ..... - 114 -

Figure 7.8 Output torque waveforms with different loads at 200r/min under current control with the AHB converter: (a) 5.0Nm (b) 10.0Nm (c) 14.9Nm (d) 20.1Nm ..... - 115 -

List of figures

---

Figure 7.9 Current waveforms with different loads at 800r/min under current control with the AHB converter: (a) 5.0Nm (b) 10.0Nm (c) 15.0Nm (d) 20.0Nm.....- 116 -

Figure 7.10 Output torque waveforms with different loads at 800r/min under current control with the AHB converter: (a) 5.1Nm (b) 10.0Nm (c) 14.9Nm (d) 20.1Nm.....- 117 -

Figure 7.11 Current waveforms with different loads at 1500r/min under voltage control with the AHB converter: (a) 6.0Nm (b) 10.0Nm.....- 118 -

Figure 7.12 Output torque waveforms with different loads at 1500r/min under voltage control with the AHB converter: (a) 6.2Nm (b) 10.1Nm.....- 118 -

Figure 7.13 Current waveforms with different loads at 200r/min under DTC method with the AHB converter: (a) 5.0Nm (b) 10.0Nm (c) 15.0Nm (d) 20.0Nm.....- 119 -

Figure 7.14 Output torque waveforms with different loads at 200r/min under DTC method with the AHB converter: (a) 5.1Nm (b) 10.2Nm (c) 15.0Nm (d) 20.1Nm.....- 120 -

Figure 7.15 Current waveforms with different loads at 800r/min under DTC method with the AHB converter: (a) 5.0Nm (b) 10.0Nm (c) 15.0Nm (d) 20.0Nm.....- 121 -

Figure 7.16 Output torque waveforms with different loads at 800r/min under DTC method with the AHB converter: (a) 5.0Nm (b) 10.0Nm (c) 15.1Nm (d) 20.2Nm.....- 122 -

Figure 7.17 Current waveforms with different loads at 1500r/min under DTC method with the AHB converter: (a) 6.0Nm (b) 10.0Nm.....- 123 -

Figure 7.18 Output torque waveforms with different loads at 1500r/min under DTC method with the AHB converter: (a) 6.2Nm (b) 10.0Nm.....- 123 -

Figure 7.19 Current waveforms with different loads at 200r/min by 140° current control with the circle converter: (a) 5.0Nm (b) 10.0Nm (c) 15.0Nm (d) 20.0Nm .....- 126 -

Figure 7.20 Output torque waveforms with different loads at 200r/min by 140° current control with the circle converter: (a) 5.0Nm (b) 10.0Nm (c) 15.0Nm (d) 20.0Nm .....- 126 -

Figure 7.21 Current waveforms with different loads at 800r/min by 140° current control with the circle converter: (a) 5.0Nm (b) 10.0Nm (c) 15.0Nm (d) 20.0Nm .....- 127 -

Figure 7.22 Output torque waveforms with different loads at 800r/min with 140° current control with the circle converter: (a) 5.0Nm (b) 10.0Nm (c) 15.0Nm (d) 20.0Nm...- 128 -

List of figures

---

Figure 7.23 Current waveforms with different loads at 200r/min with 120° current control with the circle converter: (a) 5.0Nm (b) 10.0Nm (c) 15.0Nm (d) 20.0Nm..... - 129 -

Figure 7.24 Output torque waveforms with different loads at 200r/min with 120° current control with the circle converter: (a) 5.0Nm (b) 10.0Nm (c) 15.0Nm (d) 20.0Nm .. - 130 -

Figure 7.25 Current waveforms with different loads at 800r/min with 120° current control with the circle converter: (a) 5.0Nm (b) 10.0Nm (c) 15.0Nm (d) 20.0Nm..... - 131 -

Figure 7.26 Output torque waveforms with different loads at 800r/min with 120° current control with the circle converter: (a) 5.0Nm (b) 9.8Nm (c) 15.1Nm (d) 20.0Nm .... - 132 -

Figure 7.27 Current waveforms with different loads at 1500r/min under voltage control with the circle converter: (a) 6.0Nm (b) 10.0Nm ..... - 132 -

Figure 7.28 Output torque waveforms with different loads at 1500r/min under voltage control with the circle converter: (a) 6.0Nm (b) 10.0Nm ..... - 133 -

Figure 7.29 Current waveforms with different loads at 200r/min under current control with the circle converter with extra diodes: (a) 5.0Nm (b) 10.0Nm (c) 15.0Nm (d) 20.0Nm - 134 -

Figure 7.30 Output torque waveforms with different loads at 200r/min under current control with the circle converter with extra diodes: (a) 5.1Nm (b) 10.0Nm (c) 15.2Nm (d) 20.0Nm ..... - 135 -

Figure 7.31 Current waveforms with different loads at 800r/min under current control with the circle converter with extra diodes: (a) 5.0Nm (b) 10.0Nm (c) 15.0Nm (d) 20.0Nm - 136 -

Figure 7.32 Output torque waveforms with different loads at 800r/min under current control with the circle converter with extra diodes: (a) 5.0Nm (b) 10.0Nm (c) 15.0Nm (d) 20.0Nm ..... - 137 -

Figure 7.33 Current waveforms with different loads at 1500r/min under voltage control with the circle converter with extra diodes: (a) 6.0Nm (b) 10.0Nm..... - 138 -

Figure 7.34 Output torque waveforms with different loads at 1500r/min under voltage control with the circle converter with extra diodes: (a) 6.0Nm (b) 10.0Nm ..... - 138 -

Figure 7.35 Current waveforms with different loads at 200r/min under DTC method with the circle converter: (a) 5.0Nm (b) 10.0Nm (c) 15.0Nm (d) 20.0Nm..... - 141 -

Figure 7.36 Output torque waveforms with different loads at 200r/min under DTC method with the circle converter: (a) 5.0Nm (b) 10.0Nm (c) 15.1Nm (d) 20.1Nm..... - 141 -

List of figures

---

Figure 7.37 Current waveforms with different loads at 800r/min under DTC method with the circle converter: (a) 5.2Nm (b) 10.0Nm (c) 15.0Nm (d) 20.1Nm .....- 143 -

Figure 7.38 Output torque waveforms with different loads at 800r/min by DTC with the circle converter: (a) 5.2Nm (b) 10.0Nm (c) 15.0Nm (d) 20.1Nm .....- 143 -

Figure 7.39 Current waveforms with different loads at 1500r/min by DTC with the circle converter: (a) 6.0Nm (b) 10.0Nm .....- 144 -

Figure 7.40 Output torque waveforms with different loads at 1500r/min by DTC with the circle converter: (a) 5.9Nm (b) 10.0Nm .....- 144 -

Figure 7.41 Torque-Speed performance and system efficiency comparison under fixed maximum DC link current .....- 145 -

CHAPTER 8

Figure 8.1 Optimum winding connection type for the six-phase SRM .....- 150 -

APPENDIX B

Figure B.1 Schematic of general interface circuitry between current/voltage sensor board and the DSP .....- 169 -

Figure B.2 Simplified schematic of general interface circuitry between LA 55-P and and the DSP .....- 169 -

Figure B.3 Final schematic of general interface circuitry between LA 55-P and the DSP- 171 -

Figure B.4 Simplified schematic of interface circuitry between LV 25-P and the DSP....- 171 -

Figure B.5 Final schematic of general interface circuitry between LV 25-P and the DSP- 172 -

APPENDIX C

Figure C. 1 A two-disc torsional system.....- 173 -

CHAPTER 2

Table 2.1 Typical TSFs for SRMs [46] ..... - 16 -  
Table 2.2 Switching table for three-phase SRM [60] ..... - 19 -

CHAPTER 3

Table 3.1 Components and connection requirement comparisons between proposed circle converter and AHB converter for a six-phase SRM..... - 27 -  
Table 3.2 Phase voltage combination comparison between the AHB converter and the circle converter ..... - 32 -  
Table 3.3 Phase voltage combination comparison of the proposed circle converter with the conduction width limitation..... - 34 -  
Table 3.4 Device parameters and dynamic simulation settings of the model ..... - 39 -  
Table 3.5 Device losses comparisons ..... - 40 -  
Table 3.6 System efficiency comparisons ..... - 41 -

CHAPTER 4

Table 4.1 Twelve voltage vectors for AHB converter..... - 47 -  
Table 4.2 Switching table of DTC method for six-phase AHB converter ..... - 49 -  
Table 4.3 Six voltage vectors for the circle converter ..... - 51 -  
Table 4.4 Switching table for the DTC method with the circle converter..... - 52 -

CHAPTER 5

Table 5.1 Design parameters of the six-phase SRM prototype [32] ..... - 70 -  
Table 5.2 Settings of the 2D FEA model for the single-phase excitation simulation ..... - 71 -

List of tables

---

Table 5.3 Six phase conduction combinations.....- 83 -  
Table 5.4 Settings of the FEA model of the high speed multi-phase excitation simulation - 88 -

CHAPTER 7

Table 7.1 Single-phase average torque comparison between FEA and experimental test - 107 -  
Table 7.2 Multi-phase average torque and torque ripple comparisons between FEA and  
experimental test .....- 109 -  
Table 7.3 Torque ripple comparison between simulation and experimental test of the AHB  
converter.....- 124 -  
Table 7.4 System efficiency comparison between three converters with traditional control  
methods .....- 139 -  
Table 7.5 Torque ripple comparison between simulation and experimental test of the circle  
converter.....- 145 -  
Table 7.6 System efficiency comparison under fixed maximum DC link current .....- 146 -

## Acronyms and symbols

---

### List of Symbols

$T^*$	Torque reference
$T_e$	Instantaneous electromagnetic torque
$T_{av}$	Average torque
$V_k$	Terminal voltage of phase k
$i_k$	Current of phase k
$\Psi_k$	Flux linkage of phase k
$R_k$	Resistance of phase k
$\theta$	Rotor position
$e$	Back-EMF
$\omega$	Rotational speed
$J$	Rotational inertia
$B$	Frictional coefficient
$T_L$	Load torque
$W_e$	Electric energy
$W_c$	Co-energy
$W_m$	Mechanical energy
$W_f$	Magnetic field stored energy
$T_{max}$	Maximum value of torque
$T_{min}$	Minimum value of torque
$\theta_{on}$	Turn-on angle
$\theta_{off}$	Turn-off angle
$\theta_{ov}$	Overlap angle
$\theta_p$	One rotor cycle

$T_k^*$	Torque reference of phase k
$\Delta T_{1/2}$	Inner/outer torque hysteresis band
$V1/\dots/6$	Six voltage vectors
$U1/\dots/12$	Twelve voltage vectors
$V_{dc}$	DC link voltage
$\psi_\alpha$	Stator flux linkage component along $\alpha$ -axis
$\psi_\beta$	Stator flux linkage component along $\beta$ -axis
$\psi_s$	Stator flux linkage
$\psi_s^*$	Stator flux linkage reference
$\delta$	Angle of stator flux linkage
$\Psi_a/\dots/\Psi_f$	Six phase flux linkage
C	Capacitance value
L	Inductance value
M	Mutual-inductance value
$R_{TH}$	Equivalent resistance
$f_c$	Cut off frequency of the RC filter

### List of acronyms

SRM	Switched Reluctance Motor
MCSR	Mutually Coupled switched reluctance motors
AHB	Asymmetric Half Bridge
CCC	Current Chopping Control
APC	Angle Position Control
TRR	Torque Ripple Ratio
TSF	Torque Sharing Function
DITC	Direct Instantaneous Torque Control
DTC	Direct Torque Control
FEM	Finite Element Modelling
FEA	Finite Element Analysis
N-N	North-North
N-S	North-South
DC	Direct Current
AC	Alternating Current
DSP	Digital Signal Processor
DAC	Digital to Analogue Converter
ADC	Analogue to Digital Converter
GPIO	General-Purpose Input Output
ISR	Interrupt Service Routine
ePWM	Enhanced Pulse Width Modulation
PWM	Pulse Width Modulation
IGBT	Insulated Gate Bipolar Transistor
SPI	Serial Peripheral Interface

## Acronyms and symbols

---

SCI	Serial Communications Interface
EMF	Electromotive Force
PMSM	Permanent Magnet Synchronous Machine
SPISOMI	Peripheral Interface Slave Output Master Input
MSB	Most Significant Bit
CCS	Code Composer Studio
GUI	Graphical User Interface

---

## Chapter 1. Introduction

---

This doctoral thesis presents work undertaken to develop a drive system for a novel six-phase SRM (Switched Reluctance Machine). This chapter introduces the objectives and motivation for a six-phase SRM drive system, novelties and publications arising from this work, and the structure and contents of this thesis.

### 1.1 Motivation and Objectives

SRM drives have been developed for decades. They are advantageous because of their simple structure, low manufacturing cost, high system reliability, high efficiency and wide speed range. They are one of the types of traction drive system employed for electric vehicles and are also proposed for use in the aviation industry. The biggest drawback of an SRM is its large torque ripple due to its doubly salient structure. A six-phase SRM was proposed by Newcastle University and it reduced the torque ripple by increasing phase overlapping.

This PhD thesis aims to design and build a six-phase SRM drive system to further reduce the torque ripple which has already benefitted from increased number of phases. The Objectives are:

- To design a power converter for the six-phase SRM
- To minimize the number of power devices, energy storage elements and the number of connections between the machine and the power converter
- To design a torque ripple minimization control method for the six-phase SRM
- To find an optimized decoupled winding connection configuration for the six-phase SRM
- To find an optimized winding connection configuration with smaller torque ripple for the six-phase SRM
- To build a six-phase SRM drive experimental test rig

### 1.2 Statement of Novelty

The novelty in this work originates from novel drive systems for traditional SRM drives. SRMs are already a common choice in many industry applications because they cost less and are more fault-tolerant than other motors. Although many SRM drives and control techniques have been published in the literature, a novel drive system for a six-phase SRM is

realised for the first time in this thesis. The specific novelty claims in this work are given below.

- ❖ A drive system based on traditional control techniques for six-phase SRMs
- ❖ Optimized decoupling winding connections for six-phase SRMs
- ❖ Optimized torque ripple reduction winding connections for six-phase SRMs
- ❖ A direct torque control technique to reduce torque ripple for six-phase SRMs
- ❖ Converters with minimised number of switches for six-phase SRMs

### 1.3 Publication arising from this work

- (1) Xu Deng, Barrie Mecrow and Shady Gadoue, "A novel converter topology for 6 phase switched reluctance motor drives," in *39th Annual Conference on Industrial Electronics Society (IECON) of the IEEE*, 2013, pp. 268-273.
- (2) Xu Deng, Barrie Mecrow, Shady Gadoue, and Richard Martin, "A torque ripple minimization method for six-phase switched reluctance motor drives," in *XXII International Conference on Electrical Machines (ICEM)*, 2016, pp. 955-961.
- (3) Xu Deng, Barrie Mecrow, Haimeng Wu and Richard Martin, "Design and Development of Low Torque Ripple Variable-Speed Drive System with Six-Phase Switched Reluctance Motors," *IEEE transaction on Energy Conversion*, accepted.
- (4) Xu Deng, Barrie Mecrow, Richard Martin and Shady Gadoue, "Effects of Winding Connection on Performance of a Six-Phase Switched Reluctance Machine," *IEEE transaction on Energy Conversion*, accepted.
- (5) Xu Deng, Barrie Mecrow, Richard Martin and Haimeng Wu, " Design and Analysis of a Low-Cost and High-Efficiency Variable-Speed Drive System for Six-Phase Switched Reluctance Motors with Hexagon-connected Windings," *IEEE transaction on Industrial Electronics*, under review.

### 1.4 Thesis Overview

A brief description of each chapter is provided below:

- **Chapter1: Introduction and Chapter 2: Literature Review**- these chapters cover the context of this research. Chapter 1 has described the objectives and motivation for this research and described several novelties arising from this work. Chapter 2 reviews the development history and industry applications of SRMs, and describes the torque

ripple challenges associated with their use. The mechanism behind and current solutions for torque ripple are reviewed.

- **Chapter 3: Converter Topologies for Six-Phase SRMs-** this chapter investigates possible converter topologies of the six-phase SRM drive system starting with conventional converter topologies used in three-phase SRMs. Based on analysis of the advantages and disadvantages of all the conventional converters, two converters with minimised switches for six-phase SRMs are proposed. A range of dynamic simulation models are built in MATLAB/SIMULINK to test the performance of the proposed converters. Simulations are performed in which two traditional control methods are applied to the proposed converters and compared with applying these two control methods on the conventional asymmetric half bridge (AHB) converter.
- **Chapter 4: Direct Torque Control of Six-Phase SRMs-** this chapter proposes a DTC method for the six-phase SRM. The derivation of instantaneous torque and the relationship between stator flux and torque production are discussed, and the basic principle of the DTC method is summarized. In order to apply the proposed DTC method to the six-phase SRM, the relevant stator fluxes, voltage vectors, zones arrangement and switching table are discussed. The proposed DTC method is applied to an AHB converter and proposed two converters. DTC simulation models are built in MATLAB/SIMULINK, and the results are compared with traditional control methods throughout the whole speed range.
- **Chapter 5: Effects of Winding Connection on Performance of Six-Phase SRMs-** this chapter describes the analysis of the optimum winding connection type for a six-phase SRM prototype. A Finite Element Model (FEM) for a six-phase SRM prototype is built in MAGNET. The effects of different winding configurations on torque performance and mutual-inductance are discussed. The effects of different winding connection types on torque performance are firstly analysed with a single-phase excitation. Five different winding connection types are subsequently proposed and analysed through multi-phase excitation FEM simulations. Both torque performance and mutual-inductance distributions are discussed through multi-phase excitation simulations. An optimum winding connection type is proposed.
- **Chapter 6: Design and Implementation of a Six-Phase SRM Drive System-** this chapter provides an overview of the six-phase SRM drive system, aiming to familiarise the reader with the experimental tools used for this drive system. The

design and implementation of the hardware and the software are presented, and test results show that the drive system works effectively. A 4.0kW SRM test rig is built and commissioned in Newcastle University. This test rig is designed to accommodate the study of the effects of different winding connection types, the drive capability of different power converters and the performance of different control techniques.

- **Chapter 7: Experimental Validation**-this chapter verifies the simulation results given in Chapter 3 to 5 through appropriate experimental tests. Single-phase and multi-phase excitation tests are carried out to compare the effects of the winding connection to the performance of the six-phase SRM. The traditional control techniques are tested on an AHB converter, the proposed circle converter and a circle converter with extra diodes. The proposed DTC methods are applied to an AHB converter, the proposed circle converter and a circle converter with extra diodes to reduce the torque ripple in conventional control techniques.
- **Chapter 8: Conclusions and Future Work**-this chapter concludes the thesis with a summary of work, a discussion and recommendations for future work.

This thesis includes a list of acronyms and symbols before the introduction. A reference guide to the properties of SRM drives, the design of sensor interfaces and the core program for the DSP controller can be found in the appendices.

---

## Chapter 2. Literature Review

---

Electrical machine drive technology has advanced significantly in the past few decades thanks to the continuous penetration of power electronics into power generation, transmission and consumption. The application of SRMs has become popular due to the improved performance and reduced cost of power electronic devices.

In this chapter, the history and industry applications of SRMs are reviewed and the torque ripple challenges associated with their use are described. The mechanism behind and current solutions for torque ripple are reviewed.

### 2.1 History and applications of SRMs

The operation principle of reluctance machines has been known for nearly two centuries. In 1838 a locomotive was driven by a motor in Scotland, and its working principle is very similar to present SRMs. However, limited by low level power electronics at that time, mechanical switches were used and hence led to very low operation performance and low energy conversion ratio. The stepper motor which also works on the principle of variable reluctance was patented by CL Walker in 1920.

The basic concepts of SRMs in the present form were first introduced by S.A. Nasar in his paper published in 1969[1]. He described two characteristics of this kind of machine in the paper, which are “switching” and “reluctance”. “Switching” means that SRMs have to operate with a continuous switching mode, and “Reluctance” indicates that SRMs have variable reluctance circuits between rotor and stator.

During the 1970’s and 1980’s, with the development of solid-state switching devices, fast switching devices such as transistors and thyristors became available and effectively replaced the mechanical commutator [2]. Therefore the application of SRMs rapidly became more common.

The theory and the potential of doubly salient electronically-switched reluctance motors are explored by Lawrenson in his paper published in 1980 [3]. In his paper, a matured fundamental design of a SRM drive was described and became the design basis of subsequent research on SRMs. The fundamental design consisted of an even number of salient stator and rotor poles. The stator had concentric windings and was magnetically coupled to the rotor.

Torque is developed by the tendency for the magnetic circuit to adopt a configuration of minimum reluctance [4].

SRMs and their drive systems have the advantages of simple structure, low manufacturing cost, high system reliability, high efficiency and a wide speed range, and are contenders for electric vehicle traction drives [5-12]. In recent years they have also been developed for the aviation industry [13-15].

## 2.2 Fundamental principles of SRMs

### 2.2.1 Typical topologies

With no windings on the rotor and concentrated windings on the stator, SRMs have the simplest structure of all electrical machines. Figure 2.1 shows typical SRM stator and rotor topologies.

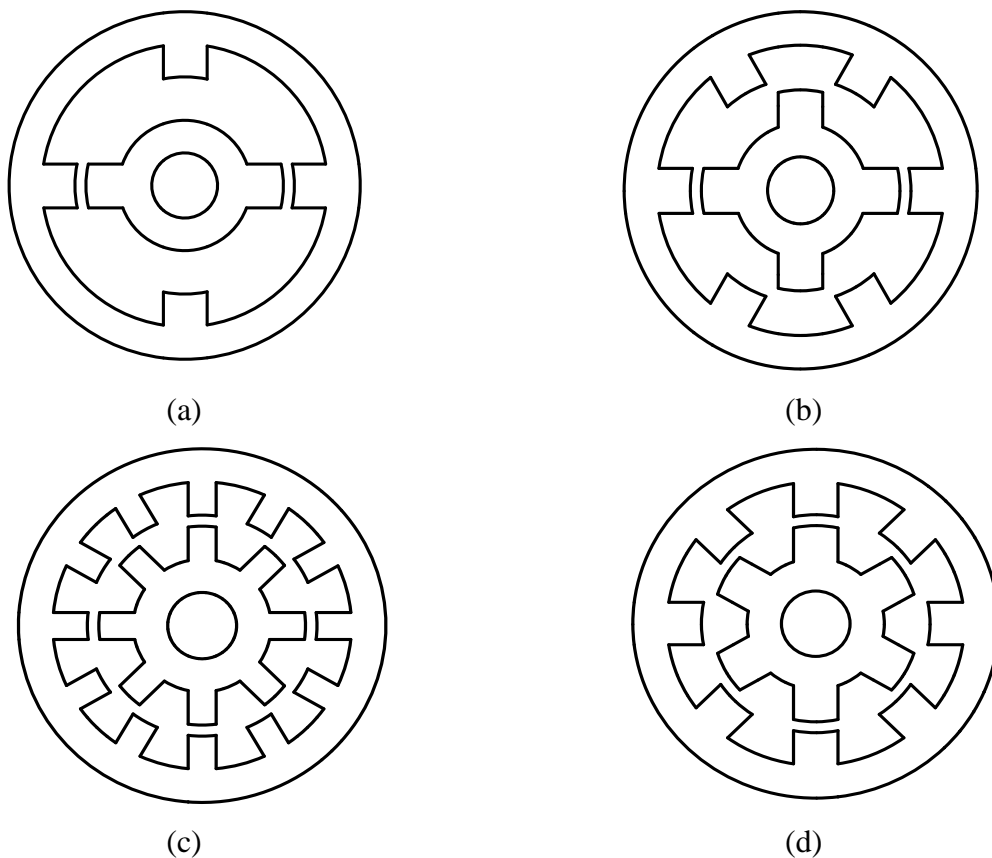


Figure 2.1 Typical SRM stator and rotor topologies: (a) two-phase 4/2 pole SRM (b) three-phase 6/4 pole SRM (c) three-phase 12/8 pole SRM (d) four-phase 8/6 pole SRM

Figure 2.1(a) presents a two-phase 4/2 pole SRM, which has only two pairs of stator teeth and one pair of rotor teeth. Lower phase numbers reduce the cost of manufacture, controller,

converter, and connections between the motor and converter. However, this machine does not have self-starting capability at the aligned position or the unaligned position [2].

Figure 2.1(b) and (c) respectively present three-phase 6/4 pole and 12/8 pole SRMs. Three-phase SRMs are the most ubiquitous structure in all applications due to their relatively low number of phases and self-starting capability. In addition, three phase 12/8 SRMs have been selected to implement bearingless technologies [16, 17], because it has four teeth in each phase which can help to generate two orthogonal radial forces simultaneously.

Figure 2.1(d) shows a four-phase 8/6 pole SRM. Compared with a three-phase SRM, it has better starting performance and less torque ripple. However, the costs of machine and drive system are higher due to increased phase number.

### 2.2.2 Mathematic model

The basic operating principle of an SRM is similar to most other electromechanical devices. It can be treated as a two-port device which has several electrical terminals and a single mechanical terminal, as shown in Figure 2.2.

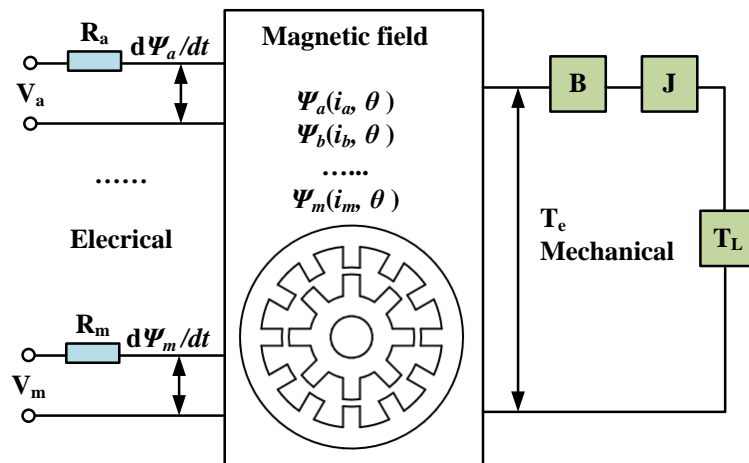


Figure 2.2 Illustration for a m-phase SRM system.

Ignoring mutual coupling between phases, the voltage equation for phase  $k$  is,

$$V_k = i_k R_k + \frac{d\psi_k(i_k, \theta)}{dt} \quad (2.1)$$

where  $V_k$  is the terminal voltage,  $i_k$  is the phase current,  $\psi_k$  is the flux linkage in volt-seconds,  $\theta$  is the rotor position and  $R_k$  is the phase resistance.

Phase flux has a nonlinear relationship with phase current and rotor position. It can be expressed as,

$$\psi_k = \psi_k(i_k, \theta) \quad (2.2)$$

Taking Equation(2.2) into Equation(2.1), Equation(2.3) is obtained,

$$\begin{aligned} V_k &= i_k R_k + \frac{\partial \psi_k}{\partial i_k} \frac{di_k}{dt} + \frac{\partial \psi_k}{\partial \theta} \frac{d\theta}{dt} \\ &= i_k R_k + \frac{\partial \psi_k}{\partial i_k} \frac{di_k}{dt} + \omega_m \frac{\partial \psi_k}{\partial \theta} \end{aligned} \quad (2.3)$$

$$\omega_m = \frac{d\theta}{dt} \quad (2.4)$$

where  $\omega_m$  is the angular velocity in rad/s. There are three terms in Equation (2.3): namely, the resistance voltage drop, the voltage drop induced by changing current, and the ‘back-EMF’  $e$  which is induced by rotor movement,

$$e = \omega_m \frac{\partial \psi}{\partial \theta} \quad (2.5)$$

The rotor mechanical equation can be subsequently expressed as Equation (2.6)

$$T_e = J \frac{d\omega_m}{dt} + B\omega_m + T_L \quad (2.6)$$

where  $J$  is the rotational inertia,  $B$  is the frictional coefficient,  $T_e$  is the electromagnetic torque, and  $T_L$  is the load torque. It is obvious that the electrical port and the mechanical port are coupled by electromagnetic torque. Hence the main issue becomes how to build a proper mathematic model of the electromagnetic torque.

The characteristics of SRMs are significantly nonlinear. It is difficult to obtain an accurate mathematic electromagnetic torque model. Some researchers use the concept of co-energy to express the average torque[4],

$$T_{av} = \frac{\Delta W_c}{\Delta \theta} \quad (2.7)$$

Where  $W_c$  is the co-energy in the SRM, which can be expressed as Equation (2.8),

$$W_c = \int_0^{\psi} \psi(\theta, i) di \quad (2.8)$$

Based on the average torque, some traditional control methods are proposed.

### 2.2.3 Traditional control methods

At low speed the motor back-EMF is low compared to the terminal voltage, thus phase current can be regulated by chopping. Figure 2.3 shows a control diagram and a typical current waveform with the traditional Current Chopping Control (CCC) method, which is employed for the SRM's low-speed operation. In the CCC method, if the turn-on angle  $\theta_{on}$  and the turn-off angle  $\theta_{off}$  are fixed, the switching signal is generated by a hysteresis controller and the average torque output is adjusted by simply changing the current reference.

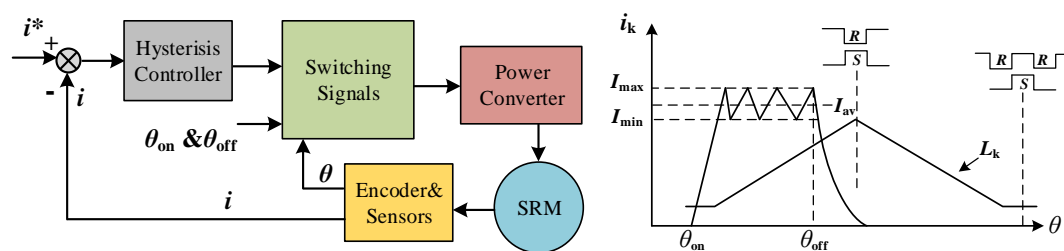


Figure 2.3 Control diagram and current waveform with the traditional CCC method

However, when rotational speed is high, the motor back-EMF rises and the available voltage may become inadequate for chopping control. In this scenario varying the conduction angle of the excitation current becomes an effective method for this application. Figure 2.4 shows a control diagram and a typical current waveform for this traditional Angle Position Control (APC) method, which is employed for high-speed operation. The average torque is controlled by changing the turn-on and turn-off angles.

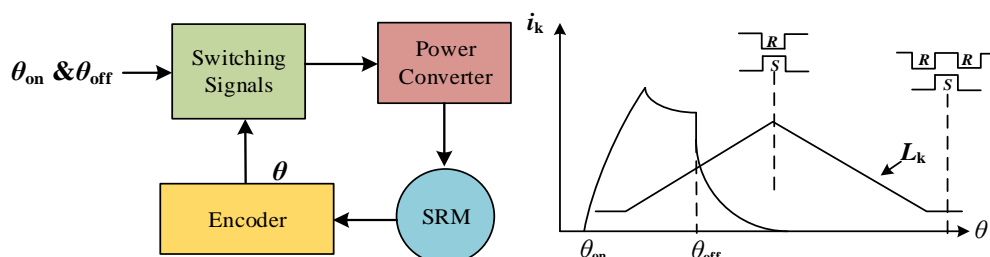


Figure 2.4 Control diagram and current waveform with the traditional APC method

The above control methods can vary the mean torque, but due to its highly nonlinear electromagnetic characteristics, the SRM suffers from high torque ripple. The Torque Ripple Ratio (TRR) is defined in Equation (2.9). Deviations from the average torque are particularly large near the phase commutation points.

$$TRR = \frac{T_{\max} - T_{\min}}{T_{av}} \times 100\% \quad (2.9)$$

### 2.3 Torque ripple and reduction methodologies for SRMs

The doubly salient structure of SRMs gives rise to nonlinear phase torque-angle-current characteristics, which dictate the amount of torque ripple during independent single-phase operation and continuous commutation. Many modifications have been performed to reduce the torque ripple and these can be classified into two categories, one based on machine design optimization and one based on control algorithms.

#### 2.3.1 Machine optimization methodologies

##### 2.3.1.1 Geometry optimization

Structural parameters of the machine, such as the air gap, outer diameter of rotor and stator, stator winding turns and pole arcs have a significant impact on torque ripple[18]. Many researchers focused on modifying the geometry to minimize the torque ripple [19-23].

Equation (2.10) is the linear torque expression considering mutual-inductance for a three-phase SRM, which indicates that mutual-inductances have the potential to increase the torque production,

$$T = \frac{1}{2} i_a^2 \frac{dL_a}{d\theta} + \frac{1}{2} i_b^2 \frac{dL_b}{d\theta} + \frac{1}{2} i_c^2 \frac{dL_c}{d\theta} + i_a i_b \frac{dM_{ab}}{d\theta} + i_b i_c \frac{dM_{bc}}{d\theta} + i_a i_c \frac{dM_{ac}}{d\theta} \quad (2.10)$$

Therefore, during the past few decades, in order to increase torque and power densities, some novel methods, such as utilizing mutual-inductance for torque production, have also been investigated, including the fully-pitched SRM [24] and a new winding distribution for SRMs called Mutually Coupled Switched Reluctance Motor (MCSR) [25, 26]. Based on this, [19] proposed a new and simple method of punching holes in one side of the rotor poles to reduce the torque ripple, as shown in Figure 2.5. With this modification, the transient ratio of self and mutual-inductance with respect to rotor movement is more sinusoidal than the model without

the punched holes. The depth of the punched hole  $L_{air}$  and the opening width of the punched hole  $L_{open}$  have significant effects on the average torque and torque ripple, whilst the distance between the punched hole and the rotor teeth  $L_{iron}$  only has a slight influence on average torque. In addition, the problem that all the derivatives of inductances drop simultaneously close to zero is solved by this modification.

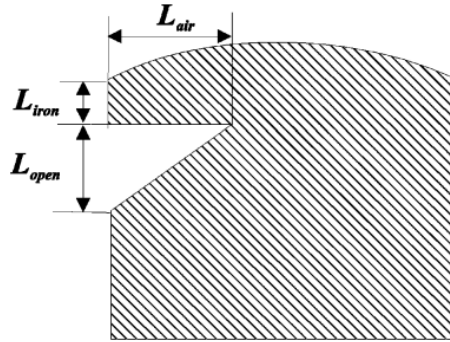


Figure 2.5 Dimensions of punched hole on rotor[19]

Another interesting torque ripple reduction method by machine structure modification is proposed by C. Yong Kwon in [20]. This paper investigated the idea that the inductance profile can be controlled by changing the air-gap profile between the stator and rotor poles. Keeping the pole arc unchanged, the stator pole face was modified and an additional pole shoe was attached to the lateral face of the rotor pole. These modifications are shown in Figure 2.6. It was shown that this method effectively reduced the undesired torque ripple of the SRM.

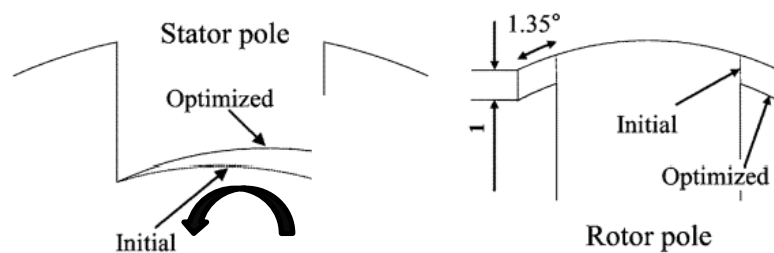


Figure 2.6 Comparison of the initial and optimized shapes[20]

In addition to the above two machine optimization methods, J. Hur proposed a rotor flux barrier inserting method in [21]. The inserted flux barriers, as presented in Figure 2.7, change radial components of magnetic flux into tangential components, so that the total tangential component is increased, resulting in reduced torque ripple and increased average torque. Six different barrier shapes are proposed, and their feasibility and performance are compared

accordingly. Two of the proposed shapes were tested in experimental work, and both of them successfully increase the average torque and reduce the torque ripple at the same time.

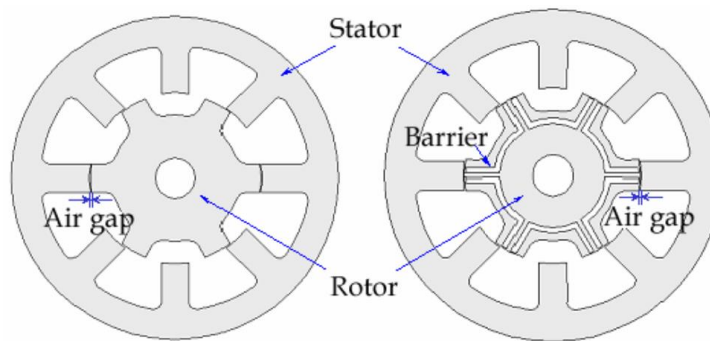


Figure 2.7 Comparison of the initial and optimized flux barrier inserted rotor shapes[21]

### 2.3.1.2 Multi-phase machines

New converter topologies make it possible to implement multi-phase inverters without an excessive numbers of power devices [27, 28]. In the last two decades, machines with a greater number of phases have become popular due to the potential for lower torque ripple, reduced phase current for a given power rating and better fault-tolerance compared with two- and three- phase machines [29, 30].

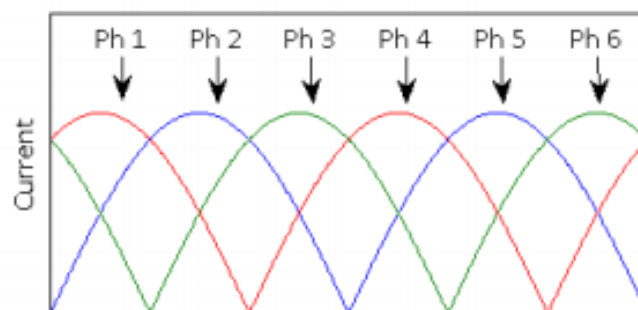


Figure 2.8 Phase current for a six-phase SRM driven by full bridge converter [31]

A six-phase SRM was recently designed in [32] and driven by a three-phase full bridge inverter with sinusoidal current waveforms injected into the stator windings. The drive topology is shown in Figure 3.4. Compared with a traditional three-phase SRM, it produced lower torque ripple. With the use of diodes, it can still have unidirectional current in each phase [31, 33]. This machine has been selected to be the research object in this thesis.

### 2.3.1.3 Winding configuration optimization

The performance evaluation and effective control of SRMs require accurate flux linkage and torque information [34-37], both of which are nonlinear functions of phase current and rotor position. The flux linkage characteristic is usually obtained across a range of rotor positions and operating current values, and this information can then be used to facilitate advanced control techniques [38-40]. This approach is based on single-phase excitation, and can be accurate under multiphase excitations in situations where mutual-inductance effects can be ignored.

As the phase number of an SRM increases, so too does the overlap between adjacent phases. This can give rise to considerable electromagnetic interaction between phases. In this case, the common analysis based on the superposition of single-phase, self-inductance characteristics is of limited use and it becomes necessary to consider mutual-inductance effects. Two winding connections for a 12/8 dual channel three-phase SRM have previously been investigated in [41], and it has been suggested that connections giving rise to long flux paths exhibit better magnetic decoupling than those with short flux-paths.

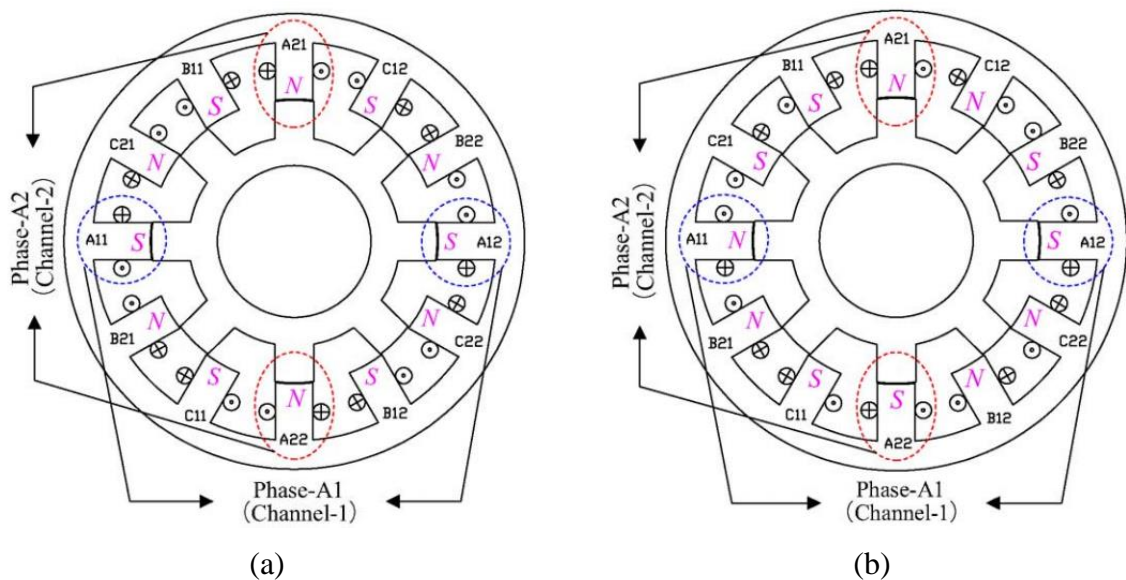
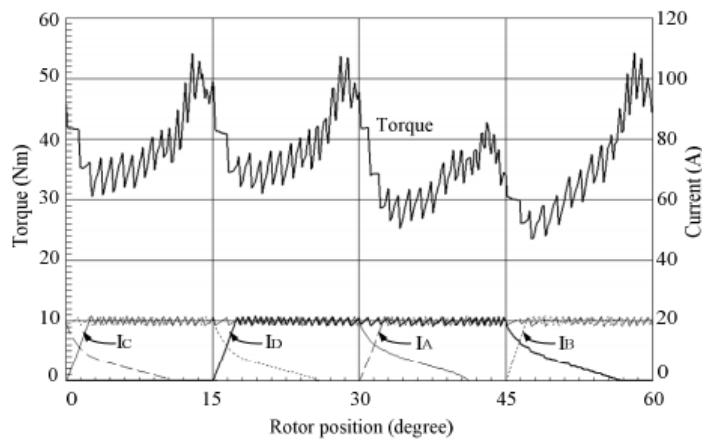


Figure 2.9 Winding connection types for a 12/8 dual channel three-phase SRM:

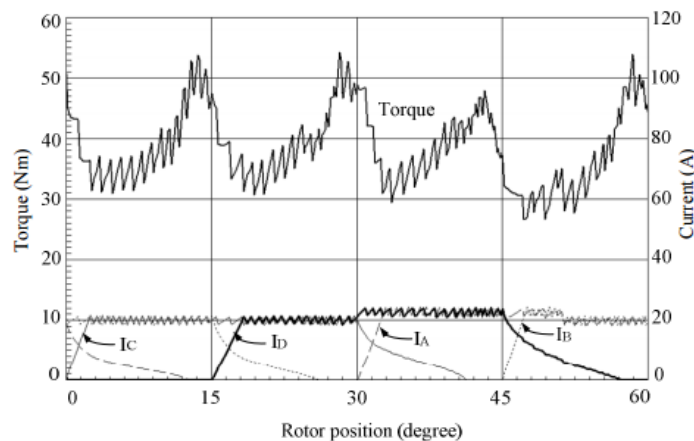
(a) NSNSNSNSNSNS (b) NNSSNNSSNNSS [41]

Single-phase and two-phase excitation modes have been researched with a four-phase SRM [42]. In this case, alternative winding connections can cause asymmetric instantaneous torque waveforms with high torque ripple as shown in Figure 2.10(a). Although regulation of the

asymmetric torque by increasing the chopping current was demonstrated in simulation as presented in Figure 2.10(b), this is not an advanced control method and has not considered the torque ripple generated by each phase. Consequently, it is clear that the mutual-inductance cannot be ignored in multi-phase excitation mode unless a decoupled winding connection is employed [43].



(a)



(b)

Figure 2.10 Transient torque waveforms: (a) with balanced current excitation (b) with increased chopping current excitation [42]

### 2.3.2 Control methods

Although machine optimization can partially reduce the torque ripple in SRMs, it is difficult and complicated to modify geometric dimensions once the machine has been manufactured. An alternative way to further decrease the torque ripple of an existing machine is to employ an advanced torque ripple reduction technique in control system.

### 2.3.2.1 Torque sharing method

The majority of torque ripple minimization control methods focus on modulation of the phase current or voltage profile to generate a specific torque command [36, 44-52]. In these methods, the torque ripple is reduced by regulating the output torque of each individual phase, which is with reference to a Torque Sharing Function (TSF)  $f_k(\theta)$  as expressed in Equation (2.11),

$$\begin{cases} T_k^* = T^* \times f_k(\theta) \\ \sum_{k=1}^n f_k(\theta) = 1 \end{cases} \quad (2.11)$$

where  $T^*$  is torque command, and  $k$  is phase number.

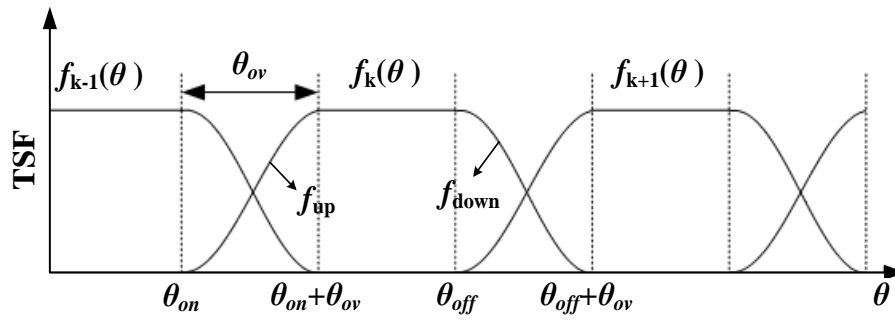


Figure 2.11 Typical TSF profile for a three-phase SRM

For a three-phase SRM, typical profiles of the TSF are shown in Figure 2.11, and can be expressed by piecewise function as described in Equation (2.12),

$$f_k(\theta) = \begin{cases} 0, & (0 \leq \theta < \theta_{on}) \\ f_{up}(\theta), & (\theta_{on} \leq \theta < \theta_{on} + \theta_{ov}) \\ T^*, & (\theta_{on} + \theta_{ov} \leq \theta < \theta_{off}) \\ f_{down}(\theta), & (\theta_{off} \leq \theta < \theta_{off} + \theta_{ov}) \\ 0, & (\theta_{off} + \theta_{ov} \leq \theta < \theta_{off} + \theta_p) \end{cases} \quad (2.12)$$

where  $\theta_{ov}$  is the overlap angle between two adjacent phases and  $\theta_p$  denotes one rotor cycle.

The main function of the TSF method is to calculate the functions ( $f_{up}(\theta)$  and  $f_{down}(\theta)$ ) between phase overlap. The first TSF for SRM torque ripple minimization was proposed in 1987 [53], and initially an exponential function was employed as the TSF. Based on the static electromagnetic characteristics of SRMs, many different TSFs have been applied to reduce

torque ripple [46], with both offline and online TSFs investigated in published literature [36, 47].

The TSFs can be classified into two groups: one based on linear functions and one based on nonlinear functions. The functions ( $f_{up}(\theta)$  and  $f_{down}(\theta)$ ) of each group are summarized in Table 2.1. Since the torque command is distributed by TSFs according to the rotor position, another responsibility of the TSF method is to generate the current or flux references and track them accurately. In this method, TSFs are designed to be as smooth as possible due to limited DC link voltage.

As shown in Table 2.1, all the nonlinear TSFs have complicated expressions, which will occupy significant computing resources in real-time tests. Although they have been verified in simulations, the accuracy of transferring the torque reference into current or flux references is not guaranteed by this method. Moreover, there are always two/three phases conducting simultaneously in multi-phase SRMs, the design of the TSFs are more complicated.

Table 2.1 Typical TSFs for SRMs [46]

Linear TSF	Cubic TSF
$f_{up}(\theta) = \frac{T^*}{\theta_{ov}} (\theta - \theta_{on})$ $f_{down}(\theta) = T^* - \frac{T^*}{\theta_{ov}} (\theta - \theta_{on})$	$f_{up}(\theta) = \frac{3T^*}{\theta_{ov}^2} (\theta - \theta_{on})^2 - \frac{2T^*}{\theta_{ov}^3} (\theta - \theta_{on})^3$ $f_{down}(\theta) = T^* - f_{up}(\theta - \theta_{off} + \theta_{on})$
Sinusoidal TSF	Exponential TSF
$f_{up}(\theta) = \frac{T^*}{2} - \frac{T^*}{2} \cos \frac{\pi}{\theta_{ov}} (\theta - \theta_{on})$ $f_{down}(\theta) = \frac{T^*}{2} + \frac{T^*}{2} \cos \frac{\pi}{\theta_{ov}} (\theta - \theta_{off})$	$f_{up}(\theta) = T^* \left[ 1 - \exp\left(\frac{-(\theta - \theta_{on})^2}{\theta_{ov}}\right) \right]$ $f_{down}(\theta) = T^* \left[ \exp\left(\frac{-(\theta - \theta_{off})^2}{\theta_{ov}}\right) \right]$

### 2.3.2.2 Direct instantaneous torque control method

To simplify the torque ripple reduction control method for SRMs, Direct Instantaneous Torque Control (DITC) methods have been proposed for three-phase SRMs [54-56]. Multi-level converters are employed to increase the control flexibility of the DITC method, although more power switches are needed [57]. The control diagram of the DITC method is presented in Figure 2.12. The main idea of this control method is to directly use the error between command and estimated torque to control the instantaneous torque.

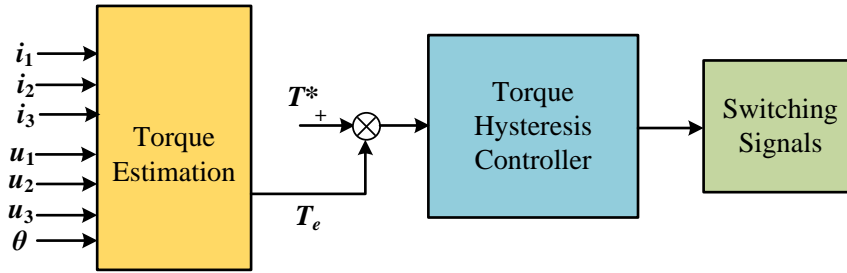


Figure 2.12 Control diagram of the DITC method

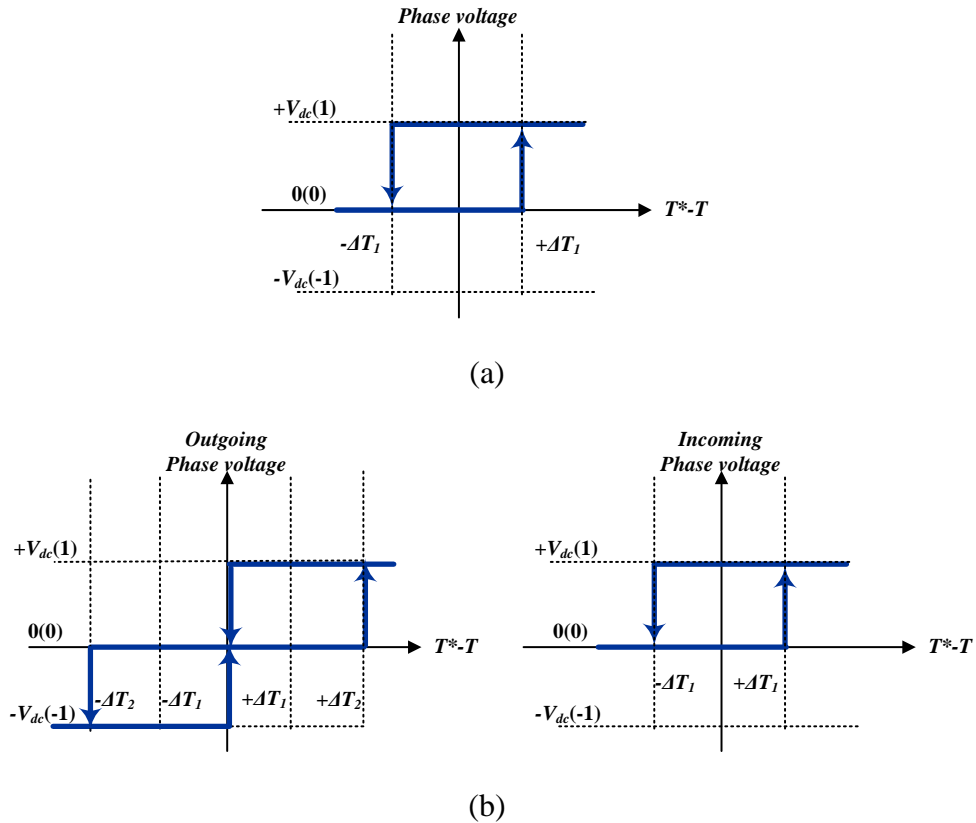


Figure 2.13 Diagram of torque hysteresis controller: (a) single phase active (b) during commutation

The details of the torque hysteresis controller are presented in Figure 2.13. As shown in Figure 2.13(a), if there is only one phase in active mode, the switching action depends on the relationship between the torque error ( $T^* - T_e$ ) and the torque hysteresis band ( $\Delta T_1$ ) only. When the torque error is larger than  $\Delta T_1$ , which means the instantaneous torque is smaller than the expected smallest value, the active phase has to be magnetized, and vice versa.

For multi-phase commutation situations, the switching principle is shown in Figure 2.13(b). The incoming phase shares the same hysteresis controller with the single-phase active situation, whilst outgoing phase has a larger torque hysteresis band ( $\Delta T_2$ ). When the incoming

phase is not available to produce enough torque within the inner hysteresis band ( $\Delta T_1$ ), the outgoing phase changes back to magnetization mode to produce more positive torque. In this way, the total torque output can be controlled without complicated TSFs.

Torque hysteresis controllers in the DITC method are highly dependent on the torque production capability of incoming and outgoing phases, and are very sensitive to switching angles. In addition, for multi-phase machines such as four-phase SRMs and six-phase SRMs, a TSF would be required in addition to DITC to distribute the torque command in multi-phase excitation mode.

### 2.3.2.3 Direct torque control method

In order to simplify the control method and improve the torque response, the concept of Direct Torque Control (DTC) of AC machines [58, 59] has been developed for SRM drives [60-65]. A novel DTC method is proposed for three-phase SRMs from analysis of their nonlinear torque characteristics [60]. This method does not require stator winding modification and can work with unipolar drives. It uses a flux hysteresis controller to keep a constant magnitude of the stator flux, and the stator flux vector is accelerated or decelerated to directly control the instantaneous torque.

Six voltage vectors  $V_1(1,0,-1)$ ,  $V_2(0,1,-1)$ ,  $V_3(-1,1,0)$ ,  $V_4(-1,0,1)$ ,  $V_5(0,-1,1)$ , and  $V_6(1,-1,0)$  are arranged in the  $360^\circ$  vector space as shown in Figure 2.14. Zones N1 to N6 are used to locate the rotational stator flux vector. At any instant, torque and stator flux have respective control requirements, which can be considered simultaneously with stator flux position to choose a reasonable voltage vector from  $V_1$  to  $V_6$ .

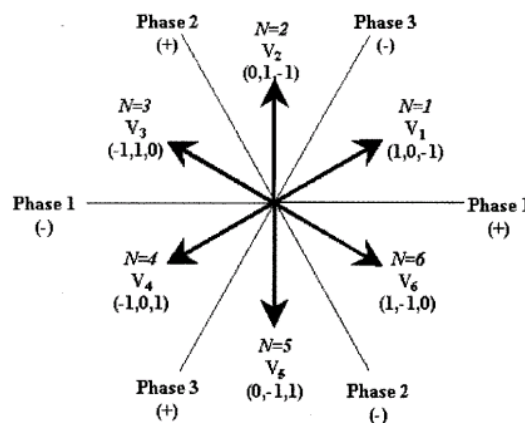


Figure 2.14 Definition of voltage vectors for three-phase SRM drive [60]

The selected principle of DTC was summarized into a switching table and is presented in Table 2.2, and  $k$  in Table 2.2 is the zone number of current stator flux.

Table 2.2 Switching table for three-phase SRM [60]

$T \uparrow \psi \uparrow$	$T \uparrow \psi \downarrow$	$T \downarrow \psi \uparrow$	$T \downarrow \psi \downarrow$
$v_{k+1}$	$v_{k+2}$	$v_{k-1}$	$v_{k+2}$

Simulation and real-time test results show that the DTC method can reduce torque ripple in a three-phase SRM with this very simple control algorithm. As higher phase numbers are being considered for torque ripple reduction, the application of this DTC method to such machines has been simulated [61, 62].

Some intelligent control methods have also been employed in SRM drive systems, such as fuzzy control [66], neural networks [67], etc., however, all of them require complex computation and are difficult to implement in real-time.

## 2.4 Power converters for SRMs

The trend of SRM converters' development can be summarised as,

- fewer switches
- fewer energy storage devices
- fewer connections between the SRM and the converter
- higher efficiency

Based on these requirements, a large number of converters are developed for SRMs [68-71]. The classification of SRM power converters is summarized in Figure 2.15.

Traditional SRM power converters can be classified as half bridge converters[72, 73], capacitive type converters[74-84], magnetic type converters[85-91], dissipative converters[92, 93], self-commutating converters[94-98]. Some of them have been widely used in the past few decades, such as the Asymmetric Half Bridge (AHB) converter, the Capacitor Dump (C-Dump) converter, the H-bridge converter, the split DC link converter, the bifilar converter and the dissipative converter.

The AHB converter is suitable for almost all SRM drives and can be directly used for the six-phase SRM, but the large switch number is still a significant weakness, exacerbated in SRM

drives with an increased number of phases. The C-Dump, H-bridge, split DC link, bifilar and dissipative converters are all designed to reduce the quantity of switches. However they all have drawbacks and application limitations. The C-Dump converter needs an extra DC: DC circuit, which increases the control difficulty. The H-bridge converter is only suitable for four or multiples of four-phase SRM. The split DC link converter only has half of the DC link voltage on each phase winding, which limits its performances especially at high speed. The bifilar converter employs an extra inductance for each phase, which increases the converter cost and volume. The dissipative converter arranges extra resistors to absorb the energy stored in phase winding inductances, and it is only suitable for low power applications due to its reduced efficiency. Consequently, all the above minimised switch number converter are not good enough for the six-phase SRM and a new converter topology has to be proposed.

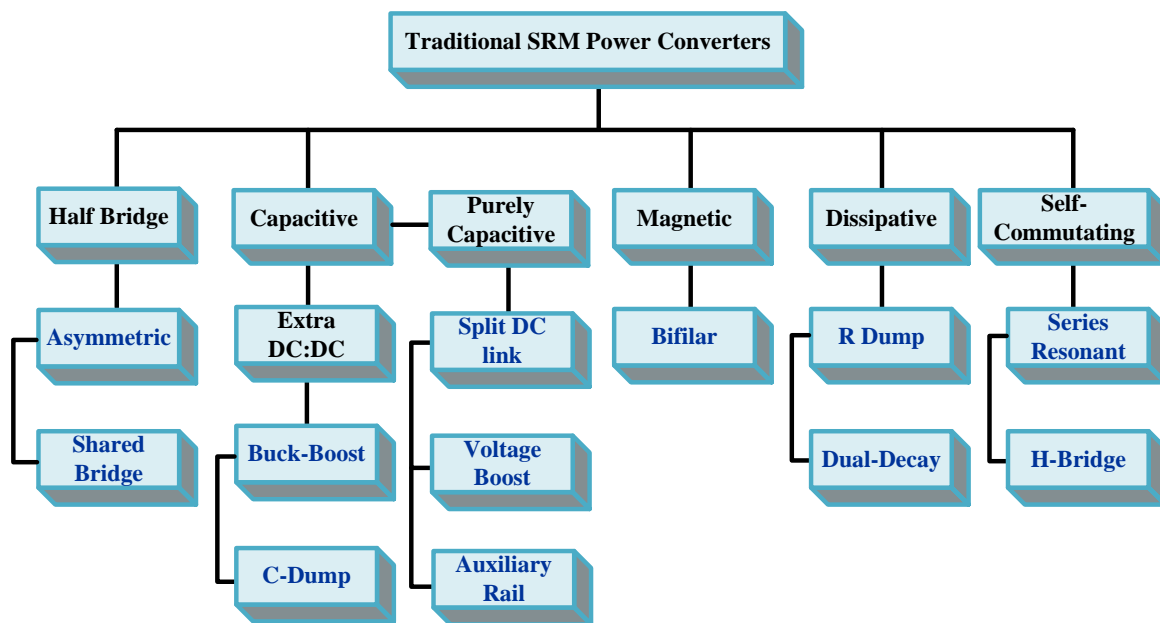


Figure 2.15 Classification of SRM power converters

## 2.5 Summary

The aim of this project is to build a low torque ripple SRM drive system, and this system will include a SRM prototype, a converter and an advanced control system. In this chapter, the fundamental theories of SRMs were introduced to explain the serious torque ripple in SRMs. The large torque ripple has been reduced by machine optimization methods and advanced control techniques proposed in the literature over the previous few decades.

A six-phase SRM is selected to be the research object in this project due to its low torque ripple. However, due to the fact of a multi-phase machine, the mutual-inductance in a six-phase SRM cannot be ignored unless employing a decoupling winding connection. Hence the optimized winding configuration for the six-phase SRM will be investigated in this project. Compared with traditional torque ripple reduction methods (TSF and DITC) for SRM drives, the DTC method is more suitable for multi-phase SRMs. Hence the DTC method will be applied to the six-phase SRM in this project to further reduce the torque ripple. The AHB converter can directly be used for the six-phase SRM, but a new converter topology still has to be designed to reduce the large number of switches.

## Chapter 3. Converter Topologies for Six-Phase SRMs

A Switched Reluctance Machine (SRM) drive system usually consists of an SRM, a power converter, gate drivers and a digital controller, of which the power converter is the key factor that affects the performance and the cost of the whole system. The investigation of converter topologies of the six-phase SRM drive system is firstly started with conventional converter topologies for three-phase SRMs. Based on the analysis of advantages and disadvantages of all the conventional converters, two minimized switching number converters are proposed, which are the circle converter and the circle converter with extra diodes. A range of dynamic simulation models are built in MATLAB/SIMULINK to test the performance of the proposed converters. Two traditional control methods are applied to the proposed converters and compared with the results obtained from applying these two control methods to the conventional asymmetric half bridge (AHB) converter.

### 3.1 Considered converter topologies for six-phase SRMs

Based on the conventional converter topologies designed for three-phase SRM drives, converters for six-phase SRM drives can be simply achieved by increasing the converter phase number. Many conventional converter topologies can be used for six-phase SRM drives which are shown as below.

#### 3.1.1 Six-phase asymmetric half bridge converter

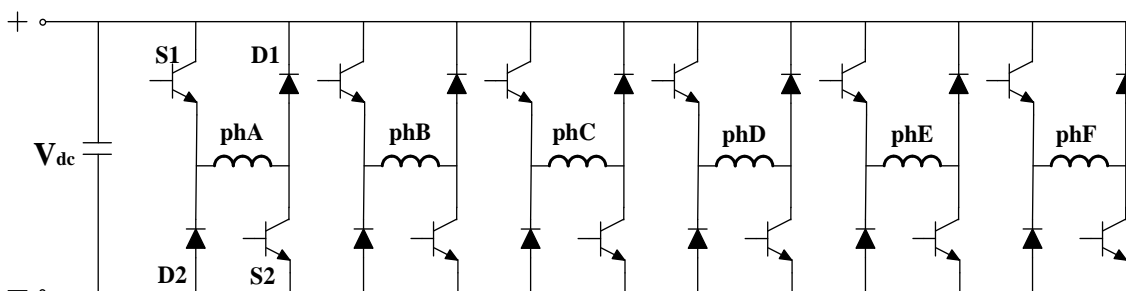


Figure 3.1 Six-phase asymmetric half bridge converter

Figure 3.1 presents a six-phase AHB converter, which is the most popular converter topology for SRM drives due to its excellent phase independence[72]. Depending on the on-off states of switches, there are three voltage states for each phase. For example, when switch S1 and S2 are on, voltage of ph1 is  $+V_{dc}$  and this state is defined as magnetization. When S2 is off, ph1 winding is short-circuited through switch S1 and diode D1 and this state is defined as

freewheeling. When switch S1 and S2 are off, the ph1 winding freewheels through diode D1 and D2, the voltage of ph1 is  $-V_{dc}$  and this state is defined as demagnetization.

However, due to DC link voltage limitation, magnetization and demagnetization speed are problems, especially at high speed. To solve these problems, a multi-level converter is employed. Figure 3.2 is a typical four-level converter for a six-phase SRM [73]. In this converter, an extra capacitor is employed to provide more flexible winding terminal voltages. In addition to normal freewheeling and magnetization states as discussed in the AHB converter, two extra states exist in this four-level converter. One is a fast magnetization state with higher terminal voltage which is  $+(V_{dc} + V_d)$ , when switch Sd, S1 and S2 are on. The other one is a fast demagnetization state with higher terminal voltage which is  $-(V_{dc} + V_d)$ , when switch Sd, S1 and S2 are off.

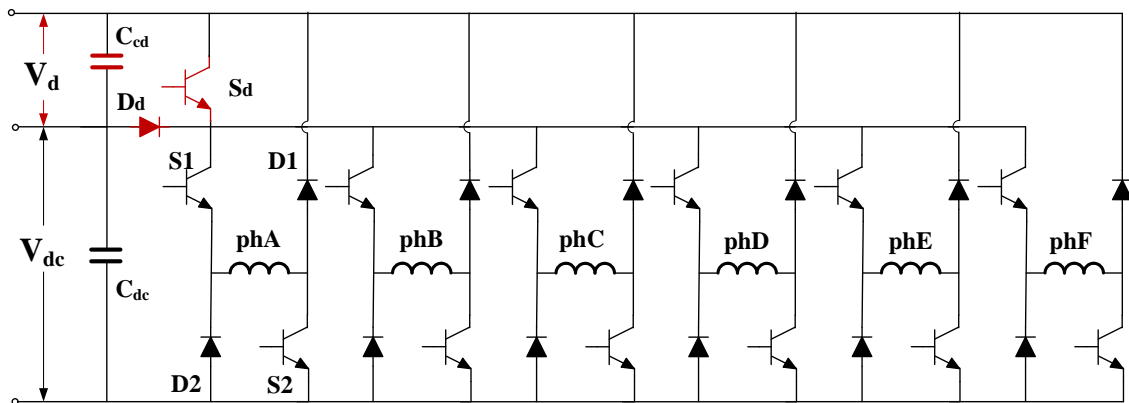


Figure 3.2 Multi-level converter for six-phase SRMs

### 3.1.2 Six-phase split DC link converter

The above two converters need at least twelve switches to drive a six-phase SRM, which increases the converter volume and leads to higher costs compared with three-phase or four-phase SRM drives. To solve this problem, some simplified one-switch-per-phase converter topologies are considered.

According to the above requirements, a six-phase split DC link converter can be employed as shown in Figure 3.3[68]. There are only six switches in this topology, thus it is a one-switch-per-phase converter. Two identical capacitors split the DC link voltage to two equal parts. Unlike to the AHB converter, there are only two switching states in each phase of this split DC link converter. When S1 is on, phase A is energized by  $+1/2V_{dc}$ , this state is defined as

‘magnetization’. When S1 is off, phase A is in a freewheeling loop along D1 and  $C_{dc2}$ , this state is defined as ‘demagnetization’. It is obvious that compared with the AHB converter, this split DC link converter has half the magnetization and demagnetization voltage, which will lead to slow commutation time.

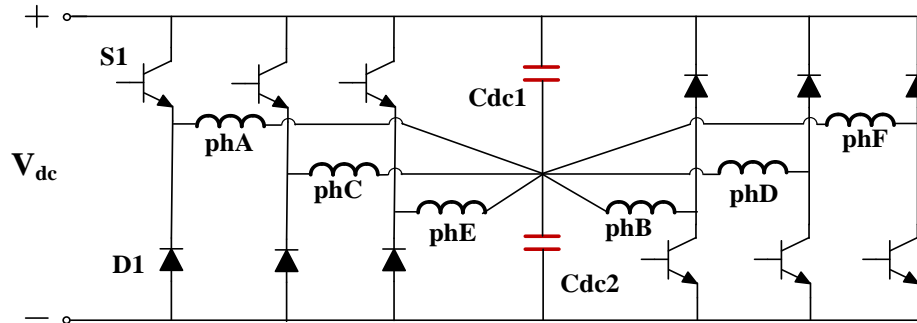


Figure 3.3 Split DC link converter for six-phase SRMs

### 3.1.3 Three-phase full bridge converter

Figure 3.4 presents a six-phase SRM driven by a three-phase full bridge converter, in which six phase windings are arranged in a delta connection [31]. The three-phase full bridge converter produces three-phase sinusoidal currents to drive three pairs of anti-parallel phase windings. In this configuration additional six diodes are used to convert the bipolar current waveform into two unipolar half waveforms, with unidirectional current in every phase.

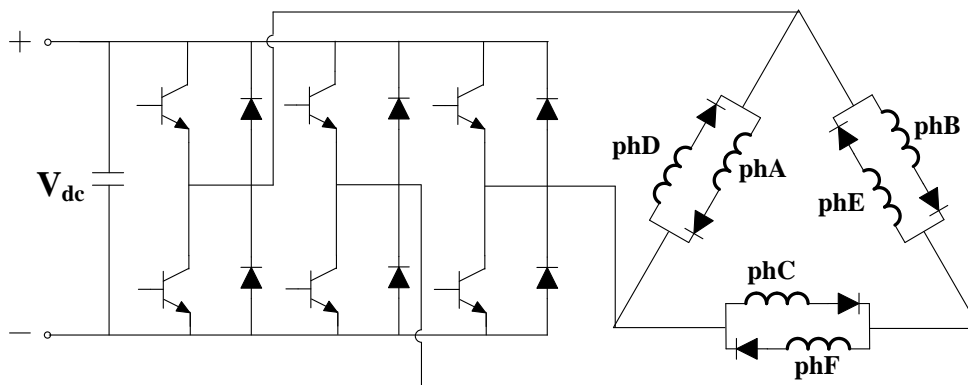


Figure 3.4 Three-phase full bridge converter for six-phase SRMs

However, all the traditional control strategies, such as CCC method and APC method for SRMs cannot be used with this converter topology. What is more, although only six switches are used in this topology, six additional diodes are required.

### 3.1.4 Six-phase dissipative converter

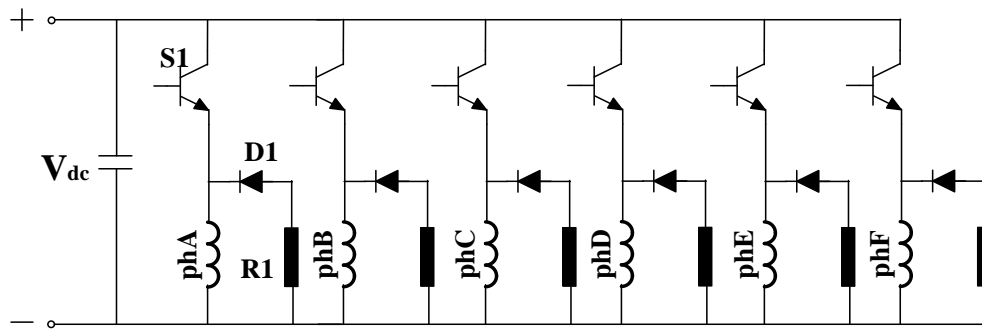


Figure 3.5 Dissipative converter for six-phase SRMs

Another typical one-switch-per-phase converter is dissipative converter. The dissipative converter for six-phase SRMs is shown in Figure 3.5, which only employs six switches and six diodes in total [68]. Unlike the other converter topologies mentioned above, this converter topology has its unique freewheeling state. A power resistor is connected in series with each phase winding to dissipate the magnetic energy stored in winding inductance after turn-off of each switch. Two pronounced disadvantages exist in this converter: one is low power efficiency due to stored energy being wasted in a resistor; the other one is an unstable voltage drop on the winding due to current decreasing in the freewheeling loop.

### 3.1.5 Six-phase bifilar converter

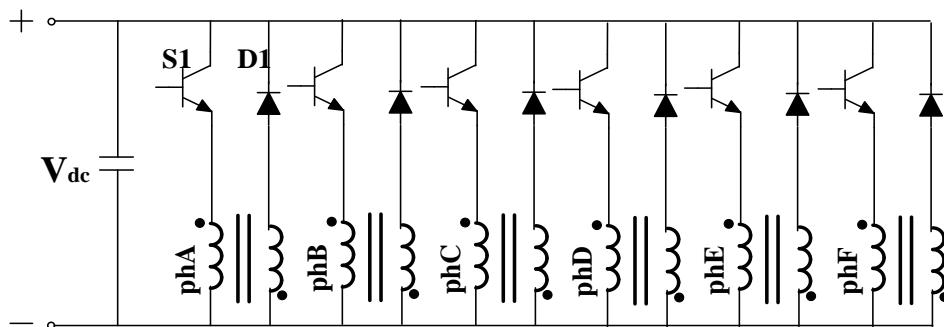


Figure 3.6 Bifilar converter for six-phase SRMs

Figure 3.6 shows a six-phase bifilar converter, in this topology only six switches and six diodes are utilized [68]. There are two closely coupled windings in each phase, which are the primary (main) winding and the secondary winding. When switch S1 is on, the main winding is in magnetization mode, and current in phase A builds up quickly. When S1 is off, the stored energy in the main winding is directly transferred to the secondary winding and return to DC link. However, some disadvantages also exist in this topology. A perfect coupling is hard to

achieve, especially considering insulation, and the additional windings limit the copper area and also cause more conduction losses.

In order to solve the problems which exist in the above converters, a new converter needs to be designed for six-phase SRM drives, which meets the following requirements:

- Minimize the number of switches;
- Minimize the number of diodes;
- Minimize the connection between motor and converter;
- Require no additional energy storage element;

### 3.2 Circle converter for six-phase SRM

Based on conventional SRM converters, a novel converter is designed for six-phase SRM drives. Figure 3.7 shows the configuration of the proposed converter. This converter has no additional energy storage element and uses fewer switches when compared with other traditional converters. As all the six phase windings are connected together forming a circle, this novel converter is named the circle converter.

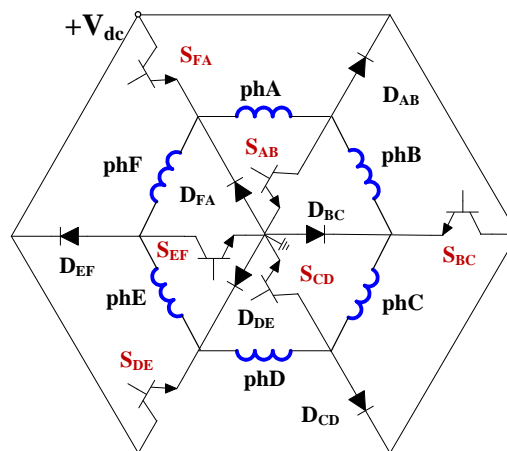


Figure 3.7 Circle converter for six-phase SRMs

Table 3.1 shows the components and connection requirement comparisons between the AHB converter and the proposed circle converter for a six-phase SRM. Compared with the AHB converter, the proposed circle converter reduces the number of switches, diodes, and connections between the motor and converter to half.

Table 3.1 Components and connection requirement comparisons between proposed circle converter and AHB converter for a six-phase SRM

	Asymmetric half bridge converter	Circle converter
No. of Switches	12	6
No. of Diodes	12	6
No. of connections between motor and converter	12	6

In the proposed circle converter, adjacent phases share one switch and one power diode. For example, as shown in Figure 3.7, phase B shares its top switch  $S_{BC}$  and bottom diode  $D_{BC}$  with phase C, meanwhile, it shares its top diode  $D_{AB}$  and bottom switch  $S_{AB}$  with phase A. Similar with the AHB converter, each phase has three operational modes in the circle converter, which are magnetization, demagnetization and freewheeling states according to the switching states of all the six switches. However, six phase windings in the circle converter do not work independently anymore because the conduction demand of one phase affects the adjacent two phases. Therefore, the traditional control strategies have to be modified for the proposed circle converter.

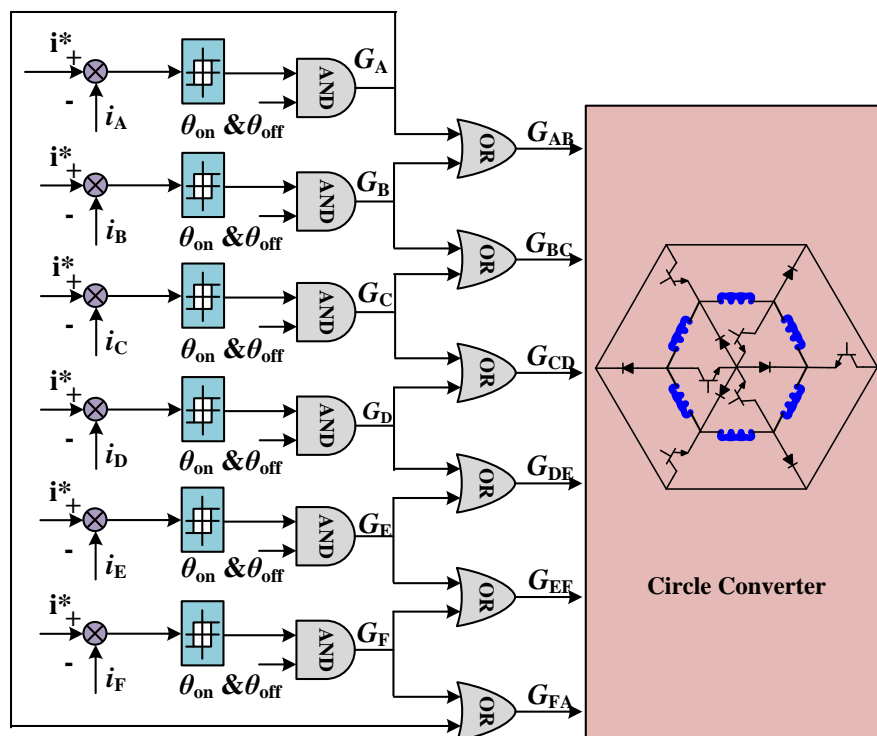


Figure 3.8 Control diagram of six-phase circle converter

Figure 3.8 illustrates the control diagram of the six-phase circle converter. In the diagram, the first two steps are similar to the traditional AHB converter. Step 1: compare the phase currents with current reference values to get the current hysteresis control results. Step 2: combine current hysteresis control results with firing angles to achieve the single phase switching signals  $G_A$  to  $G_F$ . Step 3 is further designed in order to obtain the final switching signals  $G_{AB}$  to  $G_{FA}$ . In order to guarantee enough magnetization energy, the switching signals  $G_{AB}$  to  $G_{FA}$  for the six switches in the circle converter are the logical OR operation results of each adjacent two single-phase switching signals.

### 3.3 Simulation analysis

Dynamic simulation models of a six-phase SRM prototype are developed in MATLAB/SIMULINK environment to conduct simulations with the proposed circle converter and the traditional asymmetric half bridge converter. The models use the parameters of a 12/10 conventional SRM prototype, whose electromagnetic properties are shown in Figure 3.9.

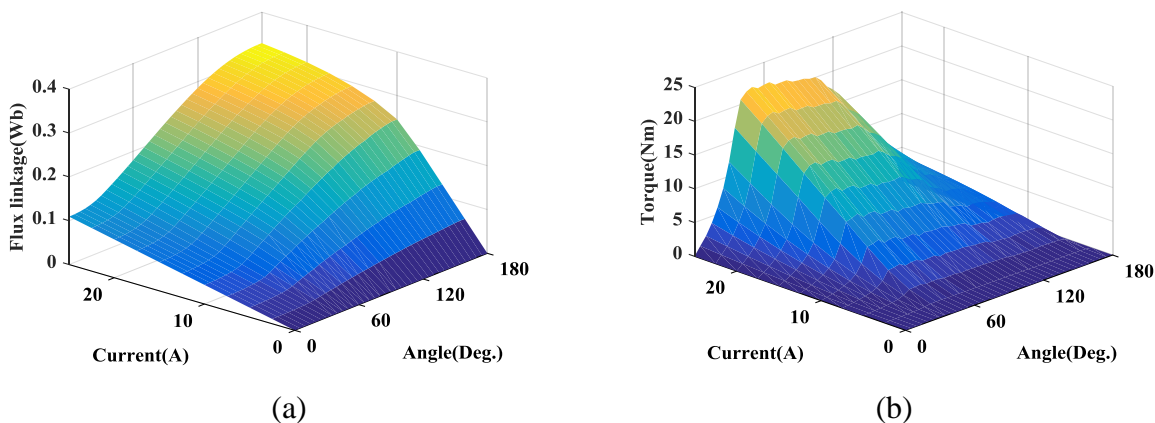


Figure 3.9 Nonlinear electromagnetic characteristics of a six-phase SRM prototype: (a) relationship between rotor position, current and flux-linkage (b) relationship between rotor position, current and torque

The dynamic simulation model is shown in Figure 3.10. This universal six-phase SRM dynamic simulation model has been with five main sub-systems: (1) a six-phase SRM is built in this dynamic model based on nonlinear electromagnetic characteristics which are shown above; (2) six-phase asymmetric half bridge converter is selected for this model; (3) since this is at very early stage of six-phase SRM drive research, the traditional CCC method and APC method are employed here, thus a hysteresis current controller is built accordingly; (4) rotor position estimation will give an accurate electrical rotor position feedback; (5) gate drive

signal generator will consider the rotor position information with turn-on, turn-off angle and the control results of hysteresis current controller to generate the gate drive signals for the power converter. The solver type here is fix-step. The step size at 200r/min is  $10^{-6}$  s.

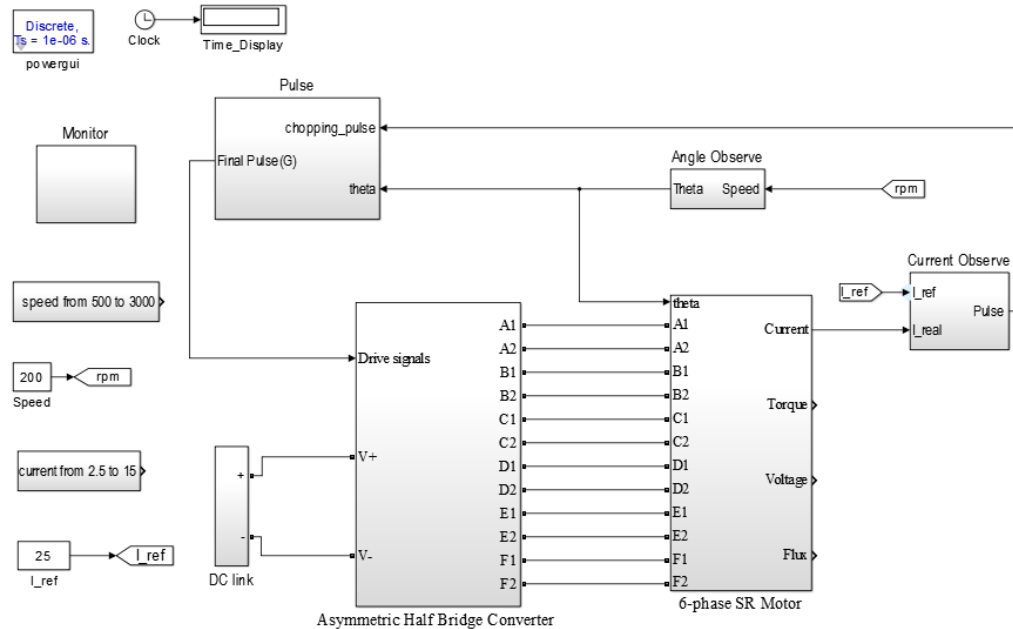
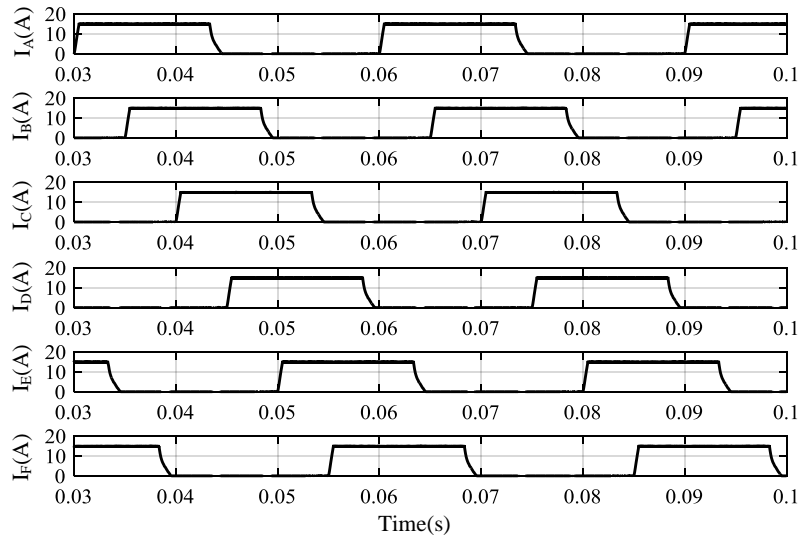


Figure 3.10 Dynamic simulation model of a six-phase SRM prototype

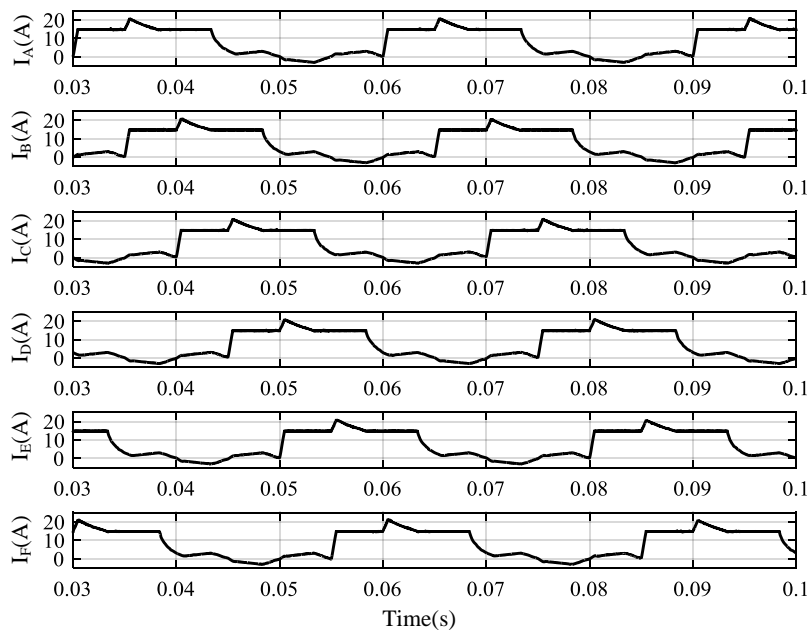
### 3.3.1 Current control

To analyse the performance of the converters at low speed, the asymmetric half bridge converter and the proposed circle converter are controlled by the CCC strategy at 200rpm. Phase reference current is 15A, hysteresis band width is  $\pm 0.5A$ , conduction width is  $160^\circ$  and DC link voltage is 200V.

Figure 3.11 shows the six phase currents under current control of the AHB converter and the circle converter. Six phase currents of the AHB converter are approximate square waveforms and have  $60^\circ$  offset between two adjacent phases in Figure 3.11(a). It is obvious that currents of the proposed circle converter in Figure 3.11(b) have significant distortions compared with the traditional AHB converter. There are two distortion parts, one is a sharp current increasing around  $60^\circ$ , and the other one is freewheeling current distortion after turn-off. There are two causes of the current distortions, which are the special connection of six windings and the phase conduction widths.



(a)



(b)

Figure 3.11 Simulation result of six phase current under current control (a) AHB converter  
(b) circle converter

In order to further explain the reasons giving rise to the current distortions, phase B is picked out as an example. When phase B reaches 0.07s which is  $60^\circ$  of phase B in Figure 3.11(b), phase C starts its magnetization routine and keeps this state until its current reaches the upper hysteresis band. In this situation, the switch  $S_{BC}$  is turned on, and switching state of phase B fully depends on the control command of switch  $S_{AB}$ . If  $S_{AB}$  is turned on, phase B is in the magnetization state. If  $S_{AB}$  is off, phase B is in the freewheeling state. Therefore, no matter

how  $S_{AB}$  operates, phase B has no chance to demagnetize and current of phase B keeps increasing.

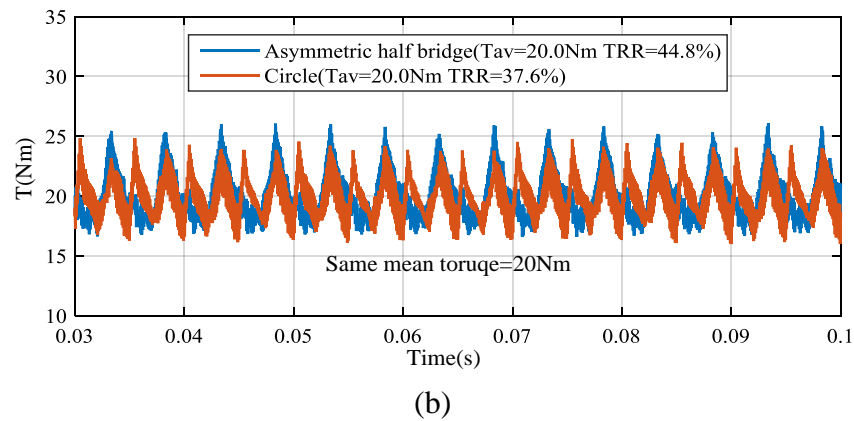
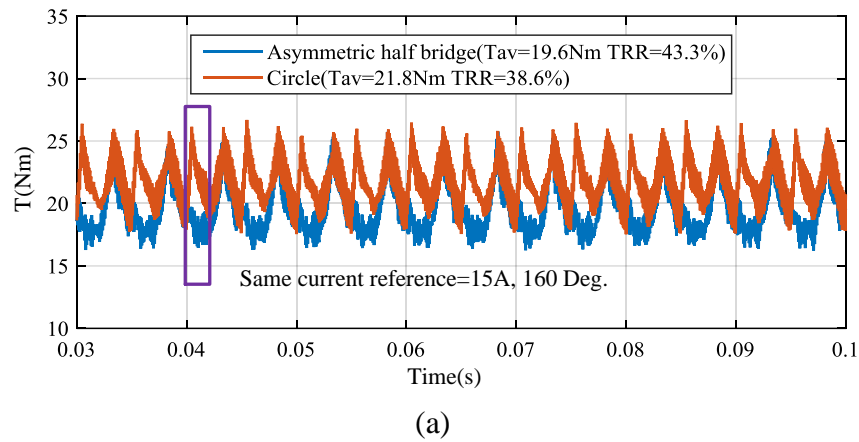


Figure 3.12 Torque comparison between AHB converter and circle converter under current control: (a) same current reference (b) same average torque

As the phase current has obvious distortions in the circle converter, output torques produced by the same reference current have some distinctions between the circle converter and the AHB converter as shown in Figure 3.12(a). The main distinction in each electrical cycle is the part in purple rectangular frame in Figure 3.12(a), where the circle converter has a sharp increase compared with the AHB converter, which is exactly caused by the current distortion around  $60^\circ$  and helps the circle converter have higher mean torque and smaller torque ripple than the traditional AHB converter.

When the proposed circle converter and the traditional AHB converter have the same output mean torque of 20Nm, the TRR (Torque Ripple Ratio) of the circle converter is slight smaller as shown in Figure 3.12(b). However, the current distortions around  $60^\circ$  seriously affect the maximum output current requirement of the power supply and it is an uncontrollable factor in

the system. Consequently, the current distortions in circle converter have to be solved by modifying the control method.

The phase voltage combination comparison between the AHB converter and the proposed circle converter is shown in Table 3.2. For the traditional AHB converter, there are three voltage states in one phase, assuming that three adjacent phases (phase k-1, phase k and phase k+1) are conducting simultaneously, thus there are  $3*3*3=27$  phase voltage combinations as shown in Table 3.2 (numbered as 1 to 27).

Table 3.2 Phase voltage combination comparison between the AHB converter and the circle converter

	The AHB converter			The circle converter			
	No.	Phase k-1	Phase k	Phase k+1	Phase k-1	Phase k	Phase k+1
Phase Voltage	1	$-V_{dc}$	$-V_{dc}$	$-V_{dc}$	$-V_{dc}$	$-V_{dc}$	$-V_{dc}$
	2	$-V_{dc}$	$-V_{dc}$	0	$-V_{dc}$	$-V_{dc}$	0
	3	$-V_{dc}$	$-V_{dc}$	$+V_{dc}$			
	4	$-V_{dc}$	0	$-V_{dc}$			
	5	$-V_{dc}$	0	0	$-V_{dc}$	0	0
	6	$-V_{dc}$	0	$+V_{dc}$	$-V_{dc}$	0	$+V_{dc}$
	7	$-V_{dc}$	$+V_{dc}$	$-V_{dc}$			
	8	$-V_{dc}$	$+V_{dc}$	0			
	9	$-V_{dc}$	$+V_{dc}$	$+V_{dc}$			
	10	0	$-V_{dc}$	$-V_{dc}$	0	$-V_{dc}$	$-V_{dc}$
	11	0	$-V_{dc}$	0	0	$-V_{dc}$	0
	12	0	$-V_{dc}$	$+V_{dc}$			
	13	0	0	$-V_{dc}$	0	0	$-V_{dc}$
	14	0	0	0	0	0	0
	15	0	0	$+V_{dc}$	0	0	$+V_{dc}$
	16	0	$+V_{dc}$	$-V_{dc}$			
	17	0	$+V_{dc}$	0	0	$+V_{dc}$	0
	18	0	$+V_{dc}$	$+V_{dc}$	0	$+V_{dc}$	$+V_{dc}$
	19	$+V_{dc}$	$-V_{dc}$	$-V_{dc}$			
	20	$+V_{dc}$	$-V_{dc}$	0			
	21	$+V_{dc}$	$-V_{dc}$	$+V_{dc}$			
	22	$+V_{dc}$	0	$-V_{dc}$	$+V_{dc}$	0	$-V_{dc}$
	23	$+V_{dc}$	0	0	$+V_{dc}$	0	0
	24	$+V_{dc}$	0	$+V_{dc}$			
	25	$+V_{dc}$	$+V_{dc}$	$-V_{dc}$			
	26	$+V_{dc}$	$+V_{dc}$	0	$+V_{dc}$	$+V_{dc}$	0
	27	$+V_{dc}$	$+V_{dc}$	$+V_{dc}$	$+V_{dc}$	$+V_{dc}$	$+V_{dc}$

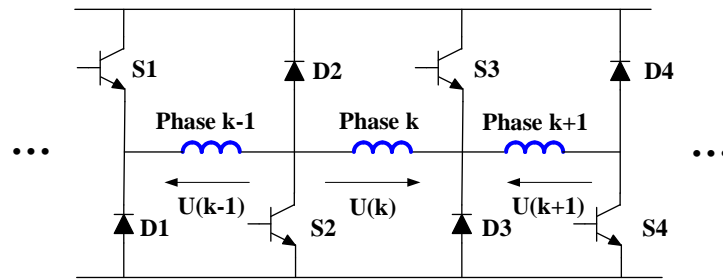


Figure 3.13 Part of the circle converter topology with three phases

However, due to less phase independence in the proposed circle converter, the conduction state of one phase affects the other two adjacent phases, consequently only 15 phase voltage combinations are available in the proposed circle converter. Part of the circle converter is shown in Figure 3.13. If phase  $k$  and phase  $k+1$  both have positive/negative DC link voltage, all the switches/diodes are on, making phase  $k$  have the same voltage as the other two phases, thus voltage combinations 4, 7, 21 and 24 are not available in the proposed converters anymore. Besides, when a phase has positive DC link voltage, two switches in this phase are on, so the adjacent phases cannot have negative DC link voltage, thus 3, 7, 8, 9, 12, 16, 19, 20, 21 and 25 are not available in the proposed converter. Moreover, the loss of the above 10 voltage combinations in the proposed circle converter leads to the current distortion around  $60^\circ$ .

Based on the analysis above, as long as phases  $k-1$  and  $k+1$  are conducting simultaneously, it is impossible to avoid the sharp current increase around  $60^\circ$ . Hence, the key factor that affects the distortion current around  $60^\circ$  is conduction width.

In order to analyse how the conduction width affects the current distortions around  $60^\circ$ , the conduction width of the circle converter is changed between  $80^\circ$  and  $160^\circ$ . Different current waveforms are subsequently observed and compared. Figure 3.14 presents the current waveforms of phase A with five different conduction widths. Five different current references are chosen to help display all the five current waveforms clearly in Figure 3.14. It is clear that current waveforms with the conduction width smaller than  $120^\circ$  do not have current distortion around  $60^\circ$  anymore. This simulation result proves that with a current conduction width limitation, current distortion round  $60^\circ$  can be effectively eliminated. Since there are only two phases conducting simultaneously, Table 3.2 is simplified as Table 3.3.

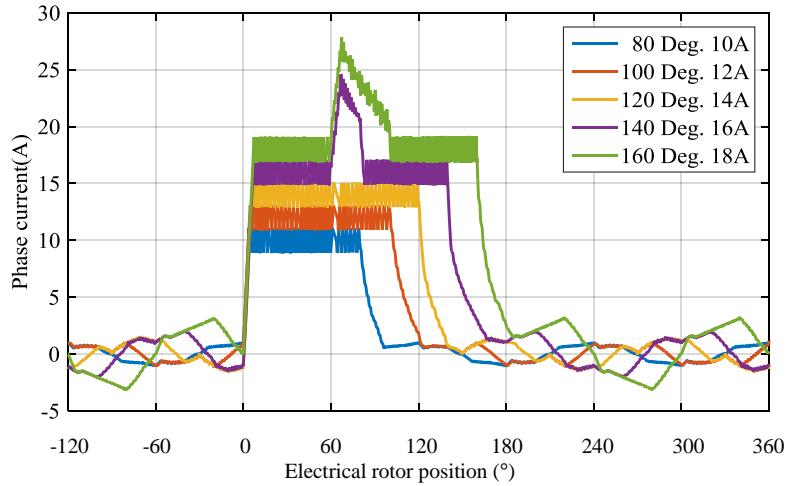


Figure 3.14 Phase current with different conduction widths of circle converter

Table 3.3 Phase voltage combination comparison of the proposed circle converter with the conduction width limitation

	No.	Phase k	Phase k+1	Current distortion
Phase voltage	1	$+V_{dc}$	$+V_{dc}$	no
	2	$+V_{dc}$	0	yes
	3	$-V_{dc}$	$-V_{dc}$	no
	4	$-V_{dc}$	0	yes
	5	0	$+V_{dc}$	yes
	6	0	$-V_{dc}$	yes
	7	0	0	no

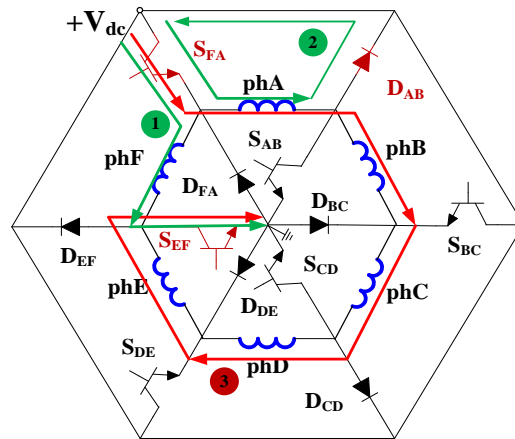


Figure 3.15 Current loops in circle converter

However the unexpected current remaining after the turn-off angle still exists and needs to be eliminated. The reason for this current distortion is the special winding connection topology of the proposed circle converter. In order to further explain the reason, a control instant of the circle converter is picked out and shown in Figure 3.15.

At this instant, phase A and phase F are conducting phases, which means the electrical angle of phase A and phase F is between  $0^\circ$  and  $120^\circ$  (with conduction width limitation applied). When phase F is in the magnetization state (green loop 1 in Figure 3.15) and phase A is in the freewheeling state (green loop 2 in Figure 3.15), switch  $S_{EF}$  and  $S_{FA}$  are turned on, other switches are turned off. Five phases A, B, C, D and E are connected in series with DC link through  $S_{EF}$  and  $S_{FA}$  (red loop 3 in Figure 3.15), thus unexpected distortion currents are generated in inactive four phases. As long as two adjacent phases have different phase voltage, there are current distortions after turn-off, which is summarized in Table 3.3.

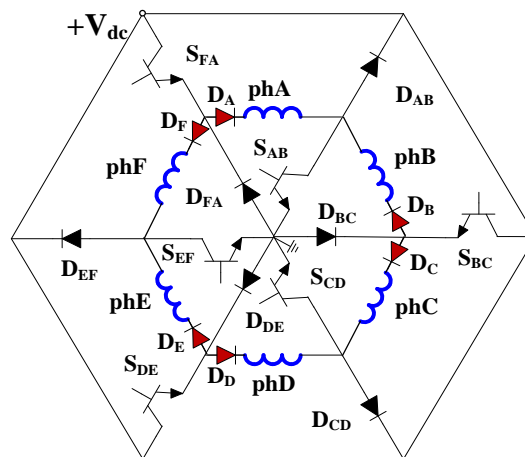


Figure 3.16 Circle converter with extra diodes for six-phase SRMs

A simple way to solve the problem which occurs in Figure 3.15 is to connect one diode in series with each phase winding to limit the current direction after turn-off. The optimized converter topology is presented in Figure 3.16. Six extra diodes (red diodes) are connected in series with the six phase windings along the excitation current directions. As the six phase windings are still in a circle, this converter is named as circle converter with extra diodes.

When the same situation of Figure 3.15 happens in Figure 3.16, the unhealthy current will directly be stopped by diode  $D_B$ , thus there is no chance for current distortion to appear. However, due to the modification of the circle converter, the number of connections between machine and the converter goes up to 9 when extra diodes are added.

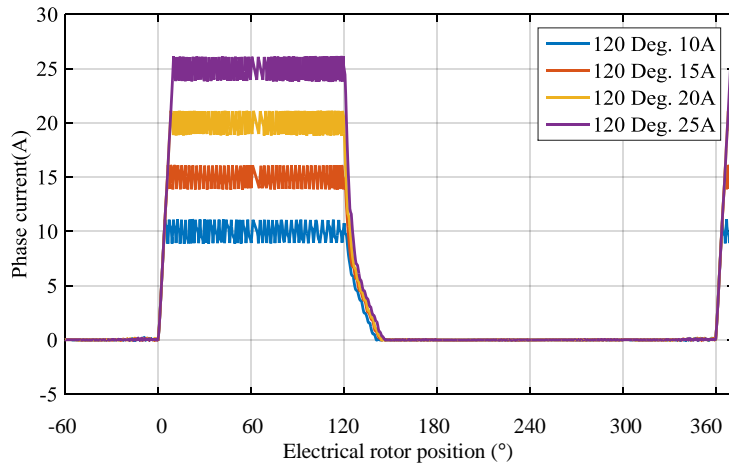


Figure 3.17 Optimized current waveforms of circle converter with extra diodes

Since the elimination solutions of the current distortions are proposed, the following simulations are conducted. The modified CCC method is applied to the circle converter with extra diodes. Current conduction widths are selected as  $120^\circ$  in the simulation and different current references are used to display the current waveforms clearly.

Figure 3.17 presents the optimized current waveforms of the circle converter with extra diodes. It is clear that the six extra diodes convert the bipolar phase currents of circle converter to unipolar and avoid the current distortion after turn-off. In addition, the extra six power diodes will give rise to extra conduction losses, which will be discussed in the following section.

### 3.3.2 Voltage control

In order to investigate the performance of the proposed converters at high speed, the APC method is employed at 1500rpm. Figure 3.18 presents six phase voltage and current waveforms of the circle converter under voltage control. DC link voltage is 200V, and conduction width is  $140^\circ$ . The phase voltages in Figure 3.18(a) have pronounced distortions after demagnetization, and the unexpected voltage drops give rise to current distortions as presented in Figure 3.18(b).

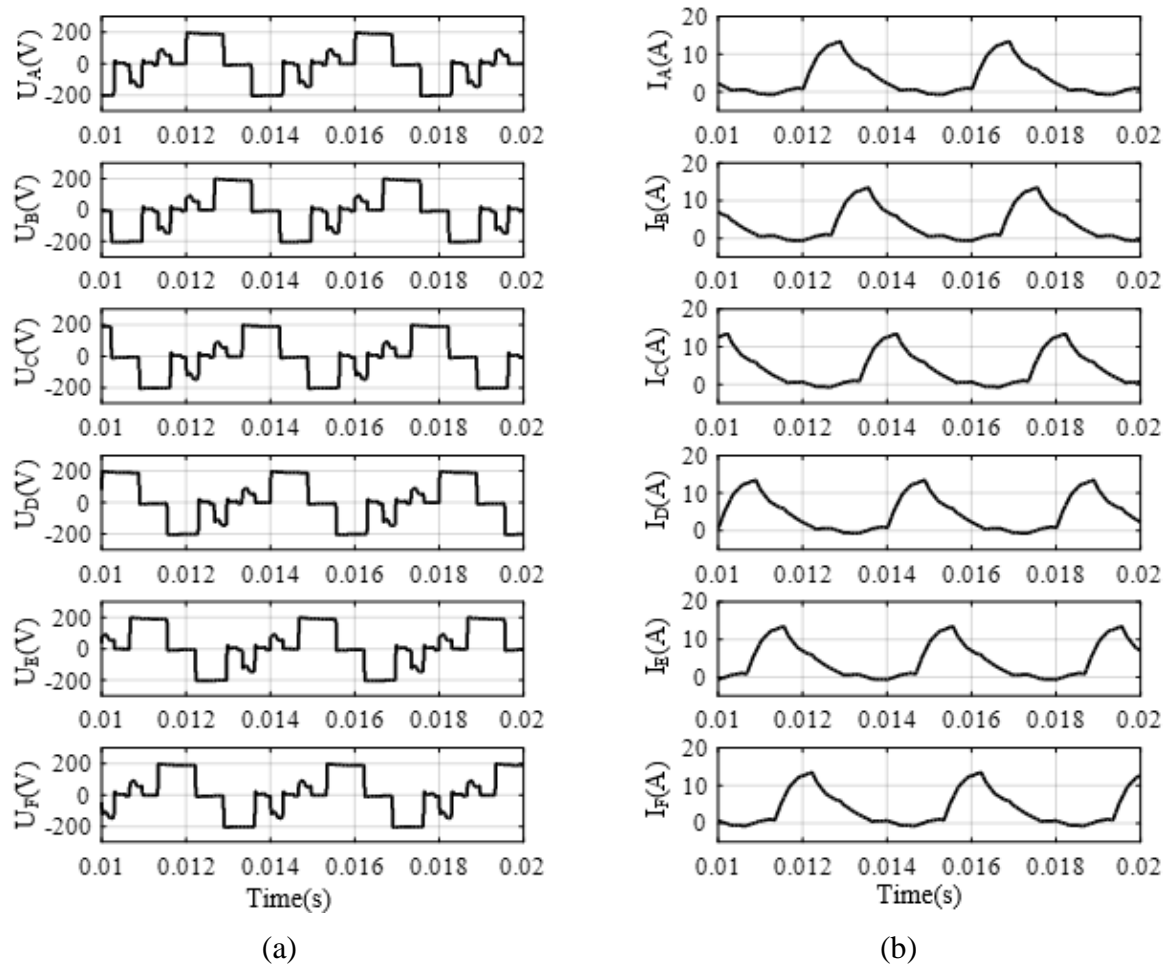


Figure 3.18 Phase voltage and current waveforms of the circle converter under voltage control: (a) six phase voltage (b) six phase current

Figure 3.19 presents six phase voltage and current waveforms for the circle converter with extra diodes under voltage control. With the current direction limitation by six extra diodes, the voltage and current distortions after demagnetization disappear.

However, the amplitude of the current distortions are very small in Figure 3.18(a). At high rotational speed, the average torque and torque ripple are very close as shown in Figure 3.20. Hence, the extra six diodes is not necessary for the circle converter at high speed.

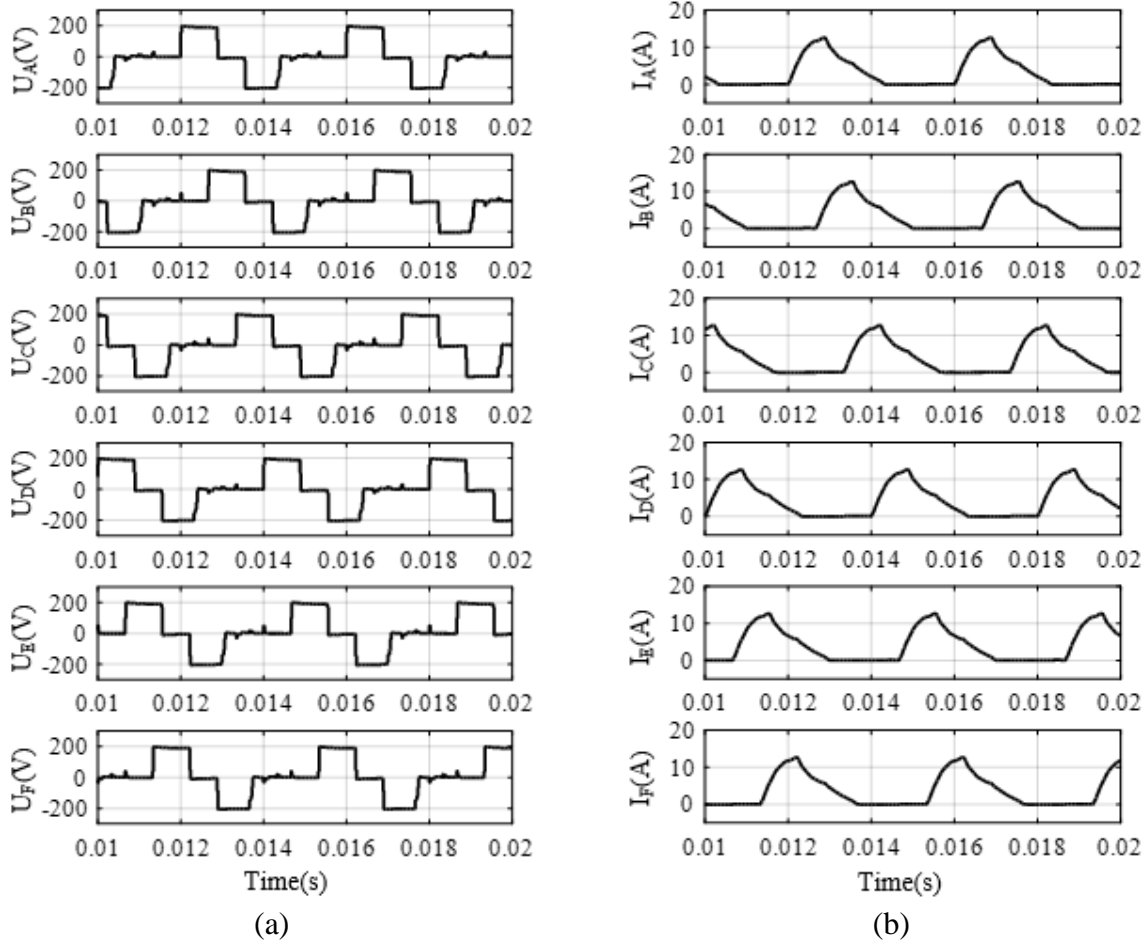


Figure 3.19 Phase voltage and current waveforms of circle converter with extra diodes under voltage control: (a) six phase voltage (b) six phase current

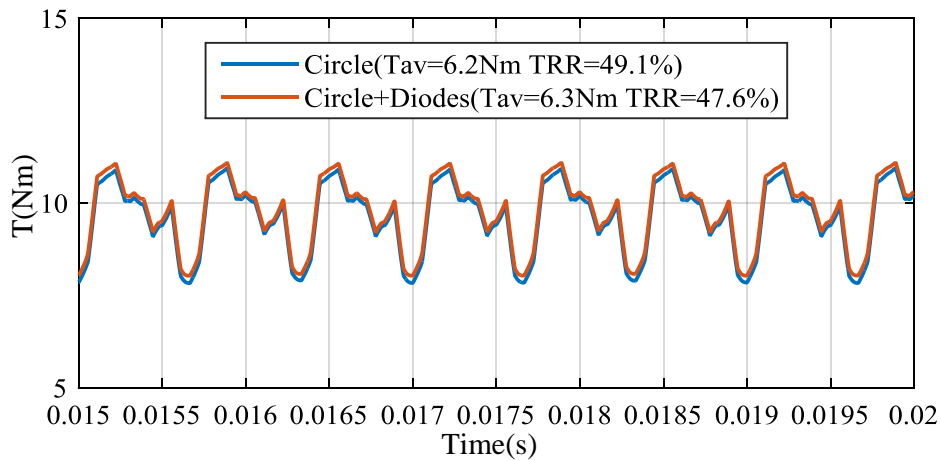


Figure 3.20 Torque comparison between circle converter and circle converter with extra diodes under voltage control

### 3.3.3 Converter loss analysis

Precise control requirements push SRM drives towards high switching frequencies, which in turn increases the relative importance of the switch loss, especially when SRM drives work in chopping mode. To compare the switch loss and conduction loss of the proposed converters and the traditional AHB converter, the same simulation parameters are chosen as follows: rotational speed is varied from 200r/min to 1600r/min, conduction width is  $120^\circ$ , reference current is 20A, and hysteresis bands are  $\pm 0.5$ A. Switch loss is calculated by Equation (3.1), where  $U_{IGBT}$  is the voltage on a switch,  $I_{IGBT}$  is the current of the switch.

$$P_{Loss} = U_{IGBT} \times I_{IGBT} \quad (3.1)$$

The IGBT and diodes parameters are set according to the models which are going to be employed in the test section. The settings of the loss simulation are shown in Table 3.4.

Table 3.4 Device parameters and dynamic simulation settings of the model

Simulation type	Discrete
Solver type	Fixed-step
Solver	Auto
Sample time	$10^{-8}$ s
IGBT internal resistance $R_{CE}$	8m $\Omega$
IGBT internal inductance $L_{on}$	30nH
IGBT forward voltage	1.8V
Freewheeling diode internal resistance $R_{on}$	5.6m $\Omega$
Freewheeling diode forward voltage	1.3V

Comparison results throughout the whole speed range are shown in Table 3.5. Due to fewer switches, the circle converters have smaller switch losses throughout the whole speed range. Due to fewer diodes, the AHB converter and the circle converter have smaller diode conduction losses. Circle converter has the smallest overall losses throughout the whole speed range. The overall losses of the circle converter with extra diodes are much larger than other two converters due to the continuous conduction losses in the six extra diodes.

Table 3.5 Device losses comparisons

	Speed(r/min)	$P_s$ (W)	$P_d$ (W)	Overall losses(W)
Asymmetric Half Bridge Converter	200	76.92	27.57	104.49
	400	75.30	25.44	100.74
	600	72.28	23.19	95.47
	800	68.61	20.79	89.40
	1000	62.78	18.54	81.32
	1200	52.61	16.12	68.73
	1400	38.75	13.68	52.43
	1600	29.52	11.16	40.68
Circle converter	200	67.02	29.52	96.54
	400	63.91	28.07	91.98
	600	61.45	26.81	88.26
	800	56.62	25.45	82.07
	1000	48.05	24.57	72.62
	1200	41.68	23.17	64.85
	1400	29.24	23.02	52.26
	1600	21.43	18.13	39.56
Circle converter with extra diodes	200	68.09	62.51	130.60
	400	64.45	61.94	126.39
	600	61.08	60.92	122.00
	800	55.57	59.83	115.40
	1000	48.76	58.34	107.10
	1200	41.86	60.03	101.89
	1400	30.07	55.48	85.55
	1600	21.76	43.57	65.33

To compare the system efficiency of the proposed converters and the conventional one, the same simulation parameters are set as follows: rotational speed is varying from 200r/min to 1600r/min. Producing the same average output torque  $T_{av}$ , output mechanical energy  $P_m$ , and

input electric energy  $P_e$  from DC power supply are shown in Table 3.6. In this simulation, the switch loss, diode conduction loss and copper loss are included in system losses.

Table 3.6 System efficiency comparisons

	Speed(r/min)	$T_{av}$ (Nm)	$P_e$ (W)	$P_m$ (W)	$\eta$ (%)
Asymmetric Half Bridge Converter	200	20.1	892	421	47.2
	400	20.1	1316	842	64.0
	600	20.2	1727	1269	73.5
	800	20.1	1986	1684	84.8
	1000	20.0	2499	2094	83.8
	1200	20.1	2937	2526	86.0
	1400	17.5	3025	2565	84.8
	1600	10.7	2227	1793	80.5
Circle converter	200	20.2	881	423	48.0
	400	20.0	1295	838	64.7
	600	20.2	1715	1269	74.0
	800	20.1	1974	1684	85.3
	1000	20.1	2500	2105	84.2
	1200	20.2	2944	2538	86.2
	1400	17.6	3042	2580	84.8
	1600	10.6	2206	1776	80.5
Circle converter with extra diodes	200	20.2	957	423	44.2
	400	20.2	1362	846	62.1
	600	20.1	1757	1263	71.9
	800	20.1	2017	1684	83.5
	1000	20.1	2542	2105	82.8
	1200	20.1	2975	2526	84.9
	1400	17.5	3028	2565	84.7
	1600	10.8	2278	1809	79.4

For the same average torque 20Nm, the circle converter has the highest efficiency in chopping mode (low speed and medium speed) while the efficiency of the AHB converter is slightly lower. The circle converter and the traditional AHB converter have very similar efficiency at high speed. The circle converter with extra diodes has the lowest efficiency throughout the whole speed range.

Consequently, considering about the efficiency and the whole cost of the drive system, the proposed circle converter is an excellent solution for the six-phase SRM drive system.

### **3.4 Summary**

In this chapter, a circle converter topology for a six-phase SRM drive is proposed, which does not need any additional energy storage element and only consists of six switches. Compared with the traditional AHB converter, the numbers of switches, diodes and the connections between the SRM and converter are reduced by half. Traditional control methods, which are the CCC and APC techniques, are successfully modified and applied to the circle converter throughout the whole speed range. In order to avoid current distortion in circle converter, the circle converter with extra diodes topology is proposed. Compared with the conventional AHB converter, the proposed circle converter offers smaller converter losses and higher efficiency. The simulation analysis in this chapter will be validated in an experimental chapter.

## Chapter 4. Direct Torque Control of Six-Phase SRMs

As converters are designed for the six-phase Switched Reluctance Machine (SRM), advanced control techniques have to be investigated to control the converters and to further reduce the torque ripple. In this chapter, a Direct Torque Control (DTC) strategy is proposed for the six-phase SRM. The study of this advanced torque ripple reduction method starts from derivation of instantaneous torque. The relationship between stator flux and torque production is subsequently discussed and the basic principle of the DTC strategy is summarized. In order to apply the proposed DTC method to the six-phase SRM, the related stator flux vectors, voltage vectors, zones arrangement and switching table are discussed. The proposed DTC method has been applied to an Asymmetric Half Bridge (AHB) converter and the proposed circle converters. DTC simulation models are built in MATLAB/SIMULINK, and all the results are compared with the traditional control methods throughout the whole speed range.

### 4.1 Basic principle of DTC method

In order to control the instantaneous torque, the nonlinear torque characteristics have to be derived. Figure 4.1 shows the energy conversion diagram considering saturation.

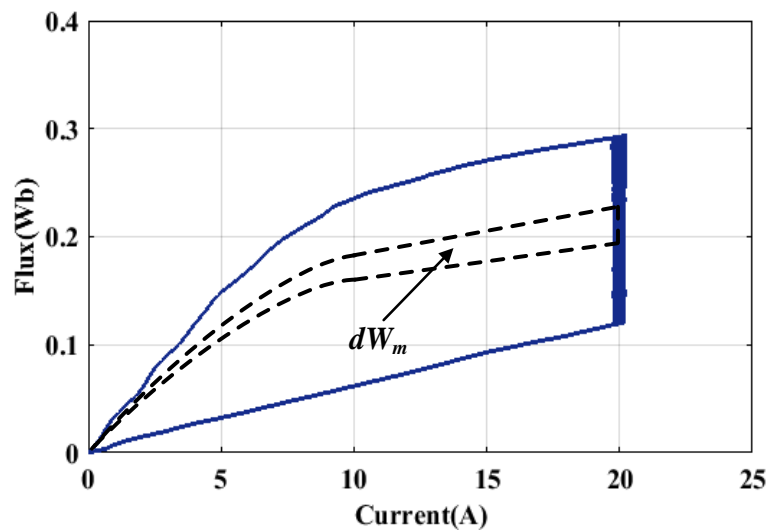


Figure 4.1 Energy conversion diagram considering saturation

In Figure 4.1 the area surrounded by the blue line is the transferred mechanical energy from one electrical cycle. The average output torque is determined by Equation (4.1).

$$T_{av} = \frac{\Delta W_m}{\Delta \theta} \quad (4.1)$$

As phase current has a first order delay relative to changes in the phase voltage and stator flux linkage [60], we can assume that during a small rotor displacement  $d\theta$ , the current is constant. Ignoring the resistive loss, the energy exchanged with the supply  $dW_e$  is given in Equation (4.2), and the change of mechanical energy  $dW_m$  is what is left after the change of magnetic stored energy  $dW_f$  as Equation (4.3).

$$\begin{aligned} dW_e &= (V - iR)idt \\ &= \left( \frac{\partial \psi}{\partial i} \frac{di}{dt} + \frac{\partial \psi}{\partial \theta} \frac{d\theta}{dt} \right) idt \\ &= i \frac{\partial \psi}{\partial \theta} \omega_m dt = eidt \end{aligned} \quad (4.2)$$

$$dW_m = dW_e - dW_f \quad (4.3)$$

Therefore, the change of mechanical energy is the area surrounded by dashed line in Figure 4.1 and is equal to  $T_e d\theta$ , so that, instantaneous output torque can be expressed as Equation (4.4)[60].

$$\begin{aligned} T_e &= \left. \frac{dW_m}{d\theta} \right|_{i=const} = \left. \frac{d(W_e - W_f)}{d\theta} \right|_{i=const} \\ &= \left. \frac{dW_e}{d\theta} \right|_{i=const} - \left. \frac{dW_f}{d\theta} \right|_{i=const} \\ &= i \left. \frac{\partial \psi(\theta, i)}{\partial \theta} \right|_{i=const} - \left. \frac{\partial W_f}{\partial \theta} \right|_{i=const} \end{aligned} \quad (4.4)$$

For a given current the flux-linkage and the magnetic stored energy both rise as the rotor comes into alignment and both fall once past alignment, i.e. they both always have the same polarity. Furthermore, the magnitude of the rate of change of stored energy will always be less than the first term in Equation (4.4), hence Equation (4.4) can be further simplified as (4.5). As current is assumed to be a constant, the second term of Equation (4.5) is expressed as Equation (4.6),

$$T_e \approx i \left. \frac{\partial \psi(\theta, i)}{\partial \theta} \right|_{i=const} \quad (4.5)$$

$$A = \left. \frac{\partial \psi(\theta, i)}{\partial \theta} \right|_{i=const} \quad (4.6)$$

where the symbol of instantaneous torque  $T_e$  is completely dependent on the symbol of the second term of Equation (4.5), which is expressed as A in Equation (4.6). If Equation (4.6) is negative, the instantaneous torque  $T_e < 0$ , and vice versa. In other words, to produce a positive torque, the stator flux amplitude should increase with respect to rotor position, whereas to produce a negative torque, stator flux should decrease with respect to rotor position. If stator flux  $\psi$  can be controlled to be a constant magnitude, the change of  $T_e$  only depends on the velocity change of stator flux with respect to rotor movement. Therefore a positive value of Equation (4.6) is defined as flux acceleration, whereas a negative value of Equation (4.6) is defined as flux deceleration. Hence, the DTC control technique for SRMs is as follows:

- (a) The stator flux-linkage vector of the motor is kept at a constant magnitude by selecting an appropriate voltage vector.
- (b) The torque can be controlled by accelerating or decelerating the stator flux vector relative to the rotor movement.

#### 4.1.1 DTC method for six-phase AHB converter

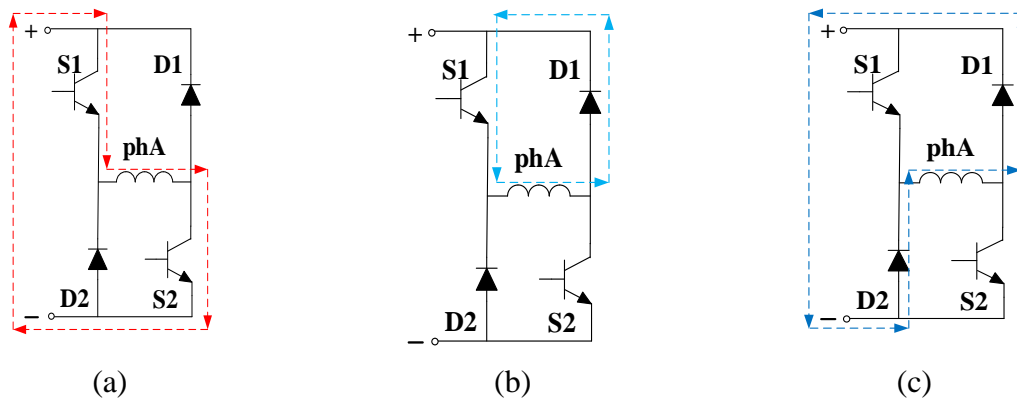


Figure 4.2 Phase voltage states: (a) state '+1' (b) state '0' (c) state '-1'

A classical AHB power converter for a six-phase SRM is shown in Figure 3.1. According to the on-off states of the switches, each phase winding has three voltage states. For example, when switch S1 and S2 are on, phA winding voltage is  $+V_{dc}$  and this state is defined as '+1' as shown in Figure 4.2(a). As shown in Figure 4.2 (b), when S2 is off, phA winding is short-

circuited through switch S1 and diode D1 and this state is defined as '0'. When switch S1 and S2 are off, phA winding freewheels through diode D1 and D2, phA winding voltage is  $-V_{dc}$  and this state is defined as '-1' as shown in Figure 4.2(c).

At any instant each phase is in a specific voltage state and a voltage vector  $U$  can be created by the common action of all the six phases. However, this voltage vector is a time function and it has no corresponding relation to the stator flux space vector. In order to build a relationship between them for further analysis, the direction of the voltage vector of one phase is consistently selected with the stator flux space vector of this phase in the time-space coordinate system.

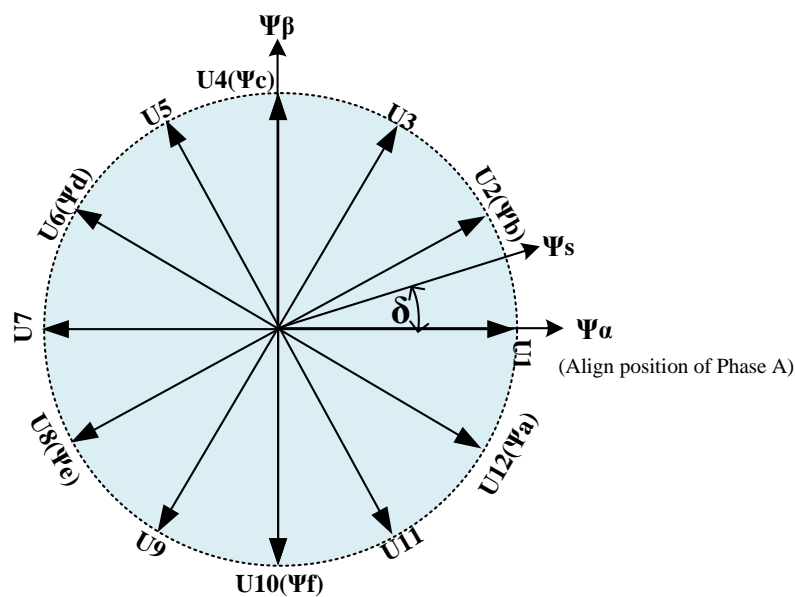


Figure 4.3 Arrangement of flux directions and voltage vectors

As shown in Figure 4.3, U2, U4, U6, U8, U10 and U12 have the same voltage directions as phases A to F, and there are three adjacent phases conducting simultaneously in these six voltage vectors. For more flexible control, a three-phase SRM employs six voltage vectors, thus the six-phase SRM needs to employ twelve voltage vectors. A six-phase SRM has six stator flux directions, separated by  $60^\circ$ , to achieve a balanced voltage vector arrangement. The extra six voltage vectors can be produced by a combination of the original flux directions. The stator flux is adjusted by the 12 voltage vectors U1 to U12.

Table 4.1 gives twelve voltage vectors for the AHB converter with the DTC method. All the even number voltage vectors have the same direction with defined six phase flux, and there are three phases conducting at same time to follow the direction and produce more positive

torque. All the odd number voltage vectors are along the angular bisector of two adjacent phase fluxes, in this situation there are two adjacent phases conducting at same time and two of the remaining four phases are freewheeling.

Table 4.1 Twelve voltage vectors for AHB converter

U1 (+1,+1, 0,-1,-1, 0)	U2 (+1,+1,+1,-1,-1,-1)
U3 ( 0,+1,+1, 0,-1,-1)	U4 (-1,+1,+1,+1,-1,-1)
U5 (-1, 0,+1,+1, 0,-1)	U6 (-1,-1,+1,+1,+1,-1)
U7 (-1,-1, 0,+1,+1, 0)	U8 (-1,-1,-1,+1,+1,+1)
U9 ( 0,-1,-1, 0,+1,+1)	U10 (+1,-1,-1,-1,+1,+1)
U11(+1, 0,-1,-1, 0,+1)	U12 (+1,+1,-1,-1,-1,+1)

According to the stator flux relationship shown in Figure 4.4, the amplitude of stator flux is a combination value of the six phase flux vectors according to Equation (4.7), (4.8) and (4.9). The position of the stator flux is calculated by Equation (4.10).

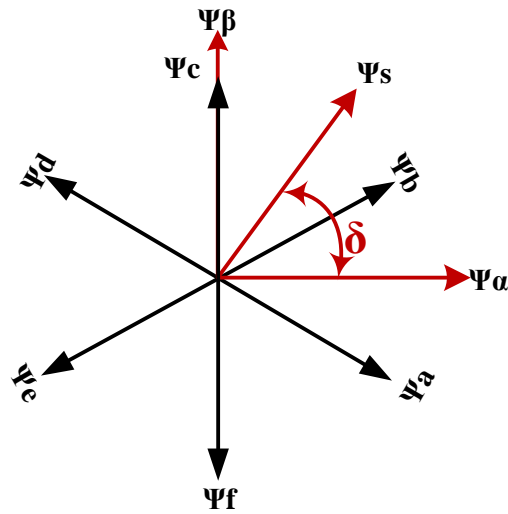


Figure 4.4 Definition of stator flux

$$\psi_{\alpha} = (\psi_a + \psi_b - \psi_d - \psi_e) \cos 30^{\circ} \quad (4.7)$$

$$\psi_{\beta} = (-\psi_a + \psi_b + \psi_d - \psi_e) \sin 30^{\circ} + \psi_c - \psi_f \quad (4.8)$$

$$\psi_s = \sqrt{\psi_{\alpha}^2 + \psi_{\beta}^2} \quad (4.9)$$

$$\delta = \arctan \left( \frac{\psi_{\beta}}{\psi_{\alpha}} \right) \tag{4.10}$$

In order to locate the stator flux, the coordinate system is divided into 12 zones N1 to N12. Every zone occupies 30° and every voltage vector is located in the central axis of each zone, as shown in Figure 4.5.

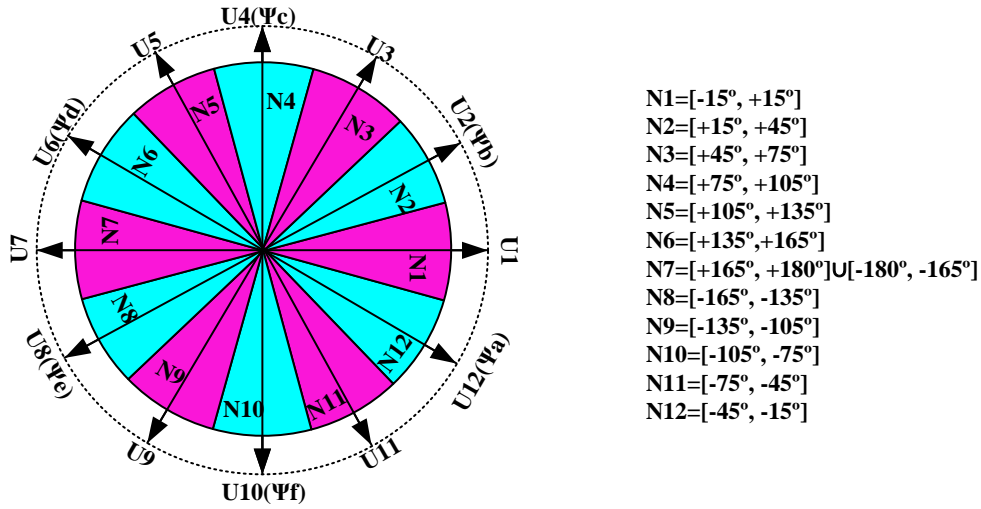


Figure 4.5 Zones arrangement for AHB converter

According to the DTC principle, the amplitude and position of the stator flux linkage is controlled by selecting an appropriate voltage vector: for this purpose the flux linkage discrete expression is shown in differential form as Equation (4.11),

$$\Psi(k) = \Psi(k-1) + U(k)T_s \tag{4.11}$$

where  $T_s$  is the sample time.

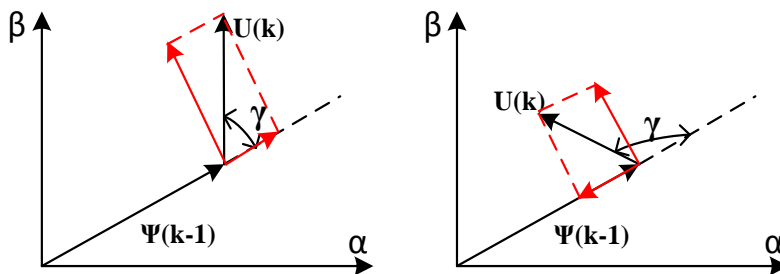


Figure 4.6 Relationship between stator flux vector and voltage vector

The relationship between the stator flux and voltage vectors is shown in Figure 4.6. If the angle between voltage vector  $U(k)$  and stator flux vector  $\Psi(k-1)$  is an acute angle,  $U(k)$  has a component along the positive direction of  $\Psi(k-1)$  and the flux amplitude increases, whereas if the angle is an obtuse angle,  $U(k)$  has component along the negative direction of  $\Psi(k-1)$  and the flux amplitude decreases. In addition, when the voltage vector  $U(k)$  is at an angle in advance of the stator flux vector, the stator flux is advanced. Providing the advance is also positive with respect to rotor electrical position, the instantaneous torque  $T_e$  increases, and vice versa.

According to the above analysis, amplitudes of stator flux and instantaneous torque are controlled by choosing appropriate voltage vectors. Taking stator flux in zone N1 in Figure 4.5 as an example, if stator flux needs to increase, voltage vectors U2, U3, U11 and U12 which have an acute angle with stator flux are selected. If stator flux needs to decrease, voltage vectors U5, U6, U7, U8 and U9 which have an obtuse angle respect to stator flux are selected. The increasing and decreasing of torque can also be determined according to whether the voltage vector leads or lags the stator flux vector.

In order to implement the DTC method, demands of stator flux and torque have to be considered simultaneously. In general, to increase both flux and torque the voltage should be applied in the next sector,  $(k+1)$ , whilst to reduce flux and torque it can be applied five sectors behind,  $(k-5)$ . If stator flux is to rise whilst instantaneous torque is to fall then the voltage vector chosen should applied in the earlier sector  $(k-2)$ , whilst to increase torque and decrease flux, the voltage should be applied four sectors ahead,  $(k+4)$ . Table 4.2 shows the switching table for six-phase AHB converter.

Table 4.2 Switching table of DTC method for six-phase AHB converter

$\Psi \uparrow T \uparrow$	$\Psi \uparrow T \downarrow$	$\Psi \downarrow T \uparrow$	$\Psi \downarrow T \downarrow$
$U(k + 1)$	$U(k - 2)$	$U(k + 4)$	$U(k - 5)$

Figure 4.7 shows the control diagram of the proposed DTC method, in which the control parameters are instantaneous torque and stator flux. Six phase flux amplitudes are obtained from integration of the phase voltage according to Equation (4.11), and therefore the amplitude and position of the stator flux vector is calculated by Equation (4.7) to Equation (4.10) in the flux estimation block. Estimated torque is calculated using measured nonlinear

magnetization characteristics of the prototype when phase current and rotor position are available from a current sensor and position encoder.

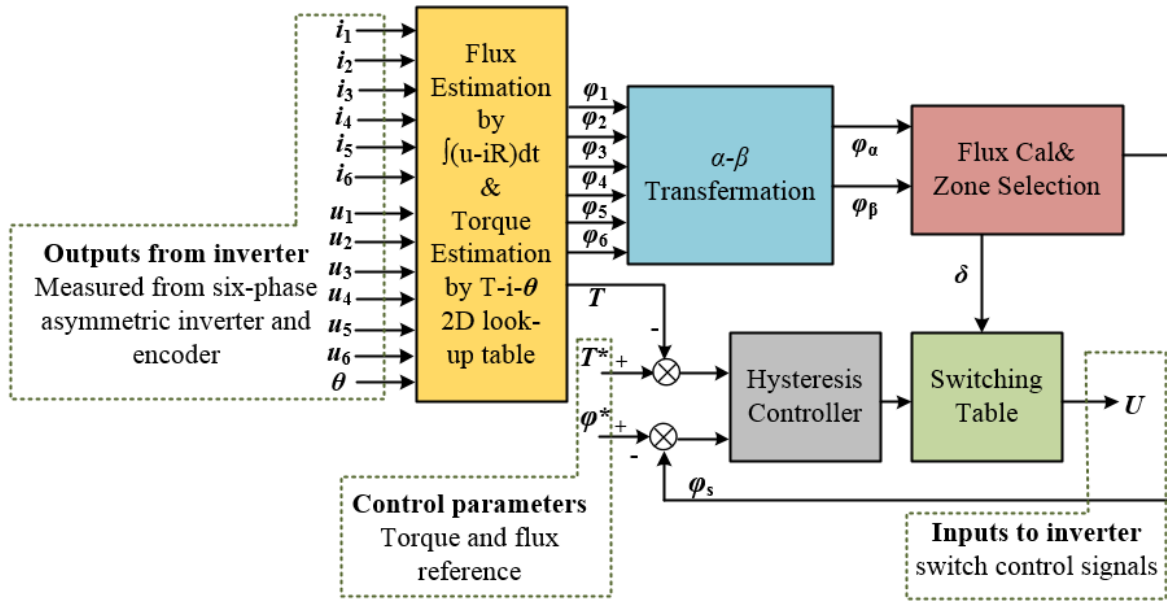


Figure 4.7 Control diagram of the proposed DTC method for a six-phase SRM

### 4.1.2 DTC method for circle converter

In order to reduce the switch number for the six-phase SRM converter, the circle converter has been proposed in Chapter 3. As traditional control methods have been successfully applied and do have some conduction width limitation, more torque ripple exists in the circle converter, therefore it will be meaningful if the DTC method can also be applied to reduce the torque ripple for this converter.

The main distinction between the six-phase AHB converter and circle converter is the phase independence, therefore the voltage vectors and switching tables of the DTC strategy for the six-phase AHB converter cannot be directly applied to the circle converter. For example, U1 in Table 4.1 is (+1,+1,0,-1,-1,0), in which two adjacent phases are conducting and two phases are freewheeling. For the circle converter, to achieve the same effect, the equivalent voltage vector V1 can be defined as (+1,+1,+1,-1,-1,-1), where ‘+1’ represents the on-state and ‘-1’ represents the off-state for each sharing switch. U2 in Table 4.1 is (+1,+1,+1,-1,-1,-1), in which three adjacent phases are conducting and other phases are non-conducting. For the circle converter, every switch is shared by two phases. It is obvious that there are always two

phases in freewheeling loops, therefore it is impossible to define the equivalent voltage vector with  $U_2$ . Consequently, there are only six reasonable voltage vectors that can be employed with the circle converter. Table 4.3 demonstrates the six voltage vectors for the circle converter.

Table 4.3 Six voltage vectors for the circle converter

V1 (+1,+1,+1,-1,-1,-1)	V4 (-1,-1,-1,+1,+1,+1)
V2 (-1,+1,+1,+1,-1,-1)	V5 (+1,-1,-1,-1,+1,+1)
V3 (-1,-1,+1,+1,+1,-1)	V6 (+1,+1,-1,-1,-1,+1)

As the quantity of voltage vectors are reduced from twelve to six, the zone arrangement is changed accordingly. In order to locate the stator flux, the coordinate system is divided into six zones N1 to N6. Every zone occupies  $60^\circ$  and each voltage vector is located in the central axis of each zone, as shown in Figure 4.8. The definition of stator flux is the same as the AHB converter. Stator flux amplitude and position are calculated by Equation (4.7) to (4.10). Stator flux vector and voltage vectors also fulfil the relationships in Figure 4.6.

In order to analyse the switching table in this section, take stator flux in zone N1 in Figure 4.8 as an example. If stator flux needs to increase, voltage vectors V2 and V6 which have an acute angle with the stator flux are selected. If stator flux needs to decrease, voltage vectors V3 and V5 which have an obtuse angle respect to stator flux are selected. The increasing and decreasing of torque can also be determined according to whether the voltage vector leads or lags the stator flux vector.

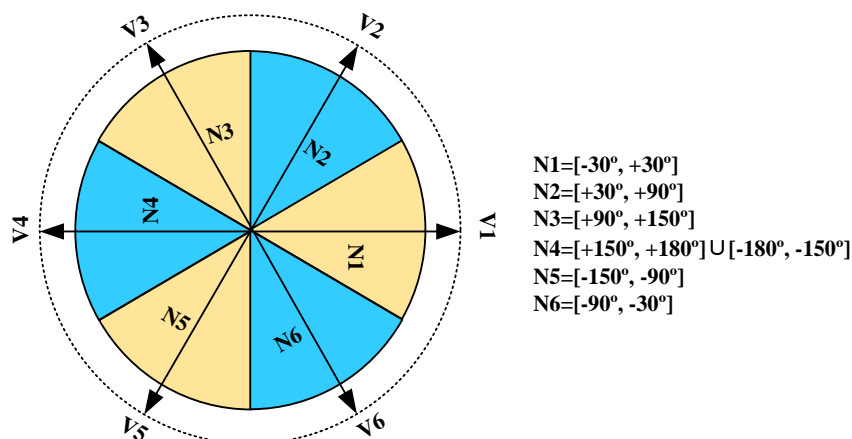


Figure 4.8 Zones arrangement for the circle converter

Considering the demands of stator flux and torque simultaneously, to increase both stator flux and torque the voltage should be applied in the next sector,  $(k+1)$ , whilst to reduce flux and

torque it can be applied two sectors behind, (k-2). If stator flux is to rise whilst instantaneous torque is to fall then the voltage vector chosen should be applied in the earlier sector (k-1), whilst to increase torque and decrease flux, the voltage should be applied two sectors ahead, (k+2). Table 4.4 shows the switching table for the six-phase circle converter.

Table 4.4 Switching table for the DTC method with the circle converter

$\Psi \uparrow T \uparrow$	$\Psi \uparrow T \downarrow$	$\Psi \downarrow T \uparrow$	$\Psi \downarrow T \downarrow$
V(k + 1)	V(k - 1)	U(k + 2)	U(k - 2)

## 4.2 Simulation analysis with the AHB converter

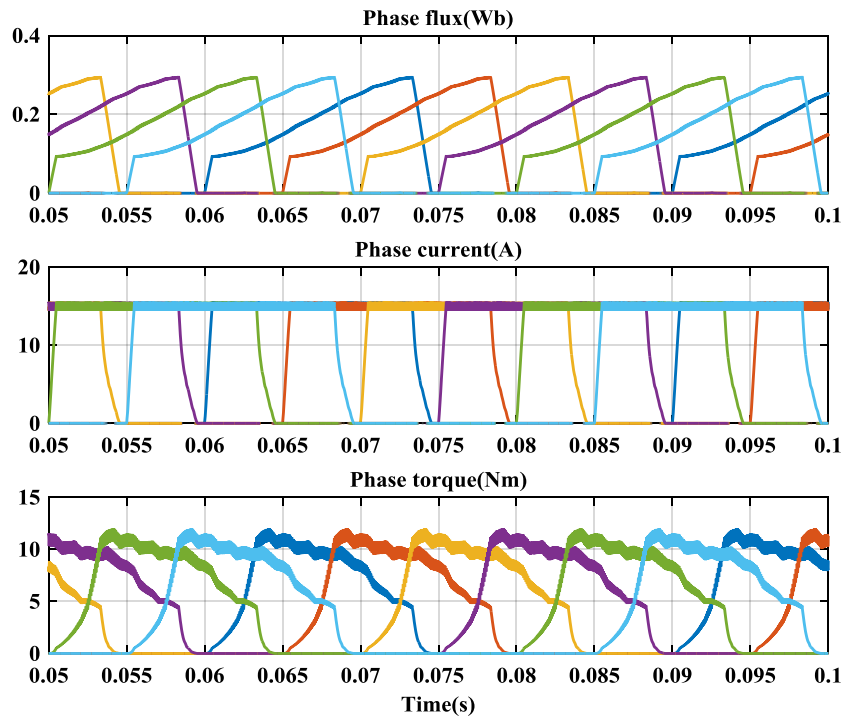
In order to compare the proposed DTC method with traditional control methods, a dynamic DTC model driven by AHB converter of the six-phase SRM is developed in MATLAB/SIMULINK environment. This model uses the same parameters of the SRM prototype as shown in Figure 3.9.

### 4.2.1 Simulation results at 200r/min ( $T_{ref}=20Nm$ )

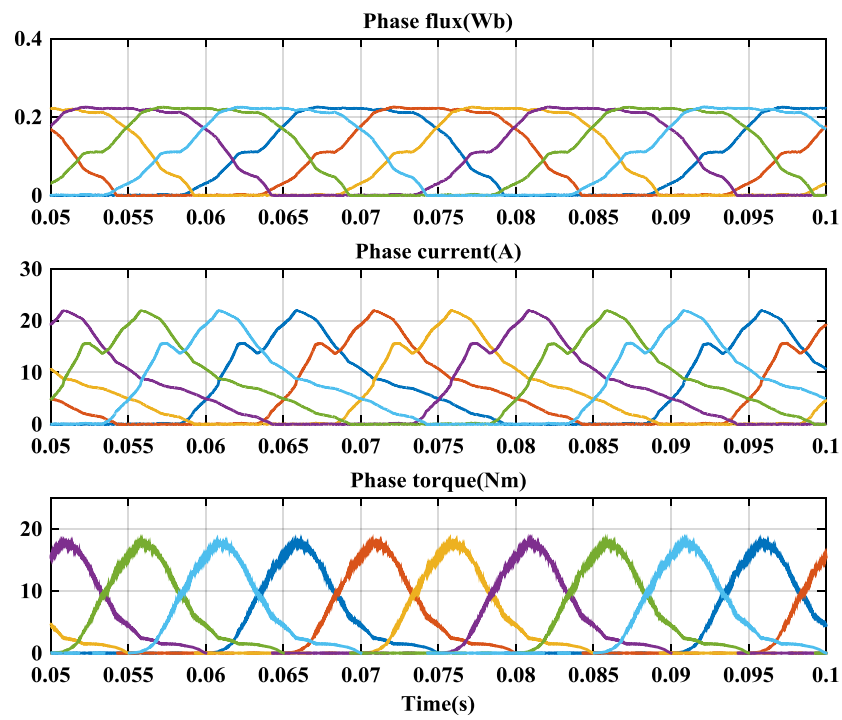
For low speed operation the simulation parameters are set at follows: DC link voltage  $V_{dc}$  is 200V; rotation speed  $n$  is 200r/min. In the CCC method the current reference  $I^*$  is 15A,  $\theta_{on}$  and  $\theta_{off}$  are  $0^\circ$  and  $160^\circ$  respectively. In the DTC control the flux-linkage reference  $\psi_s^*$  is 0.38Wb and the torque reference  $T^*$  is 20Nm.

Figure 4.9 shows simulation results of the CCC and DTC methods at 200r/min. In the traditional CCC method, phase current is controlled by a hysteresis controller to achieve an approximately square waveform. In the proposed DTC method, switching signals are generated with instantaneous torque and stator flux errors.

Compared with the traditional CCC method the phase flux linkage and current of the DTC method are very irregular due to rapid adjustment requirement of the stator flux and torque hysteresis controllers. Another significant distinction is that both the phase torque and current have larger maximum values and a wider conduction width appears in the DTC method. By observing the change of instantaneous torque and rotational speed, it is very obvious in Figure 4.9(c) that when the flux advances ahead of the rotor movement the torque increases, and when the flux lags behind the rotor movement the torque decreases.



(a)



(b)

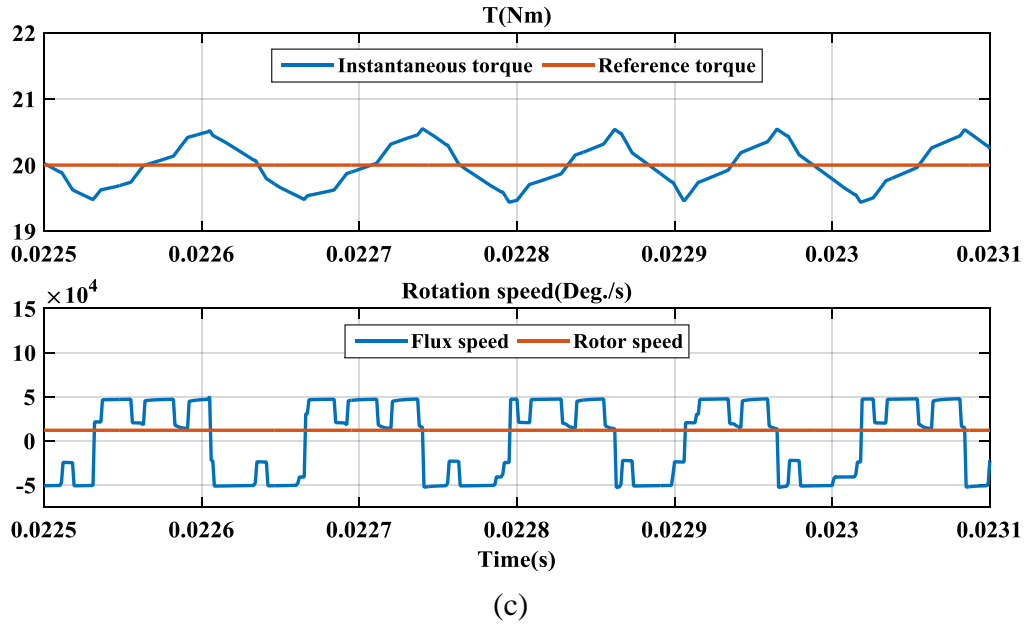
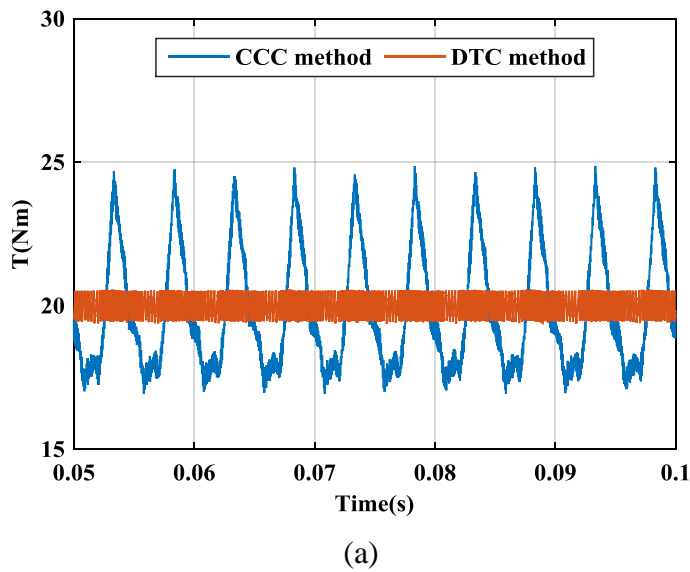
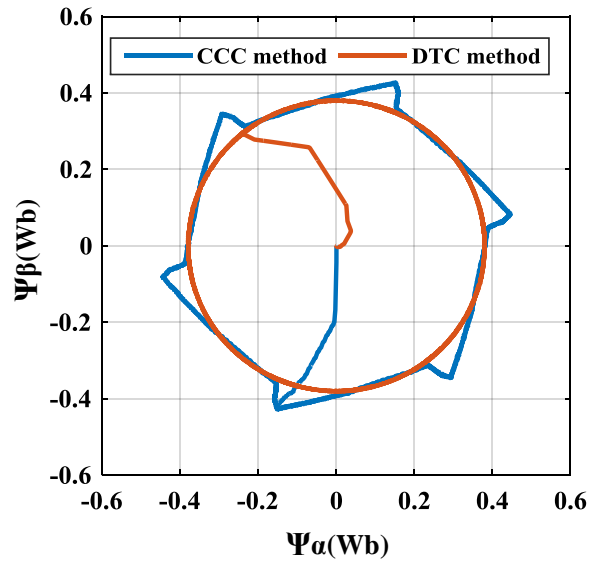


Figure 4.9 Simulation results of the AHB converter at 200r/min: (a) six phase flux, current and torque of the CCC method (b) six phase flux, current and torque of the DTC method (c) instantaneous torque and flux speed of the DTC method

For an average torque output of 19.8Nm, Torque Ripple Ratio (TRR) with the CCC method is 35.3%, whilst the DTC method reduces it to 5.1% as shown in Figure 4.10(a). By plotting stator flux vectors of the CCC method and DTC method in the x-y stationary frame in Figure 4.10(b) it can be further demonstrated that the stator flux linkage in the CCC method is close to a hexagon, whilst the DTC method has a circular trajectory.





(b)

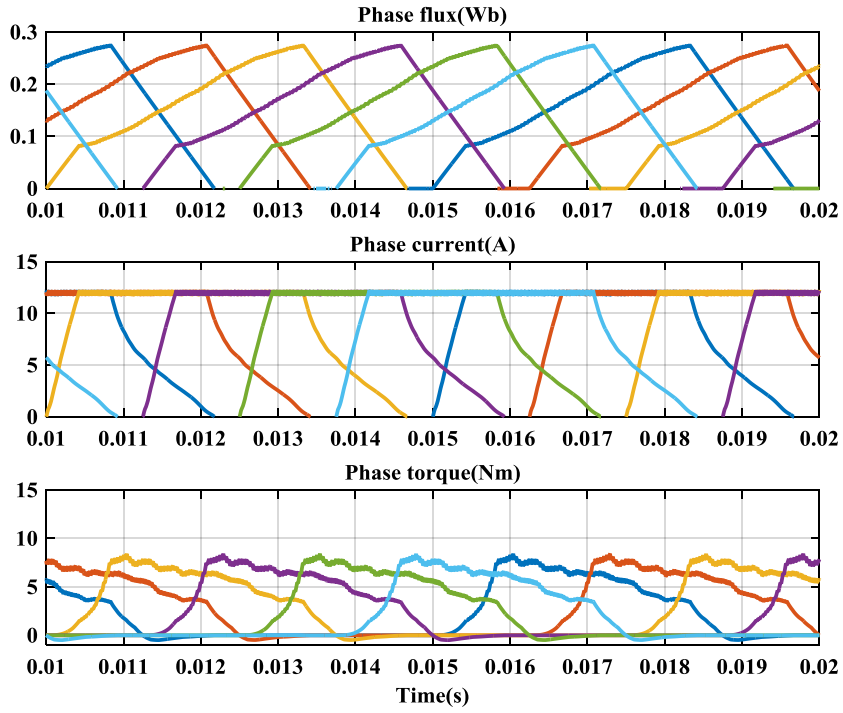
Figure 4.10 Total torque output and flux trajectory comparison of the AHB converter at 200r/min: (a) total torque output of CCC method and DTC method (b) flux trajectory of CCC method and DTC method

#### 4.2.2 Simulation results at 800r/min ( $T_{ref} = 13.5\text{Nm}$ )

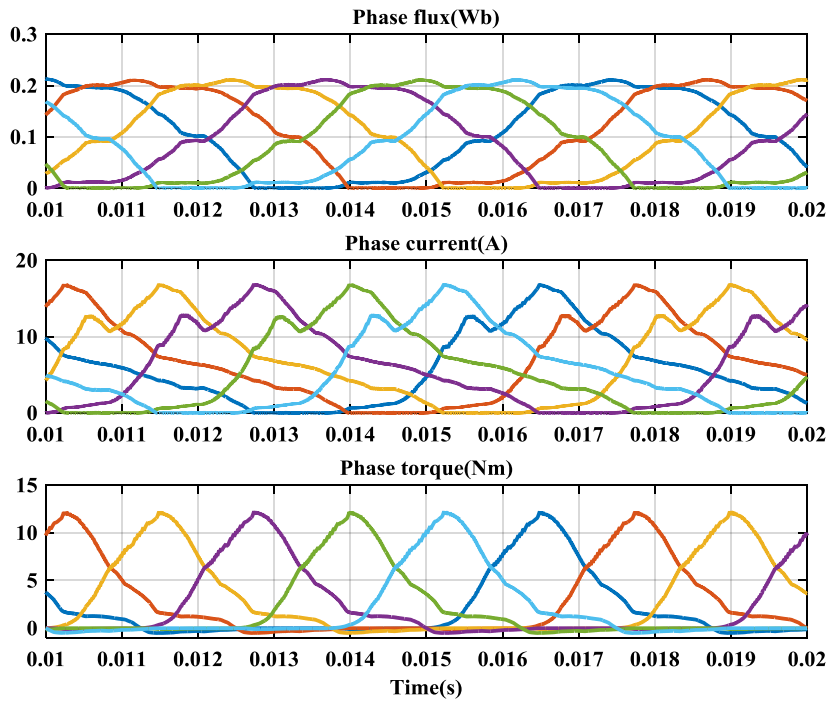
For medium speed simulation the parameters are set as follows: DC link voltage  $V_{dc}$  is 200 V, rotational speed  $n$  is 800r/min. In the DTC method the stator flux reference  $\psi_s^*$  is 0.33Wb and the torque reference  $T^*$  is 13.5Nm. In the CCC method, the current reference  $I^*$  is 12A,  $\theta_{on}$  and  $\theta_{off}$  are  $0^\circ$  and  $160^\circ$  respectively.

Simulation results are shown in Figure 4.11, including six phase flux, current and torque. Due to the DC link voltage limitation, the rate of rise and fall of current with respect to time is lower in Figure 4.11(a) than in the low speed results in Figure 4.9(b). Current results at medium speed are with pronounced current tails at turn-off. Although torque demands are different, the profiles of phase flux are very similar between Figure 4.9(b) and Figure 4.11(b).

For the same average torque output of 13.5Nm, TRR with the CCC method is 48.8%, whilst the DTC method reduces it to 11.1% as shown in Figure 4.12(a). By plotting the stator flux vectors of the CCC method and DTC method in the x-y stationary frame in Figure 4.12(b), it can be seen that stator flux linkage in the CCC method forms a hexagonal trajectory, whilst the DTC method continues to have a circular trajectory.

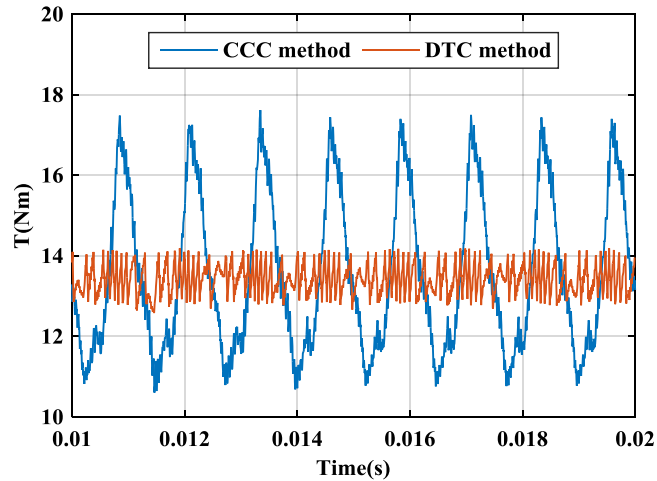


(a)

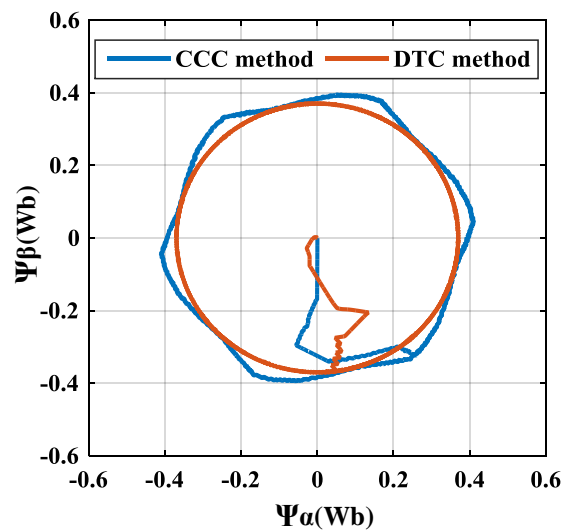


(b)

Figure 4.11 Simulation results of the AHB converter at 800r/min: (a) six phase flux, current and torque of CCC method (b) six phase flux, current and torque of DTC method



(a)

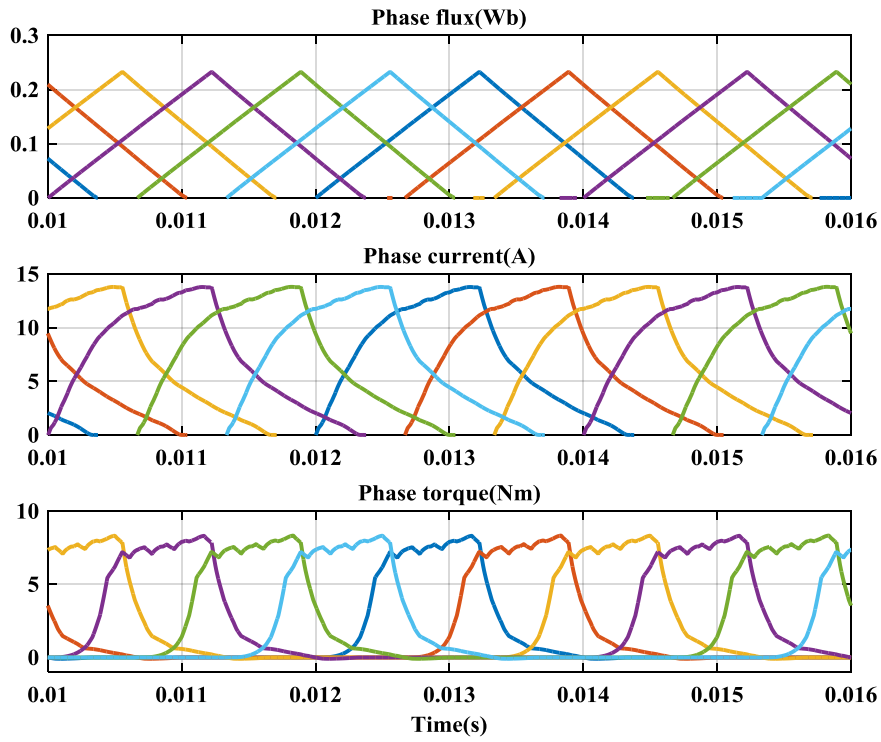


(b)

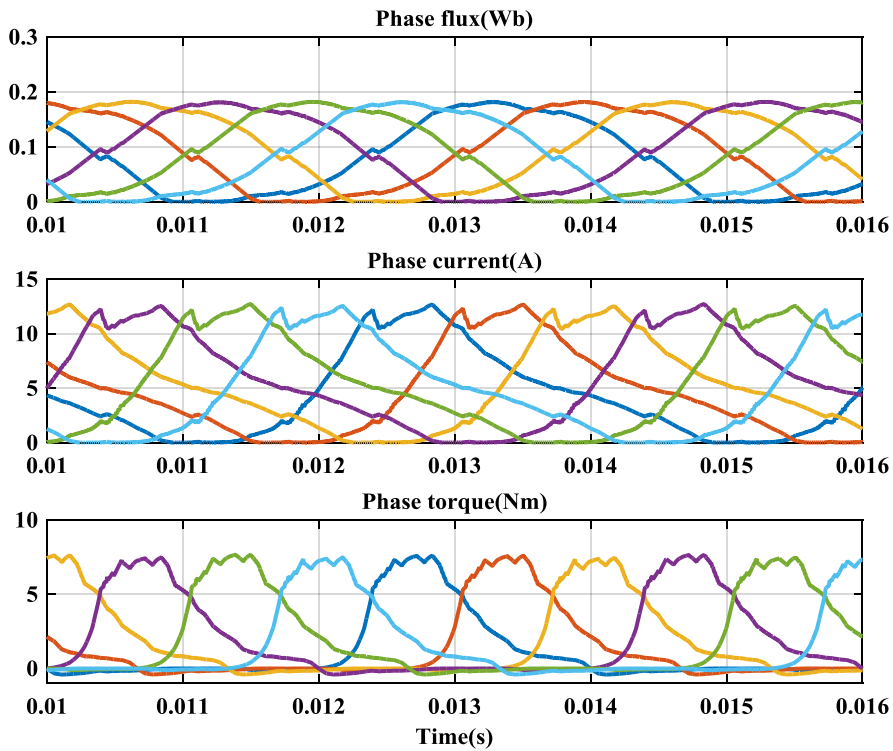
Figure 4.12 Total torque output and flux trajectory comparison of the AHB converter at 800r/min: (a) total torque output of CCC method and DTC method (b) flux trajectory of CCC method and DTC method

#### 4.2.3 Simulation results at 1500r/min ( $T_{ref} = 10\text{Nm}$ )

For high speed simulation the rotational speed is raised to 1500 r/min, with the DC link voltage kept at 200V. With the DTC method the flux reference  $\psi_s^*$  is 0.27Wb and the torque reference  $T^*$  is 10.5Nm. As the demanded current is never reached, the controller reverts to the APC method. In this case  $\theta_{on}$  and  $\theta_{off}$  are set at  $-5^\circ$  and  $110^\circ$  respectively to achieve 10Nm mean torque.



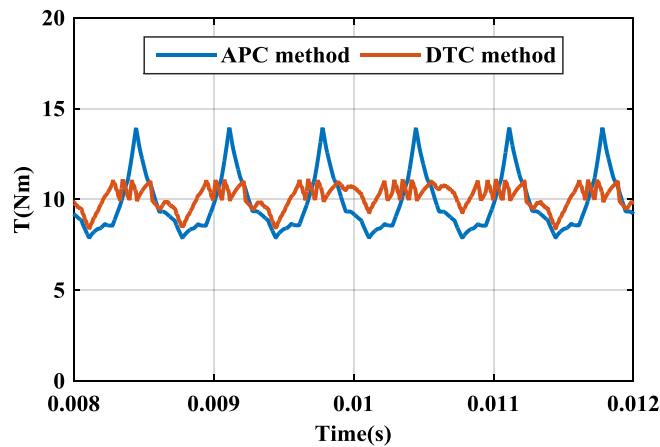
(a)



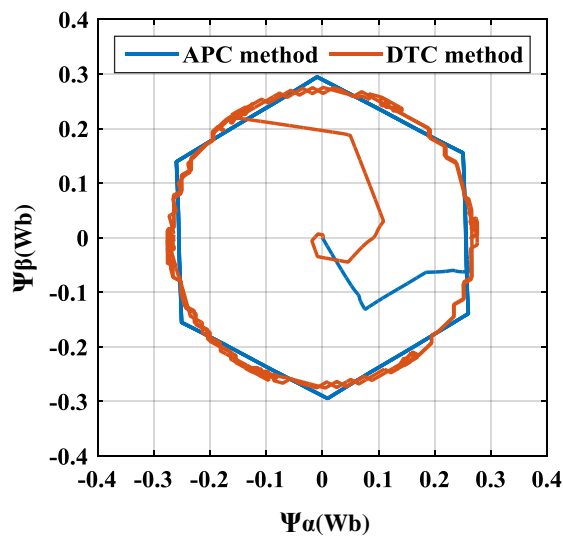
(b)

Figure 4.13 Simulation results of the AHB converter at 1500r/min: (a) six phase flux, current and torque of APC method (b) six phase flux, current and torque of DTC method

Figure 4.13 shows simulation results including six phase flux, current and torque. As shown in Figure 4.13 (a), with the APC method the phase flux increases linearly from turn-on and subsequently decreases at the same rate after turn off, creating a triangular profile. Due to the DC link voltage limitation and back-EMF increasing, phase flux cannot change as fast as at low speed and medium speed, therefore phase flux with the DTC method is smoother, and it has a longer conduction period than with the APC method. Compared with the APC phase flux trajectory, the phase flux profile with the DTC method is more rounded in appearance.



(a)



(b)

Figure 4.14 Total torque output and flux trajectory comparison of the AHB converter at 1500r/min: (a) total torque output of CCC method and DTC method (b) flux trajectory of CCC method and DTC method

For the same average output torque of 10Nm, TRR with the APC method is 58.9%, whilst the DTC method reduces it to 25.1% as shown in Figure 4.14(a). By plotting stator flux linkage

of the APC method and the DTC method in the x-y stationary frame in Figure 4.14 (b), it can be seen that stator flux linkage with the APC method is a hexagon, whilst the DTC method continues to try and produce a circular profile. Due to fewer switching events per cycle, the flux locus is less well controlled than at low speed.

### 4.3 Simulation analysis with the circle converters

In order to apply the DTC method to the proposed circle converter, a dynamic DTC model driven by the circle converter of the six-phase SRM is developed in the MATLAB/SIMULINK environment. This model uses the same parameters of the SRM prototype as shown in Figure 3.9.

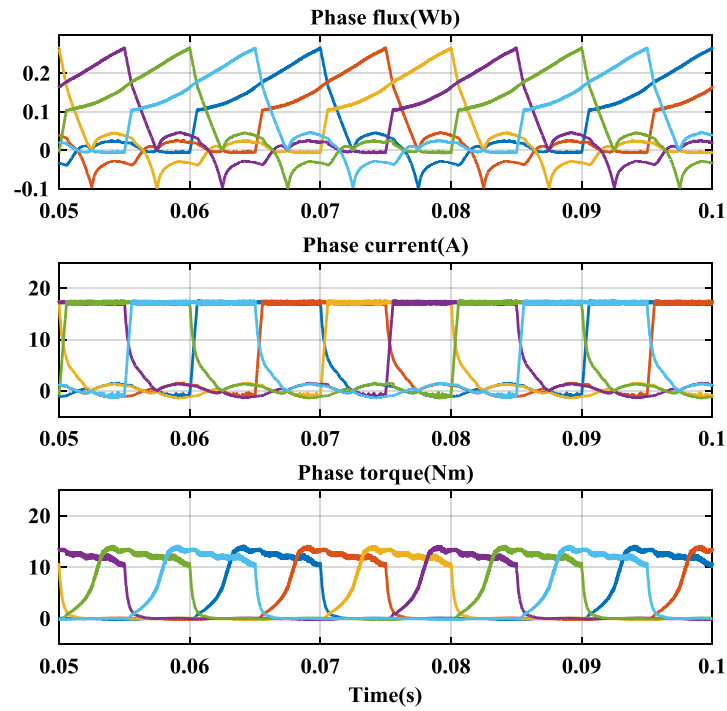
#### 4.3.1 Simulation results at 200r/min ( $T_{ref}=20Nm$ )

For low speed operation the simulation parameters are set as follows: DC link voltage  $V_{dc}$  is 200V; rotation speed  $n$  is 200r/min. In the CCC method the current reference  $I^*$  is 17.3A,  $\theta_{on}$  and  $\theta_{off}$  are  $0^\circ$  and  $120^\circ$  ( $120^\circ$  is conduction width limitation of circle converter) respectively. In the DTC method the flux-linkage reference  $\psi_s^*$  is 0.38Wb and the torque reference  $T^*$  is 20Nm.

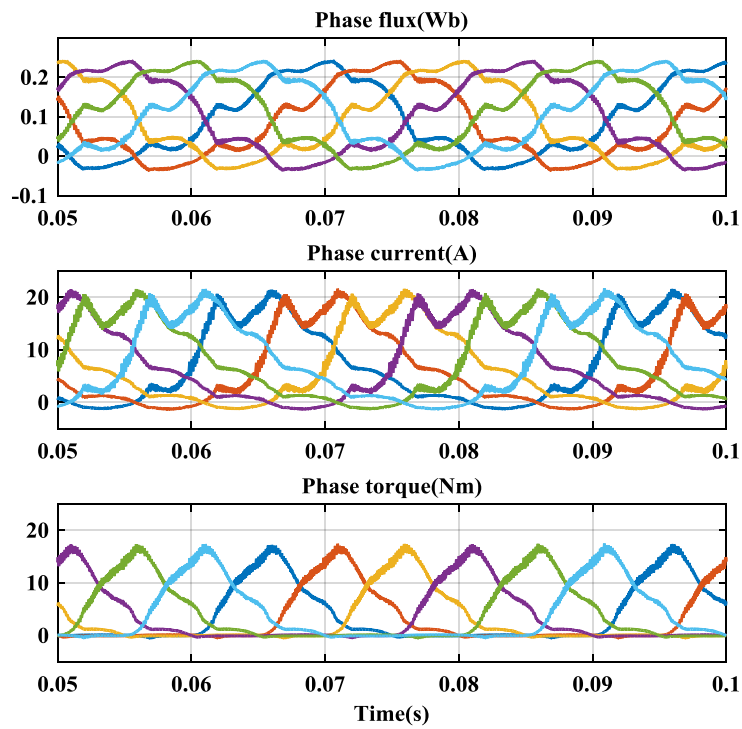
Figure 4.15 shows simulation results of the CCC and DTC methods at 200r/min. In the traditional CCC method, phase current is controlled by a hysteresis controller to achieve an approximately square waveform. In the proposed DTC method, switching signals are generated with instantaneous torque and stator flux errors.

As with the DTC method in the AHB converter, due to the rapid adjustment requirement of the stator flux and torque hysteresis controllers, comparing with CCC method the phase flux linkage and current of the DTC method in the circle converter are very irregular. Due to unavoidable effects between adjacent phases and unexpected current after the turn-off position of each phase, as mentioned in Chapter 3, the phase current of the DTC method has small distortion compared with the AHB converter. However, it does not significantly affect the torque performance in circle converter.

By observing the change of instantaneous torque and rotational speed, it is very clear that when the flux advances ahead of the rotor movement the torque increases, and when the flux lags behind the rotor movement the torque decreases, which is the same as the relationship between torque and rotational speed in Figure 4.15(c).



(a)



(b)

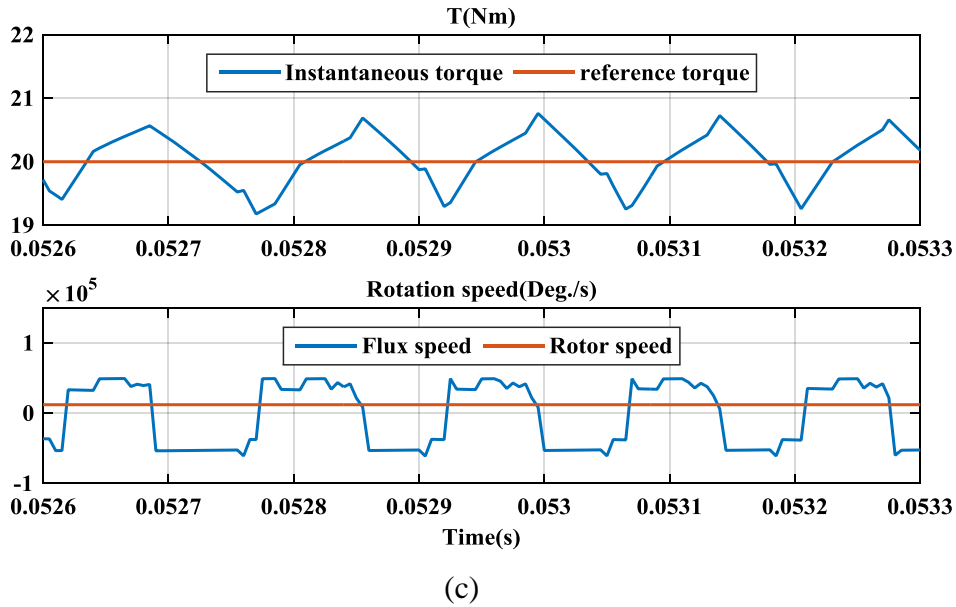
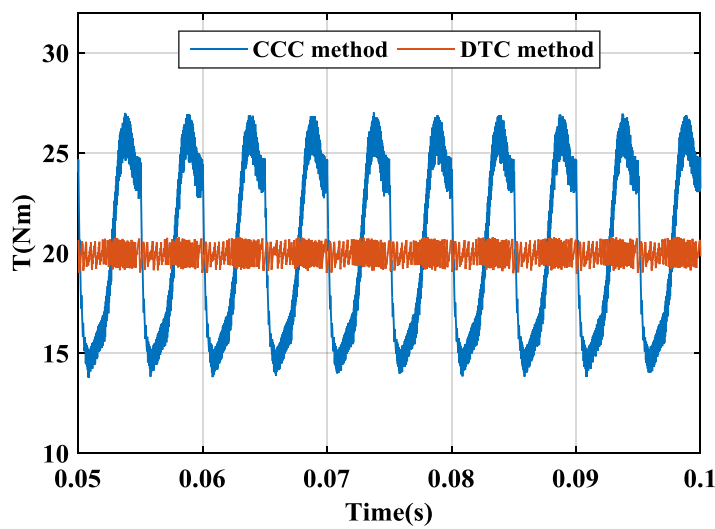
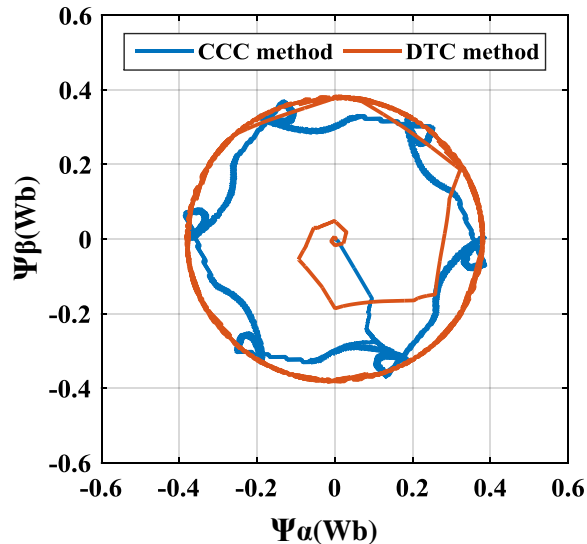


Figure 4.15 Simulation results of the circle converter at 200r/min: (a) six phase flux, current and torque of the CCC method (b) six phase flux, current and torque of the DTC method (c) instantaneous torque and flux speed of the DTC method.

For an average torque output of 19.9Nm, the TRR with the CCC method is 65.8%, whilst the DTC method reduces it to 6.8% as shown in Figure 4.16(a). By plotting stator flux of the CCC method and DTC method in the x-y stationary frame in Figure 4.16(b) it can be further demonstrated that the stator flux linkage in the CCC method is close to a hexagon, whilst the DTC method has a circular trajectory. In addition, compared with the hexagon locus in Figure 4.10(b), there are pronounced distortions in the CCC flux locus in Figure 4.16(b), which is caused by the unexpected current distortion in circle converter.



(a)



(b)

Figure 4.16 Total torque output and flux trajectory comparison of the circle converter at 200r/min: (a) total torque output of the CCC method and the DTC method (b) flux trajectory of the CCC method and the DTC method.

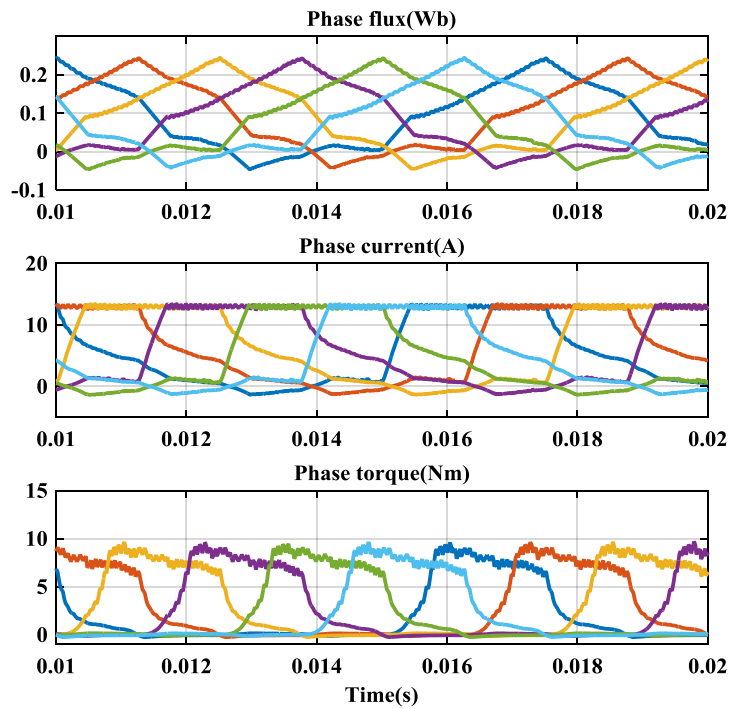
#### 4.3.2 Simulation results at 800r/min ( $T_{ref} = 13.5\text{Nm}$ )

For medium speed simulation the parameters are set at follows: DC link voltage  $V_{dc}$  is 200V, rotational speed  $n$  is 800r/min. In the DTC method the flux reference  $\psi_s^*$  is 0.33Wb and the torque reference  $T^*$  is 13.5Nm. In the CCC method, the current reference  $I^*$  is 13A,  $\theta_{on}$  and  $\theta_{off}$  are  $0^\circ$  and  $120^\circ$  respectively.

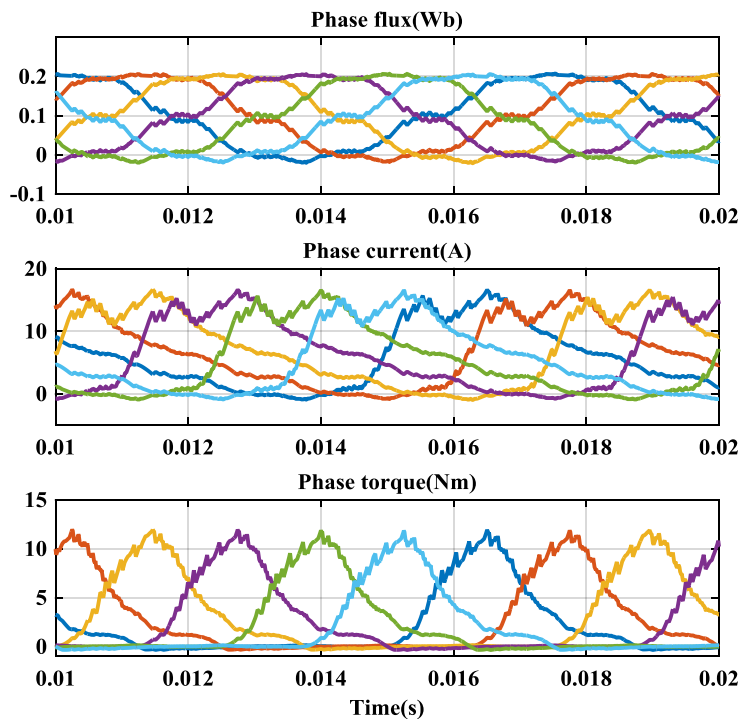
Simulation results are shown in Figure 4.17, including phase flux, current, and torque. Due to the DC link voltage limitation and back-EMF effect, the rate of rising and falling of current with respect to rotor position is lower in Figure 4.17(a) than the low speed results. Current results at medium speed have pronounced current tails after turn-off position. Although torque commands are different, the general profiles of phase flux are very similar between Figure 4.15(b) and Figure 4.17(b). However, some noises appears in Figure 4.17(b) due to the special topology of the circle converter.

For the same average torque output of 13.5Nm, TRR with the CCC method is 58.0%, whilst the DTC method reduces it to 17.1% as shown in Figure 4.18(a). By plotting the stator flux vectors of the CCC method and DTC method in the x-y stationary frame in Figure 4.18 (b), it can be seen that stator flux linkage in the CCC method forms a hexagonal trajectory, whilst

the DTC method continues to have a circular trajectory, which is relatively rounded as low speed.

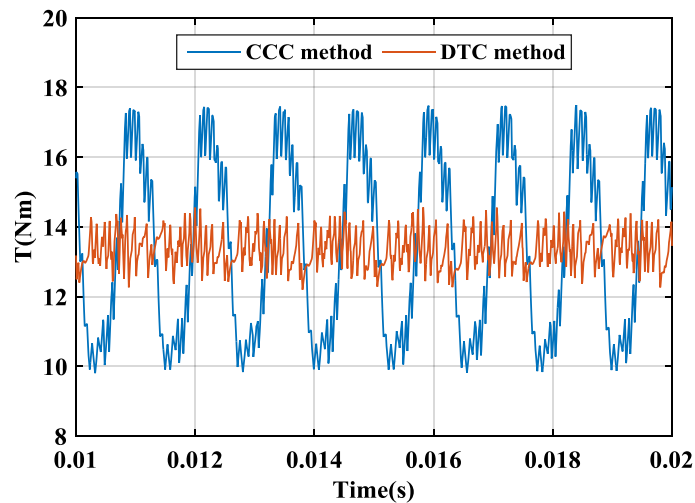


(a)

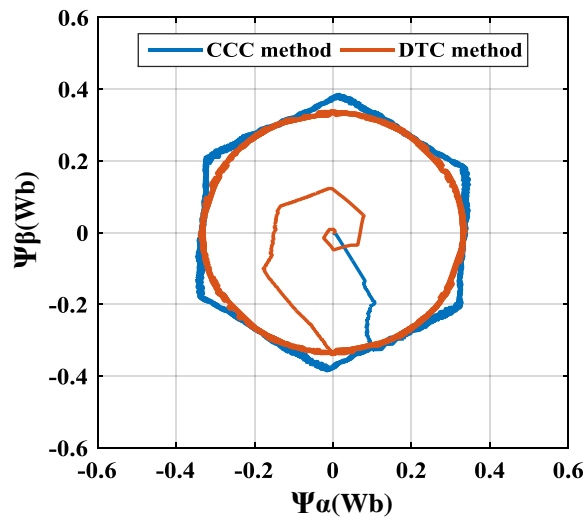


(b)

Figure 4.17 Simulation results of the circle converter at 800r/min: (a) six phase flux, current and torque of CCC method (b) six phase flux, current and torque of DTC method



(a)

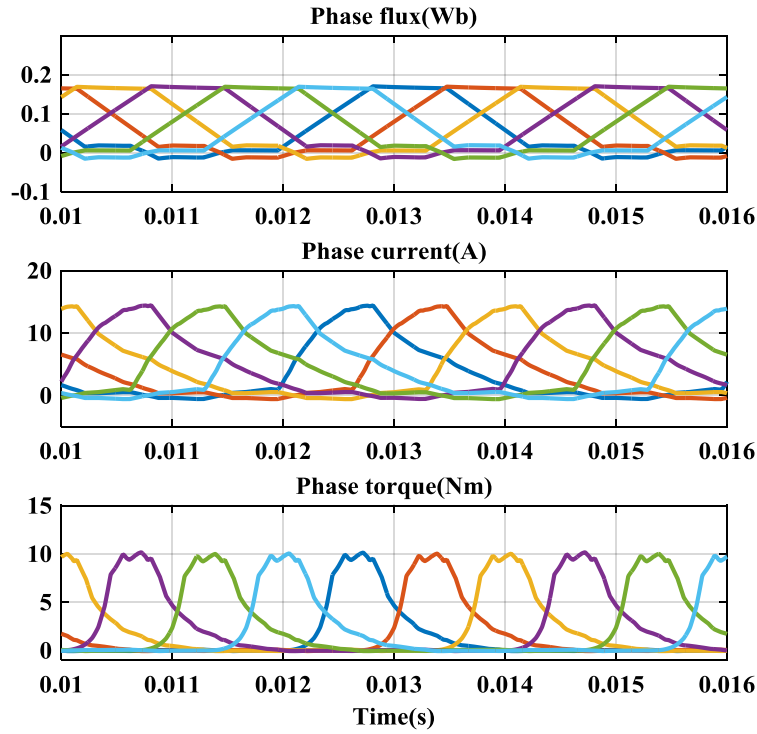


(b)

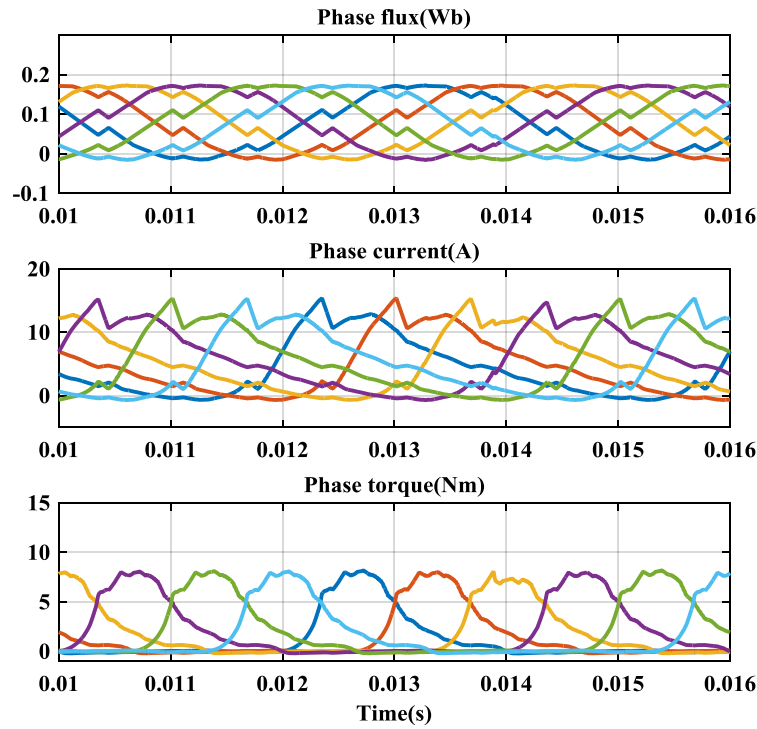
Figure 4.18 Total torque output and flux trajectory comparison of the circle converter at 800r/min: (a) total torque output of CCC method and DTC method (b) flux trajectory of CCC method and DTC method

### 4.3.3 Simulation results at 1500r/min ( $T_{ref} = 10\text{Nm}$ )

For high speed simulation the rotational speed is raised to 1500 r/min, with the DC link voltage kept at 200V. With the DTC method the flux reference  $\psi_s^*$  is 0.28Wb and the torque reference  $T^*$  is 10.5 Nm. As the demanded current is never reached, the controller reverts to the APC method. In this case  $\theta_{on}$  and  $\theta_{off}$  are set at  $-10^\circ$  and  $127^\circ$  respectively to achieve 10Nm mean torque.



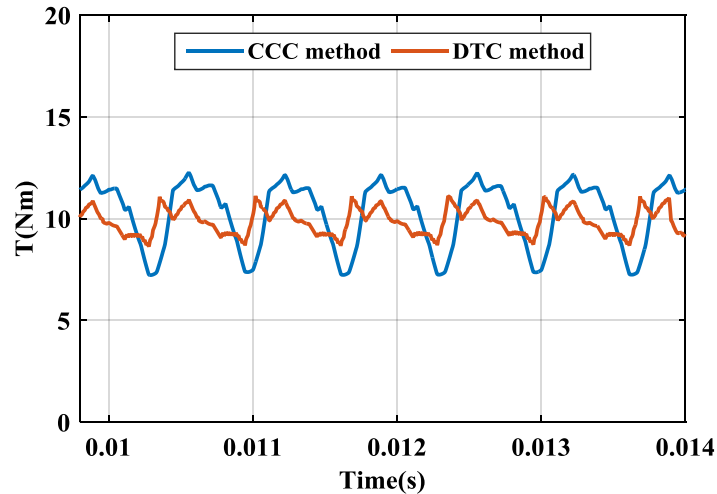
(a)



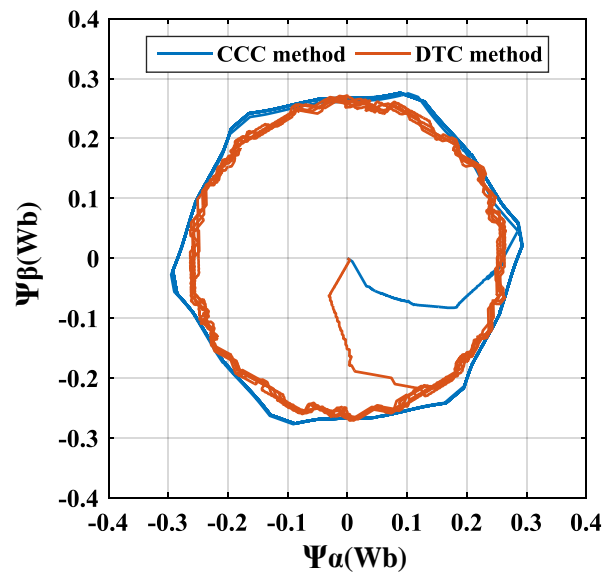
(b)

Figure 4.19 Total torque output and flux trajectory comparison of the circle converter at 1500r/min: (a) six phase flux, current and torque of APC method (b) six phase flux, current and torque of the DTC method

Figure 4.19 shows simulation results including phase flux, current and torque. As shown in Figure 4.19 (a), with the APC method the phase flux increases linearly from turn-on, keeps constant during freewheeling and subsequently decreases after turn off, creating a trapezoid profile. Due to DC link voltage and back-EMF limitation, phase flux cannot change as fast as low speed and medium speed, therefore the phase flux of the DTC method is smoother and the noise is not obvious.



(a)



(b)

Figure 4.20 Total torque output and flux trajectory comparison of the circle converter at 1500r/min: (a) total torque output of the CCC method and the DTC method (b) flux trajectory of the CCC method and the DTC method.

For the same average output torque of 10Nm, TRR with the APC method is 49.0%, whilst the DTC method reduces it to 25.5% as shown in Figure 4.20(a). By plotting stator flux linkage

of the APC method and DTC method in the x-y stationary frame in Figure 4.20(b), it can be seen that stator flux linkage with the APC method is nearly a hexagon, whilst the DTC method continues to try and produce a circular profile. Because there are fewer switching events per cycle the flux locus is less well controlled than at low speed.

#### **4.4 Summary**

In this chapter, the DTC strategy has been proposed to control a six-phase SRM drive system. Application of the DTC has the advantages of significantly reducing the amount of torque ripples normally associated with this type of machine. Simulations have been carried out on six-phase AHB converter and the proposed circle converter to verify the proposed control strategy when compared with classical control techniques including CCC and APC methods. Simulation results verified that the DTC method can reduce torque ripple significantly throughout the whole speed range. The simulation analysis in this chapter will be validated in experimental chapter.

---

## Chapter 5. Effects of Winding Connection on Performance of Six-Phase SRMs

---

In this chapter, the effect of the stator winding connection on the performance of a six-phase Switched Reluctance Machine (SRM) is investigated. Five winding connection types are proposed for the machine. Finite element analyses (FEAs) of flux distribution and output torque are presented under single-phase and multi-phase excitation for each connection and the results are used to compare the average torque and Torque Ripple Ratio (TRR) characteristics and to develop an understanding of the respective contributions of mutual inductance in torque development. An optimum winding configuration for a six-phase SRM is proposed at the end of this chapter.

### 5.1 Topology of a six-phase SRM

A six-phase SRM prototype is chosen as the study object of my PhD program. Figure 5.1 shows the rotor and the stator structure of a six-phase 12/10 traditional SRM prototype. It has no windings or magnets on the rotor and only has concentrated windings on the stator. Table 5.1 gives design parameters of this machine.



(a)



(b)

Figure 5.1 Six-phase 12/10 SRM prototype: (a) wound stator (b) rotor

Table 5.1 Design parameters of the six-phase SRM prototype [32]

Number of Stator Teeth	12
Number of Rotor Teeth	10
Axial Length	150.0mm
Stator Outer Diameter	150.0mm
Stator Inner Diameter	91.4mm
Stator Core-Back Depth	11.0mm
Stator Tooth Width	11.4mm
Airgap Length	0.3mm
Rotor Outside Diameter	90.8mm
Rotor Insider Diameter	36.0mm
Rotor Core back Depth	18.0mm
Rotor Tooth Width	11.4mm
Turns per Phase	100
Phase resistance	0.8 $\Omega$
Steel type	Standard steel (M250-35A)
Conductor size	1.4mm

## 5.2 Single-phase connection types

In SRMs, all the coils in one phase should be connected in series to obtain higher MMFs. For a six-phase motor, there are two coils in one phase, therefore there are two possible connection types in one phase, which are N-N (North-North) connection type and N-S (North-South) connection type. In order to compare these two single-phase connections, a 2D FEA model has been built in MAGNET as shown in Figure 5.2. The settings of this model are summarized in Table 5.2

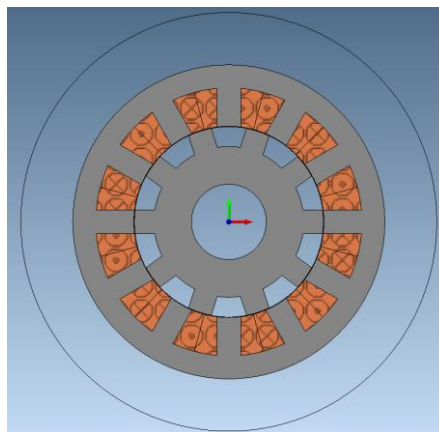


Figure 5.2 2D FEA model for the six-phase SRM

Table 5.2 Settings of the 2D FEA model for the single-phase excitation simulation

Start position	0°
Stop position	36°
Step size	0.5°
Current	5A, 10A, 15A, 20A
Solver	Static 2D
Maximum mesh size	1mm

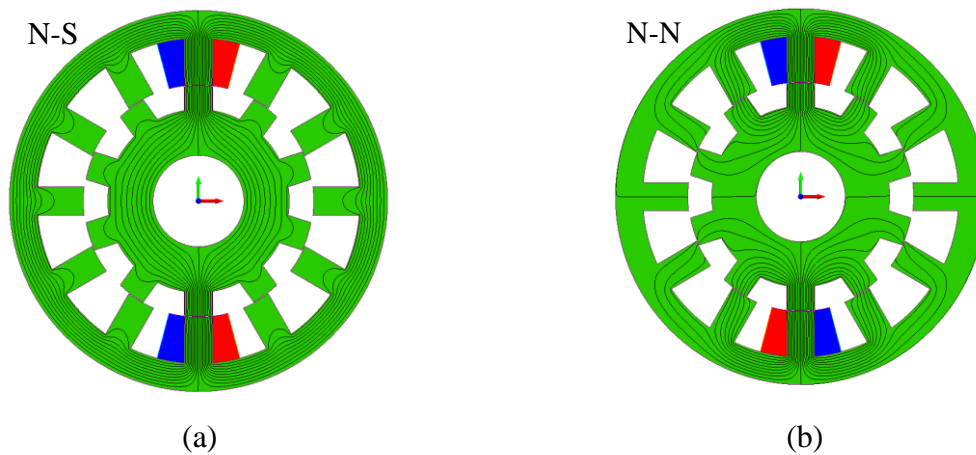
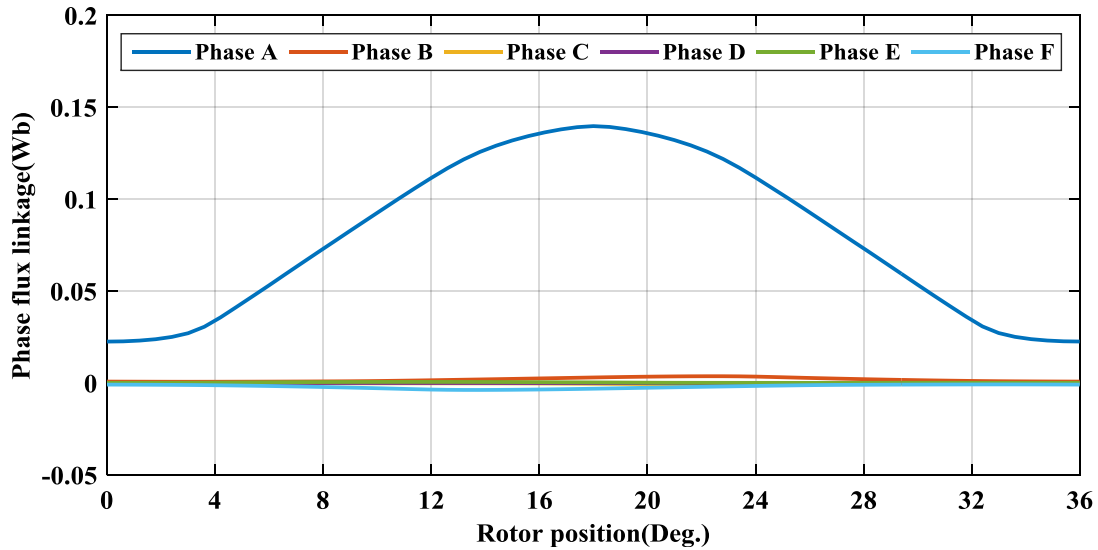


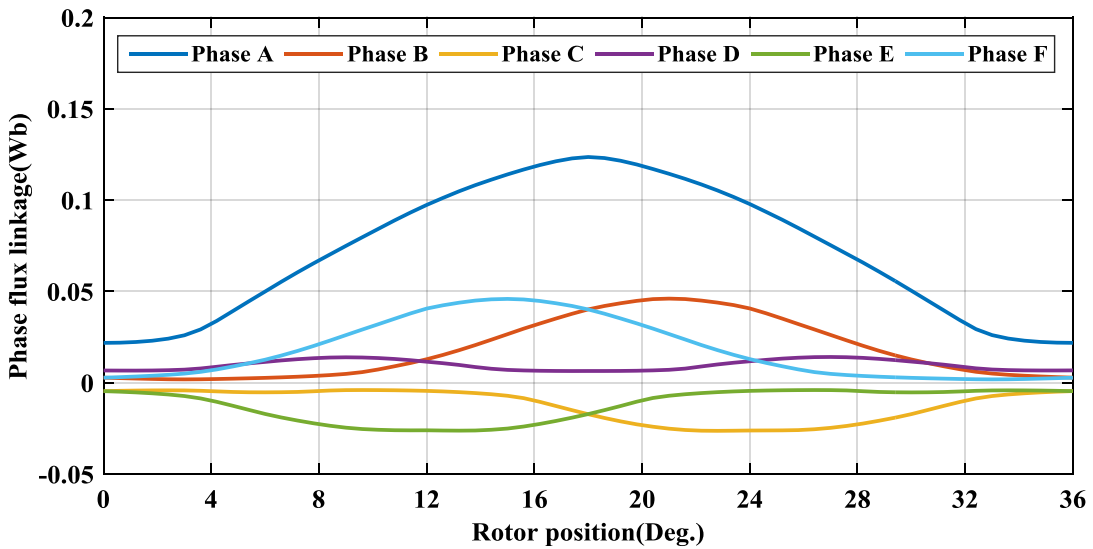
Figure 5.3 Flux distribution of single phase excitation for a six-phase SRM: (a) N-S connection (b) N-N connection.

As shown in Figure 5.3, single-phase static FEM results present flux distribution at the aligned position of the N-S and N-N connection with 180° 15A square wave current excitation. In Figure 5.3 (a), there are two long flux-paths across the full stator and rotor core, while in Figure 5.3(b), the N-N polarities of the single-phase connection give rise to shorter flux paths which link adjacent teeth.

Figure 5.4 compares the phase flux linkages from 2D FEA for the N-N and N-S connections under single-phase excitation. As can be appreciated from inspection of Figure 5.4, the single-phase N-S connection gives rise to large self-inductance and negligible mutual inductance, whereas the single-phase N-N connection gives rise to a slightly reduced self-inductance but considerable mutual inductance.



(a)



(b)

Figure 5.4 Six phase flux linkages of N-N and N-S connection with single-phase excitation

Figure 5.5 presents instantaneous motoring torque waveforms under ideal current control from 2D FEA. The single phase torque for the forward and reverse series connections is compared with the equivalent six-phase waveforms obtained by phase-shifted superposition. It is obvious that the N-S connection develops higher torque with both single phase excitation and six-phase superposition.

However, it should be noted that this approach neglects the torque contribution arising from the variation of mutual inductance in adjacent phases, which may be considerable in the N-S type as suggested by the flux linkage characteristics of Figure 5.4.

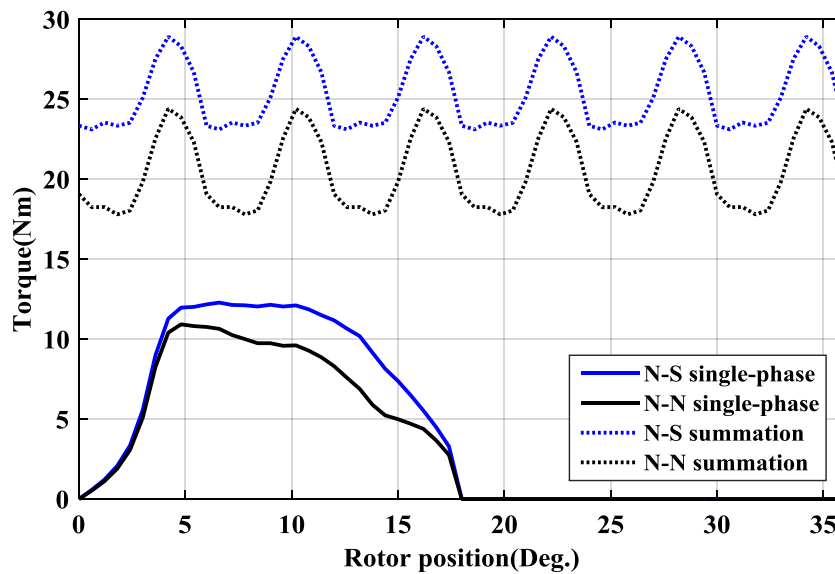
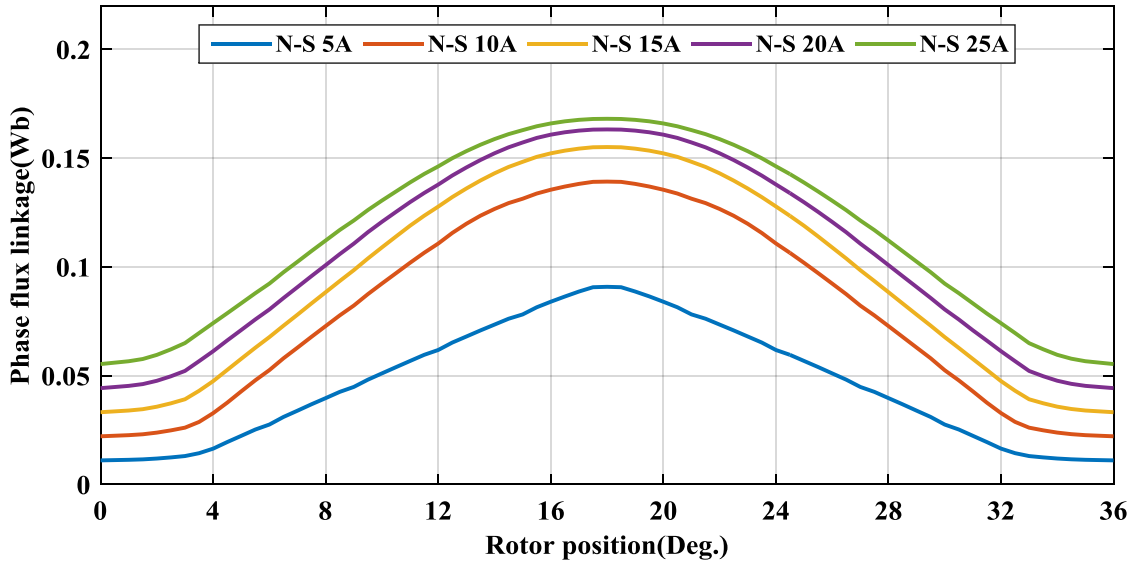


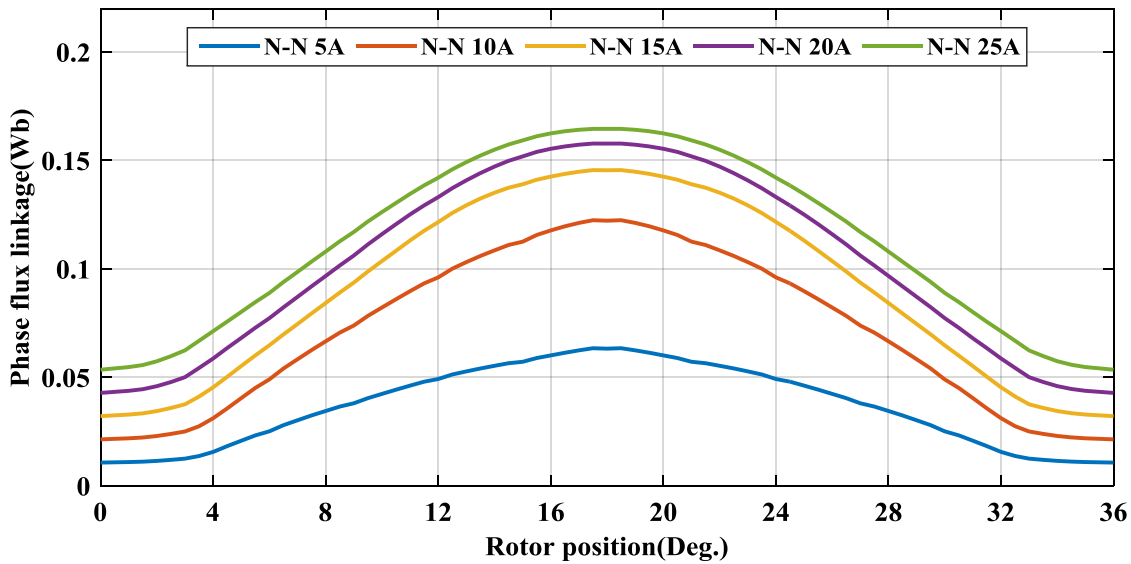
Figure 5.5 Single-phase output torque and six single-phase torque summation of N-S and N-N connection

Figure 5.6 shows the phase flux linkage of the N-S connection and N-N connection with excitation current varying from 5A to 25A. It shows that the flux linkage of the N-S connection is larger than the N-N connection through the whole current range, which means in single-phase excitation FEA, long flux-paths (N-S type) have higher flux density in the conducting teeth. Generated by the same excitation current, the difference of the phase flux linkage between N-S connection and N-N connection increases from unaligned position ( $0^\circ$ ) to aligned ( $180^\circ$ ).

In addition, compared differences of the phase flux linkage between the N-S connection and N-N connection types through the whole current range, it is noticeable that the difference between values decreases with excitation current increasing. Consequently the effect of polarity arrangement in a single-phase is reduced by magnetic saturation and affects more around the aligned position.



(a)



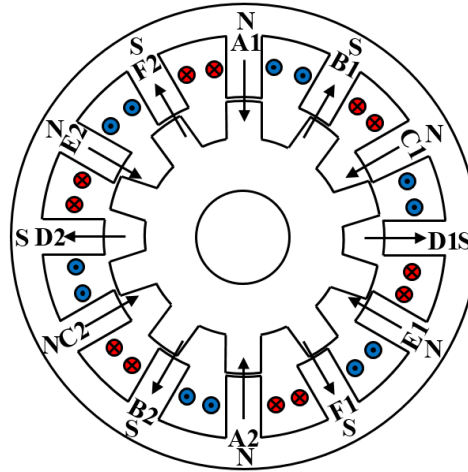
(b)

Figure 5.6 Phase flux linkage of single phase excitation: (a) N-S connection (b) N-N connection.

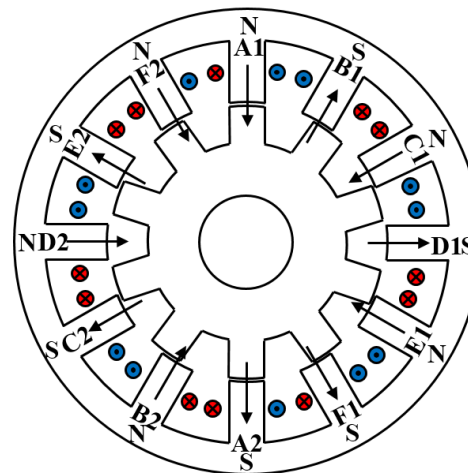
### 5.3 Five winding connection types

In order to investigate output torque and mutual inductance effects, five winding connection types are proposed as illustrated in Figure 5.7. Owing to the greater potential for phase interaction at higher phase numbers, the long/short flux path terminology is not appropriate and so a simplified classification is proposed here. Where the coil polarities of a given phase are magnetically in opposition, this is defined as the N-S connection type. Conversely, reinforcing phase coil polarities are defined as the N-N connection type. For the six-phase

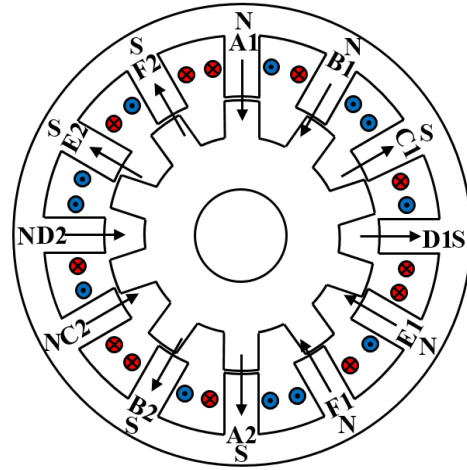
12/10 SRM under consideration there are five winding configurations which preserve an equal number of north and south polarity coils, as presented in Figure 5.7. These comprise two N-N types (1 and 4) and three N-S types (2, 3, and 5).



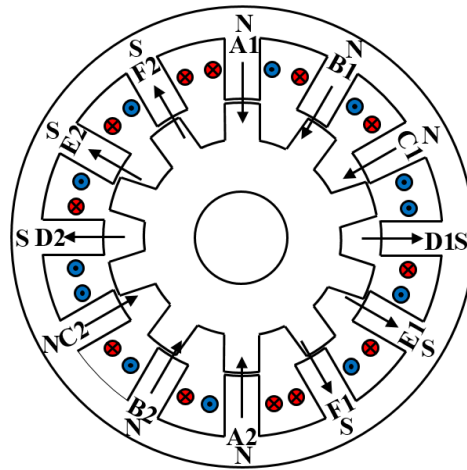
(a)



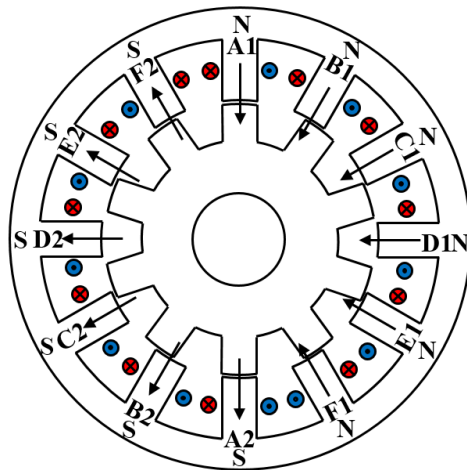
(b)



(c)



(d)



(e)

Figure 5.7 The winding connections: (a) Type 1: NSNSNSNSNSNS (b) Type 2: NSNSNSSNSNSN (c) Type 3: NNSSNNSNNS (d) Type 4: NNNSSNNSSS (e) Type 5: NNNNNSSSSSS

#### 5.4 Multi-phase FEM analysis

In order to compare the torque performance of the five winding connection types, multi-phase excitation 2D FEA is conducted. Excitation currents are  $180^\circ$  squared waveforms, the current value is 15A, and there are  $60^\circ$  offset between two adjacent phases, as shown in Figure 5.8.

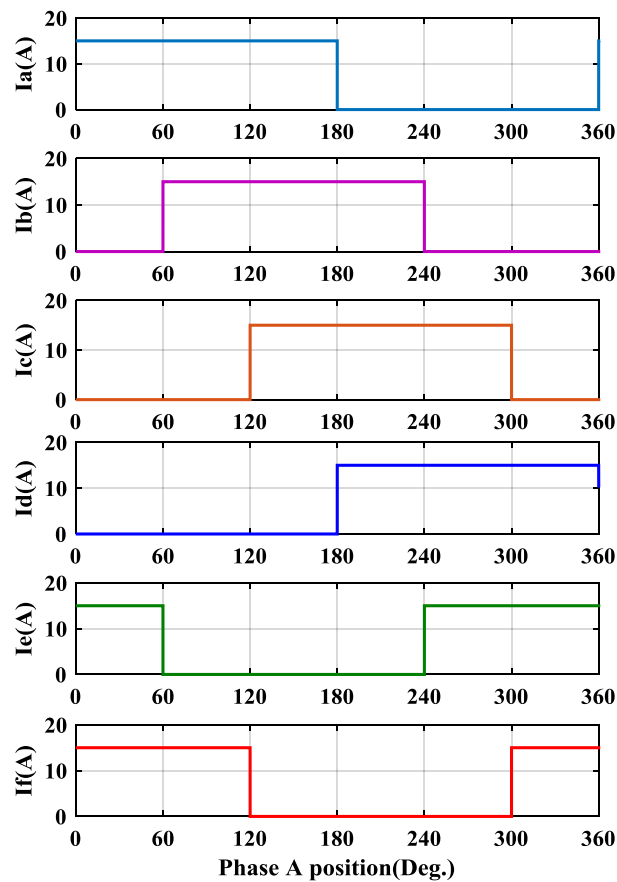


Figure 5.8 Six phase unipolar excitation currents in FEM analysis

Figure 5.9 presents instantaneous motoring torque waveforms under ideal current control with full six-phase excitation for the five winding connections. Average torque outputs of these five configurations are 24.3Nm, 24.7Nm, 23.2Nm, 14.3Nm and 20.4Nm respectively. Type 1 and Type 3 has smaller torque ripple which are 27.2% and 16.7%, while Type 5 has negative instantaneous torque with a very large torque ripple of 243.0%. Torque ripple of Types 2 and 4 are 31.5% and 58.8%. In all these five types, output torque of Types 1 and 3 are symmetric, while others are asymmetric. Further flux distribution observations of all these five configurations are taken to analyse instantaneous output torque.

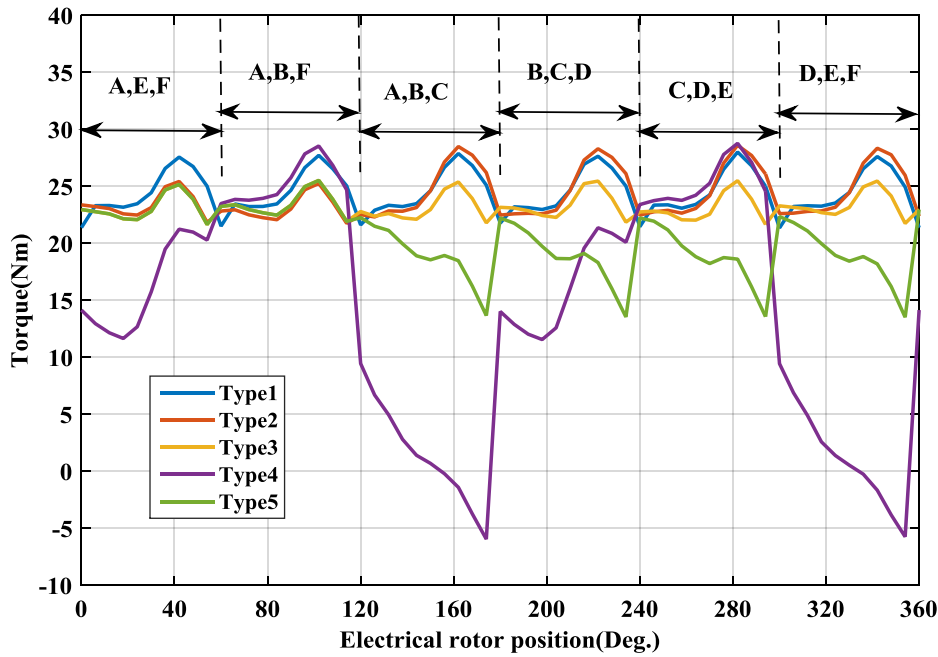


Figure 5.9 FEM output torque of five winding connection types

Picking out three typical conduction combinations, with which there are obvious instantaneous torque distinctions in Figure 5.9, the torque relationships between these five types are summarized by (5.2),

$$\begin{cases} \text{Type1} > \text{Type2} = \text{Type3} = \text{Type5} > \text{Type4}, \text{ active phases} = A, E, F \\ \text{Type1} = \text{Type4} > \text{Type2} = \text{Type3} = \text{Type5}, \text{ active phases} = A, B, F \\ \text{Type2} > \text{Type1} > \text{Type3} > \text{Type5} > \text{Type4}, \text{ active phases} = A, B, C \end{cases} \quad (5.2)$$

Regardless of the presence of short or long flux paths arising from a given winding connection, there are two fundamental factors which act to reduce the mean torque and increase the torque ripple: 1) saturation in the stator core back; and 2) unwanted flux giving rise to negative torque in a particular phase.

Negative torque production is unavoidable to some extent in all of the winding connections under consideration owing to the phase overlap and prevalence of at least some mutual coupling. However, the impact of stator core back saturation can readily be illustrated, to which end the FEA described at the start of this section is repeated here with the stator core back depth increased to 22mm (200% of the original) to prevent performance limitation in any of the winding connection types.

The results are illustrated in Figure 5.10 which shows that, in the absence of stator core back saturation, Types 1-3 and 5 develop very similar torque waveforms with Type 4 being the notably inferior exception. Furthermore, comparison with Figure 5.9 suggests that, in the absence of stator core back saturation, the torque characteristics converge on that of Type 1. Thus, with the actual stator core back limitation, it is obvious that Type 1 is preferable in that it develops greater torque, and that Types 4 and 5 are clearly inferior.

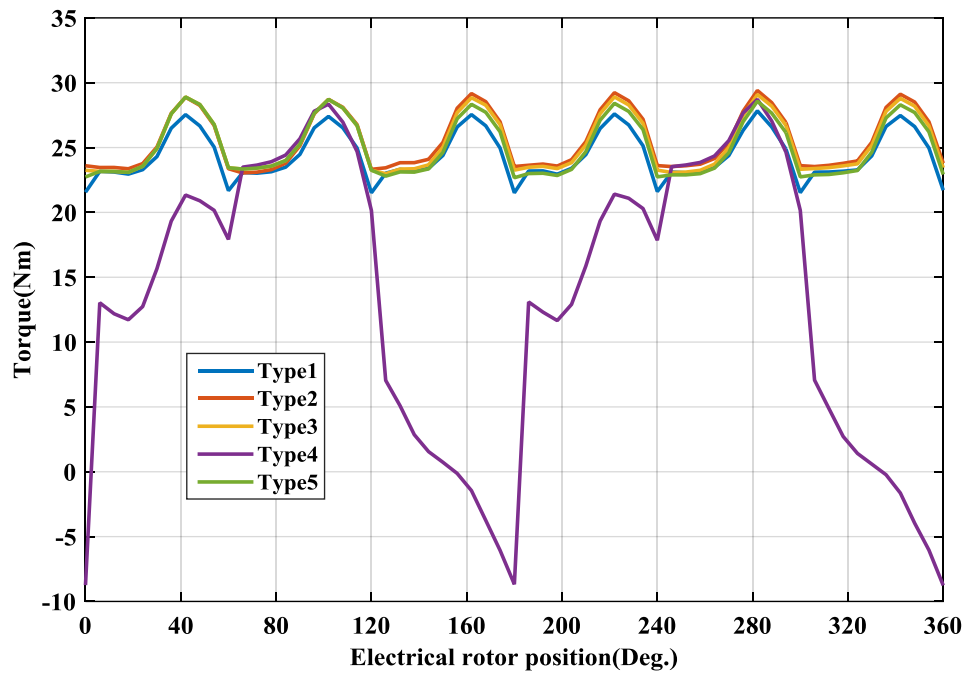


Figure 5.10 Output torques of five winding configurations with thicker core back.

In order to further explain the reasons causing different instantaneous torques in Figure 5.9, flux linkage distribution of three typical conduction combinations are observed.

When phases A, E and F are conducting as shown in Figure 5.11, the majority of the torque is produced by phases A and E whilst phase F is nearly aligned.

Producing the largest instantaneous torque, Type 1 has six short flux-paths, and the majority flux goes through the proximate four teeth and a quarter of the stator and rotor cores. Producing second largest torque, the majority of the flux of Type 2 comprises only two short paths. Types 3 and 5 have the same flux distribution, comprising two long flux-paths with the majority of flux passing through the full stator and rotor core, and producing the same instantaneous torque as Type 2. Type 4 has four short flux-paths, but unlike the other four

types it has less flux in the conducting phases than the non-conducting phases and therefore produces more negative torque at this position.

In addition, it is clear that, by comparison with Type 1, more energy is stored in the stator core back in Types 2, 3 and 5. Furthermore, Type 1 exhibits more energy in the teeth which is indicative of a higher torque contribution.

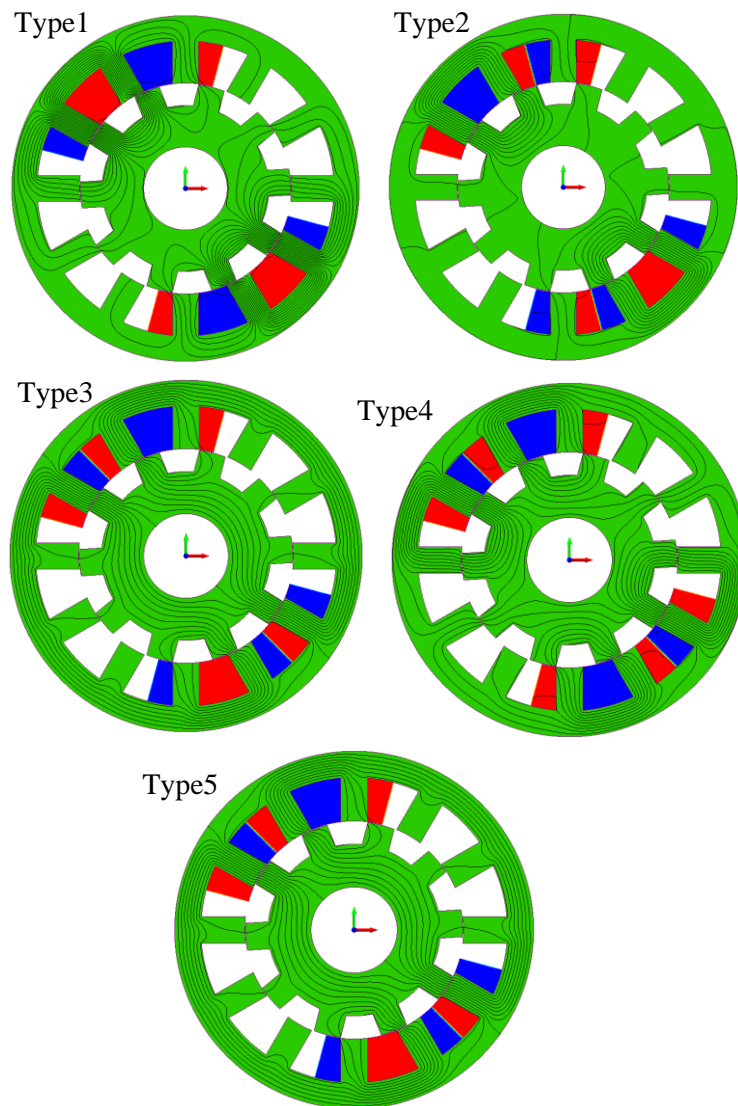


Figure 5.11 Comparisons of flux distributions when phase A,E,F are active

When, phases A, B and F are conducting as shown in Figure 5.12, the majority of the torque is produced by phases A and B whilst phase F is nearly aligned.

Type 1 keeps six short flux-paths and Type 4 has two short and two long flux-paths, and they produce the same and the largest torque at this position. Types 3 and 5 have the same flux

distribution again, and produce less torque than Types 1 and 4. Having two short flux-paths, Type 2 has the same torque as Types 3 and 5.

Furthermore, compared with other three types, Types 1 and 4 have less flux density in stator core back, exhibiting more energy in the teeth, which is indicative of a higher torque contribution.

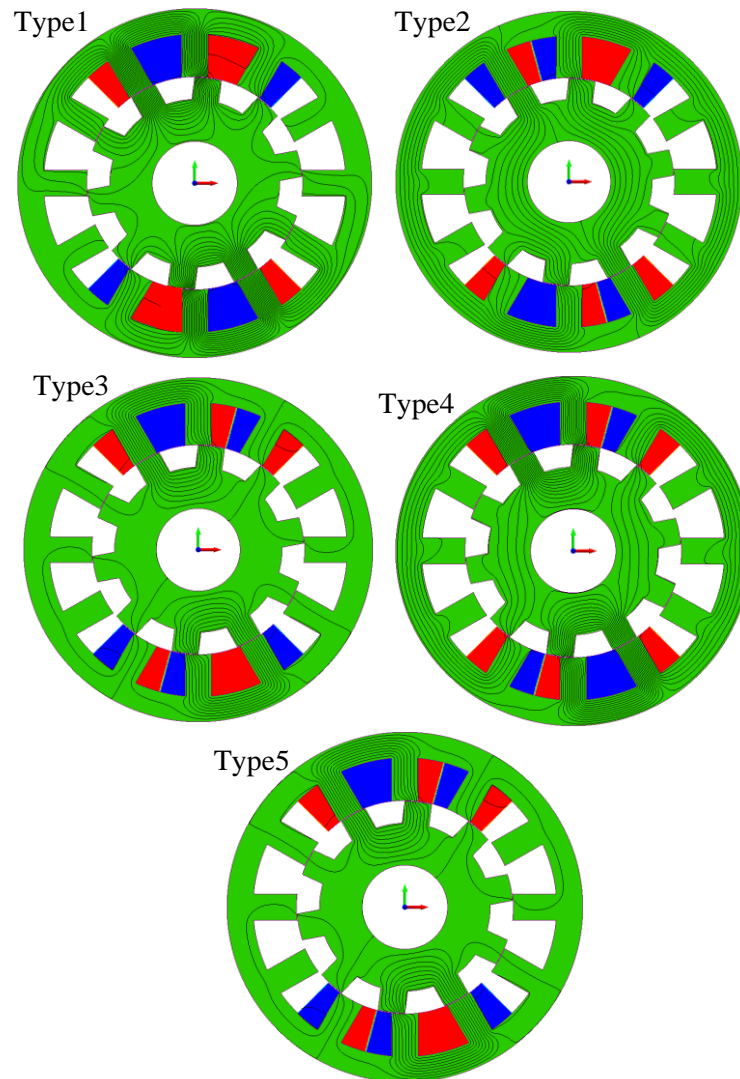


Figure 5.12 Comparisons of flux distributions when phase A,B,F are active

When phases A, B and C are conducting as shown in Figure 5.13, the majority of the torque is produced by phases B and C whilst phase A is nearly aligned.

Type 2 in Figure 5.13 has similar flux distribution to Type 4 in Figure 5.12. All the flux links the three conducting phases, thus no extra negative torque is produced, which results in Type 2 developing the largest torque in Figure 5.13. With only short flux-path in Type 1 and only

long flux-paths in Type 3, these develop the second and third greatest torque respectively at this position. Type 4 develops a reduced torque at this position owing to the negative contribution from mutual flux linking inactive phases with reducing inductance. Unlike the previous two positions, the flux distribution of Type 5 is not exactly the same as Type 3. A higher flux density appears in stator core back and lower flux density appears in conducting teeth of Type 5, which reduces instantaneous torque.

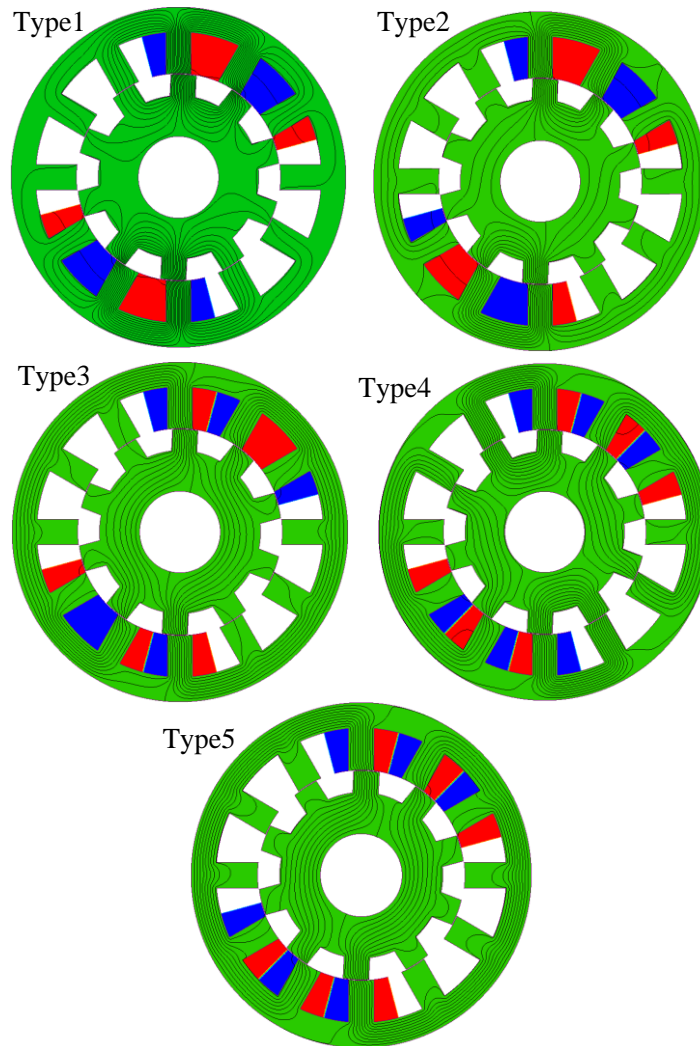


Figure 5.13 Comparisons of flux distributions when phase A,B,C are active

In conclusion, the majority of flux linkage distributes in conducting teeth in Types 1, 2, 3 and 5 at any rotor position. Slight flux linkage appears in non-conducting teeth of Types 1, 2, 3 and 5 gives rise to negative torque. The different flux density in non-conducting teeth primarily depends on polarities arrangement and is affected by stator core back saturation.

However, the situation of Type 4 is different to other four types. At some rotor position, non-conducting teeth of Type 4 has pronounced higher flux density compared with Types 1, 2, 3 and 5. This unexpected flux distribution is even worse when adjacent three conducting phases have the same polarity (Type 4 in Figure 5.13).

### 5.5 Mutual-inductance effects

Comparing with typical structured SRMs, six-phase SRM has more flexible conduction combination. In order to obtain more positive torque, there are normally three phases conducting at same time. This situation can be summarized by referring to the out-going phase, intermediate phase and in-coming phase as illustrated in Figure 5.14.

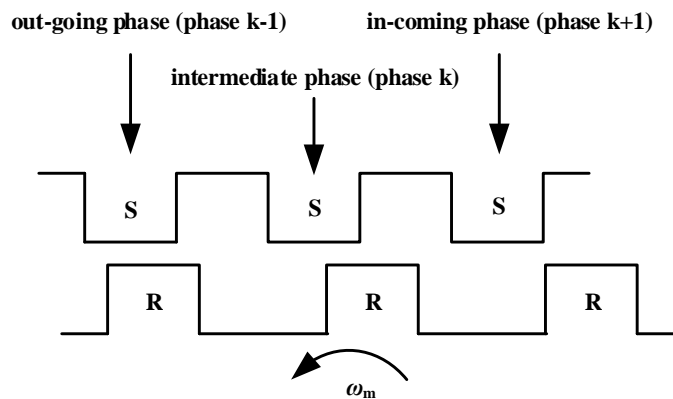


Figure 5.14 Definition of three conducting phases

At any instant, there are one out-going phase, one intermediate phase and one in-coming phase individually. Hence there are totally six different conduction combinations according to the rotor position as shown in Table 5.3.

Table 5.3 Six phase conduction combinations

$\theta_a$	Out-going	Intermediate	In-coming
0-60 Deg.	Phase E	Phase F	Phase A
60-120 Deg.	Phase F	Phase A	Phase B
120-180 Deg.	Phase A	Phase B	Phase C
180-240 Deg.	Phase B	Phase C	Phase D
240-300 Deg.	Phase C	Phase D	Phase E
300-360 Deg.	Phase D	Phase E	Phase F

For a six-phase SRM, phase flux linkages can be expressed as Equation (5.3),

$$\begin{bmatrix} \psi_A \\ \psi_B \\ \psi_C \\ \psi_D \\ \psi_E \\ \psi_F \end{bmatrix} = \begin{bmatrix} L_A & M_{AB} & M_{AC} & M_{AD} & M_{AE} & M_{AF} \\ M_{AB} & L_B & M_{BC} & M_{BD} & M_{BE} & M_{BF} \\ M_{AC} & M_{BC} & L_C & M_{CD} & M_{CE} & M_{CF} \\ M_{AD} & M_{BD} & M_{CD} & L_D & M_{DE} & M_{DF} \\ M_{AE} & M_{BE} & M_{CE} & M_{DE} & L_E & M_{EF} \\ M_{AF} & M_{BF} & M_{CF} & M_{DF} & M_{EF} & L_F \end{bmatrix} \times \begin{bmatrix} i_A \\ i_B \\ i_C \\ i_D \\ i_E \\ i_F \end{bmatrix} \quad (5.3)$$

when mutual-inductance of non-conducting phases are ignored, Equation (5.3) can be simplified and expressed by out-going phase (k-1), intermediate phase k and in-coming phase (k+1) as Equation (5.4),

$$\begin{bmatrix} \psi_{k-1} \\ \psi_k \\ \psi_{k+1} \end{bmatrix} = \begin{bmatrix} L_{k-1} & M_{(k-1)k} & M_{(k-1)(k+1)} \\ M_{(k-1)k} & L_k & M_{k(k+1)} \\ M_{(k-1)(k+1)} & M_{k(k+1)} & L_{k+1} \end{bmatrix} \times \begin{bmatrix} i_{k-1} \\ i_k \\ i_{k+1} \end{bmatrix} \quad (5.4)$$

where  $M_{(k-1)k}$ ,  $M_{(k-1)(k+1)}$  and  $M_{k(k+1)}$  are mutual-inductances between three conducting phases. Assuming phase currents are the same value  $I$  and self-inductances are same as single-phase excitation simulations, mutual-inductances of conducting phases can be derived from Equation (5.5) to Equation (5.7).

$$M_{(k-1)k} = \frac{I(L_{k-1} - L_k - L_{k+1}) - (\psi_{k-1} - \psi_k - \psi_{k+1})}{2I} \quad (5.5)$$

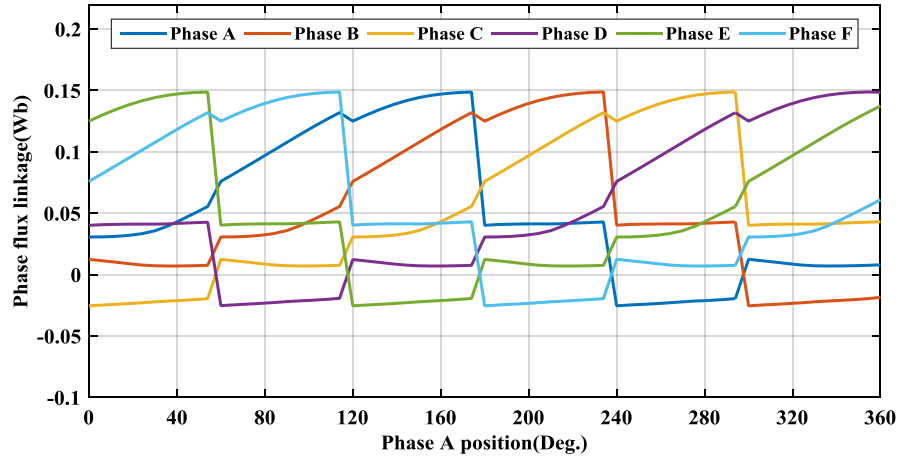
$$M_{(k-1)(k+1)} = \frac{(\psi_{k-1} - \psi_k + \psi_{k+1}) - I(L_{k-1} - L_k + L_{k+1})}{2I} \quad (5.6)$$

$$M_{k(k+1)} = \frac{(\psi_{k-1} + \psi_k - \psi_{k+1}) - I(L_{k-1} + L_k - L_{k+1})}{2I} \quad (5.7)$$

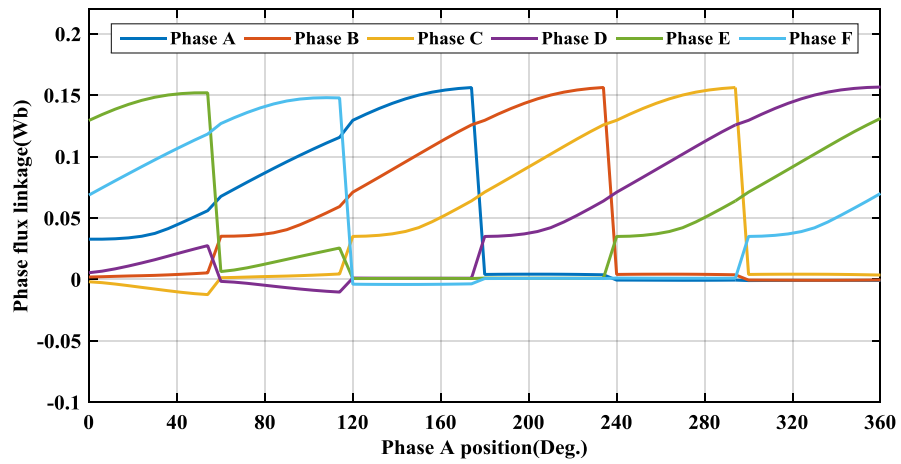
Mutual-inductance of inactive phase can be calculated by Equation (5.8),

$$M = \frac{\psi_m}{I} \quad (5.8)$$

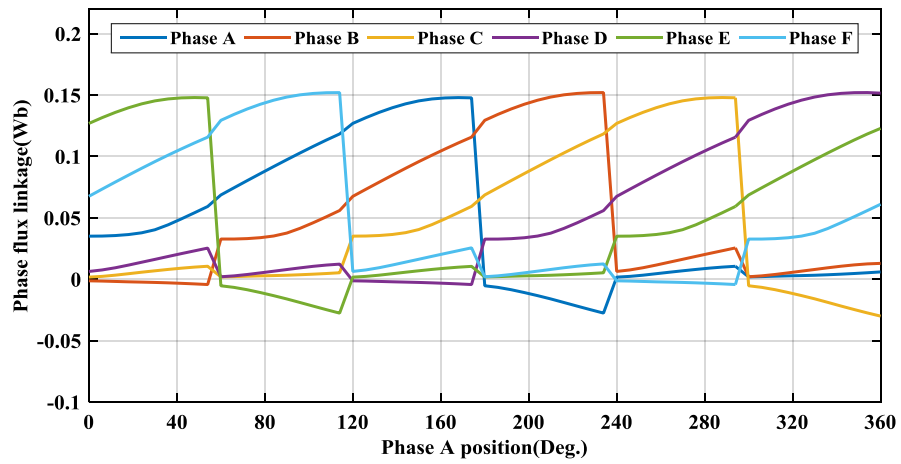
where  $\psi_m$  is the induced flux linkage in an inactive phase.



(a)



(b)



(c)

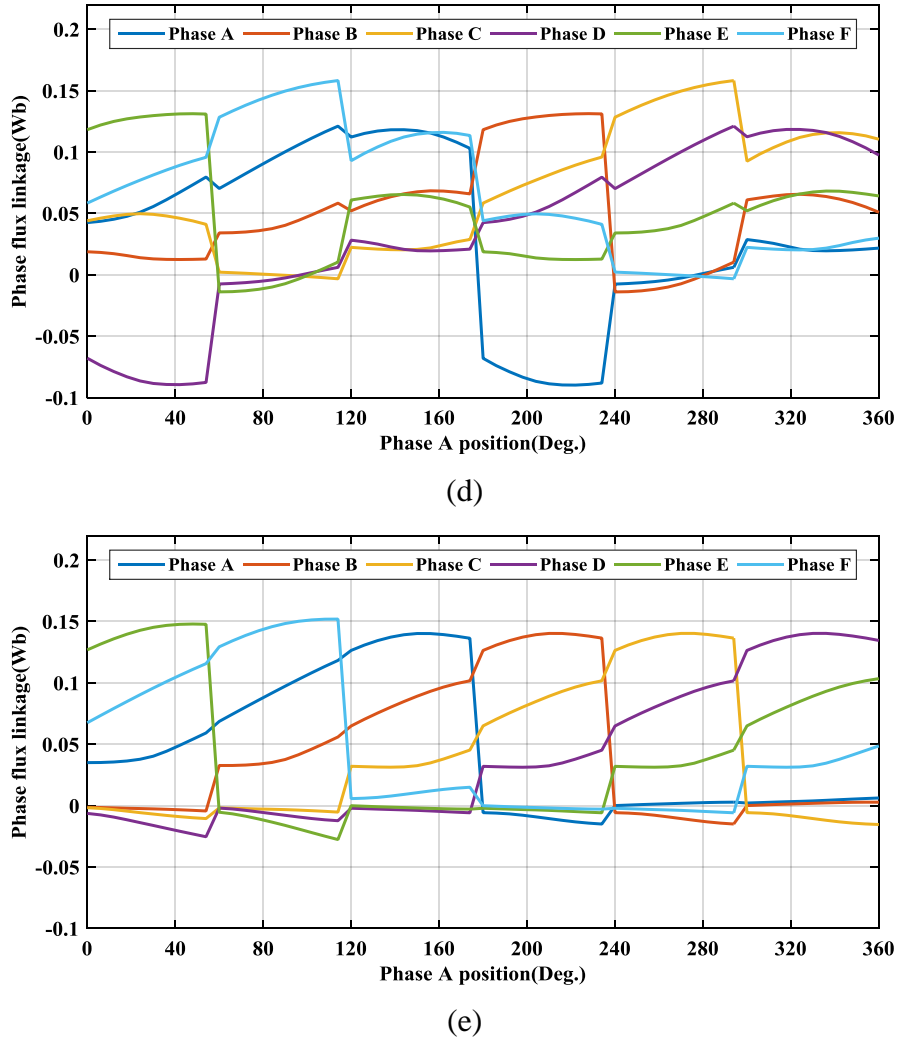
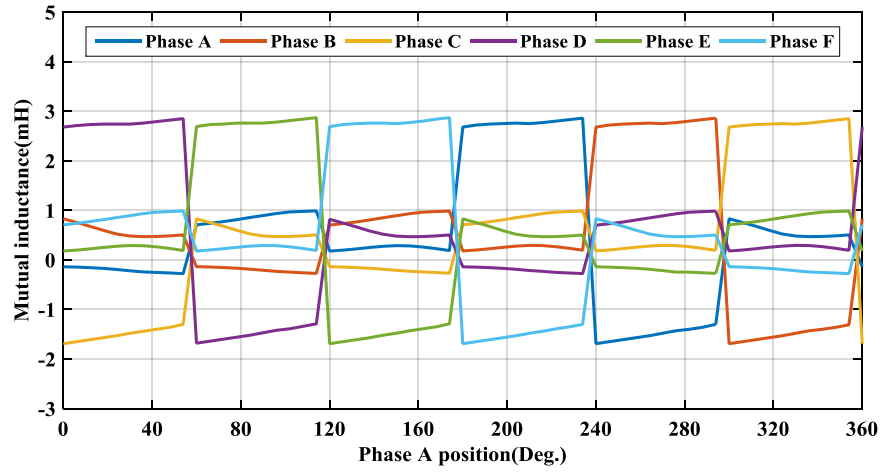
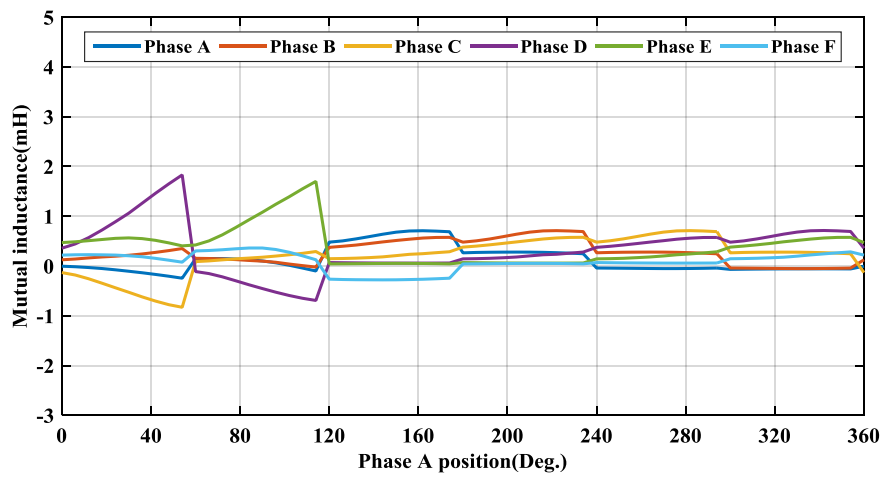


Figure 5.15 Six phase flux linkages of five different winding connection types excited by  $180^\circ$  square wave current: (a) Type 1 (b) Type 2 (c) Type 3 (d) Type 4 (e) Type 5

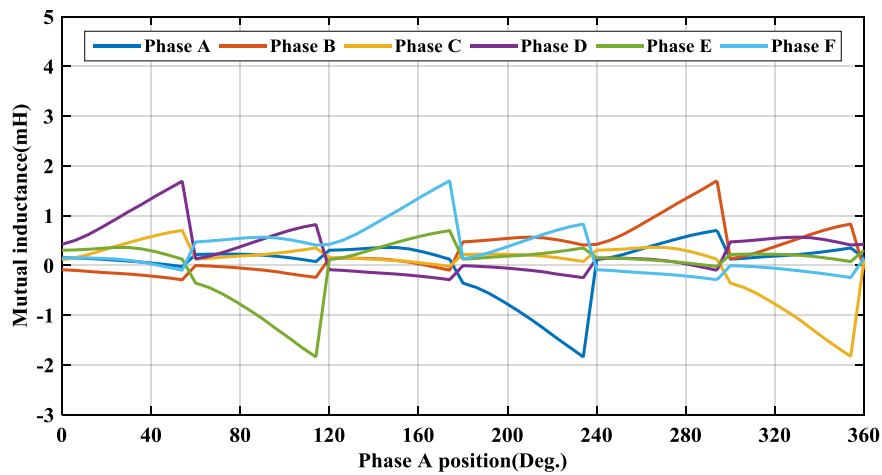
In order to calculate the mutual-inductance, six phase flux linkages are observed from FEM simulations. The excitation currents are set at 15A, simulation results of phase flux linkages are presented in Figure 5.15. Phase flux linkages of Type 1 are symmetric by every  $60^\circ$ , phase flux linkages of Type 3 are symmetric by every  $120^\circ$ , and all the other types are asymmetric. Because of unreasonable winding connections in Type 4 and Type 5, phase flux linkages are very unsatisfactory, and are not discussed here. Phase flux linkages in Type 1 to Type 3 are very similar in conducting part (when phase electrical position is between  $0^\circ$  and  $180^\circ$ ), and have obvious distinctions in non-conducting part.



(a)



(b)



(c)

Figure 5.16 Six phase mutual-inductances of three different winding connection types excited by  $180^\circ$  square wave current: (a) Type 1 (b) Type 2 (c) Type 3

Known six phase flux linkage values, mutual-inductance values can be calculated by Equation (5.5) to Equation (5.8). Calculation results are presented in Figure 5.16. The x-axis of Figure 5.16 are phase A position, therefore conducting period for phase A is  $0^\circ$  to  $180^\circ$ , active period for phase B is  $60^\circ$  to  $240^\circ$  and so on.

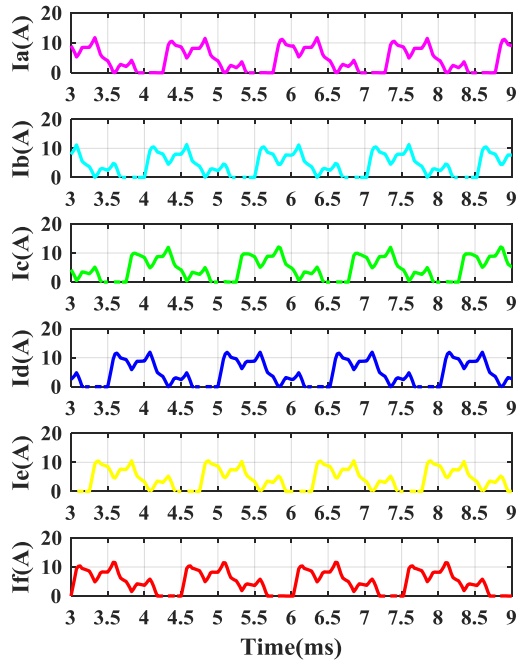
As expected, Type 1 to Type 3 have very similar mutual-inductance value during active period, all of them are between -1mH to 1mH. However, the mutual-inductance in inactive period has very obvious distinction. Mutual-inductance are close to 3mH or -2mH in inactive period in Type 1, while Type 3 only have 1.6mH as the maximum value and in Type 2 only 3 phases have obvious mutual-inductance with a maximum value less than 1.8mH.

Combining with output torque result in Figure 5.9, it is obvious mutual-inductances in Type 1 and Type 3 especially those parts in inactive period limit their total output torque, meanwhile the asymmetric mutual-inductances result in a larger torque ripple in Type 2. The serious coupling after active period will delay the freewheeling time and cause current distortion in a real-time system especially at high speed.

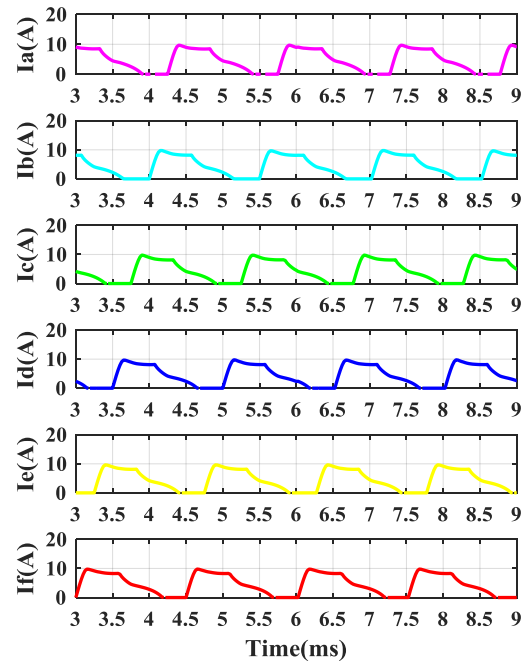
The FEAs of five different winding connection types at high speed is then conducted. The DC link voltage is 400V, rotor rotational speed is 4000r/min, advanced angle is  $10^\circ$  and conduction width is  $140^\circ$ . The simulation settings are summarized in Table 5.4. Since machine runs at high speed, the phase current cannot reach the reference anymore. The current waveforms at high speed are shown in Figure 5.17.

Table 5.4 Settings of the FEA model of the high speed multi-phase excitation simulation

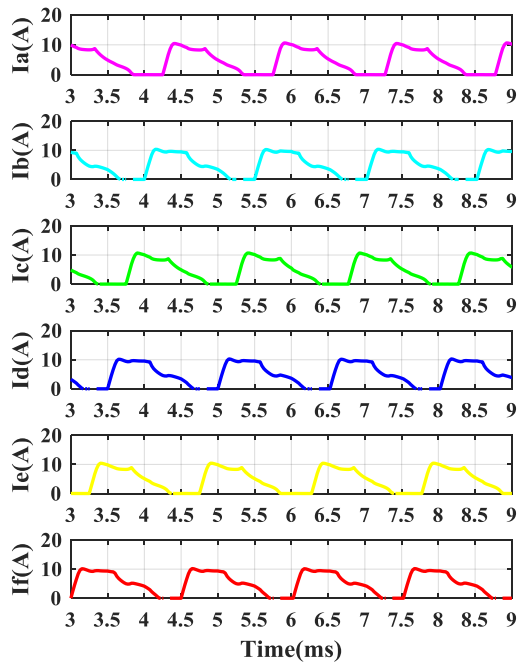
Start position (mechanical)	$0^\circ$
Stop position (mechanical)	$360^\circ$
Start time	0s
Stop time	0.015s
Speed	4000r/min
Turn-on angle (Electrical)	-10
Turn-off angle (Electrical)	130
Maximum voltage	400V
Solver	Transient 2D
Maximum mesh size	1mm
Current reference	20A



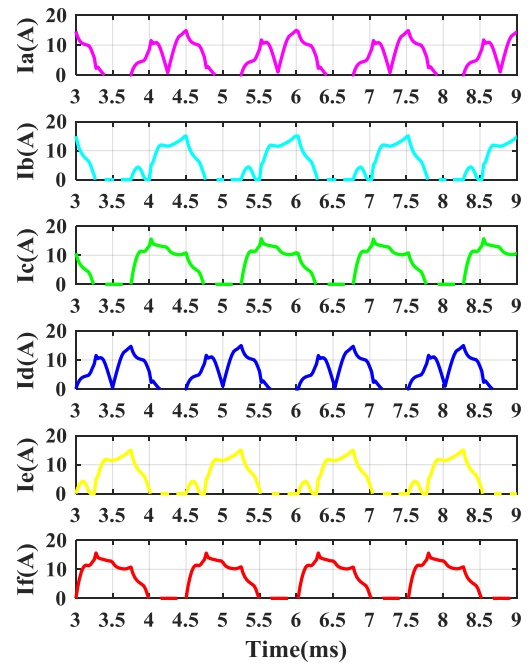
(a)



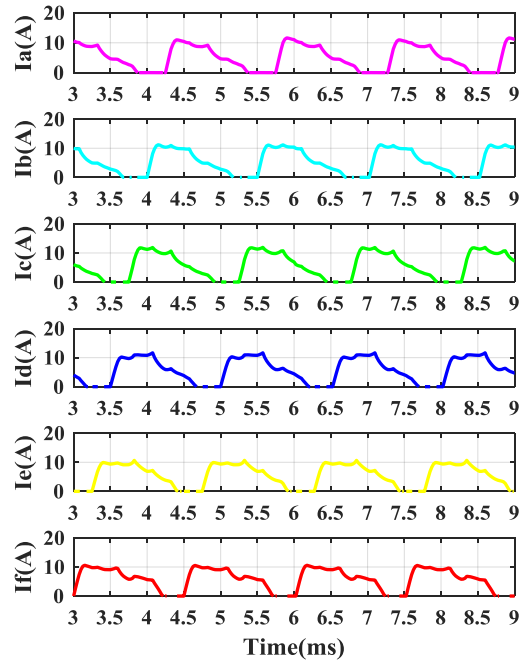
(b)



(c)



(d)



(e)

Figure 5.17 Six phase current of five different winding connection types under voltage control at high speed: (a) Type 1 (b) Type 2 (c) Type 3 (d) Type 4 (e) Type 5

As shown in Figure 5.17(a), (d) and (e), obvious current distortions appears in Types 1, 4 and 5 due to serious mutual coupling. Observing the current waveforms, it is interesting that only Types 1, 2 and 3 are symmetric, all six phase current waveforms in Type 1 and Type 2 are the same, meanwhile, current waveforms of phases A, C, E have the same shape and current waveforms of phases B, D, F have the same shape in Type 3. Referring to the magnetic poles distribution in Figure 5.7, only Types 1 and 3 is symmetric naturally giving six phase symmetric current waveforms. The reason there are symmetric current waveforms in Type 2 is the low mutual coupling, which indicates that the asymmetric winding connection in Type 2 does not affect much of the current shapes at high speed.

## 5.6 Summary

In this chapter, related FEM analyses including single-phase excitation and multi-phase excitation for the six-phase SRM prototype are implemented. Five different winding connection types are proposed and compared by torque performance and mutual-inductance effects. As the proposed Type 3 has reasonable output torque with smallest torque ripple and has less mutual-inductance, it is chosen to be the best winding connection type for the six-phase SRM prototype. The simulation analysis in this chapter will be validated in experimental chapter.

## Chapter 6. Design and Implementation of a Six-Phase SRM Drive System

This chapter provides an overview of the six-phase Switched Reluctance Machine (SRM) drive system, aiming to familiarise the reader with the experimental tools used for this drive system. The design and implementation of the hardware and the software are presented. Primarily, a 4.0kW SRM test rig is built and commissioned in Newcastle University. This test rig is designed to analyse the effects of different winding connection types, the drive capability of different power converters, and the control performance of different control techniques.

### 6.1 Overview of test rig

A schematic diagram of the test rig is illustrated in Figure 6.1. The test rig mainly contains a six-phase SRM prototype, a three-phase Permanent Magnet Synchronous Machine (PMSM), a power converter, a digital control system including a general control board by which a Digital Signal Processor (DSP) TMS320F28335 is employed, six two-channel gate drive boards, sensor systems, safety circuit, auxiliary equipment used for measurement and protection, etc.

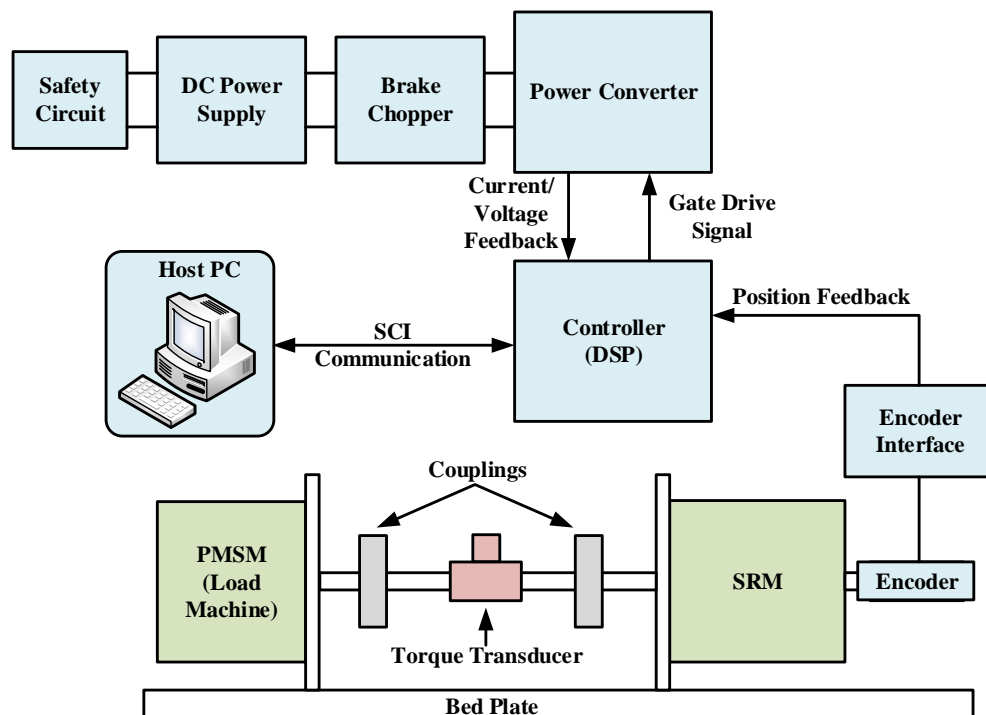
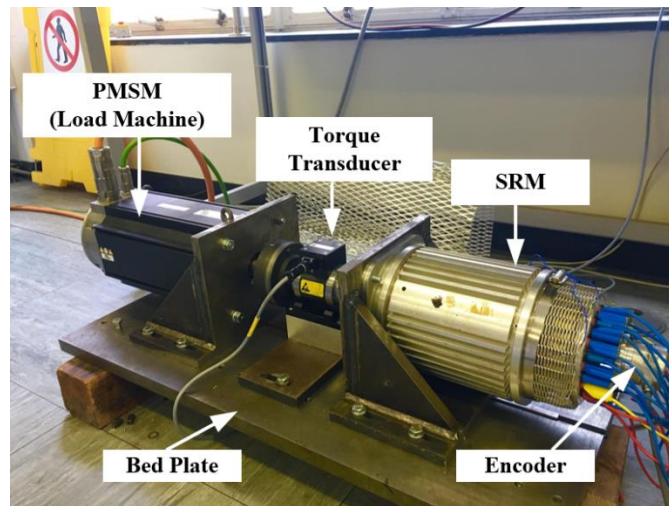
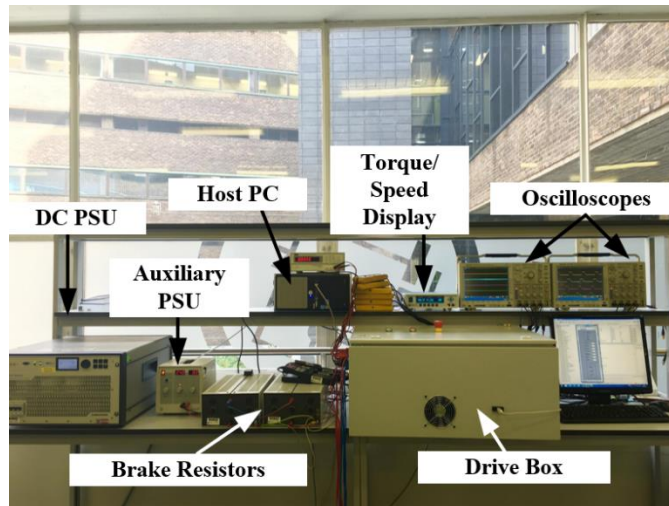


Figure 6.1 Schematic diagram of the test rig

Photographs of the test rig are shown in Figure 6.2. A SRM prototype, a load machine, a torque transducer and an encoder are mounted coaxially on bed plate in Figure 6.2(a). On the terminal of SRM prototype, there are twenty-four sockets connected with twelve windings, which can be easily connected with power converter to achieve different winding connection types proposed in Chapter 5. Figure 6.2(b) shows the drive system and auxiliary equipment including a drive box, power supplies, host PC, differential probes, oscilloscopes, etc.



(a)



(b)

Figure 6.2 Photographs of the test rig: (a) mechanical part (b) electrical part

Figure 6.3 shows the internal photographs of the drive box, all the high power components and current sensors are arranged on one side of the heat sink and all the other control boards are arranged on the other side. All the construction details will be introduced in the following sections.

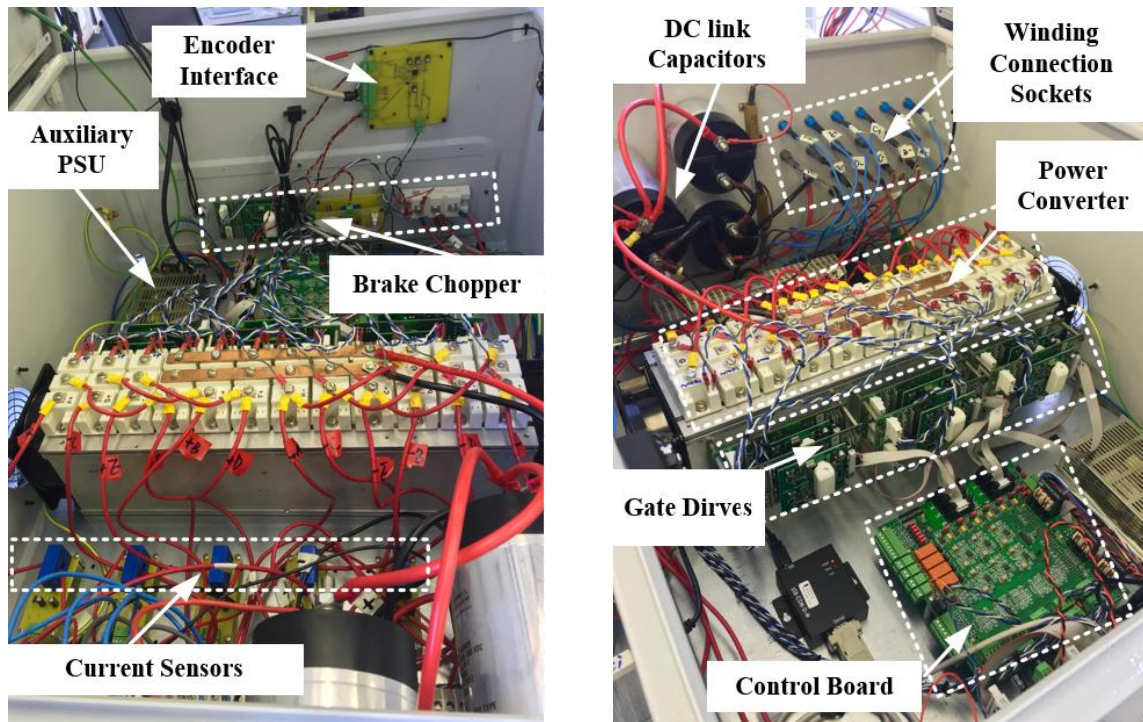


Figure 6.3 Internal photographs of the drive box

## 6.2 Hardware implementation

### 6.2.1 General control board

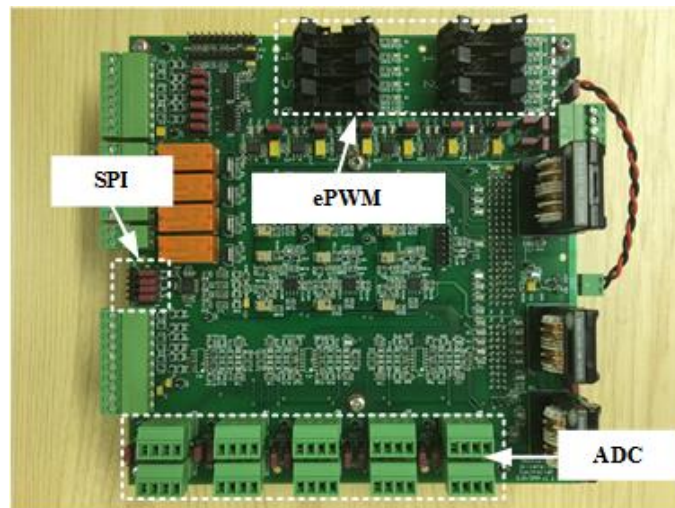


Figure 6.4 General control board

As presented in Figure 6.4, a general control board is designed as a central control module for the test rig, by which a F28335 eZdsp board is employed as shown in Figure 6.5. The digital Signal Processor (DSP) TMS320F28335 has twelve channel Pulse Width Modulation (PWM) outputs and a 16-channel Analog to Digital Converter (ADC), which can help to control twelve IGBT modules independently and convert a maximum of sixteen detected voltage

signals. On the general control board, Serial Peripheral Interface (SPI) and Serial Communications Interface (SCI) are designed, which can be used for serial communication with the host PC and the encoder.

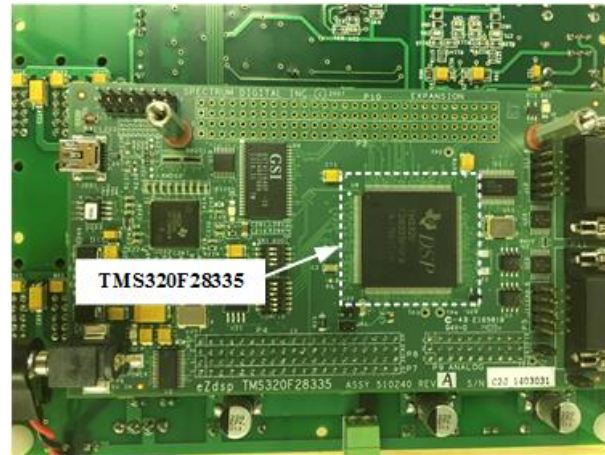


Figure 6.5 TMS320F28335 eZdsp board

## 6.2.2 Power converters and gate drivers

Figure 6.6 shows the construction of power converters and gate drive solution. Twelve fast IGBT (Insulated Gate Bipolar Transistor) modules are mounted on the top of an air cooling heat sink as shown in Figure 6.6(a), which includes six SKM150GAR12T4 IGBT modules and six SKM150GAL12T4 IGBT modules respectively. The voltage and current ratings of these two IGBT modules are 1200V and 150A. In addition, six sets of two-channel gate drive boards which consist of driver core boards and adaptor boards are chosen to generate the gate drive signals. All the gate drive boards are mounted on the side of the heat sink as shown in Figure 6.6(d).



(a)

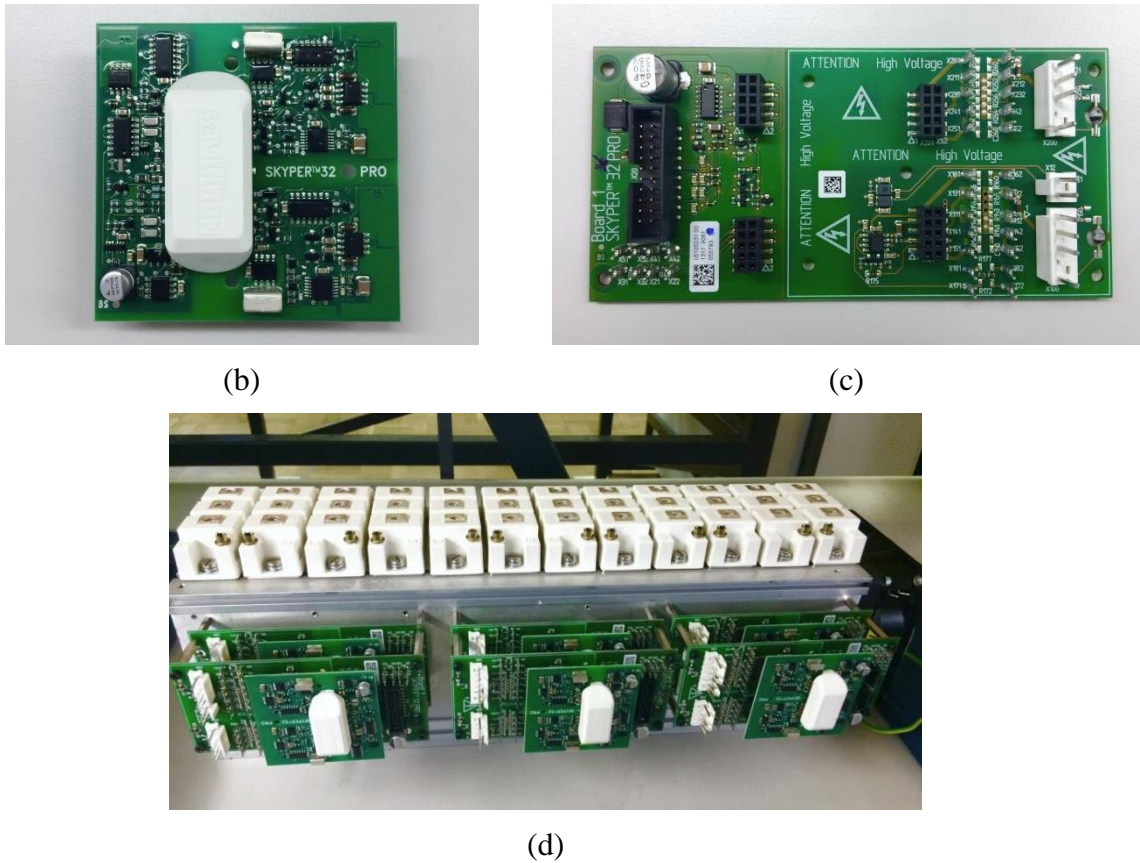
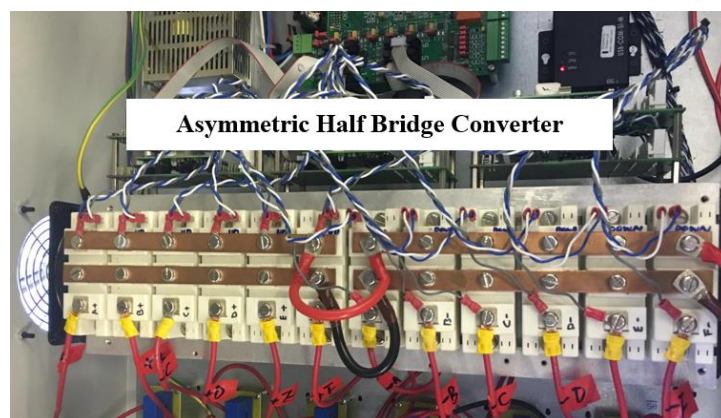
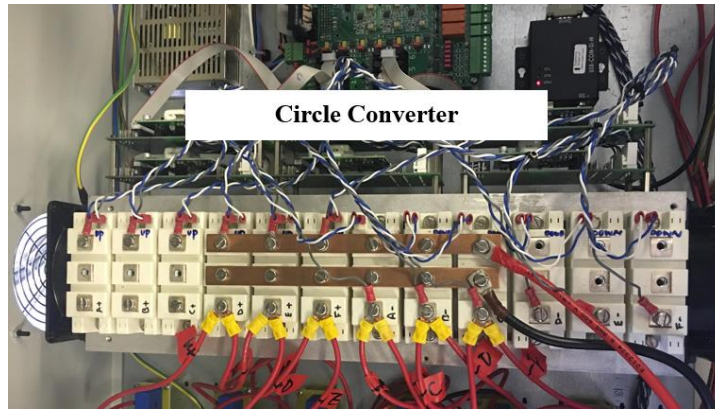


Figure 6.6 Construction of power converters and gate drive solution: (a) IGBT module SKM150GAR12T4 and SKM150GAL12T4 (b) IGBT driver core (c) adaptor board (d) heat sink assembly photograph

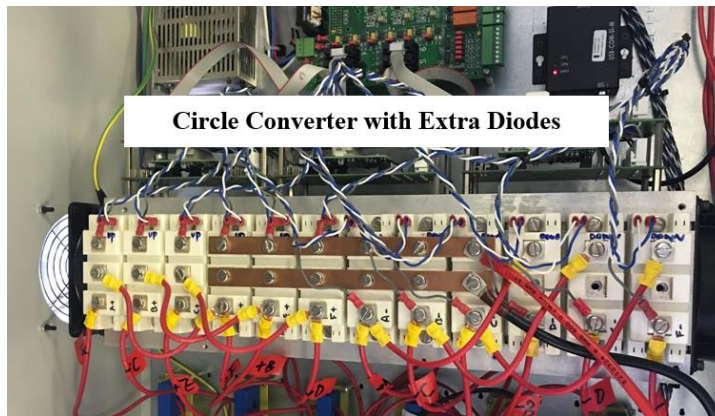
Twelve IGBT modules are employed to constitute a six-phase Asymmetric Half Bridge (AHB) converter originally as shown in Figure 6.7(a), and by changing the connections between six phase windings and IGBT modules, the proposed circle converter and circle converter with extra diodes can be simply obtained as presented in Figure 6.7(b) and Figure 6.7(c).



(a)



(b)



(c)

Figure 6.7 Construction of three different converters: (a) AHB converter (b) circle converter (c) circle converter with extra diodes

In order to test the drive signal of the DSP ePWM (enhanced Pulse Width Modulation) module and gate drive board, the following test is constructed. The duty cycle of a PWM channel is set at 0.5, the PWM waveform generated by general control board and the gate drive waveform generated by a gate drive board are shown in Figure 6.8. It shows that this gate driver works effectively.

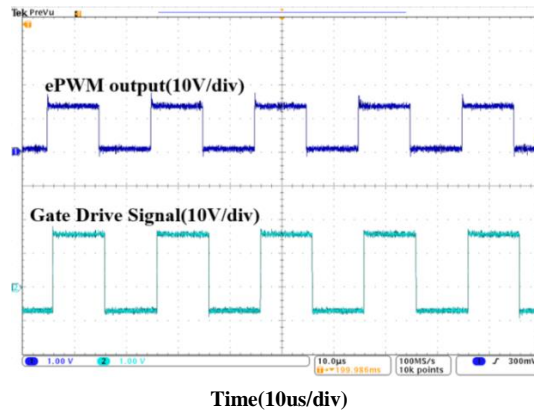
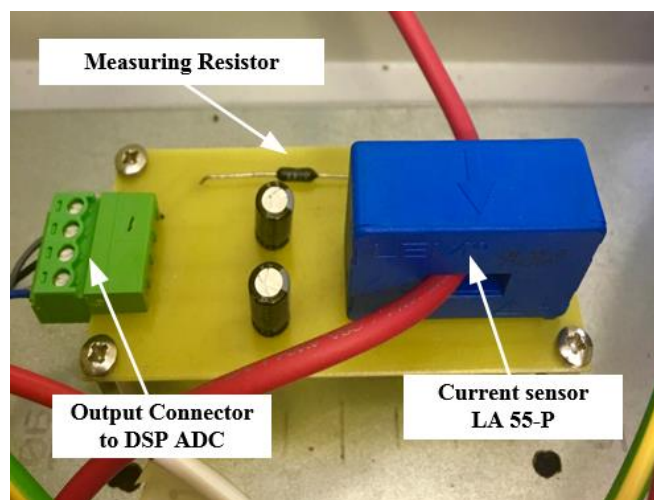


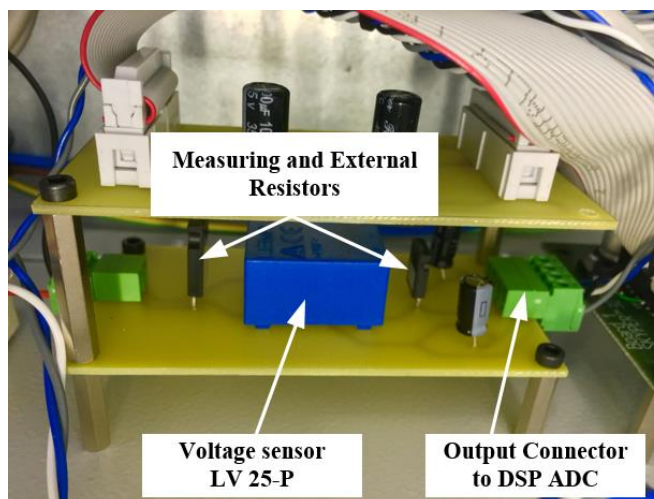
Figure 6.8 Output waveform of ePWM module and gate drive waveform

### 6.2.3 Sensors and interfaces

In order to obtain six phase currents and DC link voltage in real-time tests, six current sensors LA 55-P and a voltage sensor LV 25-P are employed in the control system to measure six phase currents and DC link voltage as presented in Figure 6.9. All the detected current and voltage signals are transduced to voltage signals and converted to digital values by DSP ADC module for the further control purpose. The measuring range of LA 55-P is  $\pm 50\text{A}$ , and its conversion ratio is 1:1000. The measuring range of LV 25-P is 10V to 1500V, and its conversion ratio is 2500:1000. A matched interface is also designed on general control boards as shown in Appendix B.



(a)



(b)

Figure 6.9 Sensor boards: (a) current sensor board (b) voltage sensor board

The tested conversion results of employed current and voltage sensors are illustrated in Figure 6.10. Both graphs demonstrate excellent linear performance at various input signals. Consequently, the current and voltage sensor interfaces work effectively in the test rig.

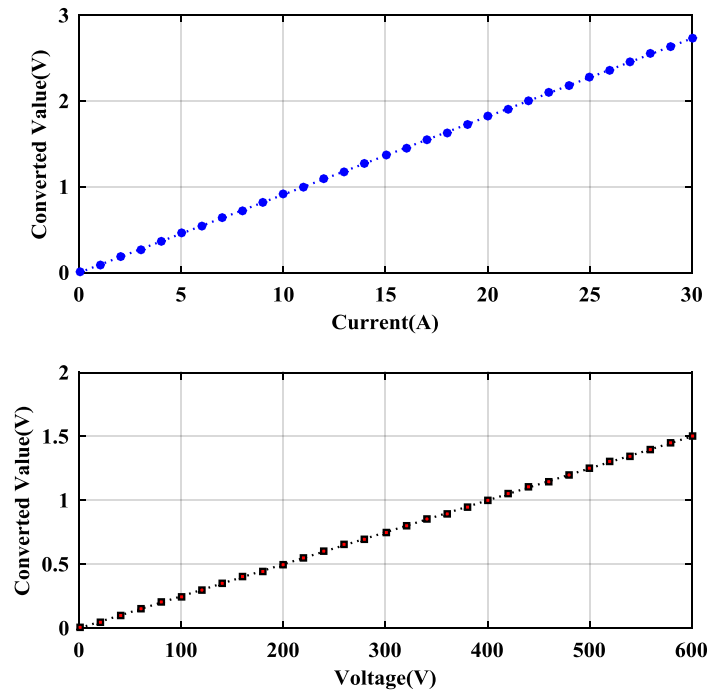


Figure 6.10 Tested conversion results of current and voltage sensor board

#### 6.2.4 The encoder and its interface



Figure 6.11 Absolute encoder HENGSTLER AC 58

A thirteen bit absolute encoder HENGSTLER AC 58 as shown in Figure 6.11 is employed in the test rig. Comparing with a traditional integral encoder, this absolute encoder has better performance without the index position. Absolute encoders provide an absolute numerical value in gray code for each angular. In the gray code system two successive values differ in

only one binary digit, which is the biggest difference between gray code and natural binary code. In the event of a power failure the present position is quickly and reliably detected.

In order to enable the general control board to use an SPI module to communicate with the absolute encoder, an additional interface board is designed as Figure 6.12. As shown in Figure 6.12(a), IC1 is a transceiver chip MAX1486EUB to generate the differential clock signals for the encoder from DSP SPI clock signal. Meanwhile this chip has to transfer differential position signals from the encoder to +3.3V CMOS level for the DSP Serial Peripheral Interface Slave Output Master Input (SPISOMI) port.

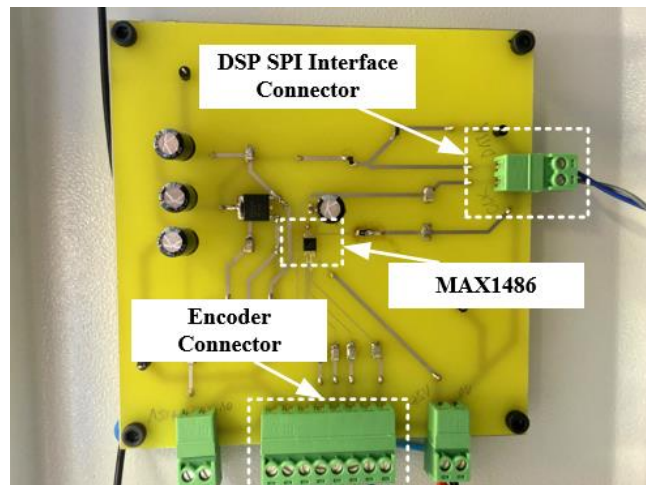
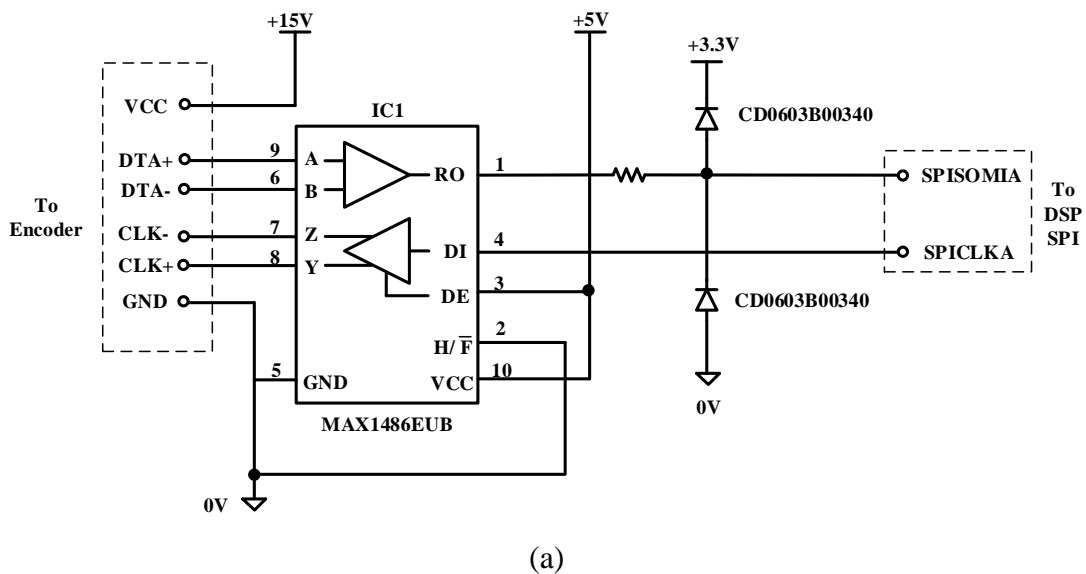


Figure 6.12 Interface between encoder and general control board: (a) schematic (b) PCB Transformation results and communication waveforms are shown in Figure 6.13, in which SPISTE is the enable signal for the DSP reading data from the shift register in the encoder,

SPICLK is the clock signal generated by DSP SPI module, SPISOMI is the output gray code from encoder.

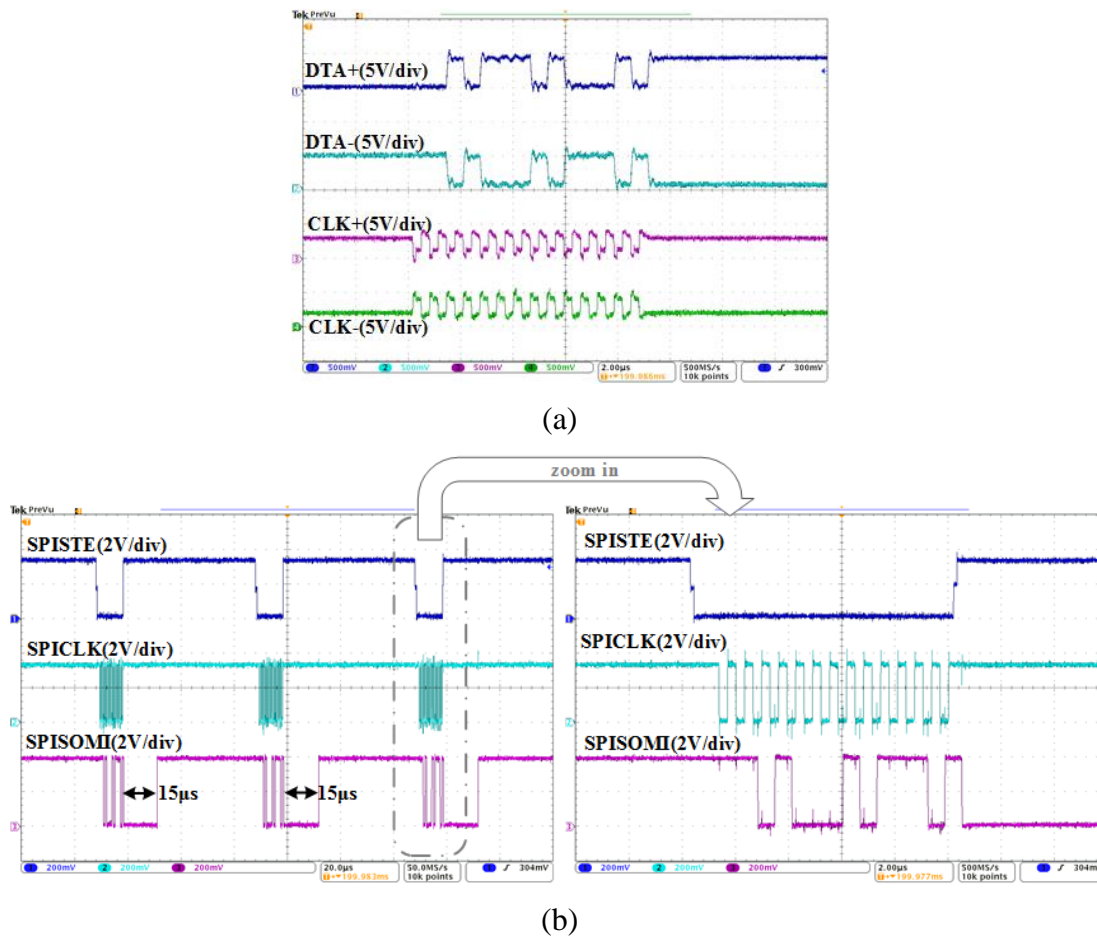


Figure 6.13 Communication waveforms between DSP SPI module and encoder: (a) differential data and clock signals on encoder side (b) enable signal, clock signal and data on DSP side

Synchronous readout of the encoder data is according to the clock rate given by the DSP SPI module. For this thirteen bit absolute encoder, fourteen clocks are needed. With the first descending clock edge the encoder data represented by special bits is loaded in the shift register of the encoder interface. With each ascending clock edge the data bits are serially readout, beginning with the Most Significant Bit (MSB). At the end of the data transfer, the data output is set to logically "0" for approximate 15µs. If within these 15µs a further clock brush reaches the encoder interface, the already transferred data is readout once again. This multiple transfer of the same data makes it possible to recognize transfer errors. After the 15µs the data output goes to its rest position, logically "1". Subsequently new encoder data can be readout.

According to the SPISOMI signal in Figure 6.13(b), the thirteen bit gray code of this position is “1101000101100”. In order to calculate the rotor position, the gray code is converted to a natural binary code according to the algorithm shown in Figure 6.14. The natural binary MSB B(12) and gray code MSB G(12) is always the same. The natural binary bit next to MSB B(11) is the result of XOR operation between B(12) and G(11). The rest natural binary bits can be obtained according to the same algorithm. Consequently rotor position can be simply achieved.

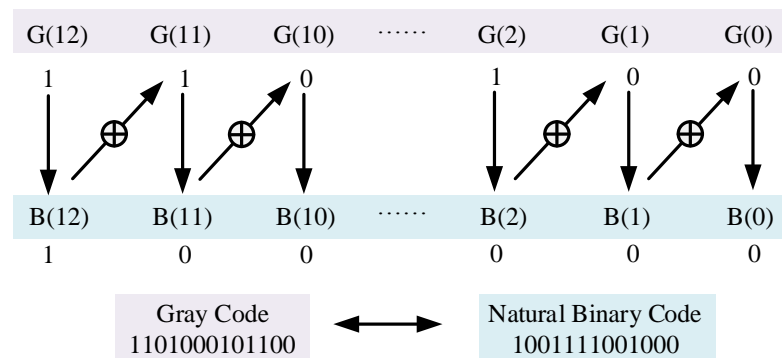


Figure 6.14 Conversion algorithm from gray code to natural binary

### 6.2.5 Safety circuit

A safety circuit is designed to protect users from directly contacting with current circuit or high voltage components. As presented in Figure 6.15, there are two micro switches, an emergency stop switch, a flush start switch, a flush stop switch and a relay in the safety circuit.

The relay (having two contactors and a coil) is arranged in the 24V safety circuit, one contactor is arranged in the safety circuit to magnetize the coil of the relay, another one is used to connect the internal safety circuit of the main DC power supply. When users press start flush button, the coil of relay is magnetized and the two contactors are closed. When users open the lid of the drive box, press the stop button or press the emergency stop button, the coil of the relay demagnetizes, two contactors of the relay subsequently cut off the safety circuit and main power supply. By using this safety design, users can make the main circuit power on and off without touching high voltage components.

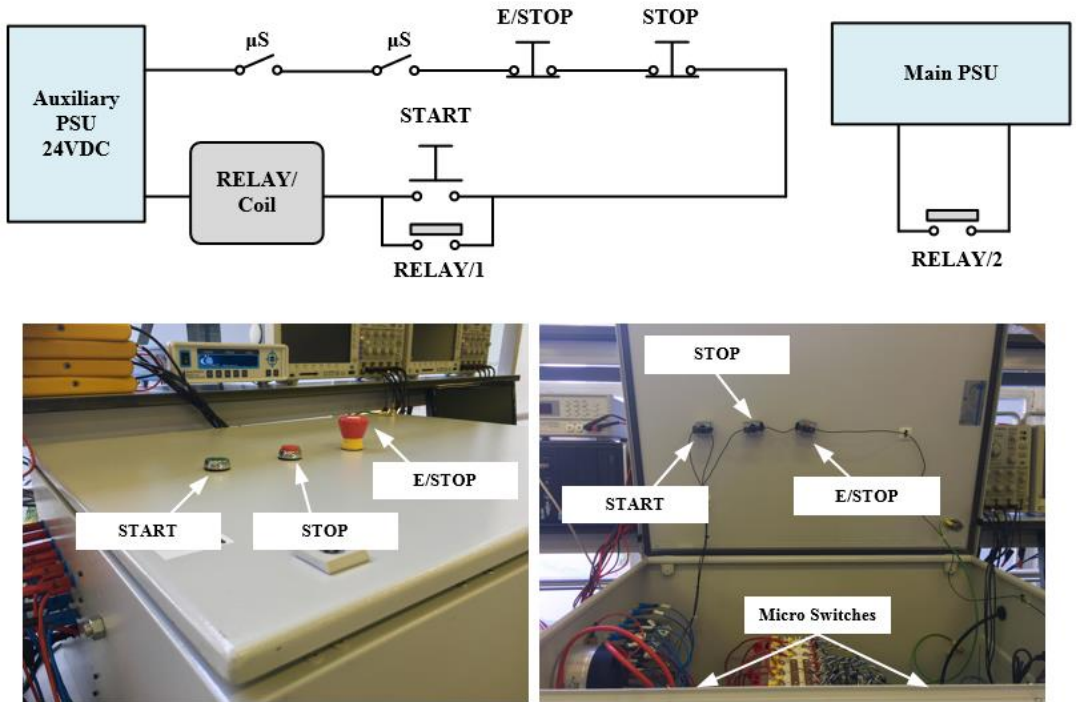


Figure 6.15 Schematic and photographs of safety circuit

### 6.2.6 Brake chopper

A brake chopper circuit illustrated with Figure 6.16 is designed for the drive system to control the DC link voltage when the load feeds energy back to the converter. It is an application of the chopper principle, using on-off control of a switching device  $S_b$ . It can limit the DC link voltage to a specified level to protect all the power devices by switching the braking energy to a power resistor  $R_b$ , where the braking energy is converted to heat.

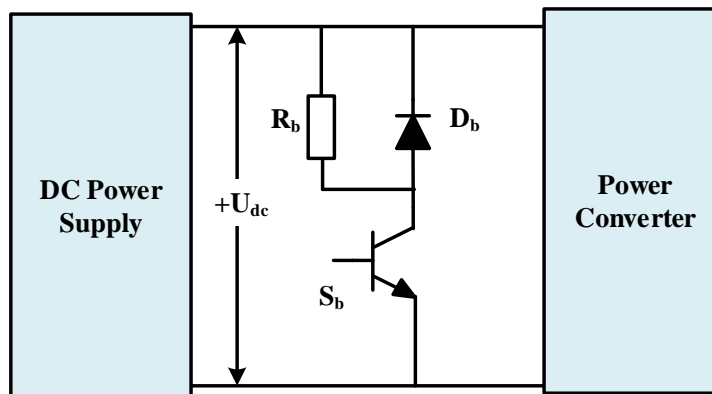


Figure 6.16 Schematic for brake chopper

### 6.3 Software implementation

In real-time tests, electromagnetic interference blocks the communication between the DSP and Code Composer Studio (CCS), which makes it difficult to change control parameters online. To solve this problem, a LABVIEW Graphical User Interface (GUI) is designed to operate together with the DSP to achieve an online controllable SRM drive system. Majority time-critical functional codes are located in the DSP internal memory to do the system initialization, realize SCI communication and conduct the SRM control strategies. The following sections give a brief introduction of the DSP programs and the LABVIEW user control panel.

#### 6.3.1 DSP

The central control module of the drive system is a TMS320F28335 DSP. Figure 6.17 shows the basic flow charts of the DSP control programs. Some of the functional DSP programs are shown in Appendix A.

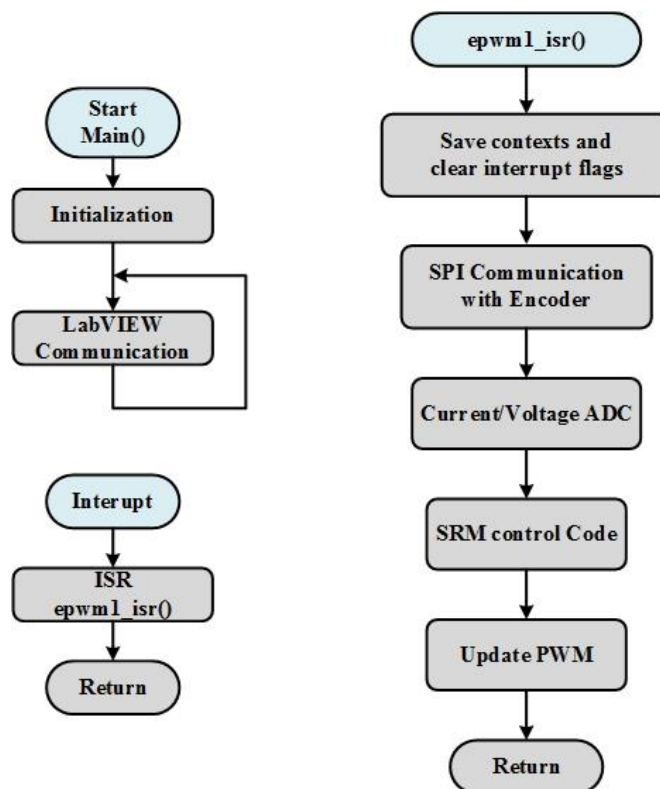


Figure 6.17 Flow charts of DSP control programs

Execution of the main function is a series of initialisation codes followed by the LabVIEW data exchange loop. This loop continuously communicates with the LABVIEW user control

panel via the RS232 interface. On the DSP, the RS232 interface is implemented with the Serial Communications Interface-A (SCI-A).

In addition to the main code there is an interrupt service routine (ISR), which contains all the application control codes. This ISR is triggered by the PWM hardware in the DSP. It contains protection codes for the brake chopper, codes for current protection, codes for the absolute encoder communication, ADC codes, SRM control codes (CCC Codes, APC codes and DTC Codes), etc.

### 6.3.2 LABVIEW

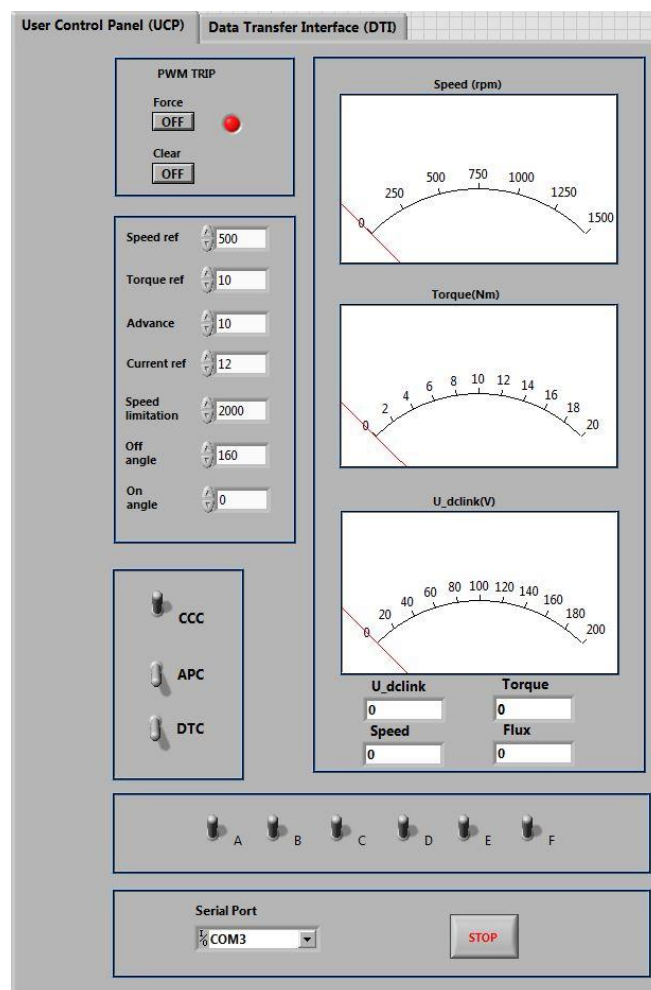


Figure 6.18 LABVIEW front user control panel

Users can perform online communication with the DSP by the LABVIEW GUI via SCI-A. The User Control Panel (UCP) view is used for continuous monitoring and control of the DSP. The communication process between the LabVIEW GUI and DSP does not involve interrupts.

By using this LABVIEW interface as presented in Figure 6.18, users can change the reference value of speed, torque, current, on-off angles and advance angle online, which means there is no need to stop the operating system to change reference settings. Three Boolean switches named CCC, APC and DTC can change the operation mode between three different control strategies. Six Boolean switches named A, B, C, D, E, and F can choose the active phases to achieve single-phase and multi-phase excitation tests. Two Boolean switches named clear and force can activate and deactivate all the twelve channel PWM outputs.

#### **6.4 Summary**

In this chapter, a six-phase SRM drive test rig is built for further experimental work. The proposed converters and conventional converter are obtained by different connections of IGBT modules. Encoder and sensor interfaces are designed and work successfully. The SRM control program, including CCC code, APC code and DTC code are designed in the DSP, the real-time drive system is controlled by the LABVIEW GUI.

## Chapter 7. Experimental Validation

In order to validate the simulation analysis in Chapter 3 to 5, this chapter implements experimental tests accordingly. Single-phase and multi-phase excitation tests are conducted to compare the effects of winding connection on performance of the six-phase Switched Reluctance Machine (SRM). The traditional control techniques are tested with the Asymmetric Half Bridge (AHB) converter, the proposed circle converter and the circle converter with extra diodes. The proposed Direct Torque Control (DTC) method is then applied to the AHB converter, the proposed circle converter and the circle converter with extra diodes to reduce the torque ripple existing with traditional control techniques.

### 7.1 Torque performance comparison of five winding connection types

#### 7.1.1 Single-phase excitation tests

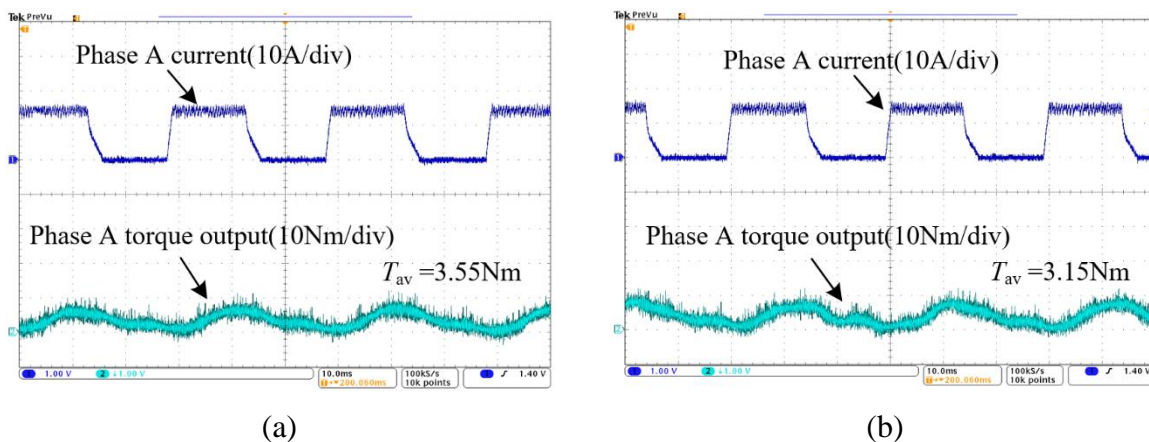


Figure 7.1 Single-phase excitation test waveforms: (a) N-S connection output torque (b) N-N connection output torque

The torque performance comparison is started with a single-phase excitation test with the AHB converter. In this section, control signals are only generated for phase A, therefore single-phase output torque is detected. In this test, the conduction width is  $180^\circ$  and the phase current reference is 15A which is same as the FEA in Figure 5.5. Figure 7.1 shows the waveforms of single-phase excitation tests, in which the N-S connection has a larger average output torque than the N-N connection, which validates that long flux-paths can produce more output torque than short flux-paths. Test results of single-phase excitation are comparable with FEA result as shown in Table 7.1. Variation between FEA and measured results is mainly due to the 2D FEA approach which neglects end leakage and thus over predicts torque.

Table 7.1 Single-phase average torque comparison between FEA and experimental test

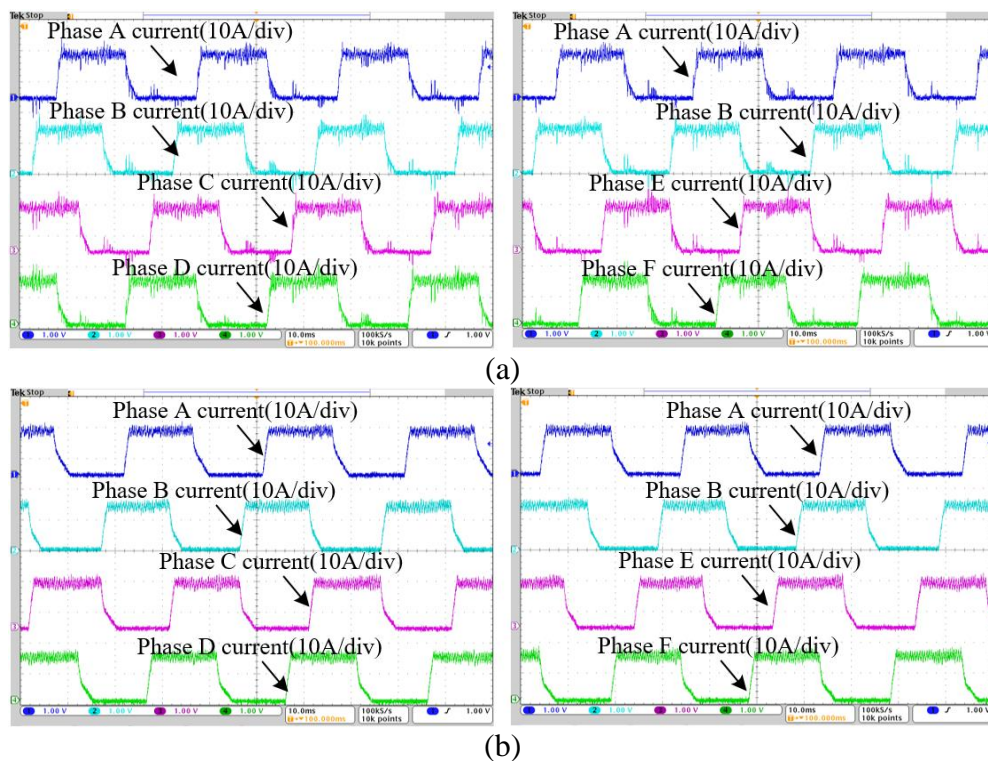
	N-S(FEA)	N-S(Test)	N-N(FEA)	N-N(Test)
$T_{av}(\text{Nm})$	3.75	3.55	3.30	3.15

### 7.1.2 Multi-phase excitation tests

In order to validate the analysis results in Chapter 5, a series of multi-phase excitation tests are conducted with the AHB converter. The Current Chopping Control (CCC) method is employed at low speed to test the torque performance of the five different winding connection types designed in Chapter 5. The Angle Position Control (APC) method is employed to test the torque performance of the five winding configurations at high speed.

#### 7.1.2.1 Current control results

In the low-speed tests, conduction widths are set at  $180^\circ$ , and phase current reference values are 15A. Figure 7.2 shows the current waveforms of the proposed five winding connection types proposed in Figure 5.7 under current control at 200r/min. Although all the current waveforms are very similar, they still have some distinctions. Types 1 and 4 have more obvious noise than other types due to their significant mutual coupling, as discussed in Chapter 5.



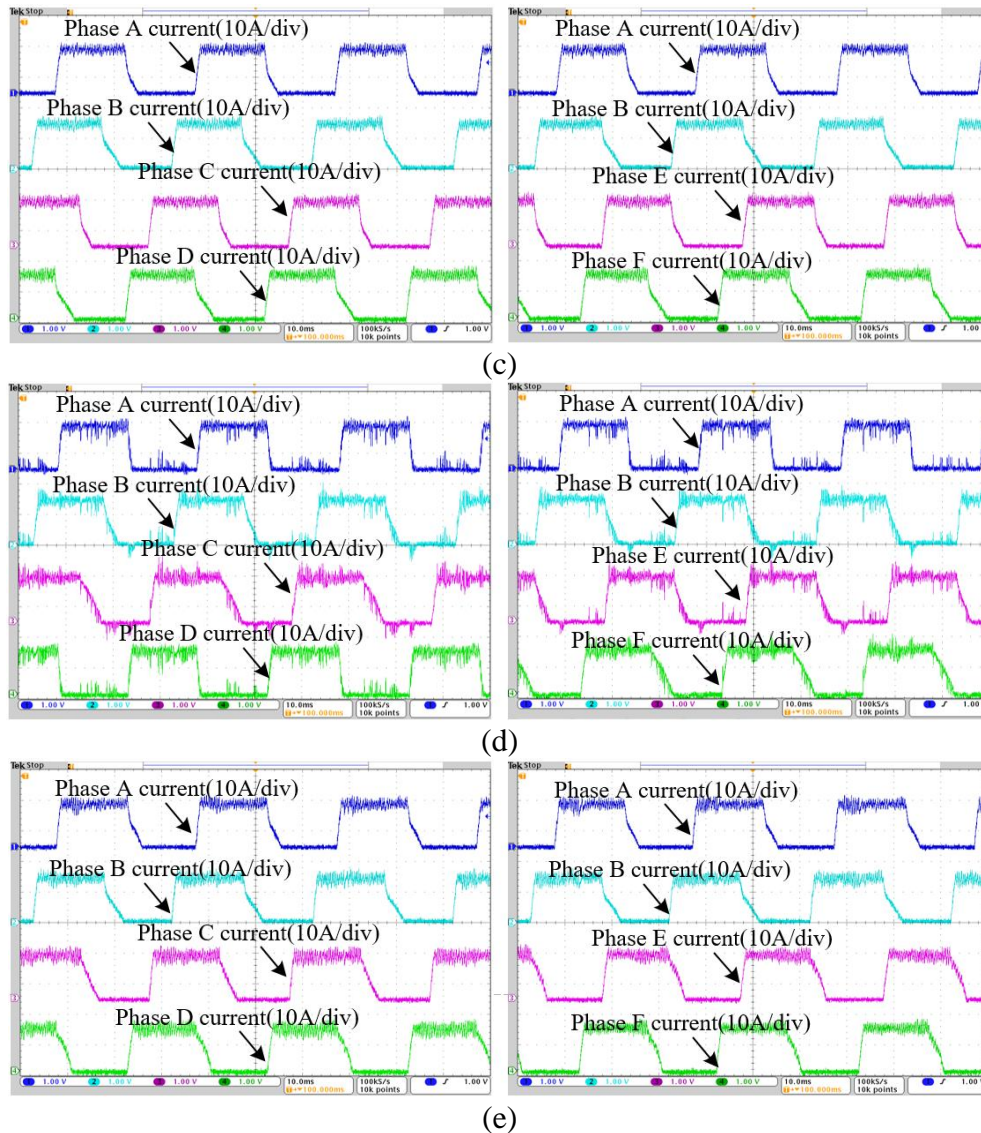


Figure 7.2 Current waveforms of five winding connection types under current control: (a) winding connection Type 1 (b) winding connection Type 2 (c) winding connection Type 3 (d) winding connection Type 4 (e) winding connection Type 5

Figure 7.3 shows the output torque waveforms of the five winding connection types. The average torque outputs of five winding connection types are 22.6Nm, 20.8Nm, 19.7Nm, 10.2Nm and 12.5Nm respectively. Torque Ripple Ratio (TRR) is 29.2%, 36.7%, 25.6%, 126.3%, and 52.1% respectively. As in the Finite Element Analysis (FEA) results in Chapter 5, Type 1 has the largest average torque, whilst Type 3 has the smallest torque ripple. Test results of multi-phase excitation are comparable with FEA result as shown in Table 7.2. There are three reasons behind differences between predicted and measured torques: 1) the 2D FEA prediction does not include end effects; 2) predictions assume perfect square waves of current and therefore neglect the rise and fall current periods; 3) the torque transducer has a limited bandwidth and torque measurements are damped by inertia of the rotor. Consequently the

higher frequency elements of electromagnetic torque are not properly captured by the measurement system.

Table 7.2 Multi-phase average torque and torque ripple comparisons between FEA and experimental test

	Type1	Type2	Type3	Type4	Type5
$T_{av}$ FEA (Nm)	24.3	24.7	23.2	14.3	20.4
TRR FEA (%)	27.2	29.2	16.7	243.0	58.8
$T_{av}$ Test (Nm)	22.6	20.8	19.7	10.2	12.5
TRR Test (%)	29.2	36.7	25.6	126.3	52.1

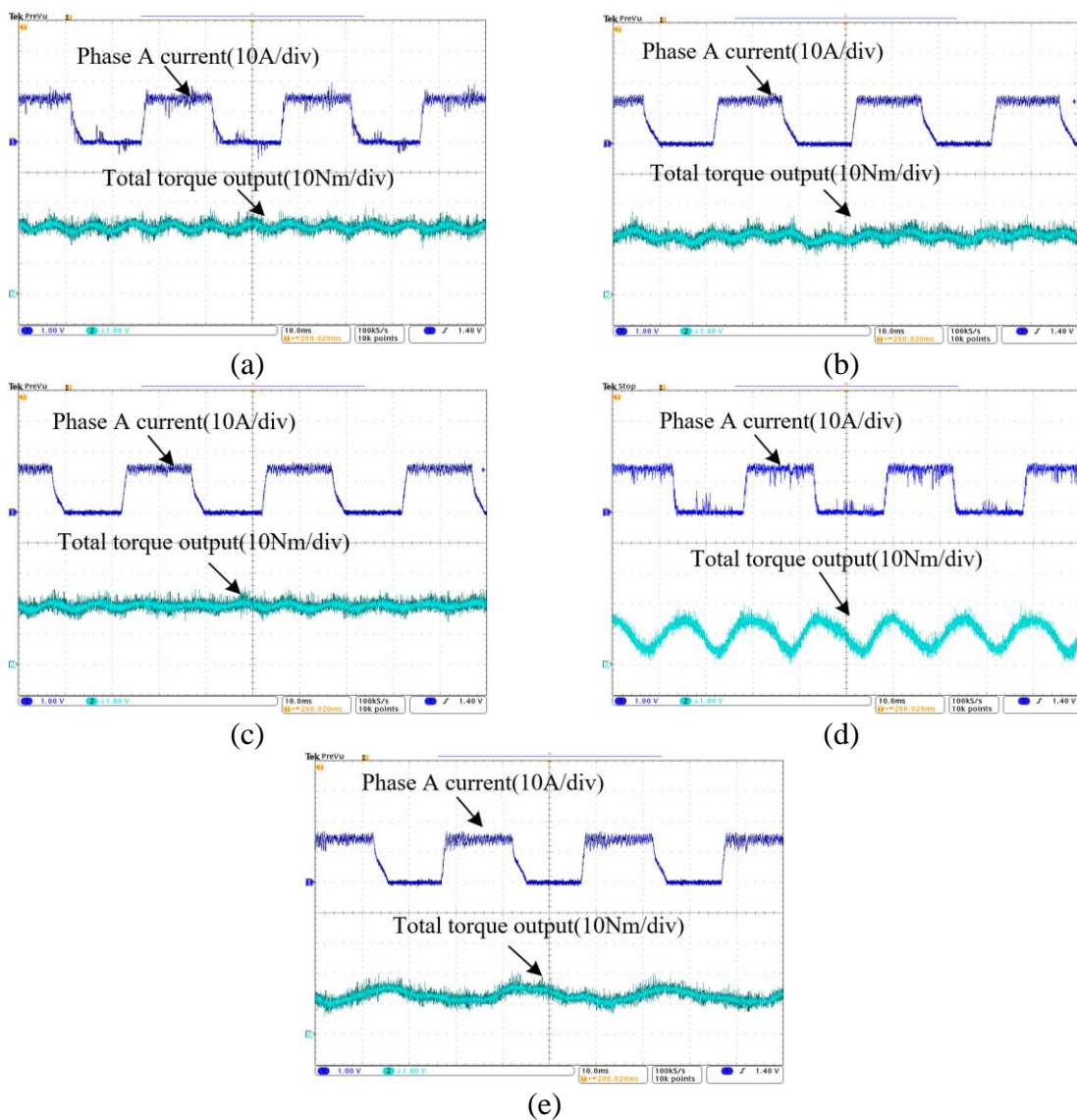
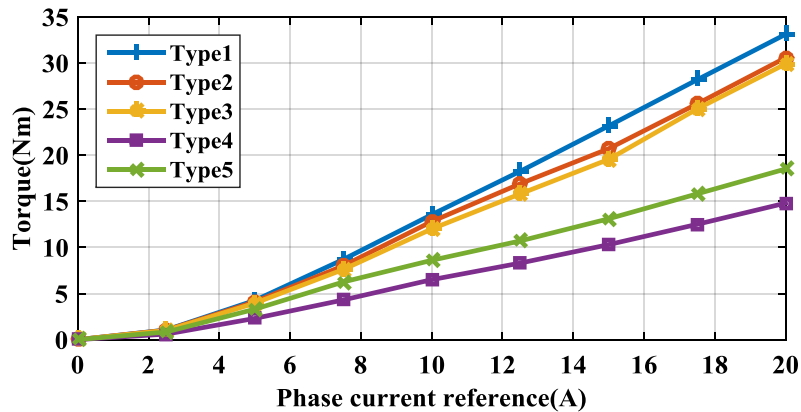
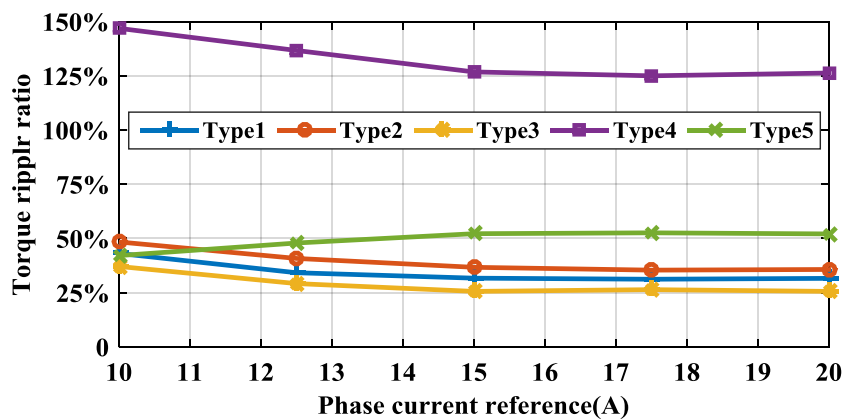


Figure 7.3 Output torque of five winding connection types under current control at 200r/min :  
 (a) winding connection Type 1 (b) winding connection Type 2 (c) winding connection Type 3  
 (d) winding connection Type 4 (e) winding connection Type 5

Figure 7.4 shows output torque of the five winding connection types under current control. Conduction widths are fixed at  $180^\circ$ , phase current reference value varies from 2.5A to 20A, therefore all the corresponding output torques can be collected. Types 1 to 3 have larger average output torque in Figure 7.4 (a), while Type 3 has the smallest torque ripple during current varying in Figure 7.4 (b).



(a)

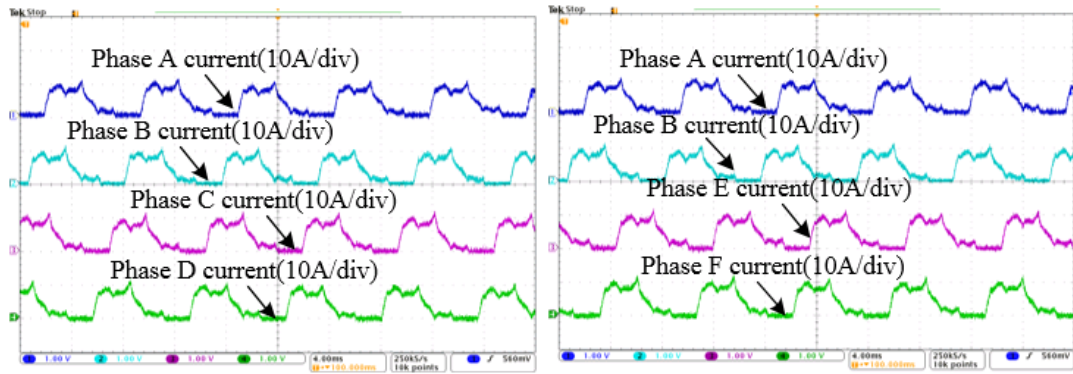


(b)

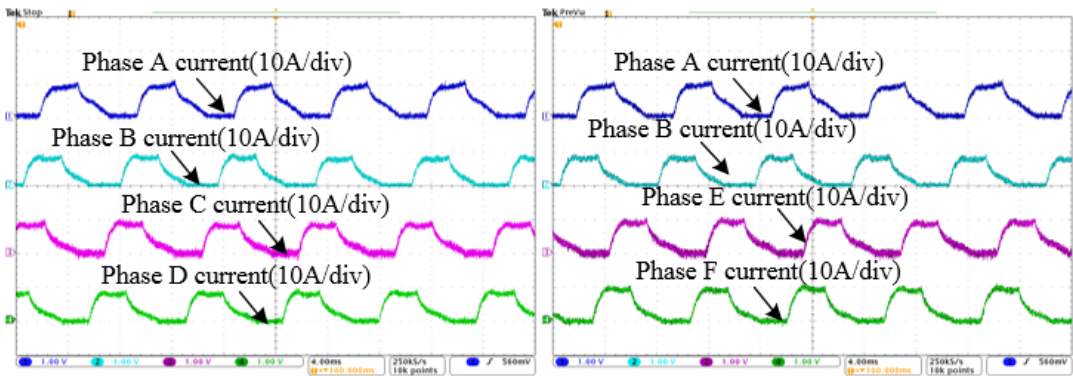
Figure 7.4 Output torque comparison of five winding connection types under current control at 200/min: (a) average output torque (b) torque ripple ratio

### 7.1.2.2 Voltage control results

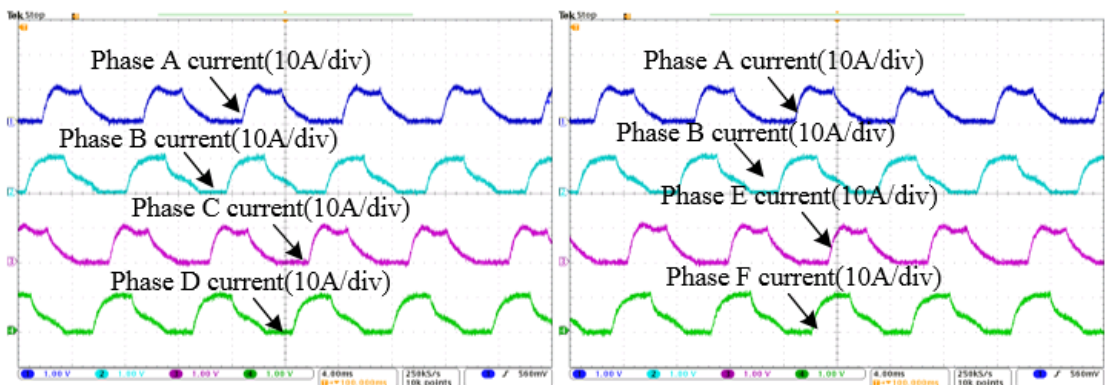
In order to further investigate the mutual-inductance effects on torque performance at higher speed, the APC method is employed. In this test, current is not controlled by chopping and is now a function of the applied voltage and machine impedance. Hence this test brings further insight into the effects of mutual-inductance.



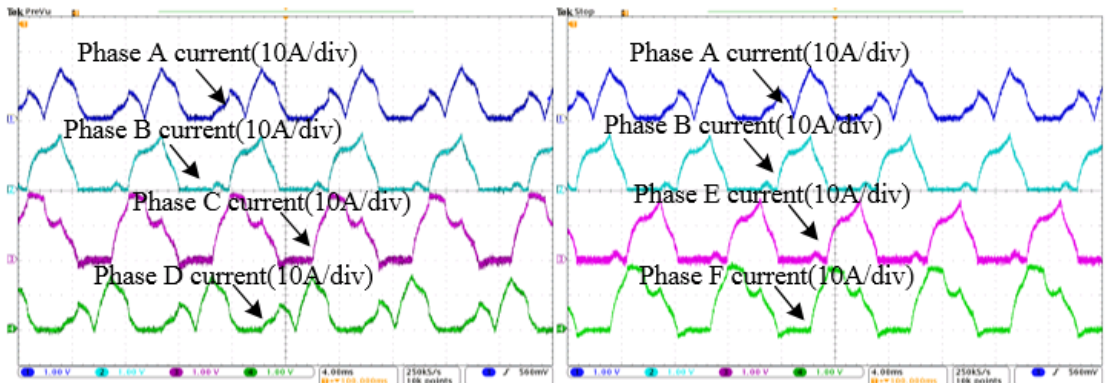
(a)



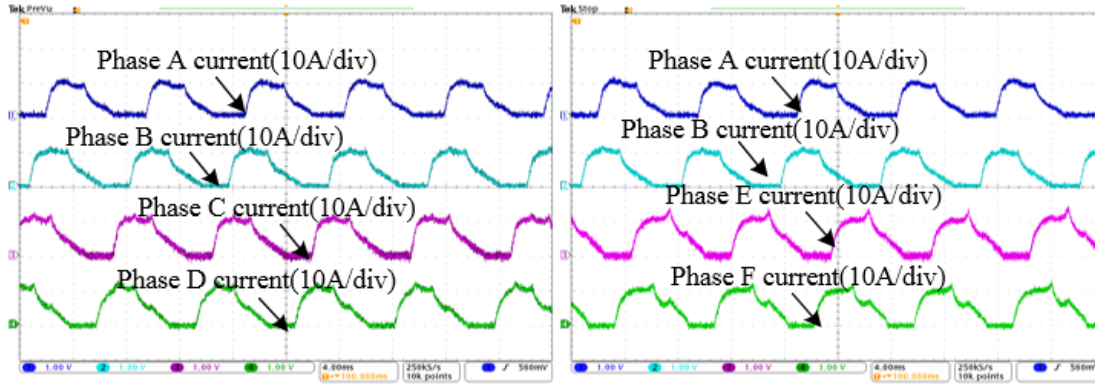
(b)



(c)



(d)



(e)

Figure 7.5 Voltage and current waveforms of five winding connection types under voltage control: (a) Type 1 (b) Type 2 (c) Type 3 (d) Type 4 (e) Type 5

Figure 7.5 shows measured phase currents for multi-phase excitation under voltage control at 800r/min. The conduction width and advance angle of this series of tests are 140° and 10°. There are serious current distortions in Types 1 and 4, which are exactly same as FEA results in Figure 5.17(a) and (d). Phase current waveforms of phases A, C, E are identical and phase current waveforms of phases B, D, F are identical in Type 3, which matches with FEA results in Figure 5.17(c). The phase current waveforms of Type 4 are very close to each other, which validates the predict that the asymmetric winding connection in Type 2 does not affect much of the current shapes at high speed.

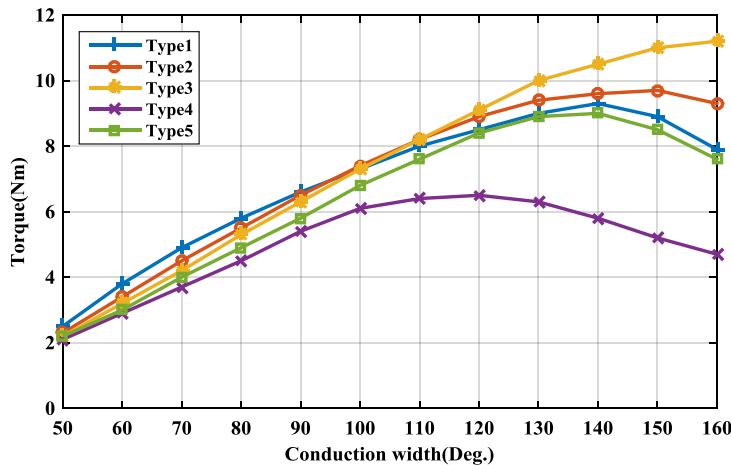


Figure 7.6 Output torque comparison of five winding connection types under voltage control To analyse the effects of mutual couplings on output torque under voltage control, the following tests are conducted. When the turn-on angle is fixed at -10°, the average output torque values are achieved by varying the turn-off angle from 40° to 150°. Test results are shown in Figure 7.6. Types 2 and 3 are generally superior above 120° of conduction owing to

better decoupling which means more current coincides with increasing inductance (more torque) and the shorter tail on the current waveform gives a reduced negative torque contribution, as shown in Figure 7.5(b) and (c). Type 1 exhibits greater torque at lower conduction angles, but at higher angles the current distortion is considerable as shown in Figure 7.5(a) which compromises the torque output.

Consequently, Type 3 is chosen to be the optimum winding connection type due to its high average torque output and low torque ripple and is employed in the following sections.

## **7.2 Experimental validation of traditional control methods and the proposed DTC method with the AHB converter**

In order to compare the torque performance of the traditional control methods and the proposed DTC method, the following tests are conducted throughout whole speed range are designed. In traditional control method tests, different phase reference currents are chosen to achieve varying average output torque at low speed and medium speed, and different conduction and advance angles are chosen to achieve varying average output torque at high speed. In the DTC method, different instantaneous torque and stator flux references are chosen to achieve varying average output torque with lower torque ripple. In this section, a 100V 48A DC power supply is employed for 200r/min and 800r/min tests to draw enough current. A 200V 30A DC power supply is employed for 1500r/min tests to get enough DC link voltage for high speed operation. Test results are shown in Figure 7.7 to Figure 7.18.

### **7.2.1 Traditional control methods**

#### **7.2.1.1 200r/min**

Traditional control methods are firstly applied to the six-phase SRM prototype. Figure 7.7 shows current waveforms with different loads at 200r/min under current control with the AHB converter. Phase current reference values to produce average torque of 5.0Nm, 10.0Nm, 15.0Nm, and 20.0Nm are 5.5A, 9.0A, 12.0A, and 15.5A respectively in this series of tests, and conduction widths are set at 160°.

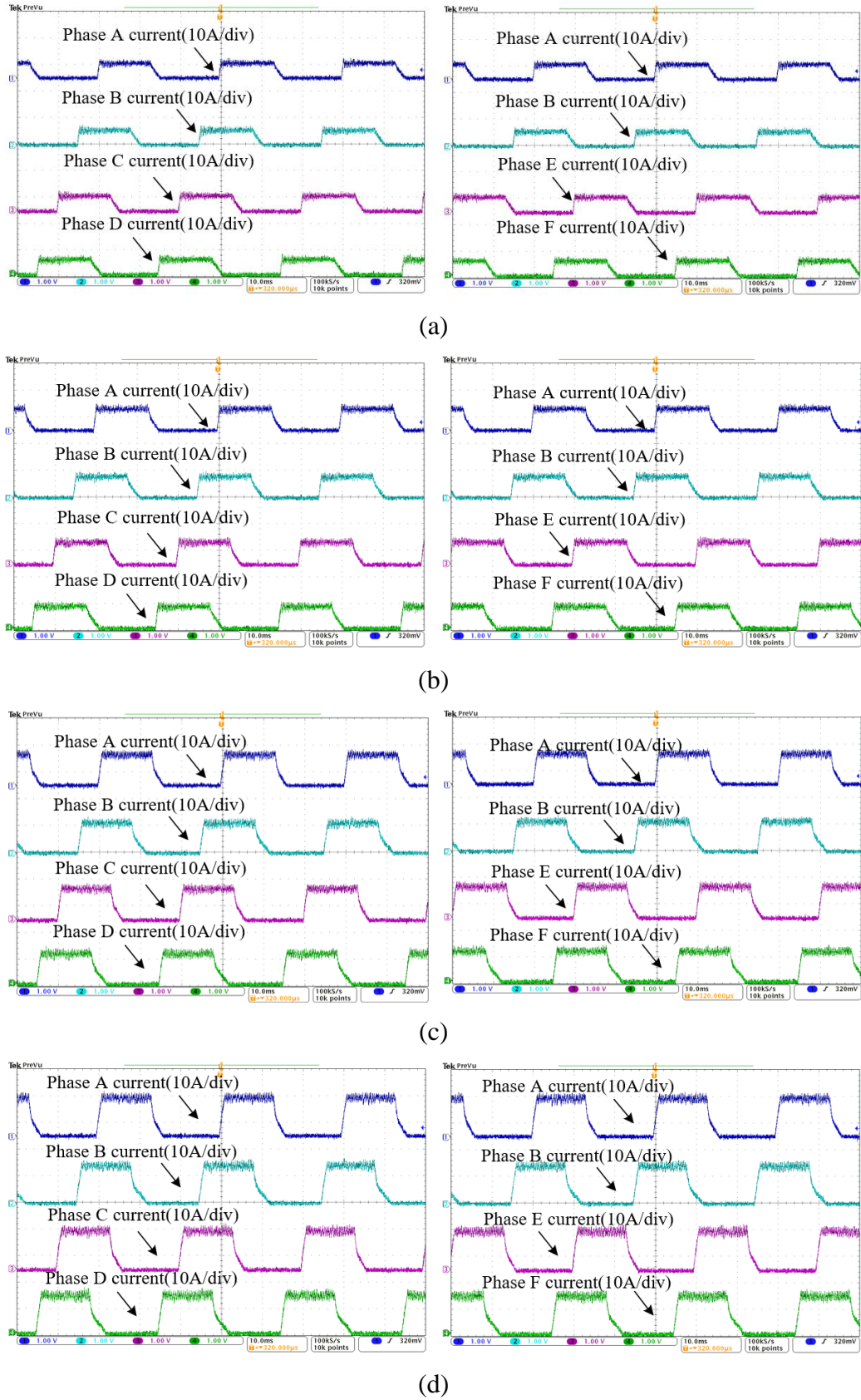


Figure 7.7 Current waveforms with different loads at 200r/min under current control with the AHB converter: (a) 5.0Nm (b) 10.0Nm (c) 15.0Nm (d) 20.1Nm

Figure 7.8 shows the Output torque waveforms with different loads at 200r/min under current control with the AHB converter. The average torque outputs are 5.0Nm, 10.0Nm, 14.9Nm and 20.1Nm. TRR is 65.3%, 42.0%, 35.2% and 29.7% respectively.

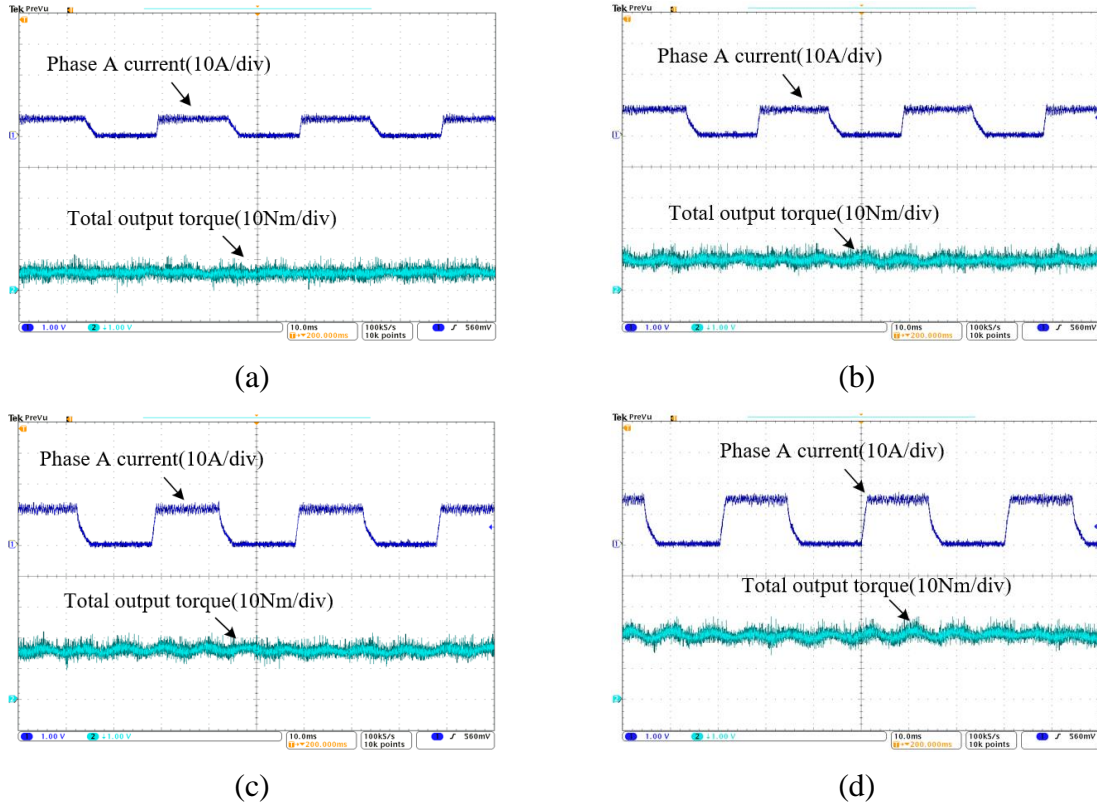
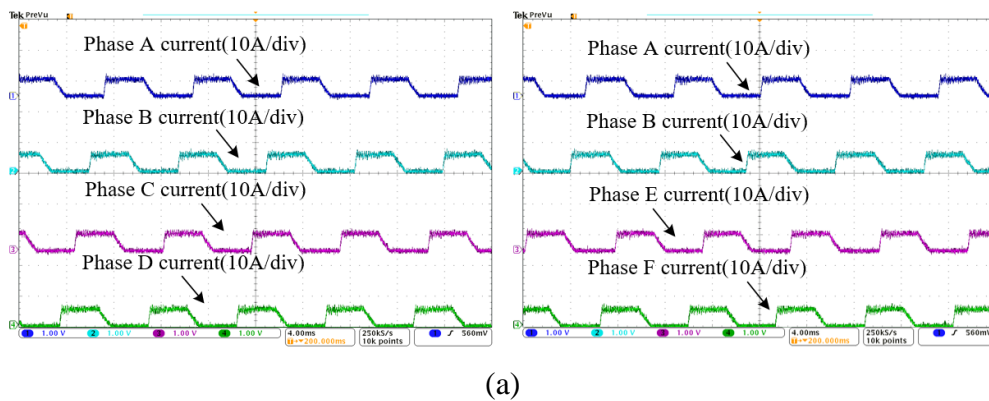


Figure 7.8 Output torque waveforms with different loads at 200r/min under current control with the AHB converter: (a) 5.0Nm (b) 10.0Nm (c) 14.9Nm (d) 20.1Nm

7.2.1.2 800r/min

Figure 7.9 shows current waveforms with different loads at 200r/min. Phase current reference value to produce average torque of 5.0Nm, 10.0Nm, 15.0Nm and 20.0Nm are 5.5A, 9.1A, 12.2A and 15.7A respectively in this series of tests, and conduction widths are set at 160°.



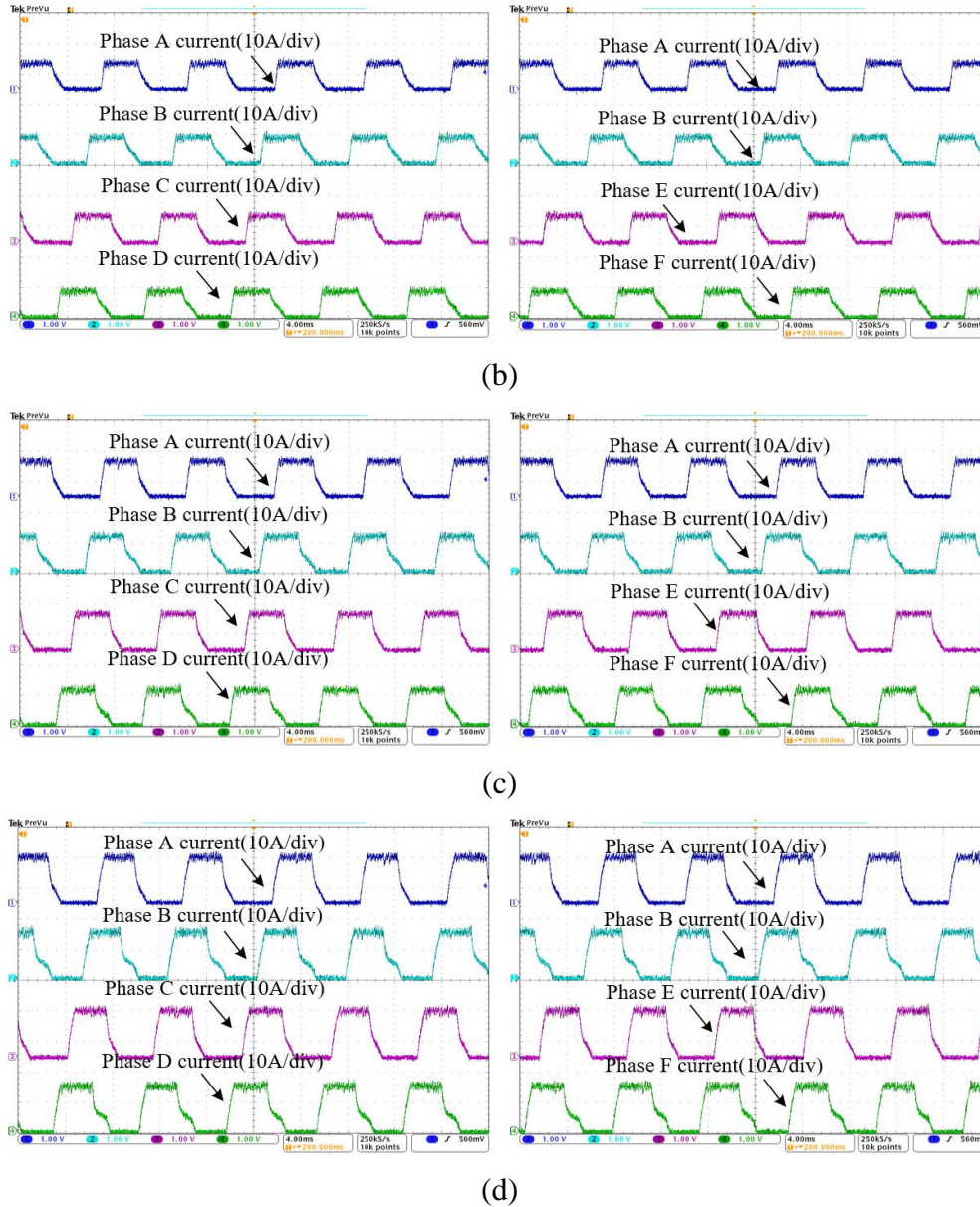


Figure 7.9 Current waveforms with different loads at 800r/min under current control with the AHB converter: (a) 5.0Nm (b) 10.0Nm (c) 15.0Nm (d) 20.0Nm

Figure 7.10 shows the Output torque waveforms with different loads at 800r/min under current control with the AHB converter. The average torque outputs are 5.1Nm, 10.0Nm, 14.9Nm and 20.1Nm. TRR is 59.0%, 47.1%, 33.0% and 29.1% respectively. It is obvious that there is low frequency ripple existing in the torque waveforms. With the FFT spectrum analysis, the frequency is obtained which is about 50Hz. The low frequency ripple is caused by torsional vibration of the shaft along its axis of rotation. The mechanical part of the drive system is simplified to be a two-disc torsional system (discussed in Appendix C). This has calculated to have a torsional vibration frequency of 58Hz. When torque changes quickly

(high torque ripple), the torque transducer is damped by the rotor inertia of the motor, the load machine and couplings, afterward the torsional vibration is active.

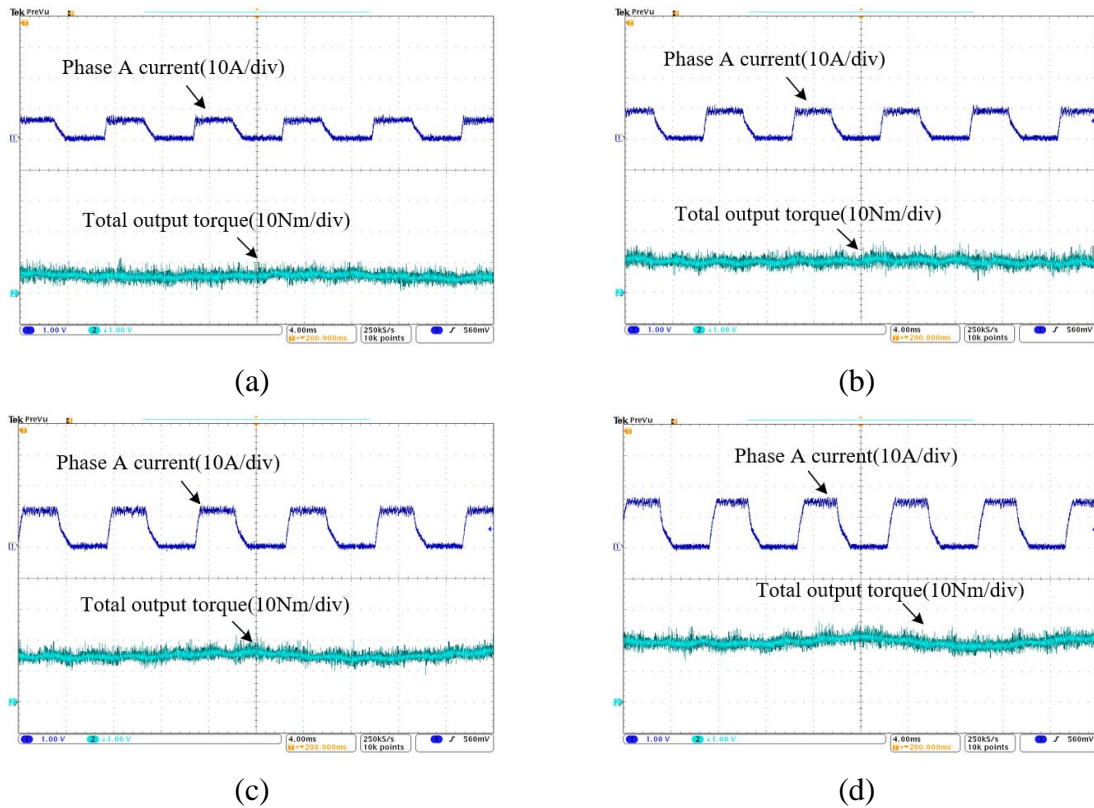
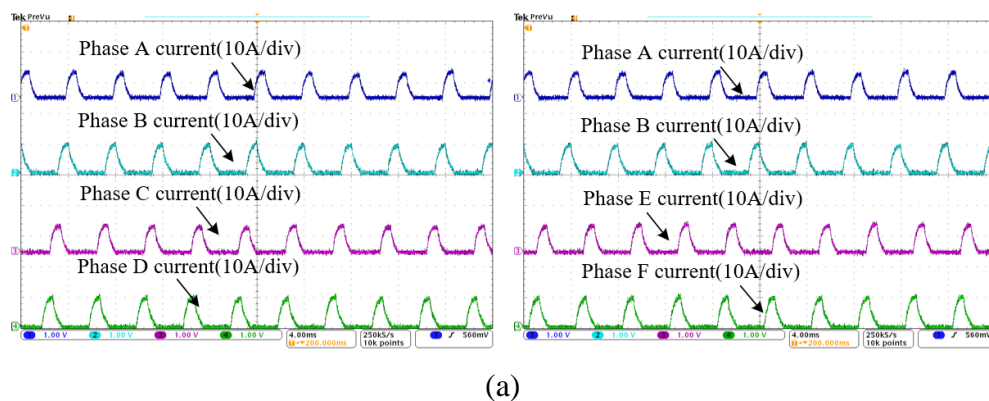


Figure 7.10 Output torque waveforms with different loads at 800r/min under current control with the AHB converter: (a) 5.1Nm (b) 10.0Nm (c) 14.9Nm (d) 20.1Nm

**7.2.1.3 1500r/min**

Figure 7.11 shows current waveforms with different loads at 1500r/min under voltage control with the AHB converter. Advance angle is set at 10°, and conduction width to produce average torque outputs of 6.0Nm and 10.0Nm in this series of tests are 71° and 90°.



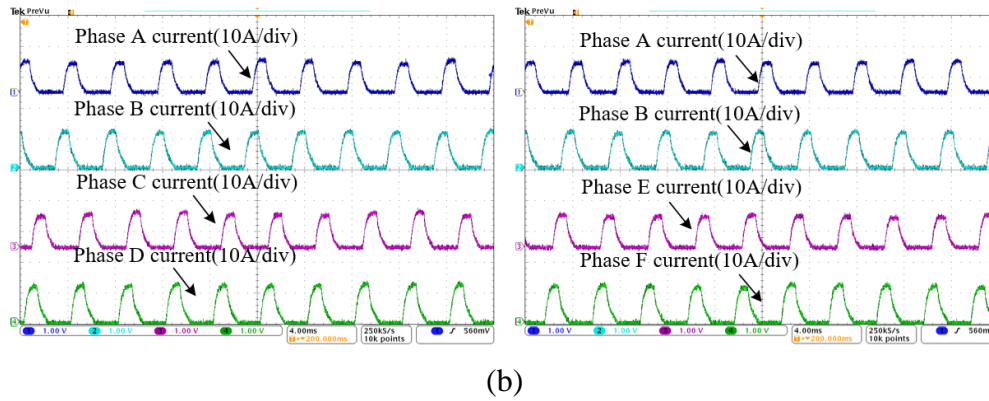


Figure 7.11 Current waveforms with different loads at 1500r/min under voltage control with the AHB converter: (a) 6.0Nm (b) 10.0Nm

Figure 7.12 shows the Output torque waveforms with different loads at 1500r/min under voltage control with the AHB converter. The average torque outputs are 6.2Nm and 10.1Nm. TRR is 76.9%, and 47.7% respectively.

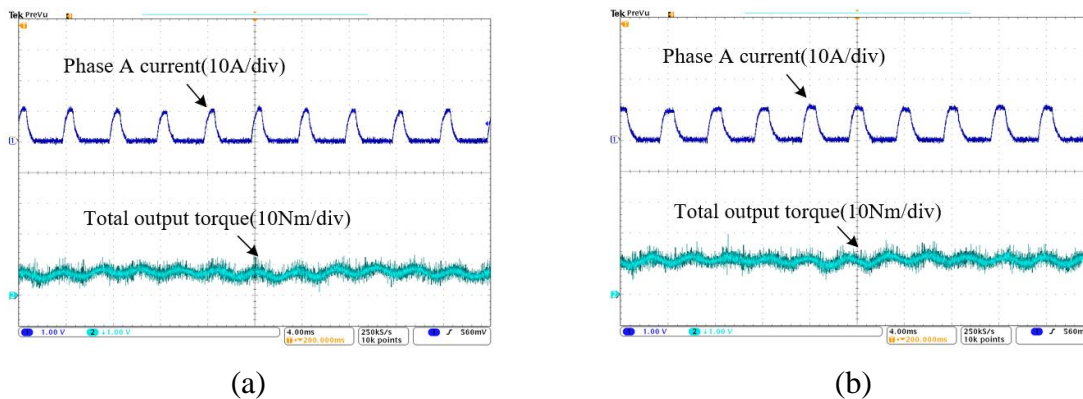


Figure 7.12 Output torque waveforms with different loads at 1500r/min under voltage control with the AHB converter: (a) 6.2Nm (b) 10.1Nm

In conclusion, there is a large torque ripple existing in this six-phase SRM prototype by traditional control methods throughout the whole speed range. In the following section, The DTC method tests are conducted with the same AHB converter to validate the torque ripple minimization effects.

## 7.2.2 DTC method

### 7.2.2.1 200r/min

Figure 7.13 shows current waveforms with different loads at 200r/min under DTC method with the AHB converter. Stator flux references are set at 0.29Wb, 0.32Wb, 0.34Wb and 0.38Wb to obtain 5Nm, 10Nm, 15Nm and 20Nm average output torque respectively.

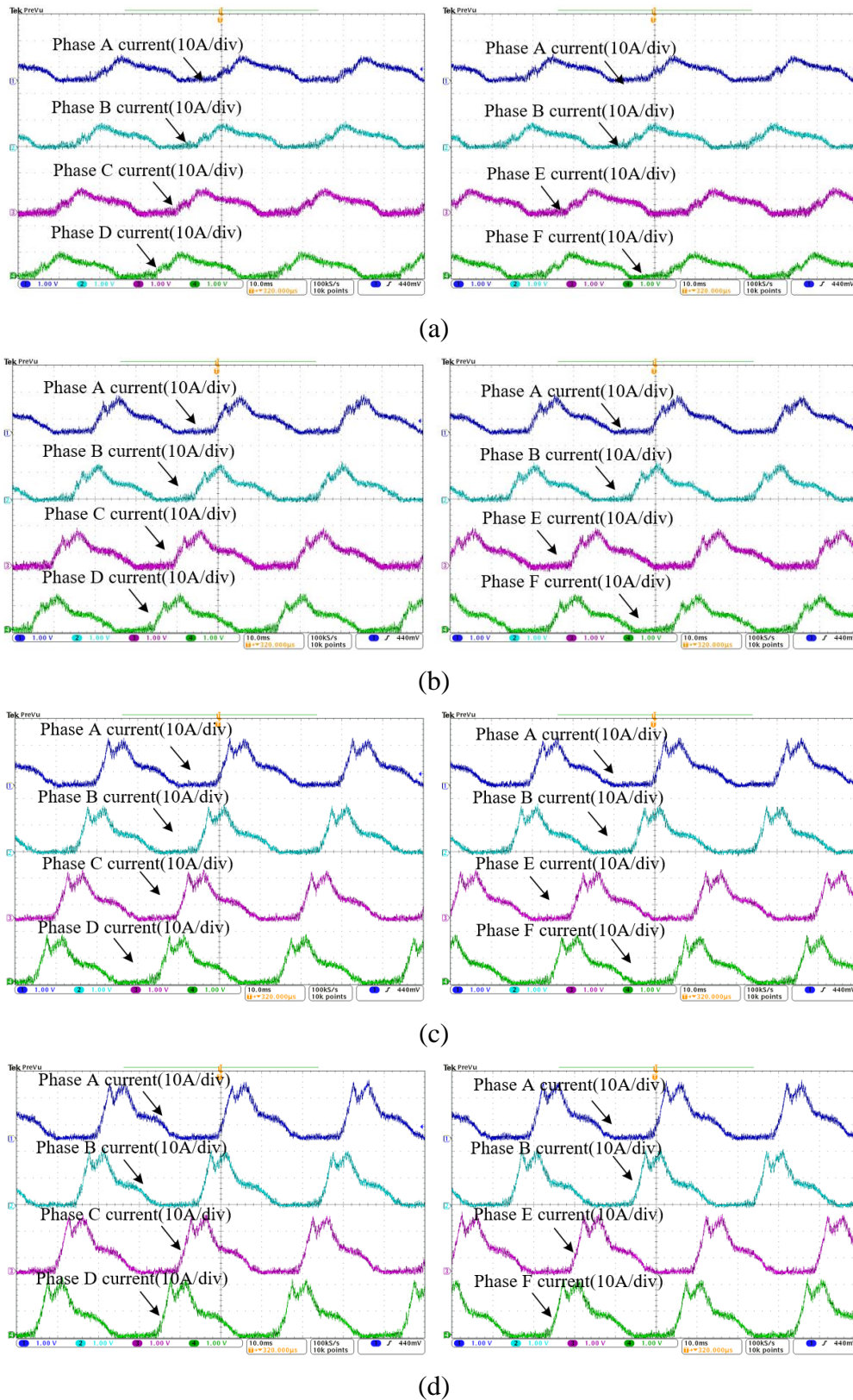


Figure 7.13 Current waveforms with different loads at 200r/min under DTC method with the AHB converter: (a) 5.0Nm (b) 10.0Nm (c) 15.0Nm (d) 20.0Nm

Different to current profiles of the CCC method, current profiles with the DTC method are very irregular and have a wider conduction width, which are comparable with simulation results in Figure 4.9(b) in Chapter 4.

Output torque waveforms are shown in Figure 7.14. The average torque outputs are 5.1Nm, 10.2Nm, 15.0Nm and 20.1Nm. TRR is 44.3%, 24.5%, 18.6% and 12.1%.

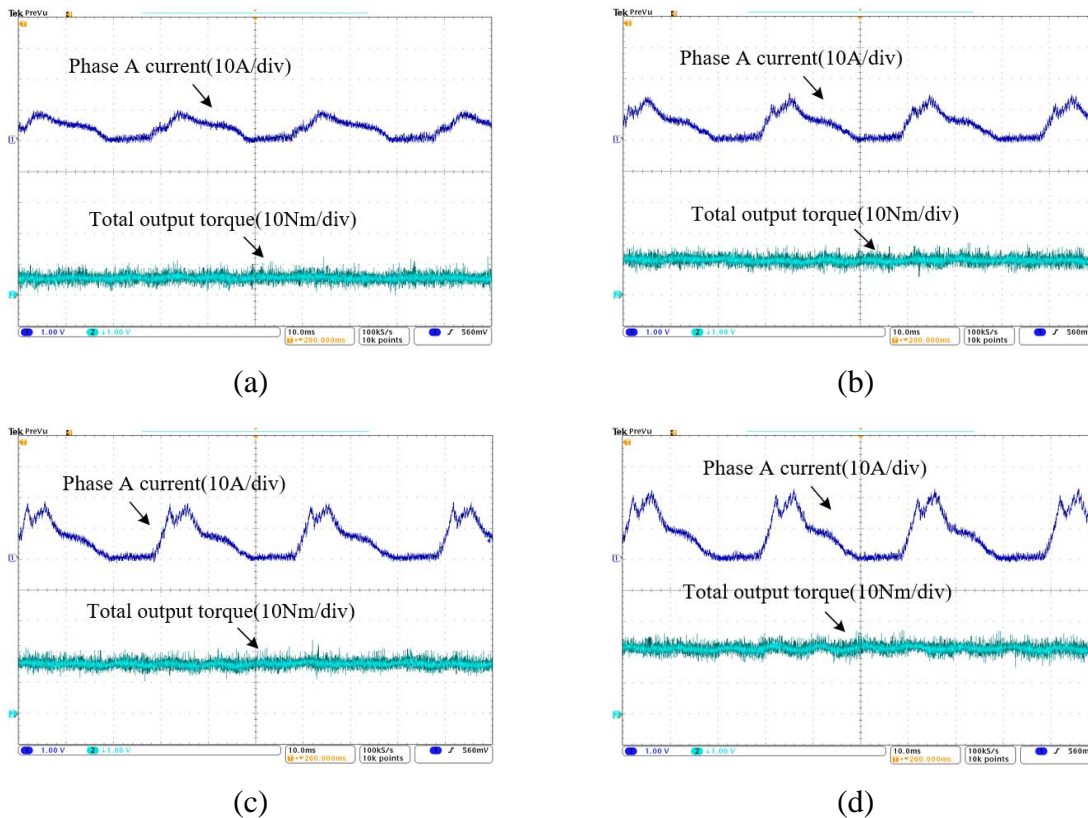
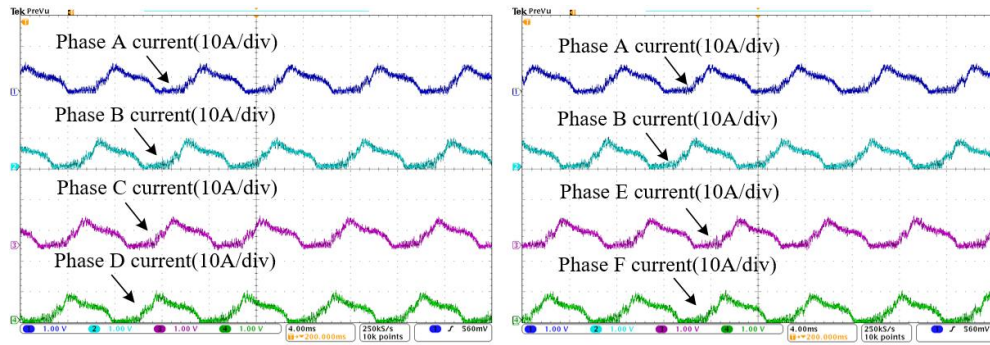


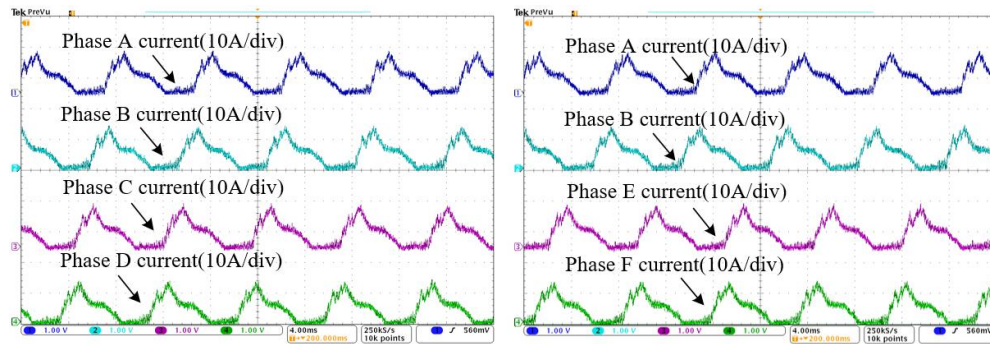
Figure 7.14 Output torque waveforms with different loads at 200r/min under DTC method with the AHB converter: (a) 5.1Nm (b) 10.2Nm (c) 15.0Nm (d) 20.1Nm

### 7.2.2.2 800r/min

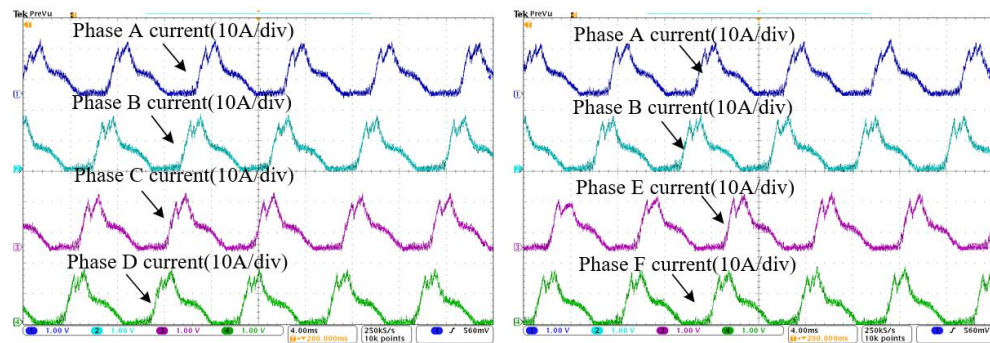
Figure 7.15 shows current waveforms with different loads at 800r/min under DTC method with the AHB converter. Stator flux references are set at 0.29Wb, 0.32Wb, 0.34Wb and 0.38Wb to obtain 5Nm, 10Nm, 15Nm and 20Nm average output torque respectively.



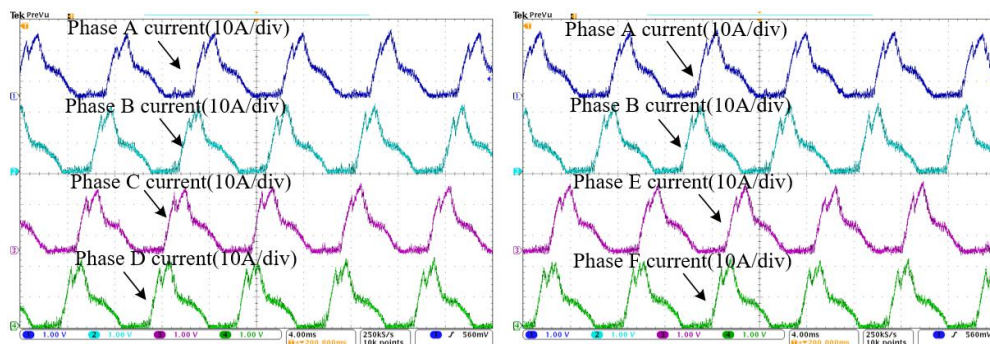
(a)



(b)



(c)



(d)

Figure 7.15 Current waveforms with different loads at 800r/min under DTC method with the AHB converter: (a) 5.0Nm (b) 10.0Nm (c) 15.0Nm (d) 20.0Nm

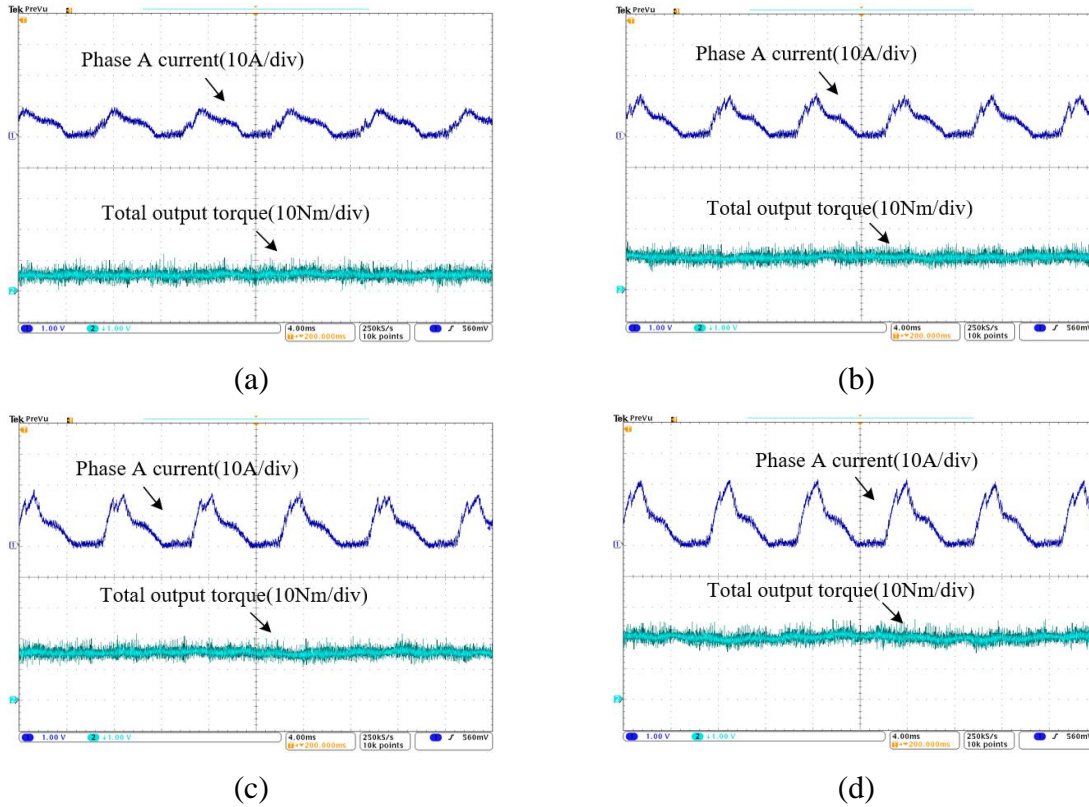
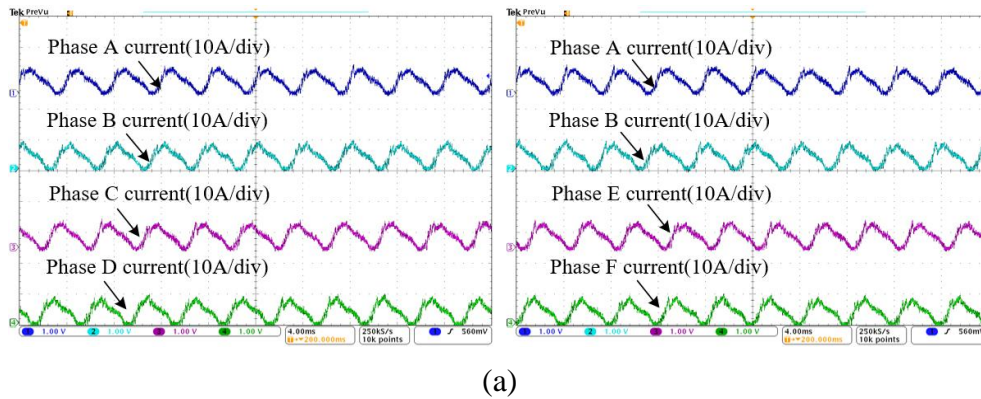


Figure 7.16 Output torque waveforms with different loads at 800r/min under DTC method with the AHB converter: (a) 5.0Nm (b) 10.0Nm (c) 15.1Nm (d) 20.2Nm

Output torque waveforms are presented in Figure 7.16. The average torque outputs are 5.0Nm, 10.0Nm, 15.1Nm and 20.2Nm. TRR is 44.5%, 23.5%, 17.8% and 17.2%.

### 7.2.2.3 1500r/min

Figure 7.17 shows current waveforms with different loads at 1500r/min under DTC method with the AHB converter. Stator flux references are set at 0.25Wb and 0.28Wb to obtain 6Nm and 10Nm average output torque.



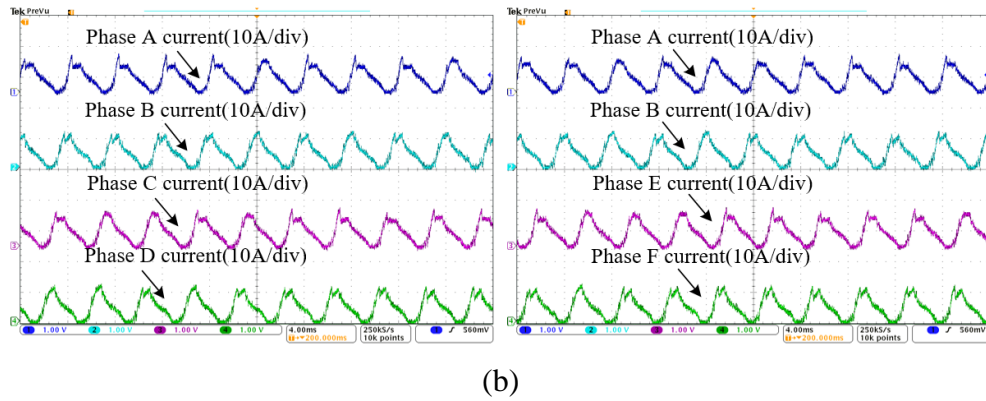


Figure 7.17 Current waveforms with different loads at 1500r/min under DTC method with the AHB converter: (a) 6.0Nm (b) 10.0Nm

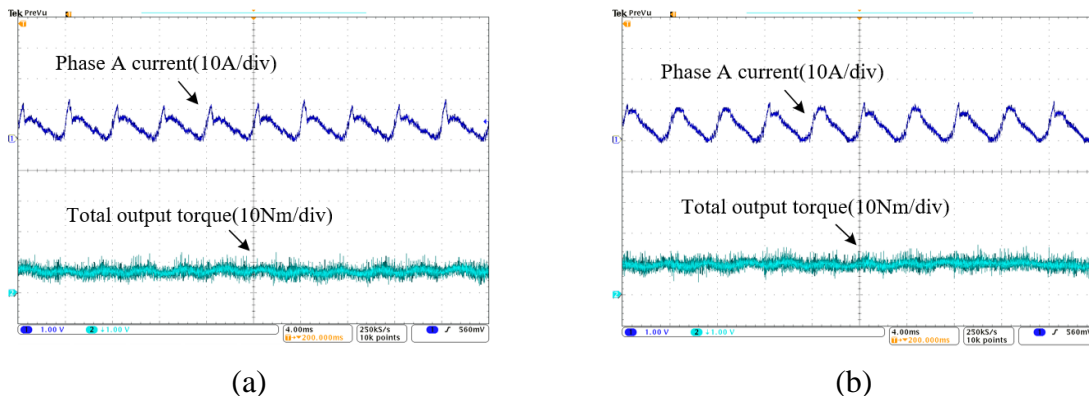


Figure 7.18 Output torque waveforms with different loads at 1500r/min under DTC method with the AHB converter: (a) 6.2Nm (b) 10.0Nm

Figure 7.18 shows the output torque waveforms with different loads at 1500r/min under DTC method with the AHB converter. The average torque outputs are 6.2Nm and 10.0Nm. TRR is 45.9% and 28.6%.

Torque ripple comparison between simulation and experimental test is shown in Table 7.3. It is obvious that both simulation and test results show that the proposed DTC method can significantly reduce torque ripple for six-phase SRMs with the AHB converter. In Table 7.3, the TRR of traditional methods in test is lower than simulation result, whilst the simulated TRR of the DTC method is lower than test. There are three reasons behind differences between simulated and measured torques: 1) in real-time system, measurement error of current transducer and analogue to digital conversion error in DSP exists. Moreover, the phase flux linkage and phase torque has errors with actual values, as they are estimated in DSP with measurement current and rotor position information, which affects the effect of the DTC method; 2) the simulation is based on the single phase characteristics of the six-phase SRM, therefore the mutual inductance is ignored. Besides, the 2D FEA prediction for single-phase

characteristics does not include end effects; 3) the torque transducer has a limited bandwidth and torque measurements are damped by inertia of the rotor. Therefore the higher frequency elements of electromagnetic torque are not properly captured by the measurement system.

Table 7.3 Torque ripple comparison between simulation and experimental test of the AHB converter

N=200r/min $T_{av}=20\text{Nm}$	Traditional methods (Simulation)	DTC method (Simulation)	Traditional methods (Test)	DTC method (Test)
TRR	33.5%	5.1%	29.7%	12.1%
N=800r/min $T_{av}=15\text{Nm}$	Traditional methods (Simulation)	DTC method (Simulation)	Traditional methods (Test)	DTC method (Test)
TRR	40.2%	15.4%	33.0%	17.8%
N=1500r/min $T_{av}=10\text{Nm}$	Traditional methods (Simulation)	DTC method (Simulation)	Traditional methods (Test)	DTC method (Test)
TRR	58.9%	25.1%	47.7%	28.6%

### 7.3 Experimental validation of traditional control methods and the proposed DTC method with the proposed converters

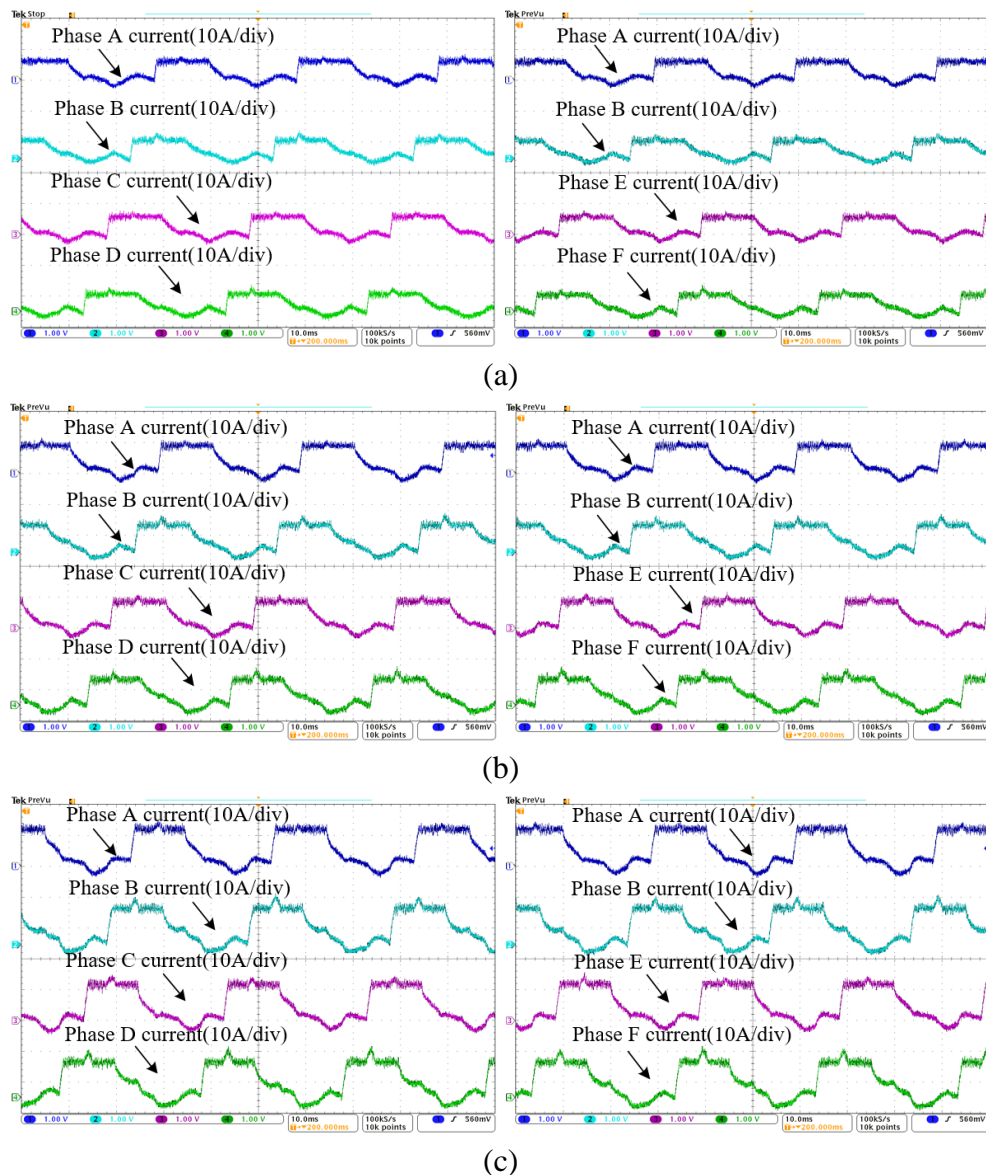
In order to compare the performance of the proposed two converters with the AHB converter, the following tests are designed. Firstly, the circle converter is tested with the traditional CCC and APC methods. In the CCC method, two typical conduction widths ( $120^\circ$  and  $140^\circ$ ) are chosen to validate the effects of conduction width on performance of the circle converter. The circle converter with extra diodes is subsequently tested with traditional methods to validate improved current by adding extra diodes. In addition, the DTC method is applied to the circle converter and circle converter with extra diodes to further reduce the torque ripple. In this section, the 100V 48A DC power supply is employed for 200r/min and 800r/min tests to draw enough current. A 200V 30A DC power supply is employed for 1500r/min test to get enough DC link voltage for high speed operation.

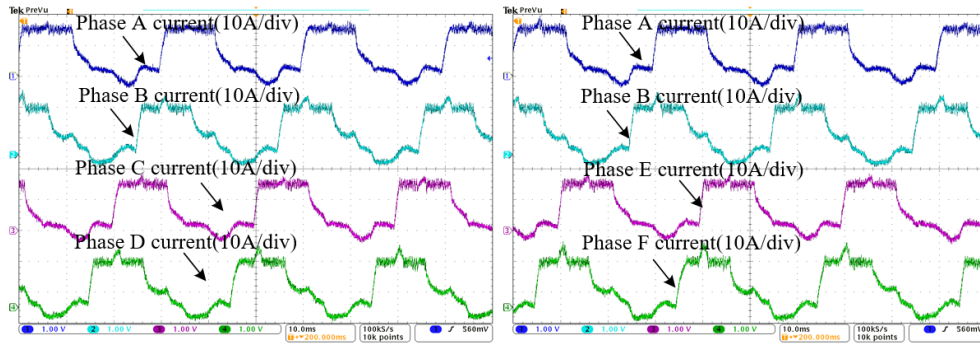
### 7.3.1 Circle converter with traditional control methods

The first series of tests are conducted with the circle converter by the traditional methods. Test results are shown in Figure 7.19 to Figure 7.28.

#### 7.3.1.1 200r/min with 140° conduction width

Figure 7.19 shows current waveforms with different loads at 200r/min by 140° current control with the circle converter. Phase current reference values to produce average torque of 5.0Nm, 10.0Nm, 15.0 Nm and 20.0Nm are 6.0A, 9.5A, 12.5A and 15.8A respectively. Same as simulation results, all the six phase currents have sharp increases around 60° of each phase. All the current waveforms have unexpected current after reasonable conduction area, which is same as the simulation results in Figure 3.11(b).

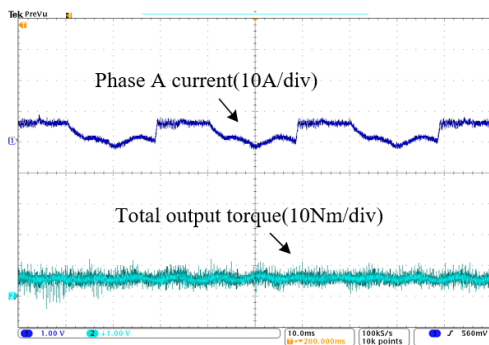




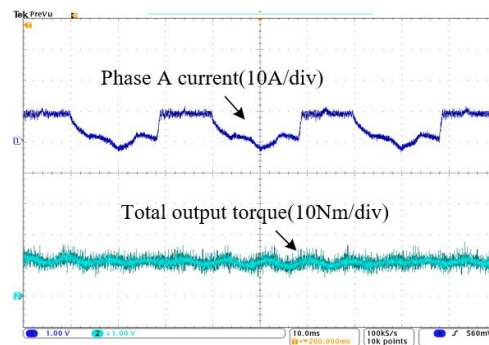
(d)

Figure 7.19 Current waveforms with different loads at 200r/min by 140° current control with the circle converter: (a) 5.0Nm (b) 10.0Nm (c) 15.0Nm (d) 20.0Nm

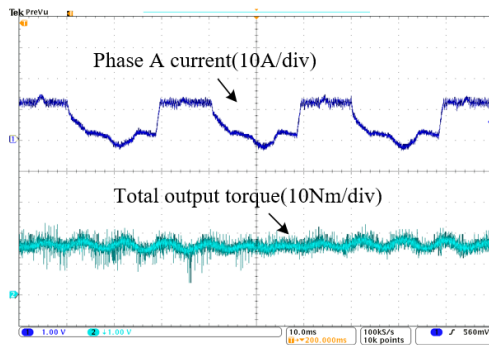
Figure 7.20 shows output torque waveforms with different loads at 200r/min by 140° current control with the circle converter. The obvious current distortions in Figure 7.19 cause more negative instantaneous torque, which leads to serious torque ripple in this series of tests as shown in Figure 7.20.



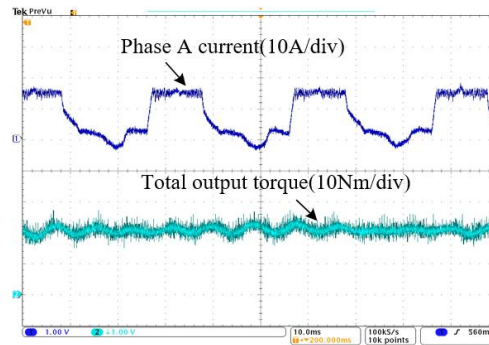
(a)



(b)



(c)



(d)

Figure 7.20 Output torque waveforms with different loads at 200r/min by 140° current control with the circle converter: (a) 5.0Nm (b) 10.0Nm (c) 15.0Nm (d) 20.0Nm

## 7.3.1.2 800r/min with 140° conduction width

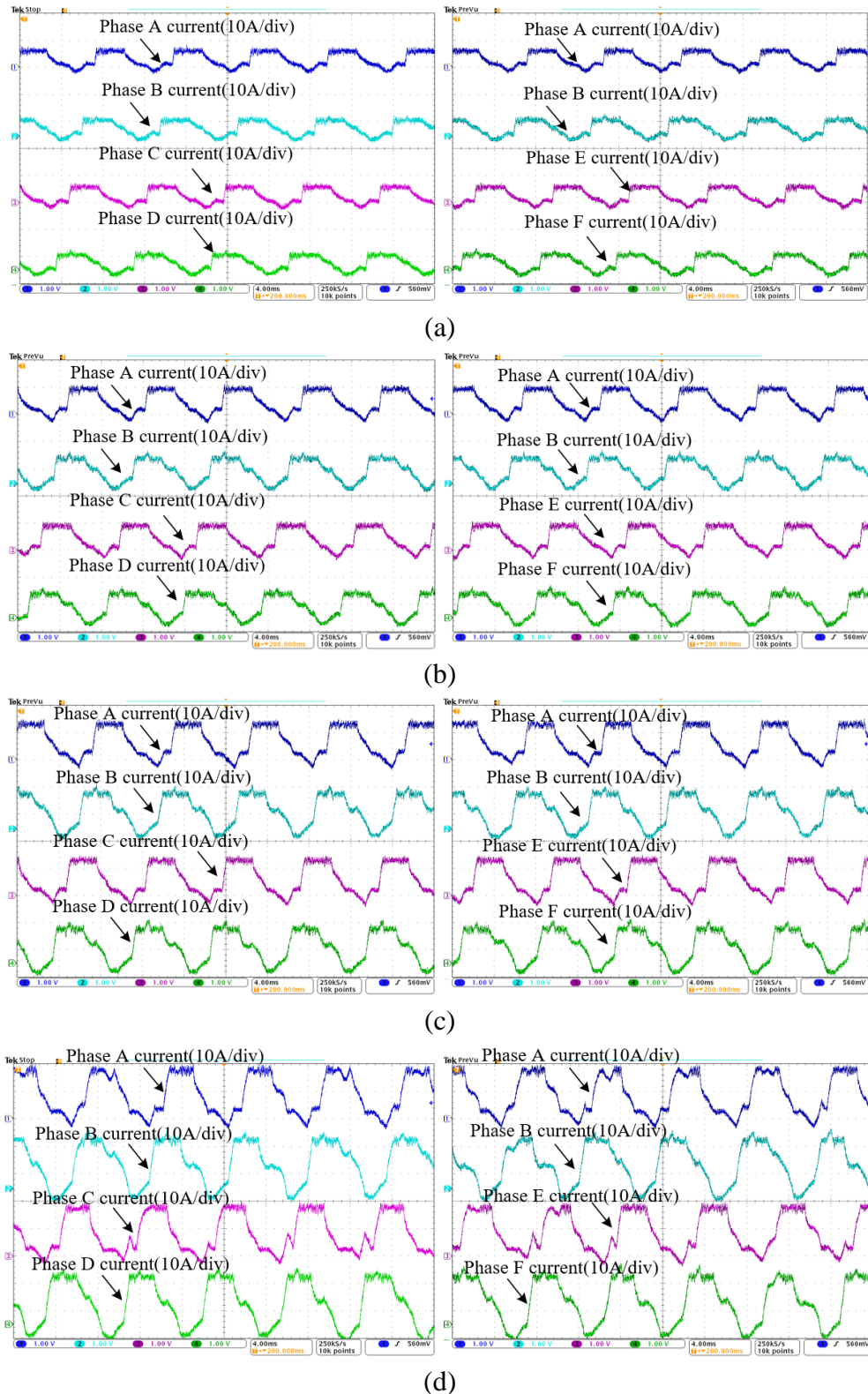


Figure 7.21 Current waveforms with different loads at 800r/min by 140° current control with the circle converter: (a) 5.0Nm (b) 10.0Nm (c) 15.0Nm (d) 20.0Nm

Figure 7.21 shows current waveforms with different loads at 800r/min with  $140^\circ$  current control with the circle converter. Phase current reference value to produce average torque of 5.0Nm, 10.0Nm, 15.0 Nm and 20.0Nm are 6.0A, 9.5A, 12.3A and 15.6A respectively, and conduction widths are set at  $140^\circ$ . As at 200r/min, obvious current distortions appear at 800r/min, and they are even worse than 200r/min.

Figure 7.22 shows output torque waveforms with different loads at 800r/min with  $140^\circ$  current control with the circle converter. Due to obvious current distortion, torque ripple in this set of tests are very large, especially with 20Nm output torque.

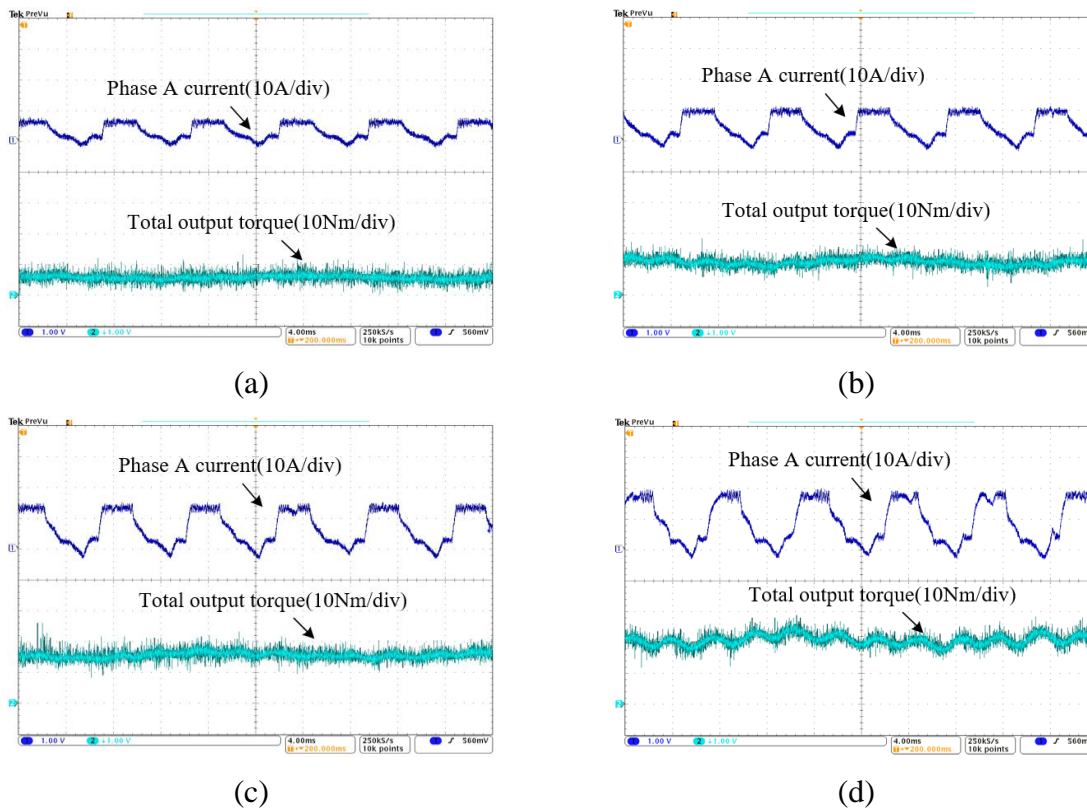


Figure 7.22 Output torque waveforms with different loads at 800r/min with  $140^\circ$  current control with the circle converter: (a) 5.0Nm (b) 10.0Nm (c) 15.0Nm (d) 20.0Nm

### 7.3.1.1 200r/min with $120^\circ$ conduction width

To avoid the sharp current increase around  $60^\circ$ , the conduction width of the traditional CCC method has to be limited at  $120^\circ$ , which has been analysed in Figure 3.14. Figure 7.23 shows current waveforms with different loads at 200r/min with  $120^\circ$  current control with the circle converter. It is very clear that all the sharp current increases around  $60^\circ$  are eliminated. Phase current reference values to produce average torque of 5.0Nm, 10.0Nm, 15.0 Nm and 20.0Nm

are 7.0A, 9.8A, 12.8A and 15.9A respectively in this set of tests, and conduction width is set at  $120^\circ$ . However, because of the special topology of circle converter, the negative currents after reasonable conduction area are not eliminable, which has been discussed in Figure 3.15.

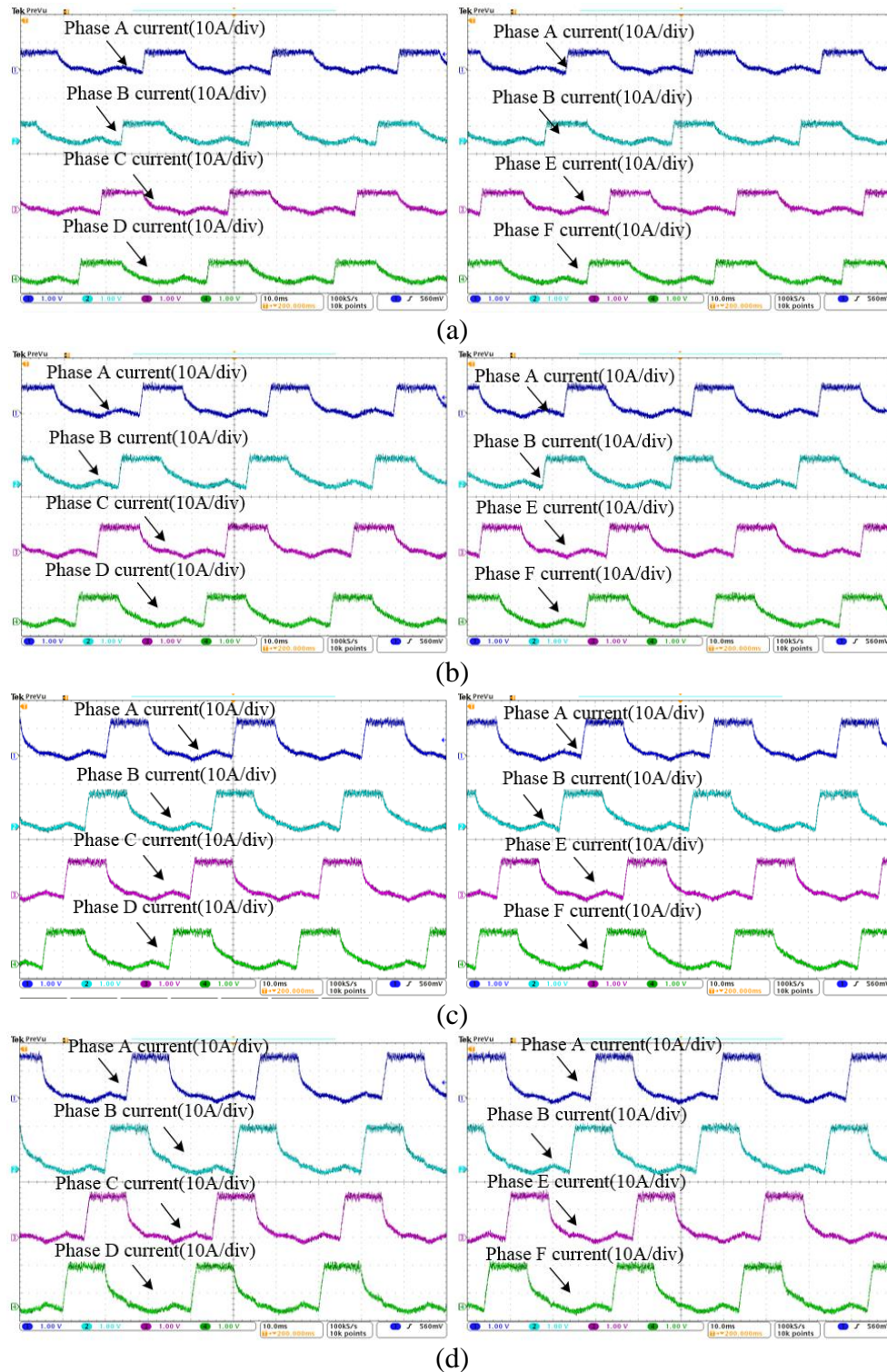


Figure 7.23 Current waveforms with different loads at 200r/min with  $120^\circ$  current control with the circle converter: (a) 5.0Nm (b) 10.0Nm (c) 15.0Nm (d) 20.0Nm

Figure 7.24 shows output torque waveforms with different loads at 200r/min with 120° current control with the circle converter. TRR is 76.5%, 45.0%, 36.7% and 42.1%. Compared with the AHB converter controlled by CCC method, circle converter has a narrower conduction width which leads to larger torque ripples.

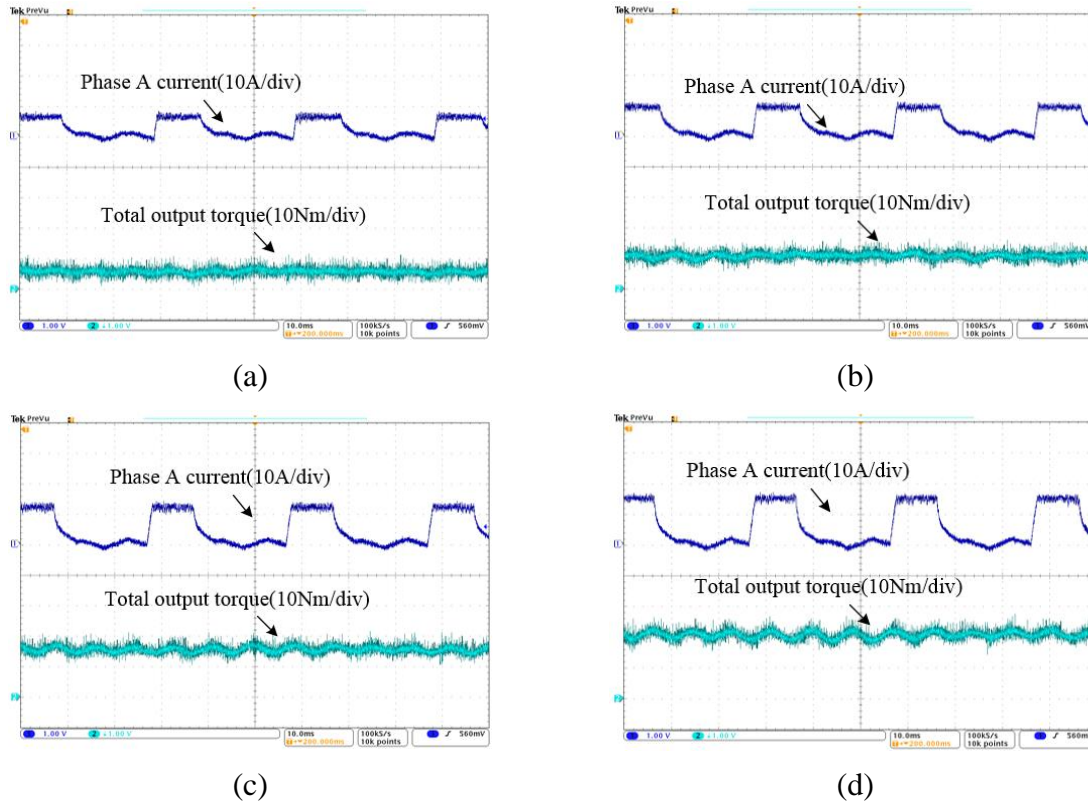
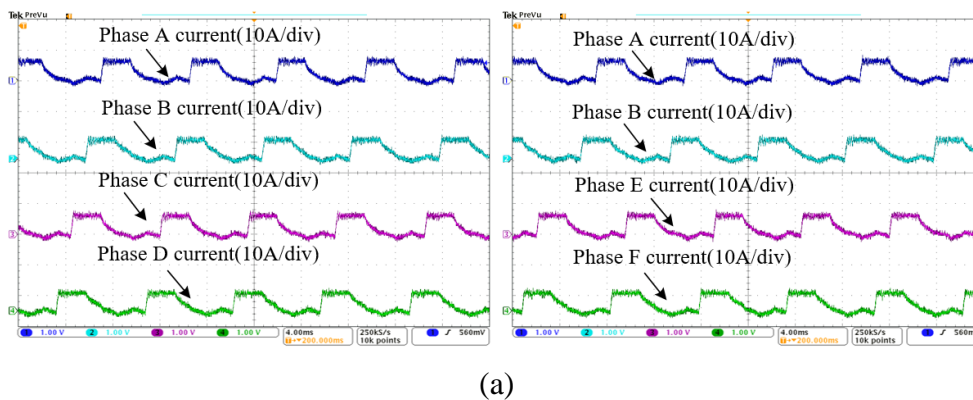


Figure 7.24 Output torque waveforms with different loads at 200r/min with 120° current control with the circle converter: (a) 5.0Nm (b) 10.0Nm (c) 15.0Nm (d) 20.0Nm

**7.3.1.2 800r/min with 120° conduction width**



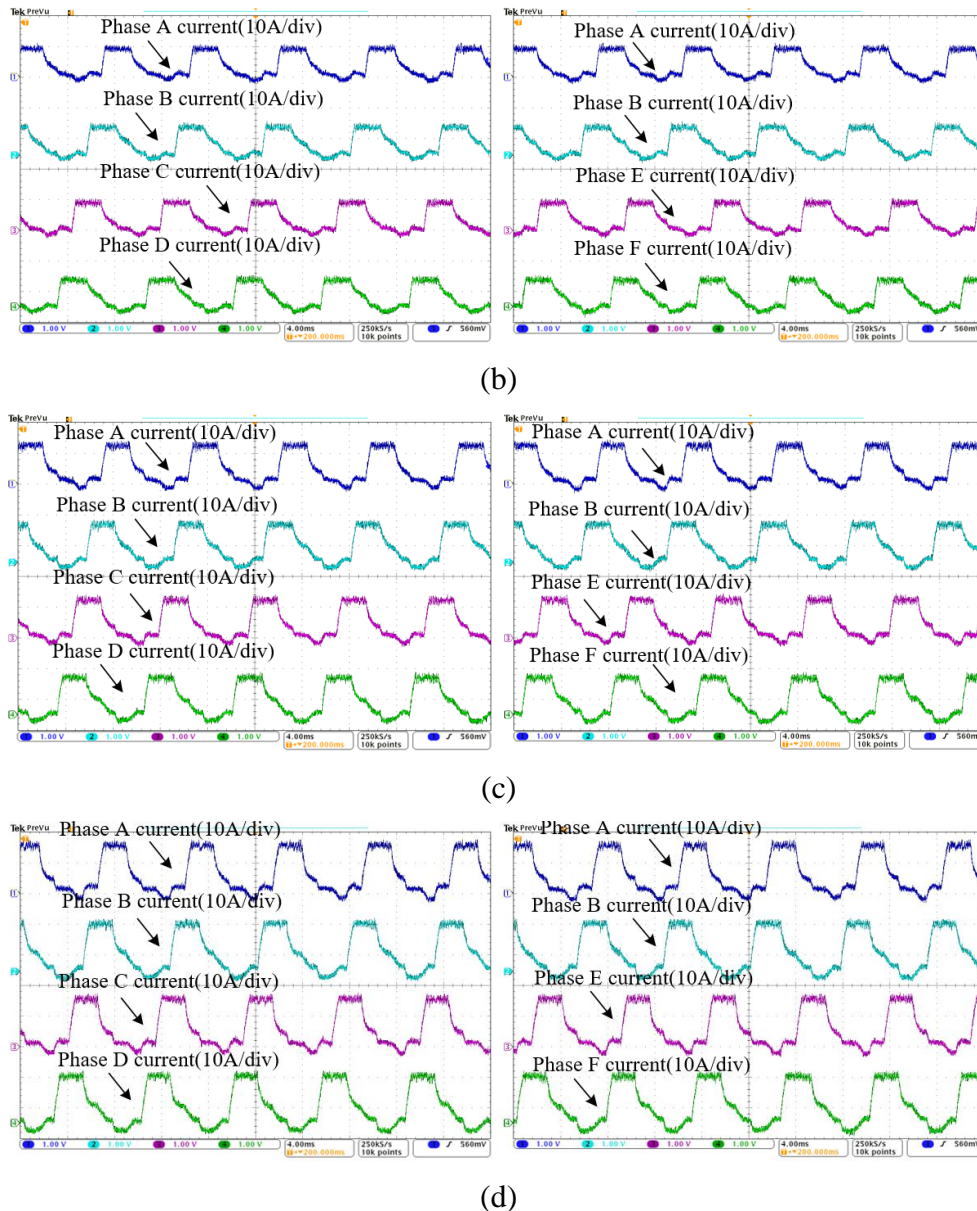


Figure 7.25 Current waveforms with different loads at 800r/min with  $120^\circ$  current control with the circle converter: (a) 5.0Nm (b) 10.0Nm (c) 15.0Nm (d) 20.0Nm

Figure 7.25 shows current waveforms with different loads at 800r/min with  $120^\circ$  current control with the circle converter. Phase current reference value to produce average torque of 5.0Nm, 10.0Nm, 15.0 Nm and 20.0Nm are 7.0A, 9.7A, 12.6A and 15.7A respectively in this series of tests, and conduction widths are set at  $120^\circ$ . As at 200r/min, the sharp current increases around  $60^\circ$  are eliminated.

Figure 7.26 shows output torque waveforms with different loads at 800r/min with  $120^\circ$  current control with the circle converter. TRR is 69.2%, 57.1%, 43.2% and 38.7%.

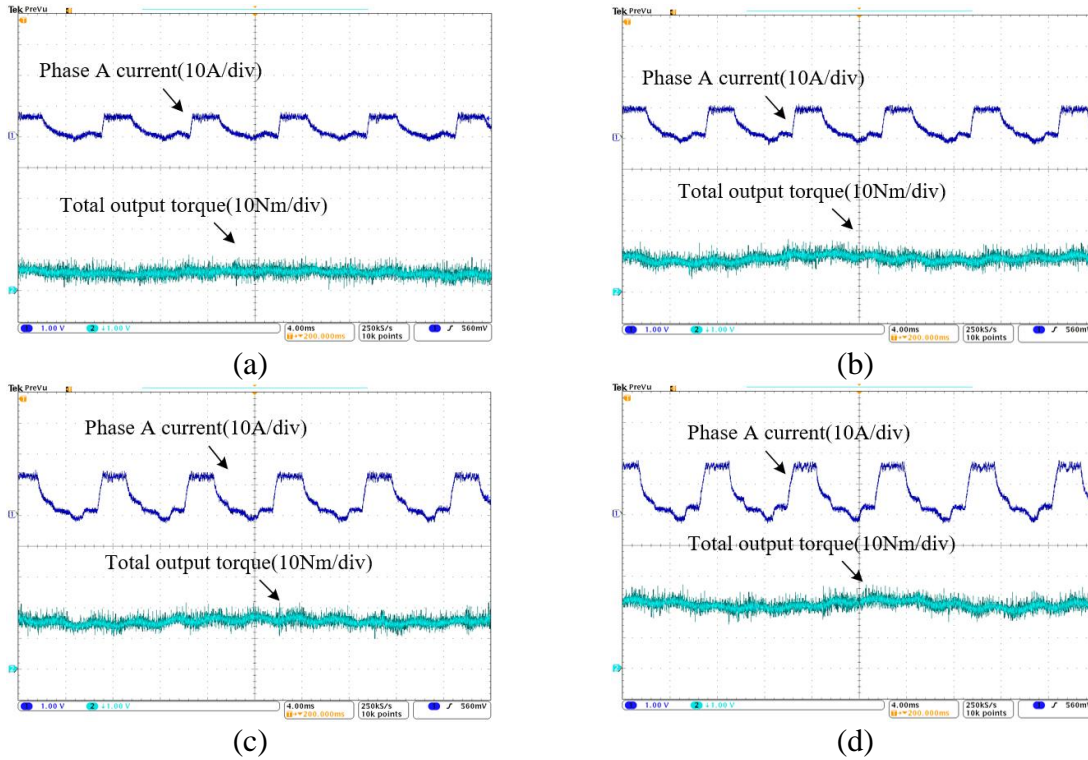


Figure 7.26 Output torque waveforms with different loads at 800r/min with 120° current control with the circle converter: (a) 5.0Nm (b) 9.8Nm (c) 15.1Nm (d) 20.0Nm

7.3.1.3 1500r/min

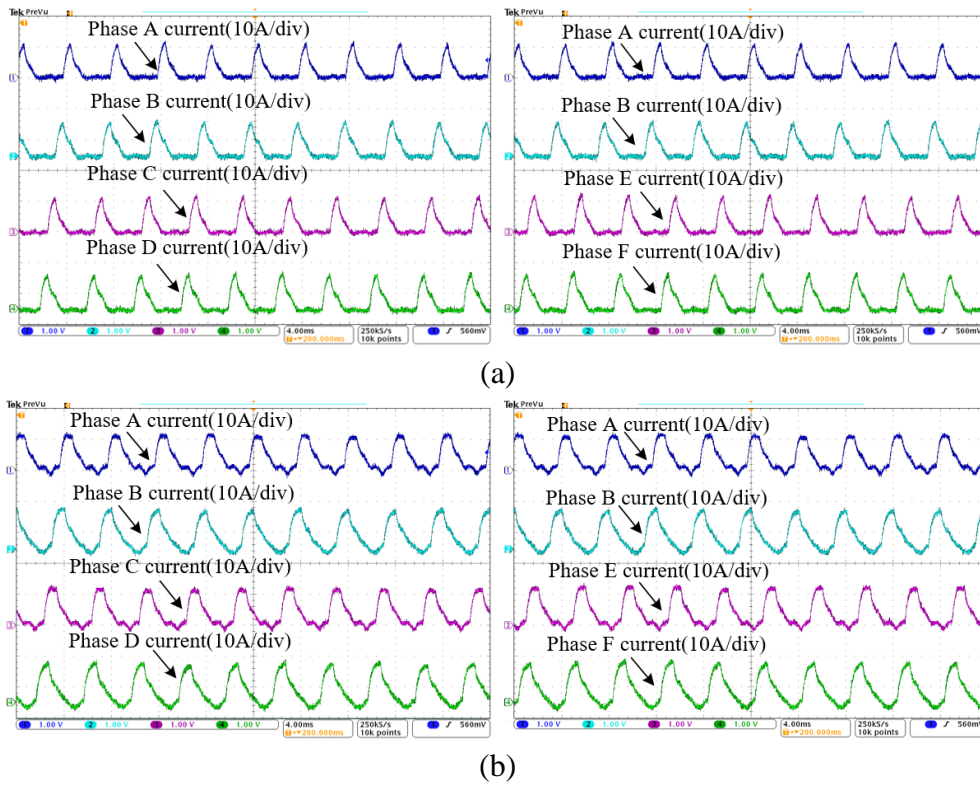


Figure 7.27 Current waveforms with different loads at 1500r/min under voltage control with the circle converter: (a) 6.0Nm (b) 10.0Nm

Figure 7.27 shows current waveforms with different loads at 1500r/min under voltage control with the AHB converter. Advance angles are set at  $10^\circ$ , and conduction width to produce average torque of 6.0Nm and 10.0Nm is  $73^\circ$  and  $95^\circ$ . Current waveforms are very similar to the AHB converter except some small negative currents after reasonable conduction area.

Figure 7.28 shows output torque waveforms with different loads at 1500r/min under voltage control with the circle converter. TRR is 72.5% and 36.9%, which are very close to the AHB converter under voltage control at 1500r/min.

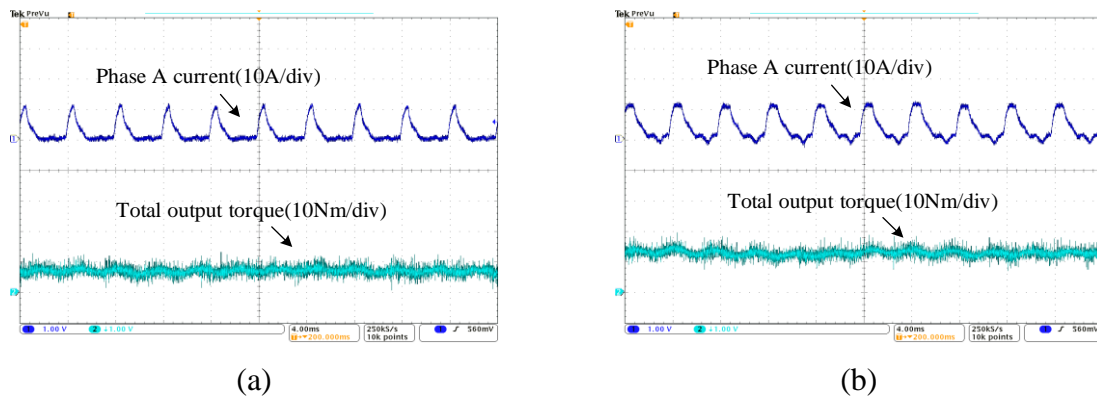


Figure 7.28 Output torque waveforms with different loads at 1500r/min under voltage control with the circle converter: (a) 6.0Nm (b) 10.0Nm

### 7.3.2 Circle converter with extra diodes by traditional control methods

In order to further eliminate the current distortions in circle converter, six power diodes are employed to limit the current direction of six phase windings. Phase current waveforms and output torque waveforms of the circle converter with extra diodes are obtained and presented in Figure 7.29 to Figure 7.34.

#### 7.3.2.1 200r/min

Figure 7.29 shows current waveforms with different loads at 200r/min under current control with the circle converter with extra diodes. Phase current reference value to produce average torque of 5.1Nm, 10.0Nm, 15.2 Nm and 20.0Nm are 6.3A, 9.3A, 12.3A, and 15.0A respectively, and conduction width is limited as  $120^\circ$ .

Profiting from the phase current direction limitation by extra diodes, current waveforms become more uniform, and negative currents are eliminated. Figure 7.30 presents output torque waveforms with different loads at 200r/min under current control with the circle

converter with extra diodes. Compared with the AHB converter controlled by the CCC method, the circle converter with extra diodes still has a narrower conduction width which leads to large torque ripple.

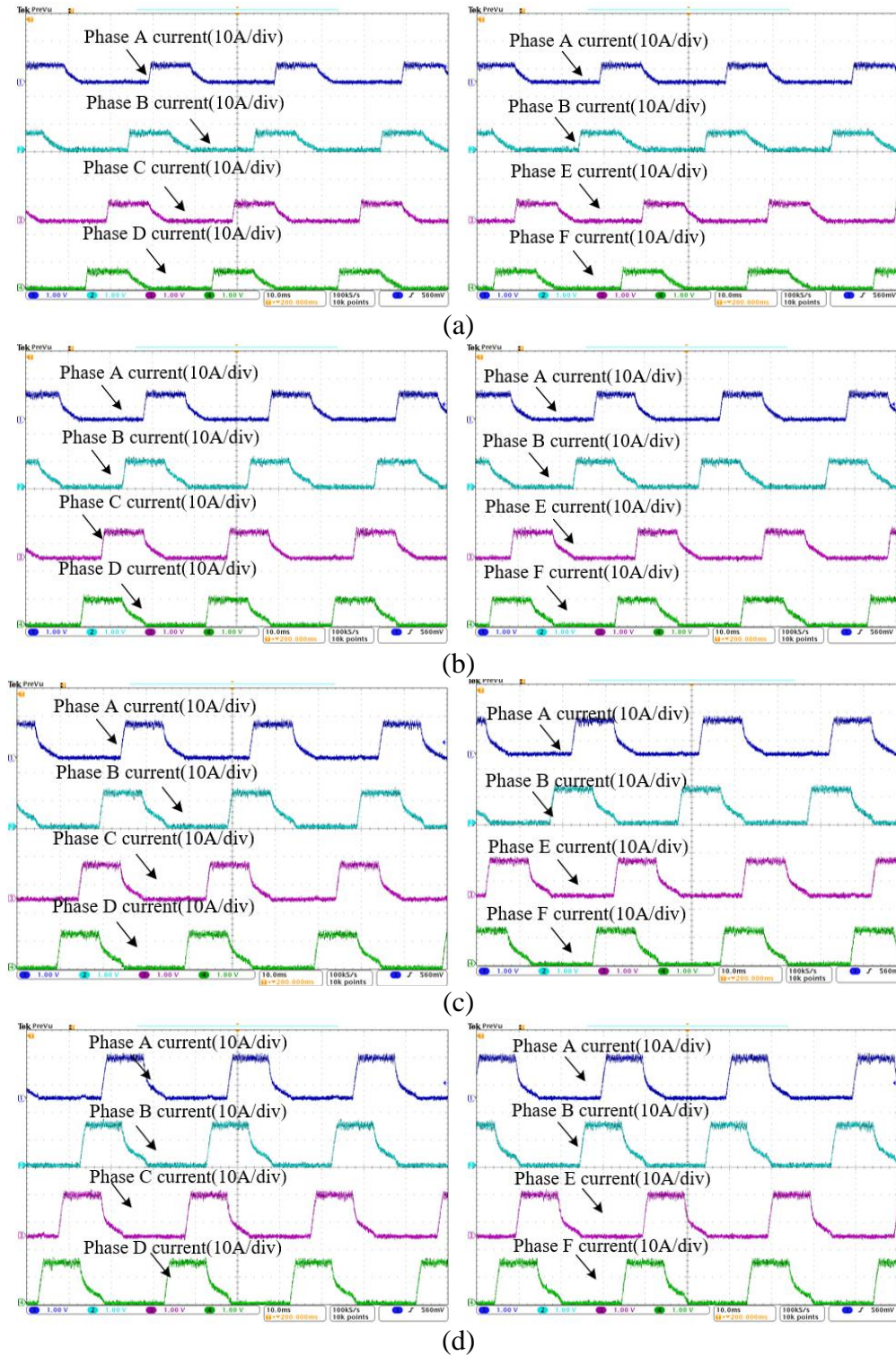


Figure 7.29 Current waveforms with different loads at 200r/min under current control with the circle converter with extra diodes: (a) 5.0Nm (b) 10.0Nm (c) 15.0Nm (d) 20.0Nm

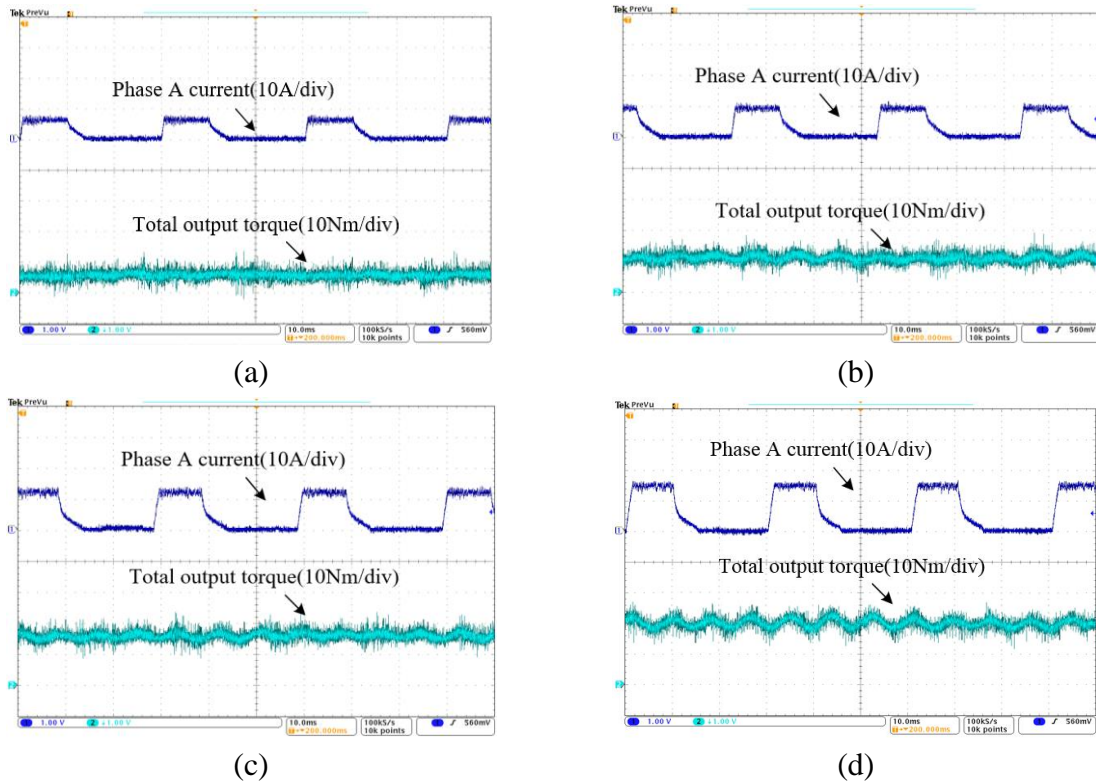
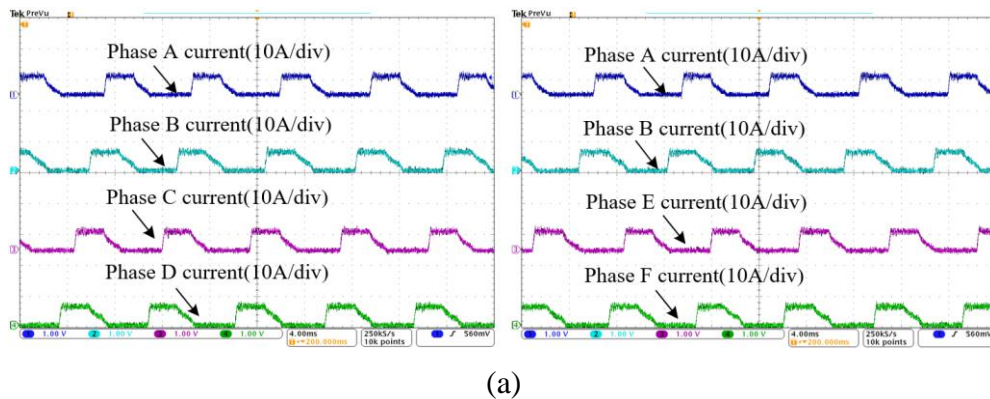


Figure 7.30 Output torque waveforms with different loads at 200r/min under current control with the circle converter with extra diodes: (a) 5.1Nm (b) 10.0Nm (c) 15.2Nm (d) 20.0Nm

### 7.3.2.2 800r/min

Figure 7.31 shows current waveforms with different loads at 800r/min under current control with the circle converter with extra diodes. Phase current reference values to produce average torque of 5.0Nm, 10.0Nm, 15.0 Nm and 20.0Nm are 6.2A, 9.2A, 12.5A, and 16A respectively, and conduction widths are set at 120° as well. Same as current waveforms at 200r/min, current waveforms at 800r/min also become more uniform, and negative currents are eliminated.



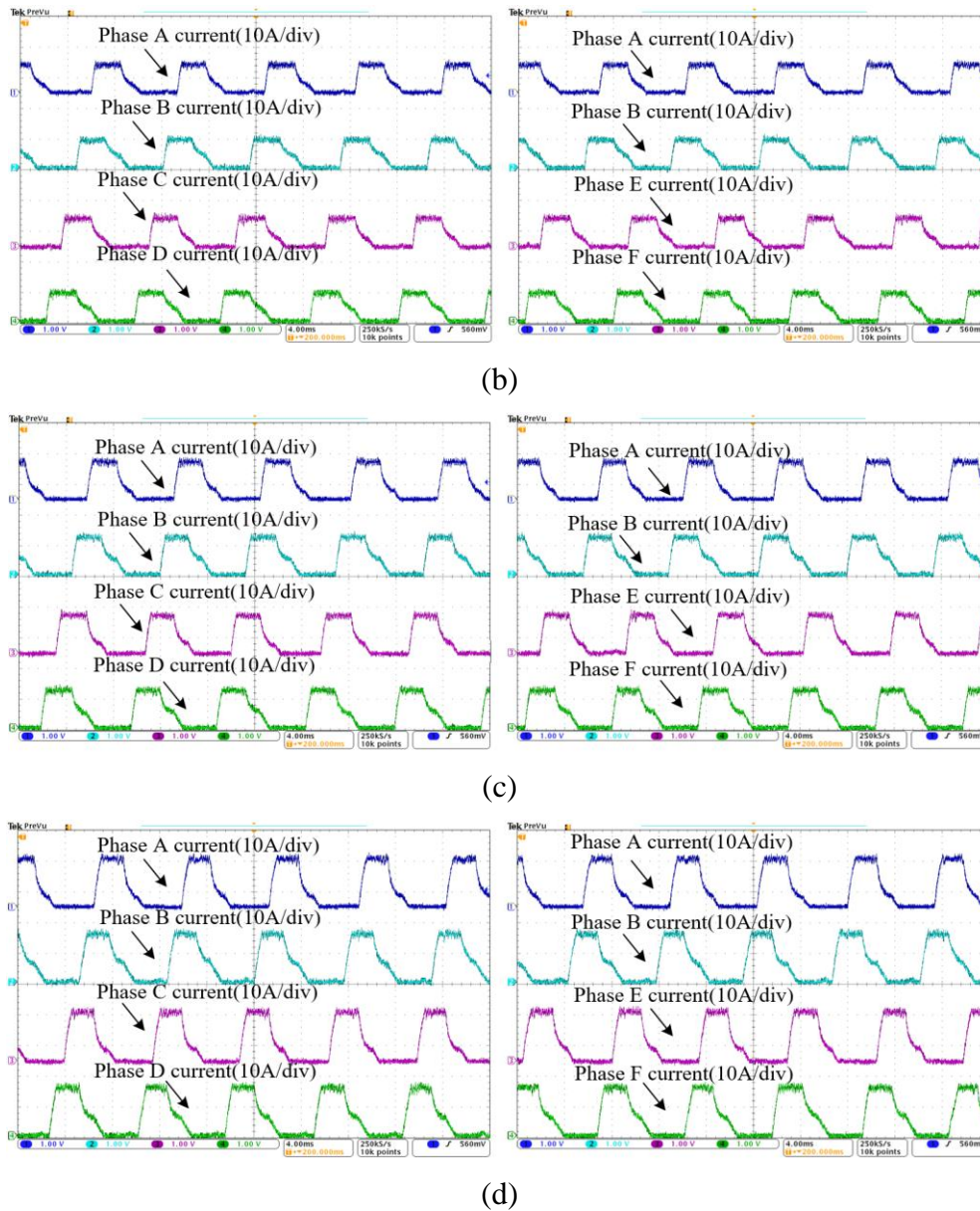


Figure 7.31 Current waveforms with different loads at 800r/min under current control with the circle converter with extra diodes: (a) 5.0Nm (b) 10.0Nm (c) 15.0Nm (d) 20.0Nm

Figure 7.32 shows output torque waveforms with different loads at 800r/min under current control with the circle converter with extra diodes. Compared with the AHB converter, due to conduction width limitation, the circle converter with extra diodes also have more serious torque ripple at medium speed.

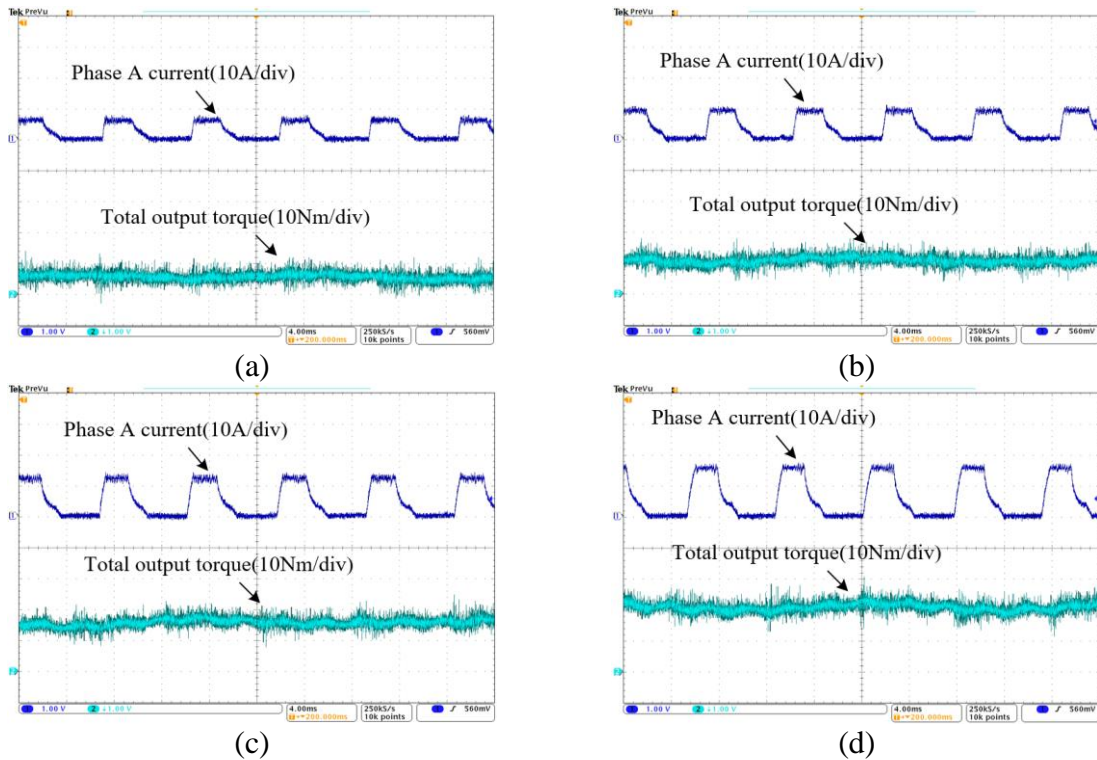
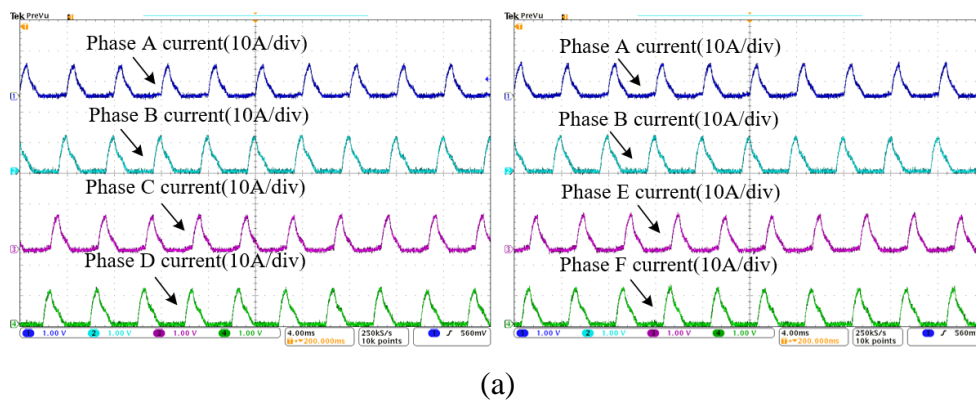


Figure 7.32 Output torque waveforms with different loads at 800r/min under current control with the circle converter with extra diodes: (a) 5.0Nm (b) 10.0Nm (c) 15.0Nm (d) 20.0Nm

**7.3.2.3 1500r/min**

Figure 7.33 shows current waveforms with different loads at 1500r/min under voltage control with the circle converter with extra diodes. Advance angle is set at  $10^\circ$ , and conduction width to produce average torque of 6.0Nm and 10.0Nm in this set of tests are  $72^\circ$  and  $95^\circ$ . Current waveforms are very close to the AHB converter at high speed.



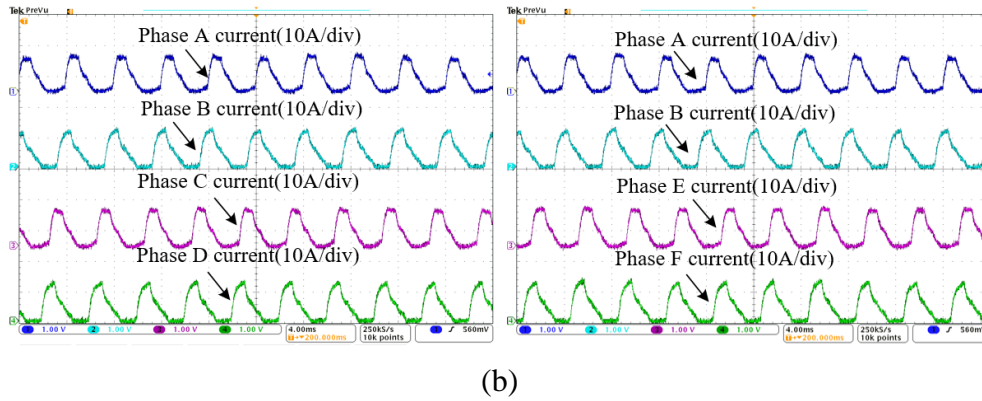


Figure 7.33 Current waveforms with different loads at 1500r/min under voltage control with the circle converter with extra diodes: (a) 6.0Nm (b) 10.0Nm

Figure 7.34 presents output torque waveforms with different loads at 1500r/min under voltage control with the circle converter with extra diodes. TRR is very close to the circle converter at high speed.

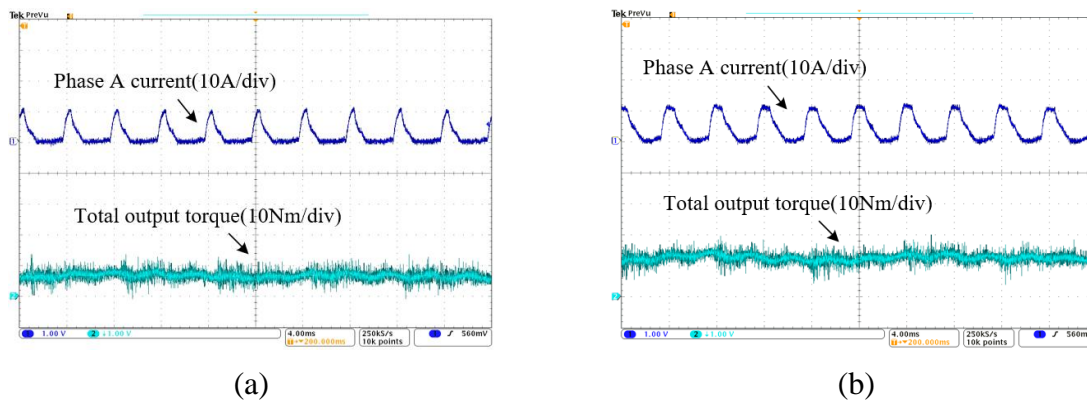


Figure 7.34 Output torque waveforms with different loads at 1500r/min under voltage control with the circle converter with extra diodes: (a) 6.0Nm (b) 10.0Nm

### 7.3.3 Efficiency comparison

In order to compare the efficiency of three different converters (the AHB converter, the circle converter and the circle converter with extra diodes), the following tests are conducted in this section. Three converters are controlled by the traditional control methods. Producing the same average torque outputs at three different speeds, the average input electric energy and the average output mechanical energy are obtained from DC power supply and torque transducer, afterwards the system efficiency of three converters are presented in Table 7.4.

Producing the same average output torque, the circle converter has the highest efficiency throughout the whole speed range, and has superiority especially at low and medium speed due to less switching losses, which has been mentioned in Chapter 3. The circle converter

with extra diodes has the lowest efficiency due to more conduction loss from extra diodes. However, this impact on loss due to use of extra diodes would be reduced with higher voltage rating converter. In addition, experimental results of efficiency are slightly smaller than the simulation results. The conduction loss of cables and auxiliary resistors and other loss in the real-time test give rise to the errors between experimental results and simulation results.

Table 7.4 System efficiency comparison between three converters with traditional control methods

	Speed(r/min)	Tav(Nm)	$\eta$ (%) (Simulation)	$\eta$ (%) (Test)
AHB converter	200	20.1	47.2	46.3
	800	20.0	84.8	82.7
	1500	10.0	83.7	82.1
Circle converter	200	20.1	52.9	50.4
	800	20.0	85.3	83.4
	1500	10.0	83.9	82.2
Circle converter with extra diodes	200	20.1	45.7	43.1
	800	20.0	83.5	81.5
	1500	10.0	82.5	80.9

### 7.3.4 The circle converter with the DTC method

From the above experimental results, it is obvious that compared with the AHB converter, the circle converter has more torque ripple due to its 120° conduction limitation in CCC method. Therefore, application of the DTC method is significantly meaningful for the circle converter to reduce the torque ripple.

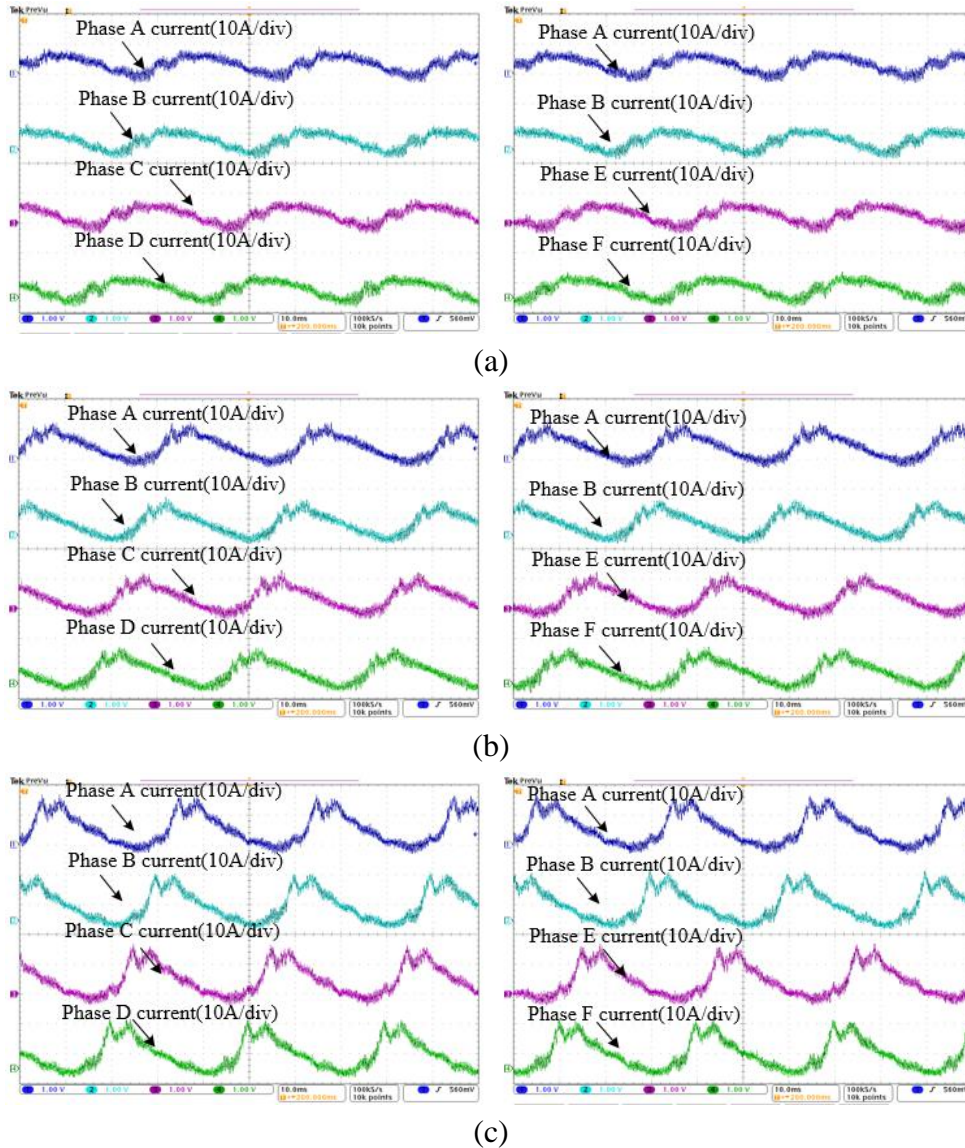
In this section, a series of tests are conducted with the circle converter using the DTC method. Experimental results are presented as Figure 7.35 to Figure 7.40.

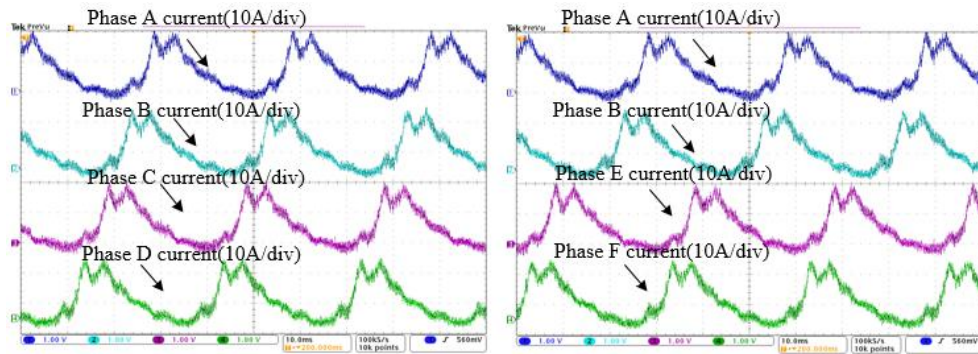
#### 7.3.4.1 200r/min

Figure 7.35 shows current waveforms with different loads at 200r/min using the DTC method with the circle converter. Stator flux references are set at 0.29Wb, 0.32Wb, 0.34Wb and 0.38Wb to obtain 5Nm, 10Nm, 15Nm and 20Nm average output torque respectively. Current

waveforms are very irregular and have more noise than the AHB converter due to less independence between adjacent phases in the circle converter.

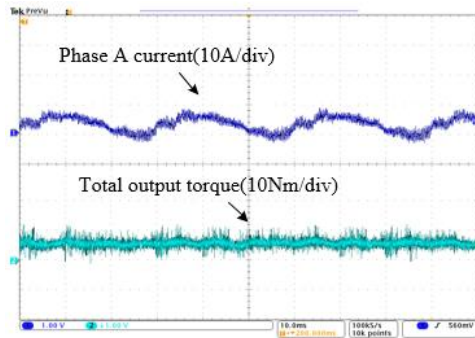
Figure 7.36 shows the output torque waveforms with different loads at 200r/min using DTC with the circle converter. The average torque outputs are 5.0Nm, 10.0Nm, 15.1Nm and 20.1Nm. Torque ripple ratio is 49.3%, 29.5%, 20.1% and 14.3%.



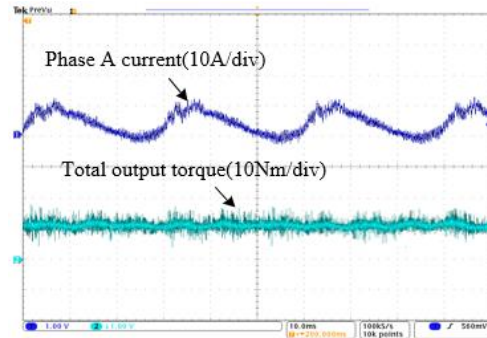


(d)

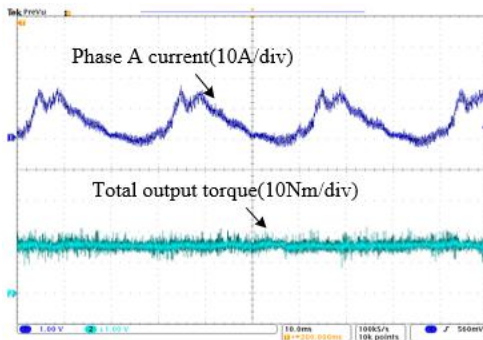
Figure 7.35 Current waveforms with different loads at 200r/min under DTC method with the circle converter: (a) 5.0Nm (b) 10.0Nm (c) 15.0Nm (d) 20.0Nm



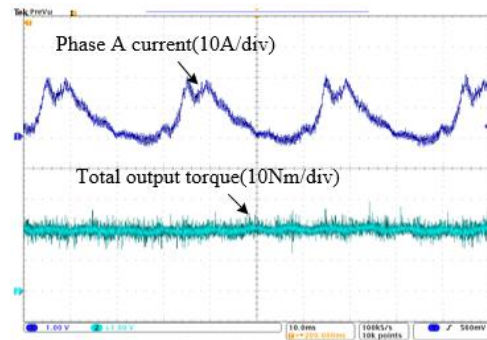
(a)



(b)



(c)



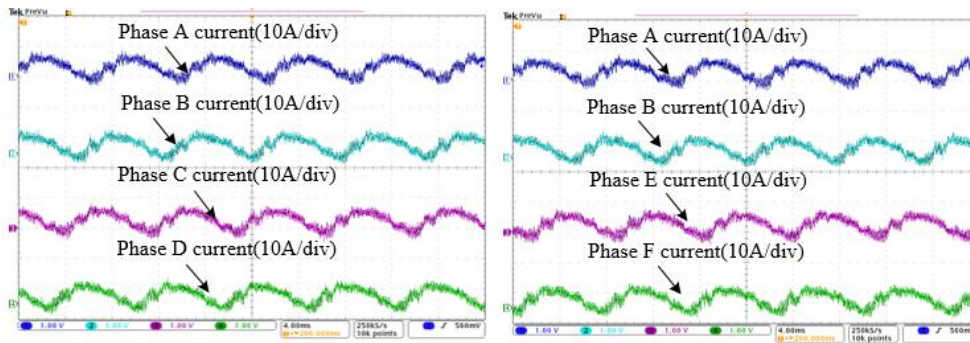
(d)

Figure 7.36 Output torque waveforms with different loads at 200r/min under DTC method with the circle converter: (a) 5.0Nm (b) 10.0Nm (c) 15.1Nm (d) 20.1Nm

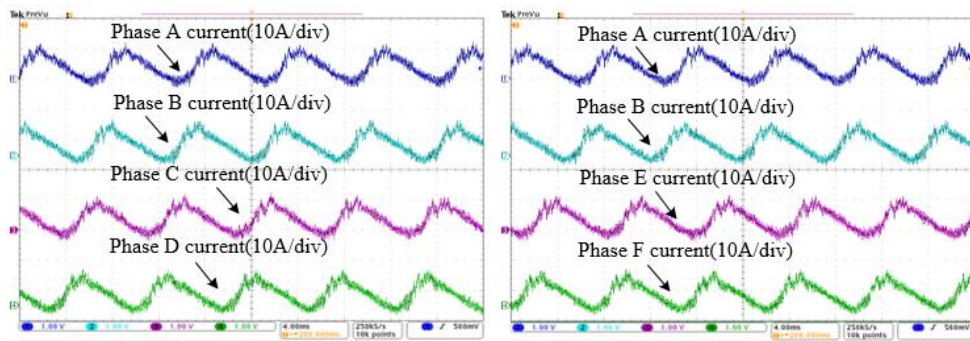
### 7.3.4.2 800r/min

Figure 7.37 shows current waveforms with different loads at 800r/min using the DTC method with the circle converter. Stator flux references are set at 0.29Wb, 0.32Wb, 0.34Wb and 0.38Wb to obtain 5Nm, 10Nm, 15Nm and 20Nm average output torque respectively. Figure 7.38 shows the output torque waveforms with different loads at 800r/min under DTC method

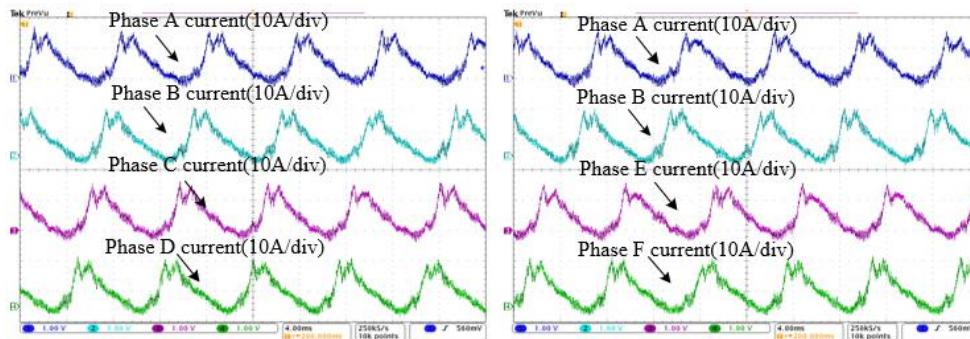
with the circle converter. The average torque outputs are 5.2Nm, 10.0Nm, 15.0Nm and 20.1Nm. TRR is 47.5%, 26.5%, 18.5%, and 17.6%.



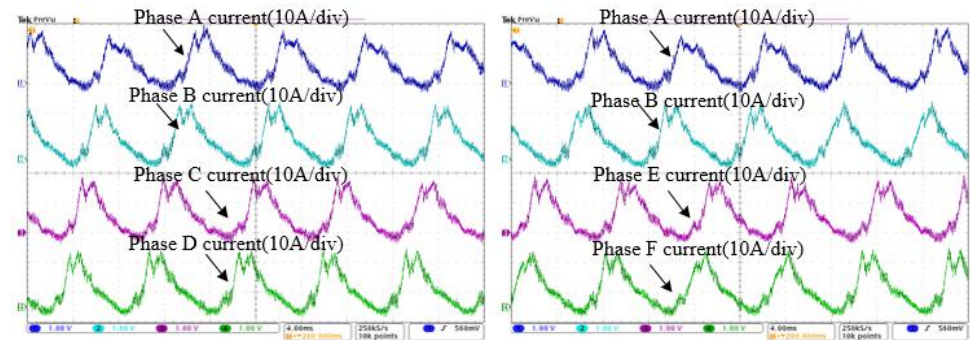
(a)



(b)



(c)



(d)

Figure 7.37 Current waveforms with different loads at 800r/min under DTC method with the circle converter: (a) 5.2Nm (b) 10.0Nm (c) 15.0Nm (d) 20.1Nm

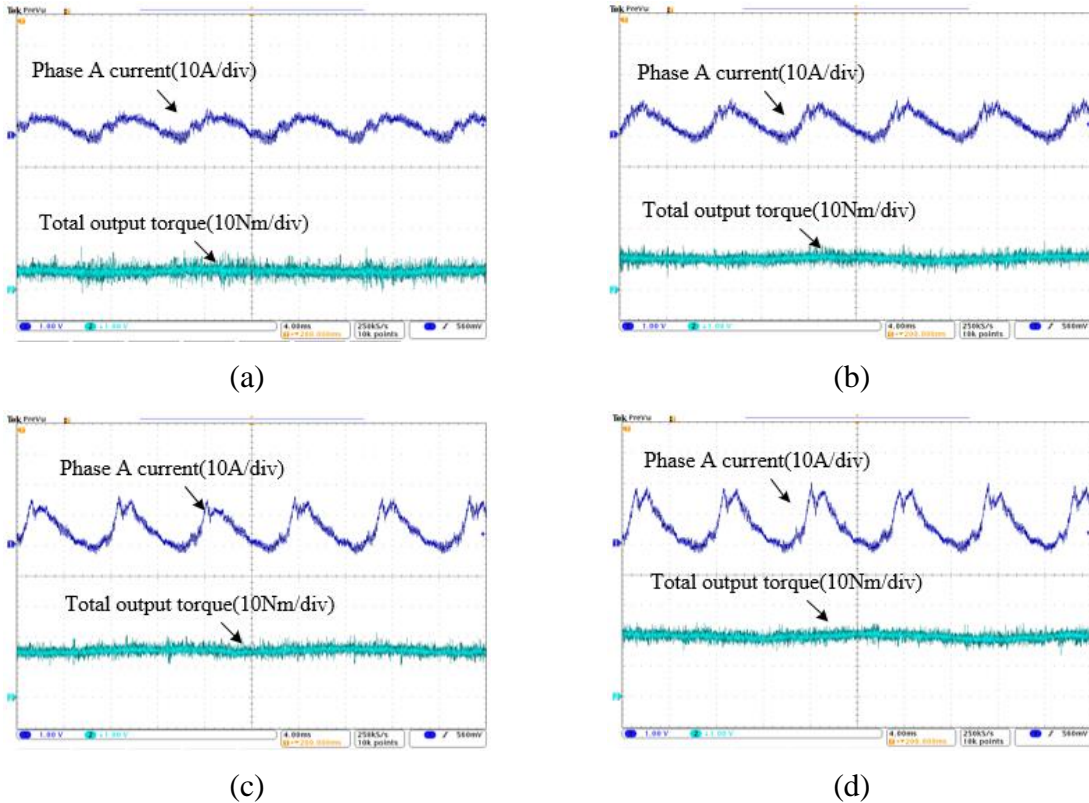
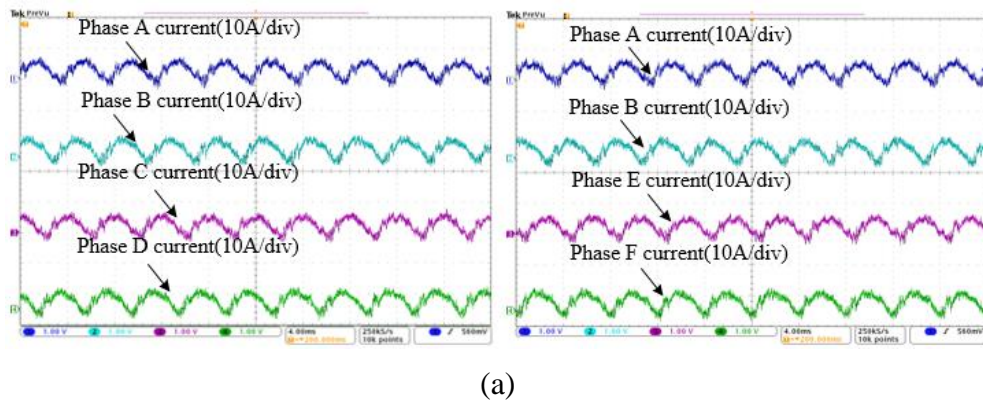
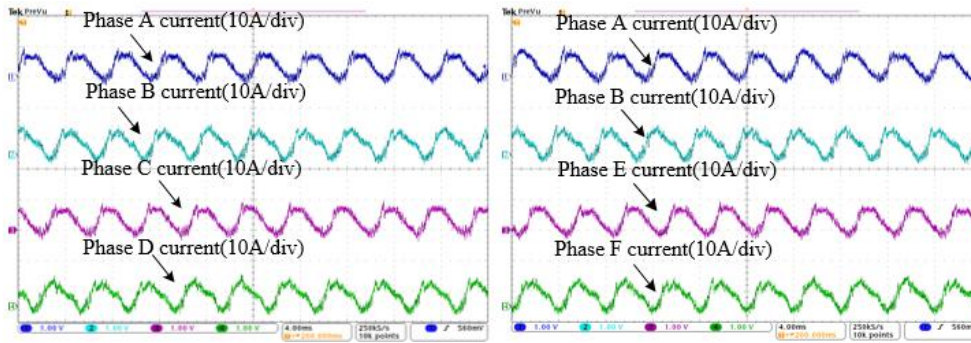


Figure 7.38 Output torque waveforms with different loads at 800r/min by DTC with the circle converter: (a) 5.2Nm (b) 10.0Nm (c) 15.0Nm (d) 20.1Nm

### 7.3.4.3 1500r/min

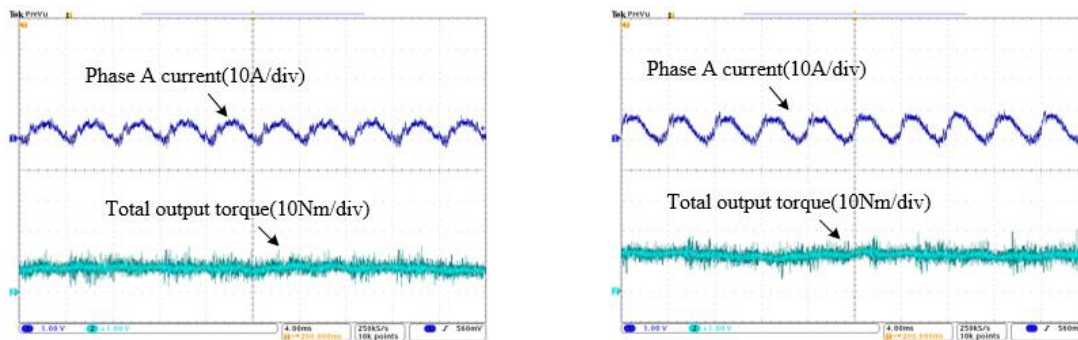
Figure 7.39 presents current waveforms with different loads at 200r/min by DTC with the circle converter. Stator flux references are set at 0.25Wb and 0.28Wb to obtain 6Nm and 10Nm.





(b)

Figure 7.39 Current waveforms with different loads at 1500r/min by DTC with the circle converter: (a) 6.0Nm (b) 10.0Nm



(a)

(b)

Figure 7.40 Output torque waveforms with different loads at 1500r/min by DTC with the circle converter: (a) 5.9Nm (b) 10.0Nm

Figure 7.40 shows the output torque waveforms with different loads at 800r/min by DTC with the circle converter. The average torque outputs are 5.9Nm and 10.0Nm respectively. TRR is 46.2% and 27.4%.

Torque ripple comparison between simulation and experimental test of the circle converter is shown in Table 7.5. Compared with the traditional control methods, the proposed DTC method can significantly reduce torque ripple throughout the whole speed range. Similar with comparison results in Table 7.2, the TRR of traditional methods in test is lower than simulation result, whilst the simulated TRR of the DTC method is lower than test. The reasons behind the difference has been discussed in the end of Section 7.2.

Table 7.5 Torque ripple comparison between simulation and experimental test of the circle converter

N=200r/min $T_{av}=20\text{Nm}$	Traditional methods (Simulation)	DTC method (Simulation)	Traditional methods (Test)	DTC method (Test)
TRR	65.8%	9.1%	42.1%	14.3%
N=800r/min $T_{av}=15\text{Nm}$	Traditional methods (Simulation)	DTC method (Simulation)	Traditional methods (Test)	DTC method (Test)
TRR	58.0%	17.1%	43.2%	18.5%
N=1500r/min $T_{av}=10\text{Nm}$	Traditional methods (Simulation)	DTC method (Simulation)	Traditional methods (Test)	DTC method (Test)
TRR	49.0%	25.5%	36.9%	27.4%

### 7.3.5 Torque-Speed Performance comparison

In order to compare the torque-speed performance of the proposed low torque ripple drive systems, the 100V, 48A DC power supply is employed throughout the whole speed range. Two low torque ripple SRM drives (the AHB converter with the DTC method and circle converter with DTC method) which have been validated in the above sections are selected in this part to compare with the traditional SRM drive (the AHB converter with traditional control methods). In this test, the maximum DC link current is set at 48A. The torque-speed curves and efficiency under fixed maximum DC link current are shown in Figure 7.41 and Table 7.6.

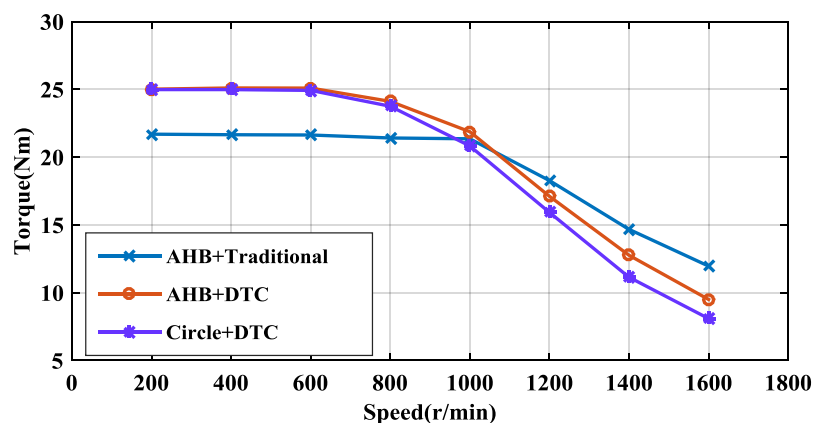


Figure 7.41 Torque-Speed performance and system efficiency comparison under fixed maximum DC link current

Table 7.6 System efficiency comparison under fixed maximum DC link current

Speed	$\eta_{\text{AHB+Traditional}}$	$\eta_{\text{AHB+DTC}}$	$\eta_{\text{Circle+DTC}}$
200r/min	46.7%	46.9%	47.6%
400r/min	69.6%	69.8%	71.6%
600r/min	76.6%	76.7%	77.3%
800r/min	82.5%	83.9%	84.1%
1000r/min	85.3%	85.7%	86.1%
1200r/min	86.0%	85.5%	85.9%
1400r/min	85.9%	85.2%	85.7%
1600r/min	86.2%	85.1%	85.7%

It is pronounced that the DTC method (red and purple in Figure 7.41) can produce larger average torque at low and medium speed, whilst the traditional control methods can produce larger average torque at high speed. By using the same AHB converter (blue and purple in Figure 7.41), efficiency of the DTC method has superiority at low and medium speed, whilst the traditional control methods have slightly higher efficiency at high speed. By employing the DTC method (red and purple in Figure 7.41), the circle converter has higher efficiency than the AHB converter throughout the whole speed range due to less switch losses. Giving almost same torque-speed envelop, the current rating of switches in the circle converter is double the rating of the AHB converter, as one switch has to carry current from two adjacent phases.

Consequently, producing lower torque ripple, the DTC method has larger average output torque and higher efficiency at low and medium speed than the traditional control methods. Employing fewer switches and diodes, the circle converter has higher system efficiency than the traditional AHB converter.

#### 7.4 Summary

In this chapter, experimental work is conducted to validate the simulation analysis in Chapters 3 to 5.

Single-phase excitation tests validate that single-phase N-S connection type can produce larger average torque than single-phase N-N connection type. Multi-phase excitation tests on five different winding connection types validate that the proposed Types 2 and 3 have

reasonable average torque and less mutual-inductance throughout the whole speed range. However, Type 2 has large torque ripple due to its asymmetric connection type. Consequently Type 3 is selected to be the optimum winding connection type for the six-phase SRM prototype.

Experimental work on the proposed two converters validates that the current distortions in the circle converter can be avoided by employing conduction width limitation and extra diodes. The circle converter has higher efficiency by traditional control methods throughout the whole speed range than the AHB converter. However, due to the conduction width limitation, the torque ripple of the proposed converters is very large compared with the AHB converter.

The DTC method has been successfully applied to the AHB converter and the circle converter. Experimental results validate that the DTC method can reduce torque ripple for the six-phase SRM throughout the whole speed range. Two low torque ripple SRM drives are consequently proposed, which are the AHB converter with the DTC method and the circle converter with the DTC method. Keeping the same VA rating with the AHB converter and giving almost same torque-speed envelop, the circle converter employs half the number of switches while each switch has double the current rating compared with the AHB converter.

---

## Chapter 8. Conclusions and Future Work

---

This thesis has described research into the design of a low torque ripple six-phase SRM drive system. Power converters, advanced control techniques and winding connection types for the six-phase SRMs are investigated in both simulation and experimental work. Future work is also included in this chapter.

### 8.1 Conclusions

#### 8.1.1 Power converters

A circle converter topology for six-phase SRM drives is proposed in the thesis. This new proposed converter topology requires no additional energy storage element and only consists of six switches. Compared with a traditional AHB (Asymmetric Half Bridge) converter, the number of switches, diodes and connections between the SRM and converter are reduced by half.

Traditional control methods, the CCC (Current Chopping Control) and APC (Angle Position Control) techniques, are successfully modified and applied to the proposed converter throughout the whole speed range. However, due to the special connection of six windings and the phase conduction widths, there are two distortion parts in the phase current, one is a sharp current increasing around  $60^\circ$ , and the other one is freewheeling current distortion after turn-off.

In order to avoid the current distortion in circle converter, a  $120^\circ$  conduction width limitation and the circle converter with extra diodes topology is proposed. However, the circle converter with extra diodes has been rejected for the low efficiency caused by continuous conduction loss. Compared with a conventional AHB converter, the proposed circle converter offers fewer converter loss and higher efficiency, which is an excellent choice for the six-phase SRM drive system.

#### 8.1.2 Advanced control techniques

The DTC (Direct Torque Control) strategy has been proposed to control six-phase SRMs. The application of the DTC method has the advantage of significantly reducing the amount of torque ripple normally associated with this type of machine.

Simulations and experiments have been carried out on the six-phase AHB converter to verify the proposed DTC method. When compared with classical control techniques including CCC and APC methods, the proposed DTC method has reduced torque ripple from 35.3% to 5.1% at 200r/min (20Nm), reduced torque ripple from 48.8% to 11.1% at 800r/min (13.5Nm) and reduced torque ripple from 58.9% to 25.1% at 1500r/min (10Nm). In experiment, the DTC method has reduced torque ripple from 24.2% to 12.1% at 200r/min (20Nm), reduced torque ripple from 33.0% to 17.8% at 800r/min (15Nm) and reduced torque ripple from 47.7% to 28.6% at 1500r/min (10Nm). Therefore, both simulation and experiment results verified that the DTC method can reduce torque ripple significantly for the six-phase SRMs with the AHB converter throughout the whole speed range. As the simulation is based on the single phase characteristics of the six-phase SRM, there are some reasonable differences between simulation and experiment torque ripple results.

There is reduced phase independence in the circle converter, consequently a modified DTC method is proposed based on the DTC method designed for the AHB converter. Simulations and experiments have been carried out on the proposed circle converter to verify the new DTC method. When compared with classical control techniques including CCC and APC methods, the proposed new DTC method has reduced torque ripple from 65.8% to 6.8% at 200r/min (20Nm), reduced torque ripple from 58.0% to 17.1% at 800r/min (13.5Nm) and reduced torque ripple from 49.0% to 25.5% at 1500r/min (10Nm). In experiment, the DTC method has reduced torque ripple from 42.1% to 14.3% at 200r/min (20Nm), reduced torque ripple from 43.2% to 18.5% at 800r/min (15Nm) and reduced torque ripple from 36.9% to 27.4% at 1500r/min (10Nm). Therefore, both simulation and experiment results verified that the DTC method can reduce torque ripple significantly for the six-phase SRMs with the circle converter throughout the whole speed range.

### **8.1.3 Winding connection types**

Five different winding connection types for a six-phase SRM are investigated and compared on the bases of torque performance and mutual inductance effects. The predictions of FEA and the results of experimental tests including single-phase excitation and multi-phase excitation are examined and compared.

Some connection types have considerable mutual-inductances, hence phase currents are more difficult to control and exhibit serious distortion at high speed. Therefore, although these have

highest average torque at low speed, they are not an ideal winding connection type for the six-phase SRM. Other types have reasonable average torque and less mutual-inductance throughout the whole speed range. However, some have large torque ripple due to their asymmetric connection type. The best type is illustrated below and is selected to be the optimum winding connection type for the six-phase SRM. It combines high mean torque and low torque ripple.

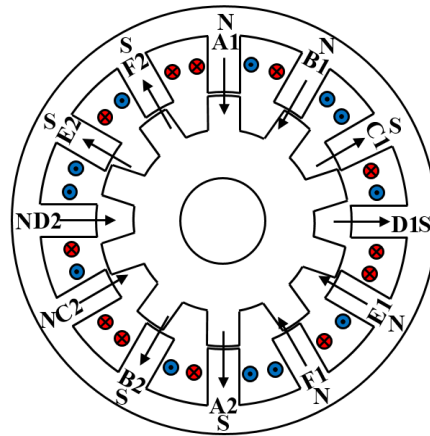


Figure 8.1 Optimum winding connection type for the six-phase SRM

It is shown how windings which have N-S arrangement produce almost identical torque in the absence of magnetic saturation in the core back. In the presence of core back saturation the winding configurations with the shortest flux loops produce more average torque. Windings with N-N arrangement have an element of negative torque due to the mutual coupling between phases. However, this can be small in some cases. Overall, with a six phase machine the shortest flux loops occur with N-N winding arrangement. At rated torque the small negative effect of mutual coupling is more than compensated by a reduction in core back saturation, so that this arrangement outperforms the N-S arrangement. All results are verified by experimentation.

## 8.2 Future work

In this project, several dynamic simulation models have been proposed. All of them are based on the measured single-phase electromagnetic characteristics of the six-phase SRM prototype, and mutual-inductances are ignored in the dynamic simulations. Hence, one of the meaningful future works is the proposal of a dynamic six-phase SRM simulation model considering mutual-inductances. As long as this dynamic simulation model is correlated against the

measurements, a much more detailed analysis of the six-phase SRM can be investigated, and additionally advanced control methods can be applied with more accuracy.

An absolute encoder is employed in the six-phase SRM drive system to obtain the rotor position information in this project. The encoder increases the cost and volume of the whole system and occupies significant computation resources in the real-time test. In order to make the six-phase SRM drive to be a viable commercial competitor among adjustable speed motor drives, compactness, reliability and robustness of its performance has to be enhanced. These factors justify the necessity for development of a high-grade position sensorless control for the six SRM drive in the future.

SRM drives are known for their high fault-tolerance, and the six-phase SRM has even higher flexibility in winding failure due to the increased phase number. The possible failure of the six-phase SRM can be discussed firstly. The fault diagnosis methods and control strategies under unhealthy conditions can be subsequently investigated in the future.

---

## References

---

- [1] S. A. Nasar, "D.C.-switched reluctance motor," *Electrical Engineers, Proceedings of the Institution of*, vol. 116, pp. 1048-1049, 1969.
- [2] T. J. E. Miller, *Switched reluctance motors and their control*: Oxford Science Publications, 1999.
- [3] P. J. Lawrenson, J. M. Stephenson, P. T. Blenkinsop, J. Corda, and N. N. Fulton, "Variable-speed switched reluctance motors," *IEE Proceedings B - Electric Power Applications*, vol. 127, pp. 253-265, 1980.
- [4] T. J. E. Miller, *Electronic Control of Switched Reluctance Machines*: Newnes, 2001.
- [5] K. M. Rahman, B. Fahimi, G. Suresh, A. V. Rajarathnam, and M. Ehsani, "Advantages of switched reluctance motor applications to EV and HEV: design and control issues," *IEEE Transactions on Industry Applications*, vol. 36, pp. 111-121, 2000.
- [6] M. Takeno, A. Chiba, N. Hoshi, S. Ogasawara, M. Takemoto, and M. Rahman, "Test Results and Torque Improvement of the 50-kW Switched Reluctance Motor Designed for Hybrid Electric Vehicles," *IEEE Transactions on Industry Applications*, vol. 48, pp. 1327-1334, 2012.
- [7] K. Kiyota and A. Chiba, "Design of Switched Reluctance Motor Competitive to 60-kW IPMSM in Third-Generation Hybrid Electric Vehicle," *IEEE Transactions on Industry Applications*, vol. 48, pp. 2303-2309, 2012.
- [8] B. Bilgin, A. Emadi, and M. Krishnamurthy, "Comprehensive Evaluation of the Dynamic Performance of a 6/10 SRM for Traction Application in PHEVs," *IEEE Transactions on Industrial Electronics*, vol. 60, pp. 2564-2575, 2013.
- [9] Z. Q. Zhu and D. Howe, "Electrical Machines and Drives for Electric, Hybrid, and Fuel Cell Vehicles," *Proceedings of the IEEE*, vol. 95, pp. 746-765, 2007.
- [10] Y. Takano, M. Takeno, N. Hoshi, A. Chiba, M. Takemoto, S. Ogasawara, *et al.*, "Design and analysis of a switched reluctance motor for next generation hybrid vehicle without PM materials," in *Power Electronics Conference (IPEC), 2010 International*, 2010, pp. 1801-1806.
- [11] A. Labak and N. C. Kar, "A novel five-phase pancake shaped switched reluctance motor for hybrid electric vehicles," in *2009 IEEE Vehicle Power and Propulsion Conference*, 2009, pp. 494-499.
- [12] J. Lin, K. W. E. Cheng, Z. Zhang, and X. Xue, "Experimental investigation of in-wheel switched reluctance motor driving system for future electric vehicles," in *Power Electronics Systems and Applications, 2009. PESA 2009. 3rd International Conference on*, 2009, pp. 1-6.
- [13] J. Kim, K. Ha, and R. Krishnan, "Single-Controllable-Switch-Based Switched Reluctance Motor Drive for Low Cost, Variable-Speed Applications," *IEEE Transactions on Power Electronics*, vol. 27, pp. 379-387, 2012.
- [14] M. Krishnamurthy, C. S. Edrington, A. Emadi, P. Asadi, M. Ehsani, and B. Fahimi, "Making the case for applications of switched reluctance motor technology in automotive products," *IEEE Transactions on Power Electronics*, vol. 21, pp. 659-675, 2006.
- [15] Y. Sozer, I. Husain, and D. A. Torrey, "Guidance in Selecting Advanced Control Techniques for Switched Reluctance Machine Drives in Emerging Applications," *IEEE Transactions on Industry Applications*, vol. 51, pp. 4505-4514, 2015.

- 
- [16] X. Cao, Z. Deng, G. Yang, and X. Wang, "Independent Control of Average Torque and Radial Force in Bearingless Switched-Reluctance Motors With Hybrid Excitations," *IEEE Transactions on Power Electronics*, vol. 24, pp. 1376-1385, 2009.
- [17] Z. Liu, Z. Deng, J. Cai, Y. Wu, and S. Wang, "Optimal design of a bearingless switched reluctance motor," in *Applied Superconductivity and Electromagnetic Devices, 2009. ASEMD 2009. International Conference on*, 2009, pp. 241-245.
- [18] R. Krishnan, *Switched Reluctance Motor Drives: Modeling, Simulation, Analysis, Design, and Applications*: Hoboken, 2001.
- [19] L. Guangjin, J. Ojeda, S. Hlioui, E. Hoang, M. Lecrivain, and M. Gabsi, "Modification in Rotor Pole Geometry of Mutually Coupled Switched Reluctance Machine for Torque Ripple Mitigating," *IEEE Transactions on Magnetics*, vol. 48, pp. 2025-2034, 2012.
- [20] C. Yong Kwon, Y. Hee Sung, and K. Chang Seop, "Pole-Shape Optimization of a Switched-Reluctance Motor for Torque Ripple Reduction," *IEEE Transactions on Magnetics*, vol. 43, pp. 1797-1800, 2007.
- [21] J. Hur, G. H. Kang, J. Y. Lee, J. P. Hong, and B. K. Lee, "Design and optimization of high torque, low ripple switched reluctance motor with flux barrier for direct drive," in *IEEE Industry Applications Conference*, 2004, vol.1, pp. 1-407.
- [22] N. K. Sheth and K. R. Rajagopal, "Optimum pole arcs for a switched reluctance motor for higher torque with reduced ripple," *IEEE Transactions on Magnetics*, vol. 39, pp. 3214-3216, 2003.
- [23] X. Ojeda, X. Mininger, M. Gabsi, and M. Lecrivain, "Sinusoidal feeding for Switched Reluctance Machine: Application to vibration damping," in *18th International Conference on Electrical Machines*, 2008, pp. 1-4.
- [24] B. C. Mecrow, "New winding configurations for doubly salient reluctance machines," *IEEE Transactions on Industry Applications*, vol. 32, pp. 1348-1356, 1996.
- [25] G. J. Li, X. Ojeda, S. Hlioui, E. Hoang, M. Gabsi, and C. Balpe, "Comparative study of Switched Reluctance Motors performances for two current distributions and excitation modes," *35th Annual Conference of IEEE in Industrial Electronics*, 2009, pp. 4047-4052.
- [26] A. Jin-Woo, O. Seok-Gyu, M. Jae-Won, and H. Young-Moon, "A three-phase switched reluctance motor with two-phase excitation," *IEEE Transactions on Industry Applications*, vol. 35, pp. 1067-1075, 1999.
- [27] B. J. Baliga, "An overview of smart power technology," *IEEE Transactions on Electron Devices*, vol. 38, pp. 1568-1575, 1991.
- [28] B. J. Baliga, "Trends in power semiconductor devices," *IEEE Transactions on Electron Devices*, vol. 43, pp. 1717-1731, 1996.
- [29] J. A. Haylock, B. C. Mecrow, A. G. Jack, and D. J. Atkinson, "Operation of a fault tolerant PM drive for an aerospace fuel pump application," *IEE Proceedings on Electric Power Applications*, vol. 145, pp. 441-448, 1998.
- [30] M. D. Hennen, M. Niessen, C. Heyers, H. J. Brauer, and R. W. D. Doncker, "Development and Control of an Integrated and Distributed Inverter for a Fault Tolerant Five-Phase Switched Reluctance Traction Drive," *IEEE Transactions on Power Electronics*, vol. 27, pp. 547-554, 2012.
- [31] J. D. Widmer, B. C. Mecrow, C. M. Spargo, R. Martin, and T. Celik, "Use of a 3 phase full bridge converter to drive a 6 phase switched reluctance machine," in *6th IET International Conference on Power Electronics, Machines and Drives 2012*, pp. 1-6.
- [32] T. Celik, "Segmental Rotor Switched Reluctance Drives," *Ph.D. Thesis*, Aug. 2011.

- 
- [33] R. Martin, J. D. Widmer, B. C. Mecrow, M. Kimiabeigi, A. Mebarki, and N. L. Brown, "Electromagnetic Considerations for a Six-Phase Switched Reluctance Motor Driven by a Three-Phase Inverter," *IEEE Transactions on Industry Applications*, vol. 52, pp. 3783-3791, 2016.
- [34] P. Pillay, M. Ahmed, and M. Samudio, "Modeling and performance of a SRM drive with improved ride-through capability," *IEEE Transactions on Energy Conversion*, vol. 16, pp. 165-173, 2001.
- [35] M. Takiguchi, H. Sugimoto, N. Kurihara, and A. Chiba, "Acoustic Noise and Vibration Reduction of SRM by Elimination of Third Harmonic Component in Sum of Radial Forces," *IEEE Transactions on Energy Conversion*, vol. 30, pp. 883-891, 2015.
- [36] Y. Jin, B. Bilgin, and A. Emadi, "An Offline Torque Sharing Function for Torque Ripple Reduction in Switched Reluctance Motor Drives," *IEEE Transactions on Energy Conversion*, vol. 30, pp. 726-735, 2015.
- [37] S. K. Sahoo, S. K. Panda, and J. X. Xu, "Iterative learning-based high-performance current controller for switched reluctance motors," *IEEE Transactions on Energy Conversion*, vol. 19, pp. 491-498, 2004.
- [38] Z. Jinhui and A. V. Radun, "A New Method to Measure the Switched Reluctance Motor's Flux," *IEEE Transactions on Industry Applications*, vol. 42, pp. 1171-1176, 2006.
- [39] P. Debiprasad and V. Ramanarayanan, "Mutual Coupling and Its Effect on Steady-State Performance and Position Estimation of Even and Odd Number Phase Switched Reluctance Motor Drive," *IEEE Transactions on Magnetics*, vol. 43, pp. 3445-3456, 2007.
- [40] N. Radimov, N. Ben-Hail, and R. Rabinovici, "Inductance measurements in switched reluctance machines," *IEEE Transactions on Magnetics*, vol. 41, pp. 1296-1299, 2005.
- [41] W. Ding, D. Liang, and Z. Luo, "A comparative study of performances for a dual channel switched reluctance machine with different winding connections," in *International Conference on Electrical Machines and Systems*, 2011, pp. 1-5.
- [42] Q. Bingni, S. Jiancheng, L. Tao, and Z. Hongda, "Mutual coupling and its effect on torque waveform of even number phase switched reluctance motor," in *International Conference on Electrical Machines and Systems*, 2008, pp. 3405-3410.
- [43] G.J.Li, J. Ojeda, E. Hoang, M. Lecrivain, and M. Gabsi, "Comparative Studies Between Classical and Mutually Coupled Switched Reluctance Motors Using Thermal-Electromagnetic Analysis for Driving Cycles," *IEEE Transactions on Magnetics*, vol. 47, pp. 839-847, 2011.
- [44] I. Husain and M. Ehsani, "Torque ripple minimization in switched reluctance motor drives by PWM current control," *IEEE Transactions on Power Electronics*, vol. 11, pp. 83-88, 1996.
- [45] V. P. Vujicic, "Minimization of Torque Ripple and Copper Losses in Switched Reluctance Drive," *IEEE Transactions on Power Electronics*, vol. 27, pp. 388-399, 2012.
- [46] X. D. Xue, K. W. E. Cheng, and S. L. Ho, "Optimization and Evaluation of Torque-Sharing Functions for Torque Ripple Minimization in Switched Reluctance Motor Drives," *IEEE Transactions on Power Electronics*, vol. 24, pp. 2076-2090, 2009.
- [47] Y. Jin, B. Bilgin, and A. Emadi, "An Extended-Speed Low-Ripple Torque Control of Switched Reluctance Motor Drives," *IEEE Transactions on Power Electronics*, vol. 30, pp. 1457-1470, 2015.

- [48] S. Kurian and G. K. Nisha, "Torque ripple minimization of SRM using torque sharing function and hysteresis current controller," in *International Conference on Control Communication & Computing India (ICCC)*, 2015, pp. 149-154.
- [49] T. H. Kim, D. H. Lee, and J. W. Ahn, "Advanced non-linear logic torque sharing function of SRM for torque ripple reduction," in *31st International Telecommunications Energy Conference*, 2009, pp. 1-4.
- [50] M. Dowlatshahi, S. M. S. Nejad, and J. W. Ahn, "Torque ripple minimization of switched reluctance motor using modified torque sharing function," in *21st Iranian Conference on Electrical Engineering (ICEE)*, 2013, pp. 1-6.
- [51] Q. Sun, J. Wu, C. Gan, M. Shen, and Y. Hu, "Investigation of direct torque control and torque sharing function strategy for switched reluctance motor applications," in *18th International Conference on Electrical Machines and Systems (ICEMS)*, 2015, pp. 864-868.
- [52] M. Wang and G. Wang, "Analysis in start-up performance of SRM based on direct instantaneous torque control," in *2011 International Conference on Electrical and Control Engineering (ICECE)*, 2011, pp. 4721-4724.
- [53] M. Ilic-Spong, T. J. E. Miller, S. R. Macminn, and J. S. Thorp, "Instantaneous Torque Control of Electric Motor Drives," *IEEE Transactions on Power Electronics*, vol. PE-2, pp. 55-61, 1987.
- [54] N. H. Fuengwarodsakul, M. Menne, R. B. Inderka, and R. W. D. Doncker, "High-dynamic four-quadrant switched reluctance drive based on DITC," *IEEE Transactions on Industry Applications*, vol. 41, pp. 1232-1242, 2005.
- [55] R. B. Inderka and R. W. A. A. D. Doncker, "DITC-direct instantaneous torque control of switched reluctance drives," *IEEE Transactions on Industry Applications*, vol. 39, pp. 1046-1051, 2003.
- [56] J. Castro, P. Andrada, and B. Blanque, "Minimization of torque ripple in switched reluctance motor drives using an enhanced direct instantaneous torque control," in *XXth International Conference on Electrical Machines (ICEM)*, 2012, pp. 1021-1026.
- [57] J. Liang, D. H. Lee, and J. W. Ahn, "Direct instantaneous torque control of switched reluctance machines using 4-level converters," *IET Electric Power Applications*, vol. 3, pp. 313-323, 2009.
- [58] I. Takahashi and T. Noguchi, "A New Quick-Response and High-Efficiency Control Strategy of an Induction Motor," *IEEE Transactions on Industry Applications*, vol. IA-22, pp. 820-827, 1986.
- [59] L. Zhong, M. F. Rahman, W. Y. Hu, and K. W. Lim, "Analysis of direct torque control in permanent magnet synchronous motor drives," *IEEE Transactions on Power Electronics*, vol. 12, pp. 528-536, 1997.
- [60] A. D. Cheok and Y. Fukuda, "A new torque and flux control method for switched reluctance motor drives," *IEEE Transactions on Power Electronics*, vol. 17, pp. 543-557, 2002.
- [61] P. Chanchaoensook, "Direct instantaneous torque control of a four-phase switched reluctance motor," in *International Conference on Power Electronics and Drive Systems*, 2009, pp. 770-777.
- [62] R. S. Kumar and J. A. Vasanth, "Intelligent neuro controller based speed and torque control of five phase switched reluctance motor," in *International Conference on Information Communication and Embedded Systems (ICICES)*, 2013, pp. 966-973.
- [63] S. Guiying, L. Zhida, Z. Zhenghan, and W. Xiang, "Direct torque control of switched reluctance motors," in *International Conference on Electrical Machines and Systems*, 2008, pp. 3389-3392.

- [64] R. Jeyabharath, P. Veena, and M. Rajaram, "A Novel DTC Strategy of Torque and Flux Control for Switched Reluctance Motor Drive," in *International Conference on Power Electronics, Drives and Energy Systems*, 2006, pp. 1-5.
- [65] S. Sau, R. Vandana, and B. G. Fernandes, "A new direct torque control method for switched reluctance motor with high torque/ampere," in *39th Annual Conference of the IEEE Industrial Electronics Society*, 2013, pp. 2518-2523.
- [66] S. Mir, M. S. Islam, T. Sebastian, and I. Husain, "Fault-tolerant switched reluctance motor drive using adaptive fuzzy logic controller," *IEEE Transactions on Power Electronics*, vol. 19, pp. 289-295, 2004.
- [67] H. S. Lim, D. G. Roberson, N. S. Lobo, and R. Krishnan, "Novel flux linkage control of switched reluctance motor drives using observer and neural network-based correction methods," in *31st Annual Conference of IEEE Industrial Electronics Society, 2005*, pp.11-16.
- [68] M. Barnes and C. Pollock, "Power electronic converters for switched reluctance drives," *IEEE Transactions on Power Electronics*, vol. 13, pp. 1100-1111, 1998.
- [69] S. Vukosavic and V. R. Stefanovic, "SRM inverter topologies: a comparative evaluation," in *Industry Applications Society Annual Meeting*, 1990, vol.2, pp. 946-958.
- [70] S. Vukosavic and V. R. Stefanovic, "SRM inverter topologies: a comparative evaluation," *IEEE Transactions on Industry Applications*, vol. 27, pp. 1034-1047, 1991.
- [71] M. Krishnamurthy, B. Fahimi, and C. S. Edrington, "Comparison of Various Converter Topologies for Bipolar Switched Reluctance Motor Drives," in *Power Electronics Specialists Conference*, 2005, pp. 1858-1864.
- [72] P. J. Lawrenson, J. M. Stephenson, P. T. Blenkinsop, J. Corda, and N. N. Futon, "Variable-speed switched reluctance motors," *Electric Power Applications, IEE Proceedings B*, vol. 127, pp. 253-265, 1980.
- [73] H. Le-Huy, P. Viarouge, and B. Francoeur, "Unipolar converters for switched reluctance motors," in *Industry Applications Society Annual Meeting, 1989*, vol.1, pp. 551-560.
- [74] W. F. Ray, P. J. Lawrenson, R. M. Davis, J. M. Stephenson, N. N. Fulton, and R. J. Blake, "High-Performance Switched Reluctance Brushless Drives," *IEEE Transactions on Industry Applications*, vol. IA-22, pp. 722-730, 1986.
- [75] S. Chan and H. R. Bolton, "Performance enhancement of single-phase switched-reluctance motor by DC link voltage boosting," *IEE Proceedings B - Electric Power Applications*, vol. 140, pp. 316-322, 1993.
- [76] L. Dong-Hee, L. Jianing, K. Tae-Hyoung, and A. Jin-Woo, "Novel passive boost power converter for SR drive with high demagnetization voltage," in *International Conference on Electrical Machines and Systems*, 2008, pp. 3353-3357.
- [77] A. Young-Joo, H. Soon-Ill, J. Cheol-Je, C. Young-Bae, and N. Chang-Ju, "Performance of switched reluctance motor driven by novel C-dump inverter," in *Conference on Proceedings. Computer, Communication, Control and Power Engineering*, 1993, vol.5, pp. 585-588.
- [78] K. I. Hwu and C. M. Liaw, "DC-link voltage boosting and switching control for switched reluctance motor drives," *IEE Proceedings on Electric Power Applications*, vol. 147, pp. 337-344, 2000.
- [79] R. Hong-Je, K. Won-Ho, R. Geun-Hie, K. Wook, P. Ji-Ho, and W. Chung-Yuen, "A new split source type converter for SRM drives," in *IEEE Power Electronics Specialists Conference, 1998*, vol.2, pp. 1290-1294.

- 
- [80] L. Jianing, S. Seung-Hun, L. Dong-Hee, and A. Jin-Woo, "Novel passive boost converter for 3-phase Switched reluctance motor," in *International Conference on Electrical Machines and Systems*, 2009, pp. 1-5.
- [81] Y. G. Dessouky, B. W. Williams, and J. E. Fletcher, "A novel power converter with voltage-boosting capacitors for a four-phase SRM drive," *IEEE Transactions on Industrial Electronics*, vol. 45, pp. 815-823, 1998.
- [82] K. Kyu-Dong, S. Doo-Jin, and H. Uk-Youl, "Application modified C-dump converter for industrial low voltage SRM," in *IEEE International Symposium on Industrial Electronics*, 2001, vol.3, pp.1804-1809.
- [83] Y. Yong-Ho, R. Dae-Hee, K. Se-Joo, K. Duck-Kyu, and W. Chung-Yuen, "Current hysteresis controlled resonant C-dump converter for switched reluctance motor drive," in *Power Electronics Specialists Conference*, 2004, vol.2, pp. 1329-1334.
- [84] S. Mir, I. Husain, and M. E. Elbuluk, "Energy-efficient C-dump converters for switched reluctance motors," *IEEE Transactions on Power Electronics*, vol. 12, pp. 912-921, 1997.
- [85] E. Afjei, M. Asgar, and S. Ataei, "A New modified bifilar Drive Circuit for Switched Reluctance Motor," in *Joint International Conference on Power System Technology and IEEE Power India Conference*, 2008, pp. 1-4.
- [86] W. F. Ray and R. M. Davis, "Inverter Drive for Doubly Salient Reluctance Motor: Its Fundamental Behaviour, Linear Analysis and Cost Implications," *IEE Journal on Electric Power Applications*, vol. 2, pp. 185-193, 1979.
- [87] L. Feng, L. Yuefeng, and T. A. Lipo, "A new variable reluctance motor utilizing an auxiliary commutation winding," *IEEE Transactions on Industry Applications*, vol. 30, pp. 423-432, 1994.
- [88] L. Yue, J. D. Lloyd, and G. E. Horst, "Switched reluctance motor with DC assisted excitation," in *Industry Applications Conference*, 1996, vol.2, pp. 801-807.
- [89] J. Tae-Uk, K. Suk-Tai, S. Se-Jin, and H. Young-Moon, "2-stage commutated SRM with auxiliary winding," in *IEEE International Symposium on Industrial Electronics*, 2001, vol.2, pp. 1413-1417.
- [90] A. R. Kazemi, M. Asgar, E. Afjei, and A. Siadatan, "A novel sensorless method for rotor position detection in bifilar SRM drive," in *IEEE International Conference on Power and Energy (PECon)*, 2010, pp. 438-443.
- [91] A. R. Kazemi, M. Asgar, E. Afjei, and A. Siadatan, "A new rotor position detection method using bifilar windings and resonant circuit in SRM drive," in *IEEE International Conference on Power and Energy (PECon)*, 2010, pp. 744-748.
- [92] R. Krishnan and P. N. Materu, "Design of a single-switch-per-phase converter for switched reluctance motor drives," *IEEE Transactions on Industrial Electronics*, vol. 37, pp. 469-476, 1990.
- [93] R. Krishnan and S. Lee, "Analysis and design of a single switch per phase converter for switched reluctance motor drives," in *Power Electronics Specialists Conference*, 1994, vol.1, pp. 485-492.
- [94] C. Shi, J. Qiu, and R. Lin, "A Novel Self-Commutating Low-Speed Reluctance Motor for Direct-Drive Applications," *IEEE Transactions on Industry Applications*, vol. 43, pp. 57-65, 2007.
- [95] S. S. Park and T. A. Lipo, "New series resonant converter for variable reluctance motor drive," in *Power Electronics Specialists Conference*, 1992, vol.2, pp. 833-838.
- [96] J. Corda and E. Skopljak, "Four-phase switched reluctance drive using pulse-width modulation control with four switches," in *Electrical Machines and Drives*, 1991, pp. 77-80.

## References

---

- [97] L. He, H. Sun, J. Gao, and J. Bai, "Performance Research of Two Topologies of Power Converter for SRM," in *Asia-Pacific Power and Energy Engineering Conference*, 2012, pp. 1-4.
- [98] J. Ye and A. Emadi, "Power electronic converters for 12/8 switched reluctance motor drives: A comparative analysis," in *IEEE Transportation Electrification Conference*, 2014, pp. 1-6.

---

## Appendix A Program for DSP Controller

---

In this section, some of functional programs are presented, including main routine, ISR, and subroutines for SCI communication. Execution of main function is a series of initialisation codes followed by the LabVIEW data exchange loop. This loop continuously communicates with the LabVIEW user control panel via the RS232 interface to get SRM control parameters, update button states, and send data to LABVIEW. In addition to main routine there is an ISR named epwm1\_isr, which is triggered by the PWM hardware in the DSP. This ISR contains all the application control codes, which help to calculate rotor position, convert real-time current/voltage, calculate real-time flux/torque, and implement CCC/APC/DTC strategy for SRM prototype.

```
int main(void)
{
// Initialise System Control:
// PLL, WatchDog, enable Peripheral Clocks.
  InitSysCtrl();
// Initialise the pins for the SCI-A port.
  InitSciaGpio();
// Initialise the pins for the SPI-A port.
  InitSpiaGpio();

// Initialise GPIO pins for ePWM1, ePWM2, ePWM3, ePWM4, ePWM5, ePWM6
  InitEPwm1Gpio();
  InitEPwm2Gpio();
  InitEPwm3Gpio();
  InitEPwm4Gpio();
  InitEPwm5Gpio();
  InitEPwm6Gpio();

// Initialise GPIO (gate drive reset, relays, DAC and test points)
  gpio_init();

// Clear all interrupts and initialise PIE vector table:
// Disable CPU interrupts
  DINT;

// Initialise the PIE control registers to their default state.
// This function is found in the DSP2833x_PieCtrl.c file.
  InitPieCtrl();

// Disable CPU interrupts and clear all CPU interrupt flags:
  IER = 0x0000;
  IFR = 0x0000;

// Initialise the PIE vector table with pointers to the shell Interrupt
  InitPieVectTable();
```

## Appendix A

---

```
// user defined interrupt initialize
EALLOW;
PieVectTable.EPWM1_INT = &epwm1_isr;
EDIS;

// Set up ADC
InitAdc();

// Initialise ADC sequencer
adc_seq_init();

EALLOW;
SysCtrlRegs.PCLKCR0.bit.TBCLKSYNC = 0;    // ePWM TBCLK stopped
EDIS;

// Initialise PWM modules
InitEPwmMods();

EALLOW;
// All enabled ePWMs synchronised with rising edge of TBCLK
SysCtrlRegs.PCLKCR0.bit.TBCLKSYNC = 1;
EDIS;

// Set up Timer0 for code execution time measurement within epwm1_isr
Timer0_init();

// Set up SPI
spi_fifo_init();    // Initialise the SPI FIFO
spi_init();         // initialise SPI

// Enable CPU interrupts
// Enable CPU INT1 which is connected to PIE group 1 (as main control ISR)
IER |= M_INT3;
// Enable EPWMINT1 in the PIE: Group 3 interrupt 1 (i.e. INT3.1)
PieCtrlRegs.PIEIER3.bit.INTx1 = 1;

// Enable global Interrupts and higher priority real-time debug events:
EINT; // Enable Global interrupt INTM

// Initialise the SCI FIFO
scia_fifo_init();

// Initialise SCI for echoback
scia_echoback_init();

LoopCount = 0;           // Set LabVIEW data transfer counter to zero
ErrorCount = 0;
i=0;                    // Set RS232 character counter to zero

// IDLE loop. Just sit and loop forever:
// This loop is concerned only with communications with LabVIEW
for(;;)
{
```

## Appendix A

```

i=0; //reset input character counter
do {
    // Wait for incoming character from RS232 port
    while(SciaRegs.SCIFFRX.bit.RXFFST !=1) { } // wait for XRDY =1 for
empty state
    ReceivedChar = SciaRegs.SCIRXBUF.all; // Get character
    temp = ReceivedChar & 0xFF; // strip off the error bits
    letter[i]=temp;
    i++;
}while(temp != '\n');

// Get incoming SRM control parameters from LabVIEW GUI
nc=sscanf(letter,"%d %d %d",&par1,&par2,&p
ar3,&par4,&par5,&par6,&par7,&par8,&par9,&par10,&par11,&par12,&par13);

// Test for sensor out-of-range trip (send status to LabVIEW)
TZflag=EPwm1Regs.TZFLG.bit.OST;
// Send data to LabVIEW (UCP mode)
update_panel();
// Update LabVIEW panel push button status flags
get_control_panel_button_status();
// Implement the pushbutton commands
panel_controls();
LoopCount++; // Count LabVIEW data transfer cycles
}
return 0;
} // end main()

interrupt void epwm1_isr(void)
{
/*****voltage protection (brake chopper) *****/
if(measured_dclink_voltage>=max_dclink_voltage)
    GpioDataRegs.GPACLEAR.bit.GPIO20 = 1;
else if(measured_dclink_voltage<=min_dclink_voltage)
    GpioDataRegs.GPASET.bit.GPIO20 = 1;

/*****current protection *****/
if(((fabs(measured_current[1])>=overcurrentscale)||
(fabs(measured_current[2])>=overcurrentscale)||
(fabs(measured_current[3])>=overcurrentscale)||
(fabs(measured_current[4])>=overcurrentscale)||
(fabs(measured_current[5])>=overcurrentscale)||
(fabs(measured_current[0])>=overcurrentscale))
{
    EALLOW;
    EPwm1Regs.TZFRC.bit.OST = 1;
    EPwm2Regs.TZFRC.bit.OST = 1;
    EPwm3Regs.TZFRC.bit.OST = 1;
    EPwm4Regs.TZFRC.bit.OST = 1;
    EPwm5Regs.TZFRC.bit.OST = 1;
    EPwm6Regs.TZFRC.bit.OST = 1;
    EDIS;
    pb2 = 1;
}
}

```

## Appendix A

```

/*****SPI communicate with encoder*****/
  Bincode_pre= Bincode_cur;
// read raw gray code
  GpioDataRegs.GPACLEAR.bit.GPIO12 = 1; //SPISTE
  SpiaRegs.SPITXBUF =a; // start SPI
  while(SpiaRegs.SPIFFRX.bit.RXFFST!=1){}
  rdata=SpiaRegs.SPIRXBUF;
  GpioDataRegs.GPASET.bit.GPIO12 = 1; //close SPISTE
}

/***** Gray Code to Natural Binary Code*****/
  GrayCode=rdata;
  Gtemp=GrayCode;
  GR[13]=Gtemp>>13;
  Gtemp=Gtemp-8192*GR[13];
  GR[12]=Gtemp>>12;
  Gtemp=Gtemp-4096*GR[12];
  GR[11]=Gtemp>>11;
  Gtemp=Gtemp-2048*GR[11];
  GR[10]=Gtemp>>10;
  Gtemp=Gtemp-1024*GR[10];
  GR[9]=Gtemp>>9;
  Gtemp=Gtemp-512*GR[9];
  GR[8]=Gtemp>>8;
  Gtemp=Gtemp-256*GR[8];
  GR[7]=Gtemp>>7;
  Gtemp=Gtemp-128*GR[7];
  GR[6]=Gtemp>>6;
  Gtemp=Gtemp-64*GR[6];
  GR[5]=Gtemp>>5;
  Gtemp=Gtemp-32*GR[5];
  GR[4]=Gtemp>>4;
  Gtemp=Gtemp-16*GR[4];
  GR[3]=Gtemp>>3;
  Gtemp=Gtemp-8*GR[3];
  GR[2]=Gtemp>>2;
  Gtemp=Gtemp-4*GR[2];
  GR[1]=Gtemp>>1;
  Gtemp=Gtemp-2*GR[1];
  GR[0]=Gtemp;
  B[12]=GR[12];
  Btemp=0;
  for(j=11;j>=0;j--)
  {
    if(GR[j]==B[j+1])
      B[j]=0;
    else
      B[j]=1;
  }
  BinCode=B[0]+B[1]*2+B[2]*4+B[3]*8+B[4]*16+B[5]*32+B[6]*64+B[7]*128+B[8]*256+B[9]*512
+B[10]*1024+B[11]*2048+B[12]*4096;
  BinCode=8190-BinCode; //clockwise
  Bincode_cur=BinCode;
  theta_mech=0.04395*BinCode;

```

## Appendix A

---

```
thetatmp= theta_mech;
// calculate rotor position
(thetatmp>=324)?(thetatmp-=36):(0);
(thetatmp>=288)?(thetatmp-=36):(0);
(thetatmp>=252)?(thetatmp-=36):(0);
(thetatmp>=216)?(thetatmp-=36):(0);
(thetatmp>=180)?(thetatmp-=36):(0);
(thetatmp>=144)?(thetatmp-=36):(0);
(thetatmp>=108)?(thetatmp-=36):(0);
(thetatmp>=72) ?(thetatmp-=36):(0);
(thetatmp>=36) ?(thetatmp-=36):(0);
encoder_theta_elec=thetatmp;
encoder_theta_elec*=10;
/*****calculate 6 phase position*****/
base_angle = encoder_theta_elec+180-300;
// test A phase's align position, in my application, encoder_theta_elec=300 Deg. when A
// phase is in align position, this value may vary when change the connection between rotor
// and encoder
(base_angle>=360)?(base_angle-=360):(0);
(base_angle<0)?(base_angle+=360):(0);

//look into winding terminal side, rotate clockwise, this part decides conduction order of 6
// phase
angle[0]=base_angle+advanced_angle;
angle[1]=angle[0]+phase_offsetvalue;
(angle[1]>=360)?(angle[1]-=360):(0);
angle[2]=angle[1]+phase_offsetvalue;
(angle[2]>=360)?(angle[2]-=360):(0);
angle[3]=angle[2]+phase_offsetvalue;
(angle[3]>=360)?(angle[3]-=360):(0);
angle[4]=angle[3]+phase_offsetvalue;
(angle[4]>=360)?(angle[4]-=360):(0);
angle[5]=angle[4]+phase_offsetvalue;
(angle[5]>=360)?(angle[5]-=360):(0);

/*****trigger ADC by software*****/
AdcRegs.ADCTRL2.bit.SOC_SEQ1 = 1;//enable ADC by software
// Acquire sensor input data and apply gain and offset adjustments
// Need regular offset modification of ADC in order to have more accuracy ADC result
/*****6 phase current and DC link voltage*****/
measured_current[0] = AdcRegs.ADCRESULT0 >>4;
measured_current[0] = 0.02442*measured_current[0]-50-SENSOR_OFFSET0;

measured_current[1] = AdcRegs.ADCRESULT1 >>4;
measured_current[1] = 0.02442*measured_current[1]-50-SENSOR_OFFSET1;

measured_current[2] = AdcRegs.ADCRESULT2 >>4;
measured_current[2] = 0.02442*measured_current[2]-50-SENSOR_OFFSET2;

measured_current[3] = AdcRegs.ADCRESULT3 >>4;
measured_current[3] = 0.02442*measured_current[3]-50-SENSOR_OFFSET3;

measured_current[4] = AdcRegs.ADCRESULT4 >>4;
measured_current[4] = 0.02442*measured_current[4]-50-SENSOR_OFFSET4;
```

## Appendix A

---

```
measured_current[5] = AdcRegs.ADCRESULT5 >>4;
measured_current[5] = 0.02442*measured_current[5]-50-SENSOR_OFFSET5;

measured_dclink_voltage = AdcRegs.ADCRESULT6 >>4;
temp_v= measured_dclink_voltage;
measured_dclink_voltage = 0.2442*measured_dclink_voltage-50- SENSOR_OFFSET6;
measured_dclink_voltage=measured_dclink_voltage*3;
U_dclink=(int)(measured_dclink_voltage);

//*****flux and torque calculation*****A phase*****//
// (calculation methods of other phases are same, no longer put in Appendix)
    i_count[0]=measured_current[0];
    i_countint[0]=(int)(i_count[0]);
    i_countfloat[0]=i_count[0]-i_countint[0];

    theta_count[0]=angle[0];
    theta_countint[0]=(int)(theta_count[0]);
    theta_countfloat[0]=theta_count[0]-theta_countint[0];

    i_countint[0]/=2.5;
    theta_countint[0]/=5;
    temp1=fluxmat[i_countint[0]][theta_countint[0]];
    temp2=fluxmat[i_countint[0]][theta_countint[0]+1];
    temp3=fluxmat[i_countint[0]+1][theta_countint[0]];
    temp4=fluxmat[i_countint[0]+1][theta_countint[0]+1];

    observed_flux[0]=theta_countfloat[0]*(i_countfloat[0]*(temp1-temp2-
temp3+temp4)-temp1+temp2)+i_countfloat[0]*(temp3-temp1)+temp1;

    temp1=torquemat[i_countint[0]][theta_countint[0]];
    temp2=torquemat[i_countint[0]][theta_countint[0]+1];
    temp3=torquemat[i_countint[0]+1][theta_countint[0]];
    temp4=torquemat[i_countint[0]+1][theta_countint[0]+1];

    observed_torque[0]=theta_countfloat[0]*(i_countfloat[0]*(temp1-temp2-
temp3+temp4)-temp1+temp2)+i_countfloat[0]*(temp3-temp1)+temp1;

torque=observed_torque[0]+observed_torque[1]+observed_torque[2]+observed_torque[3]+o
bserved_torque[4]+observed_torque[5];

//Flux angle judgement
flux_x=sqrt(3)/2*(observed_flux[0]+observed_flux[1]-observed_flux[3]-observed_flux[4]);
flux_y=0.5*(-observed_flux[0]+observed_flux[1]+2*observed_flux[2]+observed_flux[3]-
observed_flux[4]-2*observed_flux[5]);
flux_total=sqrt(flux_x*flux_x+flux_y*flux_y);
fx=(int)(10000*flux_x);//for labview
fy=(int)(10000*flux_y);
flux=(int)(10000*flux_total);
fluxtheta=180/PI*atan(flux_y/flux_x);
if(flux_x<0&&flux_y>0) fluxtheta+=180;
else if(flux_x<0&&flux_y<0) fluxtheta-=180;
    if((fluxtheta>=-15)&&(fluxtheta<15)) zone=0; //zone0=N1
```

## Appendix A

```

if((fluxtheta>=15)&&(fluxtheta<45)) zone=1;
if((fluxtheta>=45)&&(fluxtheta<75)) zone=2;
if((fluxtheta>=75)&&(fluxtheta<105)) zone=3;
if((fluxtheta>=105)&&(fluxtheta<135)) zone=4;
if((fluxtheta>=135)&&(fluxtheta<165)) zone=5;
if((fluxtheta>=165)||(fluxtheta<-165)) zone=6;
if((fluxtheta>=-165)&&(fluxtheta<-135)) zone=7;
if((fluxtheta>=-135)&&(fluxtheta<-105)) zone=8;
if((fluxtheta>=-105)&&(fluxtheta<-75)) zone=9;
if((fluxtheta>=-75)&&(fluxtheta<-45)) zone=10;
if((fluxtheta>=-45)&&(fluxtheta<-15)) zone=11; //zone11=N12
torque_error=torque_ref-torque;
flux_error=flux_ref-flux_total;

/***** CCC and APC control codes *****/
if (CCC_code==1||APC_code==2)
{
for (x = 0; x< SRMPHASES; x++)
{
if ((angle[x]>onangle)&&(angle[x]<offangle))//between turn-on and turn-off angle
{
if(CCC_code==1)
{
SRM_current[x].Err=measured_current[x]-current_ref;
if(SRM_current[x].Err>Hy_width) //current is too large
SRM_current[x].Out = 0; // turn off
else if(((SRM_current[x].Err)<Hy_width)&&((SRM_current[x].Err)>-
Hy_width))//current is reasonable
asm(" RPT #2 || NOP"); //do nothing
else // current is too small
SRM_current[x].Out =1.0f; // turn on
}
else if( APC_code==2)
{
SRM_current[x].Out = 1.0f; //turn on
}
}
else
SRM_current[x].Out =0; //turn off
}
}

/***** Use par7 to par12 to activate or inactivate phases by LABVIEW *****/
EPwm1Regs.CMPA.half.CMPA=(int)EPWM_TIMER_TBPRD*SRM_current[0].Out*par7;
EPwm1Regs.CMPB= (int)EPWM_TIMER_TBPRD*SRM_current[0].Out*par7;
EPwm2Regs.CMPA.half.CMPA=(int)EPWM_TIMER_TBPRD*SRM_current[1].Out*par8;
EPwm2Regs.CMPB= (int)EPWM_TIMER_TBPRD*SRM_current[1].Out*par8;
EPwm3Regs.CMPA.half.CMPA=(int)EPWM_TIMER_TBPRD*SRM_current[2].Out*par9;
EPwm3Regs.CMPB= (int)EPWM_TIMER_TBPRD*SRM_current[2].Out*par9;
EPwm4Regs.CMPA.half.CMPA=(int)EPWM_TIMER_TBPRD*SRM_current[3].Out*par10;
EPwm4Regs.CMPB= (int)EPWM_TIMER_TBPRD*SRM_current[3].Out*par10;
EPwm5Regs.CMPA.half.CMPA=(int)EPWM_TIMER_TBPRD*SRM_current[4].Out*par11;
EPwm5Regs.CMPB= (int)EPWM_TIMER_TBPRD*SRM_current[4].Out*par11;
EPwm6Regs.CMPA.half.CMPA=(int)EPWM_TIMER_TBPRD*SRM_current[5].Out*par12;
EPwm6Regs.CMPB= (int)EPWM_TIMER_TBPRD*SRM_current[5].Out*par12;

```

## Appendix A

```
}//END of CCC&APC
```

```
/******DTC control codes******/
```

```
if(DTC_code==4)
```

```
{
```

```
  //Calculate F and T state
```

```
    if(torque_error>torque_width) TS=1; //need to increase
```

```
    else if((torque_error<= torque_width)&&(torque_error>=- torque_width))
```

```
    TS=TSP; //keep previous state
```

```
    else if(torque_error<- torque_width) TS=-1; //need to decrease
```

```
    else TS=TSP;
```

```
    TSP=TS; // memo current state
```

```
    if(flux_error>flux_width) FS=1; //need to increase
```

```
    else if((flux_error<= flux_width)&&(flux_error>=- flux_width))
```

```
    FS=FSP; //keep previous state
```

```
    else if(flux_error<- flux_width) FS=-1; //need to decrease
```

```
    else FS=FSP;
```

```
    FSP=FS; //memo current state
```

```
  //divide F and T state into 4 groups
```

```
    if((FS==1)&&(TS==1)) TFS=0; //flux increase, torque increase
```

```
    else if((FS==1)&&(TS==-1)) TFS=1; //flux increase, torque decrease
```

```
    else if((FS==-1)&&(TS==1)) TFS=2; //flux decrease, torque increase
```

```
    else if((FS==-1)&&(TS==-1)) TFS=3; //flux decrease, torque decrease
```

```
    else TFS=4;
```

```
  //define voltage vectors
```

```
    S=ST[TFS][zone];
```

```
switch(S)
```

```
{
```

```
case0:{G[0]=0;G[1]=0;G[2]=0;G[3]=0;G[4]=0;G[5]=0;G[6]=0;G[7]=0;G[8]=0;G[9]=0;G[10]=0;G[11]=0;break;}
```

```
case1:{G[0]=1;G[1]=1;G[2]=1;G[3]=1;G[4]=1;G[5]=0;G[6]=0;G[7]=0;G[8]=0;G[9]=0;G[10]=1;G[11]=0;break;}
```

```
case2:{G[0]=1;G[1]=1;G[2]=1;G[3]=1;G[4]=1;G[5]=1;G[6]=0;G[7]=0;G[8]=0;G[9]=0;G[10]=0;G[11]=0;break;}
```

```
case3:{G[0]=1;G[1]=0;G[2]=1;G[3]=1;G[4]=1;G[5]=1;G[6]=1;G[7]=0;G[8]=0;G[9]=0;G[10]=0;G[11]=0;break;}
```

```
case4:{G[0]=0;G[1]=0;G[2]=1;G[3]=1;G[4]=1;G[5]=1;G[6]=1;G[7]=1;G[8]=0;G[9]=0;G[10]=0;G[11]=0;break;}
```

```
case5:{G[0]=0;G[1]=0;G[2]=1;G[3]=0;G[4]=1;G[5]=1;G[6]=1;G[7]=1;G[8]=1;G[9]=0;G[10]=0;G[11]=0;break;}
```

```
case6:{G[0]=0;G[1]=0;G[2]=0;G[3]=0;G[4]=1;G[5]=1;G[6]=1;G[7]=1;G[8]=1;G[9]=1;G[10]=0;G[11]=0;break;}
```

```
case7:{G[0]=0;G[1]=0;G[2]=0;G[3]=0;G[4]=1;G[5]=0;G[6]=1;G[7]=1;G[8]=1;G[9]=1;G[10]=1;G[11]=0;break;}
```

```
case8:{G[0]=0;G[1]=0;G[2]=0;G[3]=0;G[4]=0;G[5]=0;G[6]=1;G[7]=1;G[8]=1;G[9]=1;G[10]=1;G[11]=1;break;}
```

```
case9:{G[0]=1;G[1]=0;G[2]=0;G[3]=0;G[4]=0;G[5]=0;G[6]=1;G[7]=0;G[8]=1;G[9]=1;G[10]=1;G[11]=1;break;}
```

```
case10:{G[0]=1;G[1]=1;G[2]=0;G[3]=0;G[4]=0;G[5]=0;G[6]=0;G[7]=0;G[8]=1;G[9]=1;G[10]=1;G[11]=1;break;}
```

## Appendix A

```

case11:{G[0]=1;G[1]=1;G[2]=1;G[3]=0;G[4]=0;G[5]=0;G[6]=0;G[7]=0;G[8]=1;G[9]=0;G[10]=1;
G[11]=1;break;}
case12:{G[0]=1;G[1]=1;G[2]=1;G[3]=1;G[4]=0;G[5]=0;G[6]=0;G[7]=0;G[8]=0;G[9]=0;G[10]=1;
G[11]=1;break;}
}
    EPwm1Regs.CMPA.half.CMPA = (int)(G[0]*EPWM_TIMER_TBPRD)*par7;
    EPwm1Regs.CMPB = (int)(G[1]*EPWM_TIMER_TBPRD)*par7;
    EPwm2Regs.CMPA.half.CMPA = (int)(G[2]*EPWM_TIMER_TBPRD)*par8;
    EPwm2Regs.CMPB = (int)(G[3]*EPWM_TIMER_TBPRD)*par8;
    EPwm3Regs.CMPA.half.CMPA = (int)(G[4]*EPWM_TIMER_TBPRD)*par9;
    EPwm3Regs.CMPB = (int)(G[5]*EPWM_TIMER_TBPRD)*par9;
    EPwm4Regs.CMPA.half.CMPA = (int)(G[6]*EPWM_TIMER_TBPRD)*par10;
    EPwm4Regs.CMPB = (int)(G[7]*EPWM_TIMER_TBPRD)*par10;
    EPwm5Regs.CMPA.half.CMPA = (int)(G[8]*EPWM_TIMER_TBPRD)*par11;
    EPwm5Regs.CMPB = (int)(G[9]*EPWM_TIMER_TBPRD)*par11;
    EPwm6Regs.CMPA.half.CMPA = (int)(G[10]*EPWM_TIMER_TBPRD)*par12;
    EPwm6Regs.CMPB = (int)(G[11]*EPWM_TIMER_TBPRD)*par12;
} //END of DTC

ISR_count1++;

/***** Housekeeping at end of ISR *****/
    AdcRegs.ADCTRL2.bit.RST_SEQ1 = 1;          // Reset SEQ1
    AdcRegs.ADCTRL2.bit.RST_SEQ2 = 1;          // Reset SEQ2
    AdcRegs.ADCST.bit.INT_SEQ1_CLR = 1;        // Clear INT SEQ1 bit
    AdcRegs.ADCST.bit.INT_SEQ2_CLR = 1;        // Clear INT SEQ2 bit

// Acknowledge this interrupt to receive more interrupts from group 1
    PieCtrlRegs.PIEACK.all = PIEACK_GROUP1;
// Latch lower 16-bits of timer0
    T0_count =CpuTimer0Regs.TIM.half.LSW;
    one_isr =65535-T0_count;

} // End of ISR

void update_panel(void)
// write to LABVIEW GUI
{
    Uint16 nc;          // sprintf error code
    static char sbuf[100]; // output string for sprintf

    nc = sprintf(sbuf,"%d %d %d %d %d %d \r\n",i0,i1,i2,i3,i4,i5);
    scia_msg(sbuf);
    nc = sprintf(sbuf,"%d %d %d %d %d %d \r\n",f0,f1,f2,f3,f4,f5);
    scia_msg(sbuf);
    nc = sprintf(sbuf,"%d %d %d %d %d %d \r\n",t0,t1,t2,t3,t4,t5);
    scia_msg(sbuf);
    nc = sprintf(sbuf,"%lu %lu %u %u \r\n",LoopCount,ISR_count1,trip_count,T0_count);
    scia_msg(sbuf);
    nc = sprintf(sbuf,"%d %d\r\n",TZflag, U_dclink);
    scia_msg(sbuf);
}

void panel_controls(void) // Implement the pushbutton commands

```

## Appendix A

---

```
{
// Clear PWM trip
  if(Clear_PWM_trip_button_status==8)
    {
      Clear_PWM_trip();
    }

  else
    pb1=0;

  if(Force_PWM_trip_button_status==64)
    {
      Force_PWM_trip();
    }
  else
    pb7=0;
}

void get_control_panel_button_status()
// Update LabVIEW panel buttons and SRM control parameters
{
  extern Uint16 par1, par2, par3, par4,par5, par6, par7,par12,par13,par14,par15;
  extern Uint16 Clear_PWM_trip_button_status;
  extern Uint16 Force_PWM_trip_button_status;
  extern Uint16 CCC_code;
  extern Uint16 APC_code;
  extern Uint16 DTC_code;
  extern float current_ref,torque_ref, flux_ref, advanced_angle,offangle,onangle;
  extern int speed_limitation,N_REF;
  Clear_PWM_trip_button_status = (par4 & 8);
  Force_PWM_trip_button_status = (par4 & 64);
  CCC_code = (par4 & 1);
  APC_code = (par4 & 2);
  DTC_code = (par4 & 4);
  Comp_2_button_status = (par4 & 128);
  current_ref=((float)(par6))/10; //amplified 10 times in labview
  torque_ref=((float)(par3))/10; //amplified 10 times in labview
  flux_ref=((float)(par5))/1000;//amplified 100 times in labview
  N_REF=par2;
  speed_limitation=par15;
  advanced_angle=par14;
  offangle=par13;
  onangle=par1;
}
```

## Appendix B Sensor Interfaces Design

Figure B.1 describes an general interface circuitry between current/voltage sensor board and the DSP.

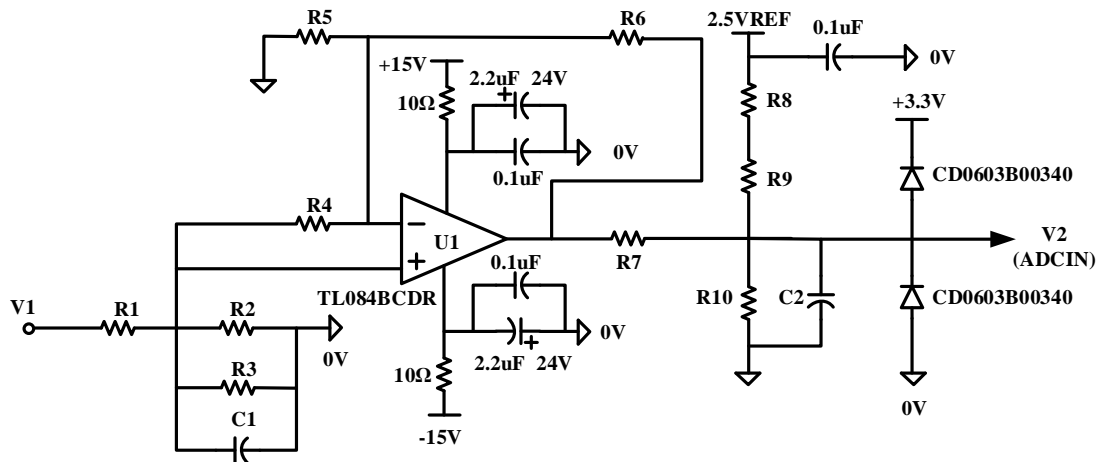


Figure B.1 Schematic of general interface circuitry between current/voltage sensor board and the DSP

LA 55-P output current has a peak to peak range of  $\pm 50\sqrt{2}$ mA. A measuring resistance of  $65\Omega$  is chosen to produce an output voltage range of  $\pm 4.6$ V. As this voltage range is greater 0-3V range of the ADC input, the op-amp U1 and its associated decoupling capacitors are not required, thus they are not fitted to the board in my application.

The remainder of the circuit has to be arranged to reduce the voltage range and also provide a positive DC offset to be compatible with the 0-3V range of the ADC input. For convenience of analysis, the circuit is simplified as shown in Figure B.2.

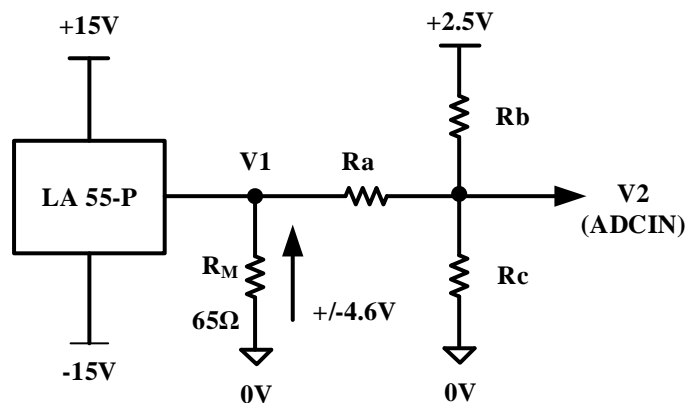


Figure B.2 Simplified schematic of general interface circuitry between LA 55-P and the DSP

## DSP

Ra, Rb and Rc in Figure B.2 have following relationships with resistors in Figure B.1.

$$Ra = R6 + R7 \quad (B.1)$$

$$Rb = R8 + R9 \quad (B.2)$$

$$Rc = R10 \quad (B.3)$$

It is necessary to find values for Ra, Rb and Rc which map the  $\pm 4.55V$  range at V1 to the 0-3V range at V2. The following Equation (B.4) represents the relationship between V1 and V2 in Figure B.2.

$$\frac{(2.5-V2)}{Rb} + \frac{(V1-V2)}{Ra} = \frac{V2}{Rc} \quad (B.4)$$

To solve for the resistance values, substitute the corresponding end-of-range values for V1 and V2.

Negative end of range: V1=-4.6V, V2=0V

$$\frac{(2.5-0)}{Rb} + \frac{(-4.6-0)}{Ra} = \frac{0}{Rc} \quad (B.5)$$

Positive end of range: V1=+4.6V, V2=3V

$$\frac{(2.5-3)}{Rb} + \frac{(4.6-3)}{Ra} = \frac{3}{Rc} \quad (B.6)$$

When initial choice of  $Rc = 20k\Omega$  is made, and then apply it to equation B.5 and B.6,  $Ra = 4.0k\Omega$  and  $Rb = 2.22k\Omega$  are yielded.

Capacitor C2 is designed to provide a low pass filter. The appropriate filter cut-off frequency  $f_c$  depends on the chosen ADC sampling rate. To calculate the value for C2, the equivalent resistance of the circuit to the left of C2 is determined by the following equation.

$$R_{TH} = (R_M + Ra) // Rb // Rc \quad (B.7)$$

By applying  $f_c$  and resistors to the following equation,

$$f_c = \frac{1}{2\pi R_{TH} C_2} \quad (B.8)$$

$C2 = 47\text{pF}$  is yielded and suitable for 2.5MHz sampling rate.

As  $R_a$  and  $R_b$  represent a series combination of two resistors as mentioned in Equation (B.1) and (B.2), we need to use standard resistor values to produce close approximations to the desired resistance value. The circuit in Figure B.3 shows the final resistor and capacitor values in red and the active circuit in blue.

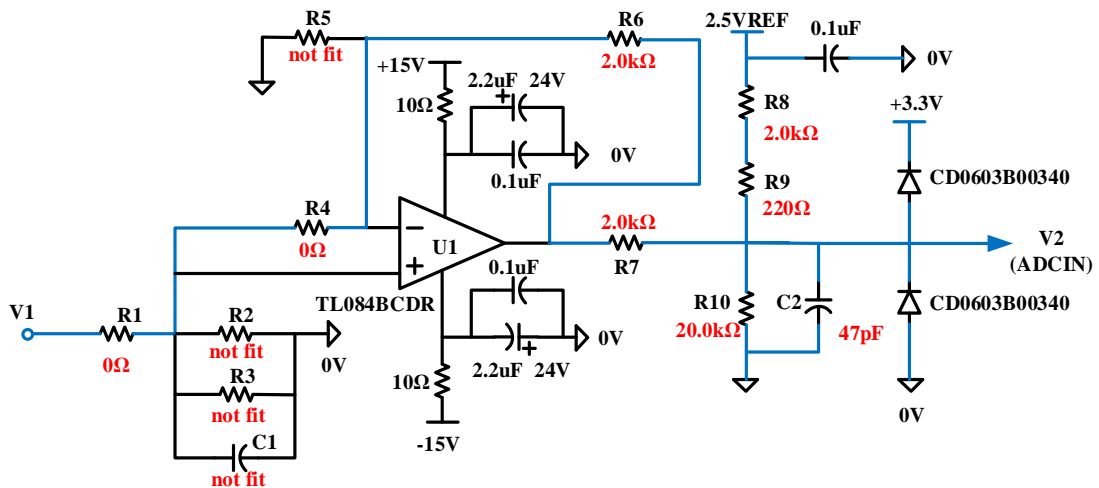


Figure B.3 Final schematic of general interface circuitry between LA 55-P and the DSP

The design method of interface for voltage sensor LV 25-P is very similar with LA 55-P, LV 25-P output current has a peak to peak range of  $\pm 25\sqrt{2}$  mA. A measuring resistance of  $200\Omega$  is chosen to produce an output voltage range of  $\pm 7.07$  V. Figure B.4 is the simplified schematic of general interface circuitry between LV 25-P and general control board. An  $100\text{k}\Omega$  external resistor  $R_{EXT}$  is selected and installed in series with the primary circuit of the transducer.

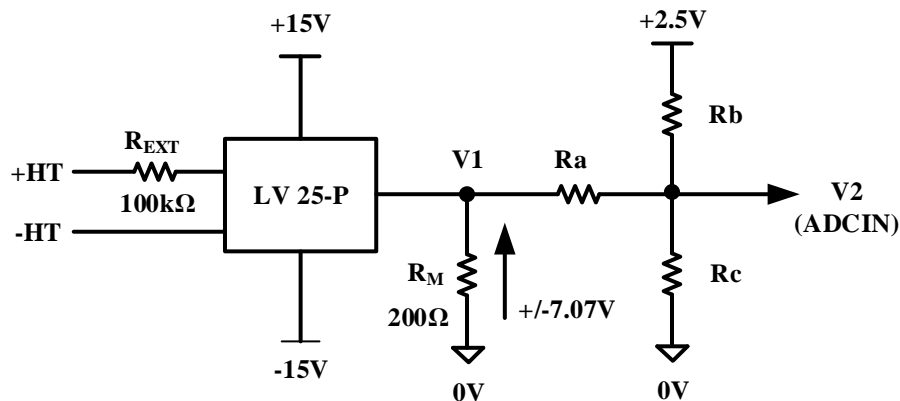


Figure B.4 Simplified schematic of interface circuitry between LV 25-P and the DSP

## Appendix B

It is necessary to find values for  $R_a$ ,  $R_b$  and  $R_c$  which will map the  $\pm 7.07V$  range at  $V_1$  to the 0-3V range at  $V_2$ . To solve for the resistance values, substitute the corresponding end-of-range values for  $V_1$  and  $V_2$ .

Negative end of range:  $V_1 = -7.07V$ ,  $V_2 = 0V$

$$\frac{(2.5-0)}{R_b} + \frac{(-7.07-0)}{R_a} = \frac{0}{R_c} \quad (\text{B.9})$$

Positive end of range:  $V_1 = +7.07V$ ,  $V_2 = 3V$

$$\frac{(2.5-3)}{R_b} + \frac{(7.07-3)}{R_a} = \frac{3}{R_c} \quad (\text{B.10})$$

An initial choice of  $R_c = 10k\Omega$  is made, and then apply it to Equation (B.9) and (B.10),  $R_a = 8.93k\Omega$  and  $R_b = 3.15k\Omega$  are yielded. By applying  $f_c$  and equivalent resistance to Equation (B.7) and (B.8),  $C_2 = 39pF$  is yielded and suitable for 2.5MHz sampling rate.

Same as current transducer interface, all the standard resistor values are chose to produce close approximations to the desired resistance value. Figure B.5 shows the final resistor and capacitor values in red and the active circuit in blue.

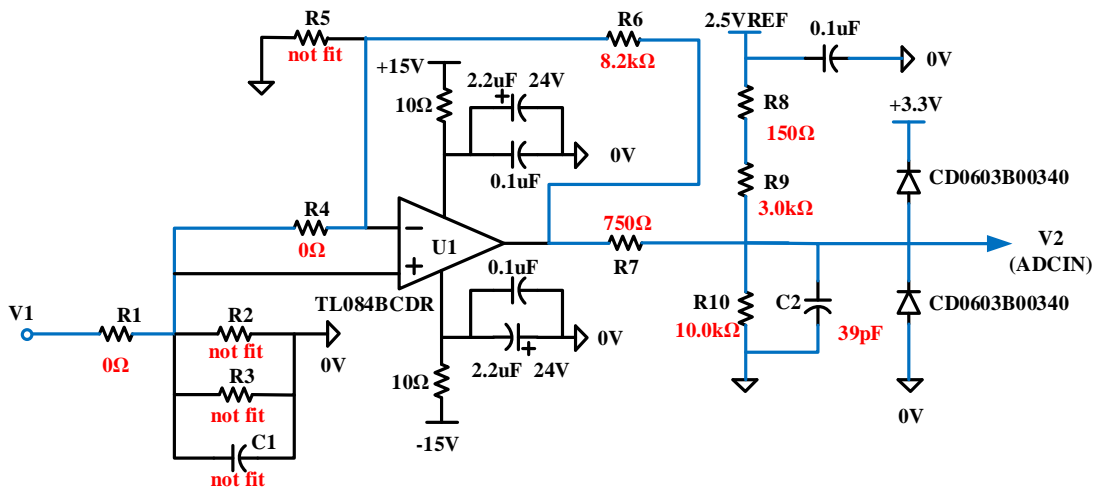


Figure B.5 Final schematic of general interface circuitry between LV 25-P and the DSP

## Appendix C Torsional vibration

The mechanical part of the drive system in this thesis is a typical two-disc torsional rotor system as shown in Figure C. 1. In this case the whole of the rotor is free to rotate as shafts of two electrical machines are mounted on frictionless bearings.

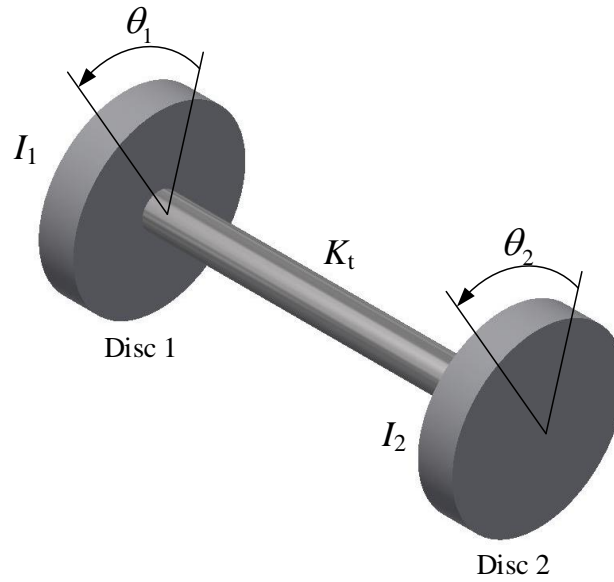


Figure C. 1 A two-disc torsional system

Assuming  $\theta_1$  and  $\theta_2$  are angular displacements of disc 1 and disc 2, respectively. The anti-clockwise direction is chosen as positive direction for both angular displacements.  $I_1$  and  $I_2$  are polar mass moment of inertia of the discs 1 and 2. Therefore,

$$-(\theta_1 - \theta_2)k_t = I_1\ddot{\theta}_1 \quad (\text{C. 1})$$

$$(\theta_1 - \theta_2)k_t = I_2\ddot{\theta}_2 \quad (\text{C. 2})$$

Where  $k_t$  is the torsional stiffness of the shaft, and  $(\theta_1 - \theta_2)$  is the relative twist of the shaft ends.

Expanding the above equations, gives

$$I_1\ddot{\theta}_1 + k_t\theta_1 - k_t\theta_2 = 0 \quad (\text{C. 3})$$

$$I_2\ddot{\theta}_2 + k_t\theta_2 - k_t\theta_1 = 0 \quad (\text{C. 4})$$

For free vibrations, they are simple harmonic motion, thus

$$\ddot{\theta}_1 = -\omega^2 \theta_1 \quad (\text{C. 5})$$

$$\ddot{\theta}_2 = -\omega^2 \theta_2 \quad (\text{C. 6})$$

Substituting Equations (C. 5) and (C. 6) into Equations (C. 3) and (C. 4), gives

$$-I_1 \omega^2 \theta_1 + k_t \theta_1 - k_t \theta_2 = 0 \quad (\text{C. 7})$$

$$-I_2 \omega^2 \theta_2 + k_t \theta_2 - k_t \theta_1 = 0 \quad (\text{C. 8})$$

Assembling Equations (C. 7) and (C. 8) in a matrix form, gives

$$\begin{bmatrix} k_t - I_1 \omega^2 & -k_t \\ -k_t & k_t - I_2 \omega^2 \end{bmatrix} \begin{bmatrix} \theta_1 \\ \theta_2 \end{bmatrix} = 0 \quad (\text{C. 9})$$

The solution of Equation (C. 9) is obtained by taking determinant of the first matrix equal to zero, which gives

$$(k_t - I_1 \omega^2)(k_t - I_2 \omega^2) - k_t^2 = 0 \quad (\text{C. 10})$$

Roots of (C. 10) are

$$\omega_1 = 0 \quad (\text{C. 11})$$

$$\omega_2 = \sqrt{\frac{(I_1 + I_2)k_t}{I_1 I_2}} \quad (\text{C. 12})$$

For the application in the thesis, the generator side inertia (total inertia of the generator rotor and the generator side coupling) is  $I_1=0.0329\text{kgm}^2$ , the motor side inertia (total inertia of the motor rotor and the motor side coupling) is  $I_2=0.0174\text{kgm}^2$ . The total torsional stiffness of the shaft is

$$k_t = \frac{1}{\frac{1}{k_s} + \frac{1}{k_1} + \frac{1}{k_2}} \quad (\text{C. 13})$$

Where  $k_s=5700$  Nm/rad is the torsional stiffness of the torque transducer,  $k_1=3000$  Nm/rad is the torsional stiffness of the generator side shaft and  $k_2=6400$  Nm/rad is the torsional stiffness of the motor side shaft.

Thus the torsional vibration frequency is

$$f_2 = \frac{\omega_2}{2\pi} = \frac{1}{2\pi} \sqrt{\frac{(I_1 + I_2)k_t}{I_1 I_2}} = \frac{1}{2\pi} \sqrt{\frac{(0.0329 + 0.0174) \frac{1}{\frac{1}{5700} + \frac{1}{3000} + \frac{1}{6400}}}{0.0329 \times 0.0174}} = 58\text{Hz} \quad (\text{C. 14})$$